HYPOXIA AND OCEAN ACIDIFICATION
IN TWO LARGE EUTROPHIC ESTUARIES:
PEARL RIVER ESTUARY AND CHESAPEAKE BAY

by

Jianzhong Su

A dissertation submitted to the Faculty of the University of Delaware in partial fulfillment of the requirements for the degree of Doctor of Philosophy in Oceanography

Fall 2019

HYPOXIA AND OCEAN ACIDIFICATION

IN TWO LARGE EUTROPHIC ESTUARIES:

PEARL RIVER ESTUARY AND CHESAPEAKE BAY

by

Jianzhong Su

Approved: ____
Mark A. Moline, Ph.D.
Director of the School of Marine Science and Policy

Approved: ____
Estella Atekwana, Ph.D.
Dean of the College of Earth, Ocean, and Environment

Approved: ____
Douglas J. Doren, Ph.D.
Interim Vice Provost for Graduate and Professional Education and
Dean of the Graduate College

I certify that I have read this dissertation and that in my opinion it meets the academic and professional standard required by the University as a dissertation for the degree of Doctor of Philosophy.

Signed: ____

Wei-Jun Cai, Ph.D.
Supervisor, Professor in charge of dissertation

I certify that I have read this dissertation and that in my opinion it meets the academic and professional standard required by the University as a dissertation for the degree of Doctor of Philosophy.

Signed: ____

Minhan Dai, Ph.D.
Supervisor, Member of dissertation committee

I certify that I have read this dissertation and that in my opinion it meets the academic and professional standard required by the University as a dissertation for the degree of Doctor of Philosophy.

Signed: ____

George W. Luther III, Ph.D.
Member of dissertation committee

I certify that I have read this dissertation and that in my opinion it meets the academic and professional standard required by the University as a dissertation for the degree of Doctor of Philosophy.

Signed: ____

William J. Ullman, Ph.D.
Member of dissertation committee

I certify that I have read this dissertation and that in my opinion it meets the academic and professional standard required by the University as a dissertation for the degree of Doctor of Philosophy.

Signed: ____

Jeremy M. Testa, Ph.D.
Member of dissertation committee

ACKNOWLEDGMENTS

I am so proud that I have two supervisors, Dr. Minhan Dai in Xiamen University (XMU) and Dr. Wei-Jun Cai in University of Delaware (UD). I sincerely thank Dr. Minhan Dai for his endless patience, tremendous support and encouragement. I have benefited greatly from what he has taught me, his persistence in critical thinking and high data quality, and his objective and prudent attitude toward resolving a scientific question. Especially thank him for giving me a great opportunity to join the XMU-UD Oceanography dual-degree program. I would also like to express my sincere gratitude to Dr. Wei-Jun Cai for his invaluable guidance, knowledge, and enthusiasm. He is always available for insightful discussion and quick responses to my questions and requests. Thank him for inspiring me to research with clear objectives as well as joy. Thank both of them for dedicating to my development as a scientist and a person.

I would like to thank my committee, Dr. George Luther, Dr. William Ullman, and Dr. Jeremy Testa for their diverse perspectives, helpful suggestions, and generous guidance on my research. I really appreciate the time and expertise they have provided.

I would like to thank Liguo Guo and Yi Xu (XMU) for training me how to perform good measurement on carbonate parameters, and their help and encouragement on my work. I would also thank Dr. Xianghui Guo, Dr. Biyan He, and Dr. Shuh-Ji Kao for their kind help on the cruises and solving my puzzles about the data as well as science. I really appreciate Dr. Najid Hussain (UD) for his hard working on sample analysis and providing generous help on my lab work.

I would like to thank my fellow lab members, past and present for their tremendous help: Qian Li, Huade Zhao, Hongjie Wang, Chao Zhang, Yan Li, Yawen Wei, Yingxu Wu, Ehui Tan, Tengxiang Xie, Li Ma, Shengyao Sun, Chenhe Zheng, Feifei Meng, Aiqin Han, Wei Qian, Baoshan Chen, Jean Brodeur, Yuanyuan Xu, Michael Scaboo, Ouyang Zhangxian, and Xue Deng. I also appreciate all the kindness from many faculty, staff and students who helped me to pursue my research goals.

I am very grateful to my family and friends for their understanding and support. I would have never gotten this far without their encouragement. Especially thank my wife for accompanying me through this wonderful journey, and giving me the best gift in the world, my son Oliver.

The research in the Pearl River Estuary (PRE) was funded by the National Natural Science Foundation of China through grants 41130857, 41576085 and 41361164001, and by the Hong Kong Research Grants Council under the Theme-based Research Scheme (TRS) through Project No. T21-602/16R. The work in the Chesapeake Bay (CB) was supported by the U.S. National Oceanic and Atmospheric Administration through grants of NA15NOS4780184, NA18NOS4780179, and NA15NOS4780190. I would also like to thank the collaborators from the research groups of Drs. Jianping Gan, Fengling Yu in the PRE project, and Drs. Jeremy Testa, Ming Li, Jeffrey Cornwell, Cassie Gurbisz, George W. Waldbusser, Chaoying Ni, Deb P. Jaisi in the CB project for their contributions to my manuscripts.

TABLE OF CONTENTS

Appendix

LIST OF TABLES

LIST OF FIGURES

ABSTRACT

Eutrophication-induced hypoxia in the coastal oceans has increased in spatial extent, duration, and severity since at least the 1950s. The sources of organic matter that fuels microbial degradation remain an issue closely related to the policy-making and management strategies. The Pearl River Estuary and the Chesapeake Bay, two of the largest estuaries in the world, both suffer from eutrophication and subsequent hypoxia with different severity under distinct hydrological settings and physical forcing. We conducted field surveys in these two large eutrophic estuaries to reveal the spatial distributions of carbonate system and oxygen, to distinguish the main biogeochemical control, and to quantify the relative contributions of allochthonous (terrestrial) and autochthonous (marine) organic matter to oxygen consumption in the hypoxic zones. Eutrophication can also enhance ocean acidification in the coastal regions. However, less is known about how eutrophic and seasonally hypoxic and anoxic water bodies resist coastal acidification. Based on a spatially-decoupled patterns of removal and addition of Ca^{2+}, TA, and DIC along the main stem of the Chesapeake Bay as well as mineralogical evidence, we reveal that the recovering submerged aquatic vegetation induced by sustained nutrient reduction can serve as an efficient factory to produce $CaCO_3$ solids, which are subsequently transported into the downstream corrosive subsurface waters, and dissolve to buffer pH decrease. This positive feedback to coastal restoration can shed light on eutrophication and acidification studies in coastal systems emerging with recovery signs.

Chapter 1

INTRODUCTION

1.1 Coastal eutrophication and hypoxia

Eutrophication is defined as an increase in the rate of supply of organic matter to an ecosystem (Nixon, 1995). Nutrient enrichment is recognized as the most important cause of eutrophication among other drivers, such as water turbidity declines, water residence time increases, and declines in grazing pressure on phytoplankton (Nixon, 2009). Excessive nutrient inputs to the coastal areas stimulate primary production and consequently fuel the microbial degradation of phytoplankton-derived organic material, which consumes oxygen and produces carbon dioxide (CO_2) (Fennel and Testa, 2018). Once the dissolved oxygen (DO) concentration decreases to < 2 mg L^{-1}, it meets a threshold commonly defined as hypoxia (Vaquer-Sunyer and Duarte, 2008; Rabalais et al., 2010). Eutrophication-induced hypoxia in the coastal oceans has increased in spatial extent, duration, and severity since at least the middle of the twentieth century (Diaz and Rosenberg, 2008; Zhang et al., 2013; Rabalais et al., 2014). There are more than 500 hypoxic sites in the coastal waters reported since 1950, and few of them (< 10%) were ever known to have hypoxia before 1950 (Breitburg et al., 2018). Coastal hypoxia is detrimental to a variety of aquatic and benthic organisms and habitats, causing mass mortality, habitat loss, and enhancement of benthic nutrient efflux to the overlying water column, which would further degrade the coastal environments (Breitburg, 2002; Rutger et al., 2002; Wu, 2002). The increase of eutrophication-induced hypoxia and its subsequent detrimental effects on ecosystems have made hypoxia a focus of scientific research and applied science in recent decades (Rabalais et al., 2014).

1.2 Principle of hypoxia formation

Coastal hypoxia in systems subject to anthropogenic perturbations can have different temporal and spatial scales of variability. Time scales vary from hours and days (diel or episodic) to weeks and months (seasonal) to year-round and decades (persistent), while spatial scales vary from small tributaries to rivers and estuaries to bays and inland seas to inner shelves (Diaz and Rosenberg, 2008; Kemp et al., 2009; Rabalais et al., 2010). Although hypoxic conditions span wide temporal and spatial ranges, the principles of hypoxia formation are fundamental (Fig. 1.1) (Rabalais et al., 2010; Cai et al., 2011). Typically, thermohaline stratification provides a physical barrier to impede oxygen replenishment from the surface to the bottom water (Kemp et al., 2009). The rich nutrients in riverine inputs usually stimulate high primary production in the estuarine/coastal regions, supplying large amounts of organic matter to the isolated bottom water. Then, the microbial degradation of organic matter may consume oxygen at a faster rate than reaeration of the bottom water, eventually resulting in the occurrence of hypoxia (Kemp et al., 2009; Rabalais et al., 2010; Zhang et al., 2010). In other words, the organic matter is the ultimate cause of hypoxia under favorable physical settings (Rabouille et al., 2008; Rabalais et al., 2014).

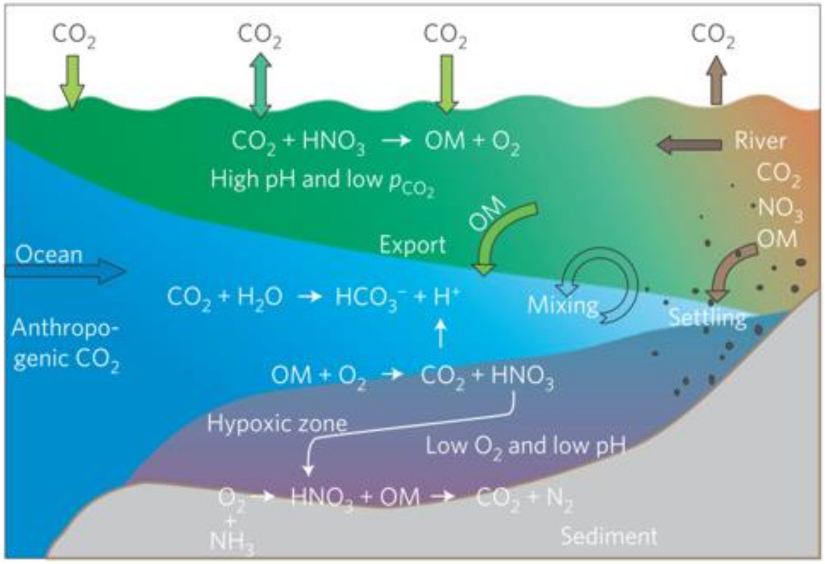

Figure 1.1: A conceptual model for eutrophication-induced hypoxia and enhanced acidification in the coastal subsurface water (Cited from Cai et al. (2011)). River runoff delivers nutrient and organic matter from the land to the coastal ocean, and nutrient enrichment stimulates high primary production in the surface water. Subsequent settling and respiration of the organic matter below the pycnocline consumes oxygen and produce CO_2 and acid, resulting in the concurrence of hypoxia and enhanced acidification in the coastal subsurface water.

1.3 Debate about the sources of oxygen-consuming organic matter

The oxygen-consuming organic matter may come from outside the aquatic system (i.e., allochthonous source) or be internally generated within the system (i.e., autochthonous source) (Paerl, 2006; Rabalais et al., 2010). The allochthonous organic matter (Alloc-OC) is usually derived from the land, including not only natural inputs such as vascular plant detritus, soil leaching and erosion, but also anthropogenic inputs such as municipal and industrial wastewater, and agricultural runoff. In contrast, autochthonous organic matter (Autoc-OC) usually refers to the eutrophication-stimulated primary production of phytoplankton in the estuaries/bays/coastal oceans.

The Autoc-OC is conventionally considered to be more labile (i.e., higher quality) than the Alloc-OC. A main reason is that algae do not require the carbon rich polymeric materials (e.g., lignin, cellulose and hemicellulose) included in physical support structures as the terrestrial vascular plants, and are thus more nitrogen and aliphatic rich than terrestrial organic matter (Hedges and Oades, 1997; Baldock et al., 2004). Therefore, a large amount of literature suggests that Auto-OC dominates oxygen consumption in the coastal hypoxia (Zimmerman and Canuel, 2000; Boesch et al., 2009; Carstensen et al., 2014; Rabalais et al., 2014).

However, recent studies propose a changing paradigm that the terrestrial organic matter is less degraded than what we previously thought (i.e., terrestrial organic matter represents highly degraded remnants of vascular plant sources that have aged in soils), and can be even more labile due to a priming effect (Bianchi, 2011). The priming effect means the enhanced degradation of recalcitrant organic matter in the presence of possible priming substrates, such as phytoplankton exudates, heterotroph metabolites and high nutrient cycling (Bianchi 2011), which eventually leads to the enhanced release of OM-derived carbon and nutrient as well as the enhanced consumption of oxygen. For instance, on the Louisiana continental shelf, evidence from long gravity cores suggested that enhanced river discharge and associated terrestrial organic matter input significantly contributed to the formation of recurring, natural bottom water hypoxia over at least the last 1000 ^{14}C years (Swarzenski et al., 2008). Moreover, isotopic and chemical biomarkers indicated that terrestrial organic matter from the Mississippi River and adjacent coastal marshes was comparatively less degraded, and experienced enhanced post-depositional decay in the fluid muds across the Louisiana shelf, which might thus be an important source to oxygen consumption (Bianchi et al., 2011). Additionally, Wang et al. (2018a) illustrated that terrestrial organic matter contributed significantly to oxygen consumption in river-dominated low salinity regions, while marine organic matter overwhelmingly fueled microbial degradation and drove the formation of hypoxia in the high-salinity shelf area in the northern Gulf of Mexico (Wang et al., 2018a). Quantifying the relative contributions from Alloc-OC vs. Autoc-OC to oxygen consumption is closely related to the policy-making and management strategies that aim to reverse the negative effects of eutrophication and consequent hypoxia. Therefore, it is very important to quantify the distinct fractions of oxygen-consuming organic matter pool, because reducing the organic loading from land would require different management strategies relative to reducing nutrient loads (Rabalais et al., 2010).

1.4 Eutrophication and hypoxia in the Pearl River Estuary

The Pearl River is the second largest river in China and ranks the thirteenth in the world in terms of freshwater discharge (Cai et al., 2004; Dai et al., 2008). It consists of three tributaries, and discharges into the northern South China Sea through three sub-estuaries via eight outlets (Guo et al., 2008). Lingding yang, the largest sub-estuary, is conventionally regarded as the Pearl River Estuary (PRE), which is surrounded by several large urban areas including Guangzhou, Shenzhen, Zhuhai, Hongkong, and Mecau. The large human population, rapid economic development and urbanization have contributed to a series of environmental problems, such as eutrophication (Huang et al., 2003; Dai et al., 2008), harmful algae blooms (Huang et al., 2004), and hypoxia in the PRE (Yin et al., 2004; Dai et al., 2006; Ye et al., 2012; He et al., 2014; Qian et al., 2018).

In the upper estuary (i.e., upstream of Humen Outlet), dissolved inorganic nitrogen concentration of the freshwater endmember could reach up to 760 μmol L^{-1}, 570 μmol L^{-1} and 380 μmol L^{-1} in winter, spring and summer, respectively (Dai et al., 2014). Hypoxia occurs year-round throughout the water column in the severely polluted, turbid and well mixed upper estuary (He et al., 2014). Oxygen budget analysis demonstrated that microbial respiration of allochthonous organic matter and nitrification of ammonia from sewage discharge and local urban runoff are the two major processes responsible for the severe oxygen depletion, while benthic respiration and primary production appeared to be minor contributors (Dai et al., 2008; He et al., 2014). The mid-estuary (i.e., inner Lingdingyang) is dominated by physical mixing between river water and seawater, thus hypoxia is commonly absent in this region (Guo et al., 2009; Qian et al., 2018).

In the lower estuary (i.e., outer Lingdingyang and adjacent coastal waters), dissolved inorganic nitrogen concentration decreases rapidly to below ~50-100 μmol L^{-1} in all seasons, due to mixing and dilution by seawater and utilization by phytoplankton primary production as the turbidity decreases and light availability increases (Dai et al., 2014). Geochemical and microfaunal evidence showed that severe oxygen depletion in the bottom water likely began to appear since the late 1970s (Ye et al., 2012). In contrast to the year-round hypoxia in the upper estuary, the hypoxia in the lower estuary was reported as an episodic phenomenon in summer (Yin et al., 2004; Rabouille et al., 2008; Ye et al., 2012; Qian et al., 2018), due to its shallow depth, short water residence time and relatively strong physical forcings (e.g., current, tide, wind-driven mixing, typhoon) (Rabouille et al., 2008). A recent study revealed that eutrophication and primary production have been increasing and the annual minimum bottom water DO has been declining over the past 25 years, suggesting that the lower PRE has emerged as a seasonal hypoxic zone (Qian et al., 2018). Several studies have used the bulk composition parameters (C/N, $\delta^{13}C$ and $\delta^{15}N$) and biomarkers to explore the distribution and sources of organic matter in surface sediments of the lower PRE and the adjacent coastal water (Hu et al., 2009; He et al., 2010; Yu et al., 2010). However, no studies have focused on tracing the origin of oxygen-consuming organic matter, which really participates in the oxygen consumption and drives hypoxia formation. These studies are essential to gain our knowledge of hypoxia formation in a highly eutrophic estuary under dynamic physical settings, and are urgently needed by policy-makers to recognize the key drivers of hypoxia and take efficient and sufficient measures to reverse the passive effects of eutrophication and hypoxia.

1.5 Eutrophication and hypoxia in the Chesapeake Bay

The Chesapeake Bay is the largest estuary in the United States. Due to a large watershed area and long dendritic bay shorelines, the Chesapeake Bay is susceptible to human perturbations, and suffers from long-term eutrophication and hypoxia/anoxia (Kemp et al., 2005). Eutrophication in the Chesapeake Bay began after European colonization in the 17^{th} and 18^{th} centuries (Brush, 2009), and the nutrient loading increased steadily from the 1950s through the late-1980s (Hagy et al., 2004), after which loads stabilized and declined as a result of sustained management actions (Lefcheck et al., 2018). Seasonal bottom water hypoxia and anoxia begin to develop in the deep main channel in late spring and decline in late summer or early fall (Hagy et al., 2004; Murphy et al., 2011). Based on a long-term dataset during 1950 to 2001, Hagy et al. (2004) revealed that the summer hypoxic volumes in the Chesapeake Bay have increased significantly and dramatically, with a trend expanding more southward and closer to the water surface. Through analyzing more recent data (1984-2009), Murphy et al. (2011) further demonstrated that hypoxic volume significantly increased in early summer (June to the first half of July), which is largely controlled by enhanced water stratification, and slightly decreased in late summer (late July to August), which is mainly regulated by the reducing nutrient loading. Moreover, a recent study has attributed the earlier hypoxia peak and breakup in 2000-2015 (vs. 1985-1999) to the winter-ward and north-ward migration of the spring bloom (Testa et al., 2018).

There is a distinct regional trend of net ecosystem metabolism (production minus respiration) along the salinity gradient in the Chesapeake Bay, with net heterotrophy prevailing in the upper bay, balanced metabolism in the mid-bay and net autotrophy in the lower bay (Kemp et al., 1997). The net heterotrophy is caused by the allochthonous organic matter input from river runoff and high turbidity, which enhances respiration and inhibits photosynthesis (Smith and Kemp, 1995). As the turbidity decreases seaward, the nutrient-stimulated primary production dominates the organic matter pool from the mid- to lower bay (Flemer, 1970; Smith and Kemp, 1995; Kemp et al., 1997). Many studies have discussed the source and fate of the existing organic matter in the surface sediment or suspended particulate organic matter in the Chesapeake Bay (Biggs, 1970; Biggs and Flemer, 1972; Roden et al., 1995; Kemp et al., 1997; Fisher et al., 1998), among which some were based on bulk composition parameters or/and biomarkers (Horrigan et al., 1990; Canuel and Zimmerman, 1999; Canuel, 2001; Sigleo and Macko, 2002; Zimmerman and Canuel, 2002; Bratton et al., 2003; Loh et al., 2006). Despite these extensive studies, none of them have included direct quantitative measurements of the relative contributions of Autoc-OC vs. Alloc-OC to oxygen consumption in the hypoxic zone of the Chesapeake Bay. Such studies are necessary to reinforce budget analyses and to improve our understanding of hypoxia drivers, within the context of climate change (Najjar et al., 2010; Orth et al., 2017) and recent nutrient reductions (Lefcheck et al., 2018; Testa et al., 2018).

1.6 Indicators for the source of the existing organic matter

Bulk organic $\delta^{13}C$ and C/N ratios are widely used as powerful indicators to trace the origin and flow of organic matter in the estuaries and marshes (Fig. 1.2) (Peterson et al., 1985; Cifuentes et al., 1988; Fogel et al., 1989; Thornton and McManus, 1994). Terrestrial plants are typically depleted in nitrogen compounds with C/N > 14, while freshwater/marine phytoplankton and bacterioplankton OM sources are characterized by higher nitrogen content with C/N < 8 (Goñi et al., 2003). Moreover, C3 vascular plants are characterized by an isotopic composition that is relatively depleted in ^{13}C with $\delta^{13}C$ < -25‰, while C4 plants such as *Spartina* show significantly more enriched $\delta^{13}C$ values (~ -13‰) (Peterson and Fry, 1987). Marine phytoplankton exhibits intermediate values (-21~ -18‰) (Fry and Sherr, 1989). However, freshwater algae is characterized by a broader range of $\delta^{13}C$ (-30~ -25‰) due to the different concentrations and sources of DIC in these environments (Lamb et al., 2006).

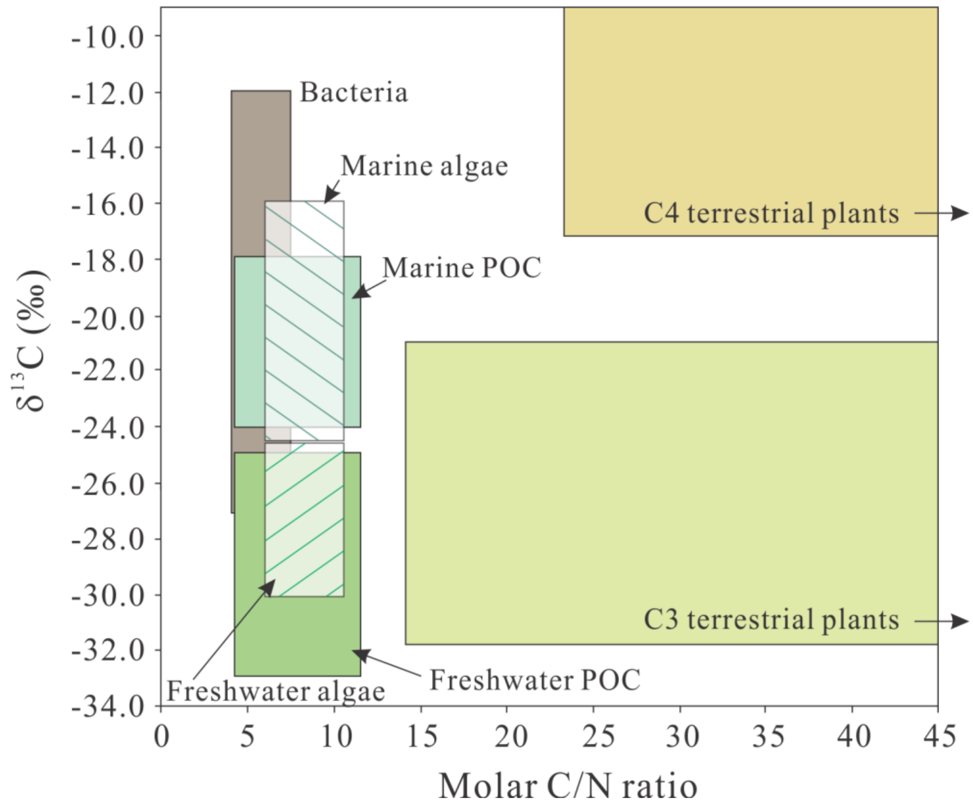

Figure 1.2: Typical ranges of δ^{13}C and molar C/N ratio for organic inputs to coastal environments, modified from Fig. 2 in Lamb et al. (2006). Note that weight ratio adopted in the original figure was converted into molar ratio by multiplying by 1.17.

More recently, proxies based on biomarker (e.g., lipid, sterol, pigment and lignin) contents and ratios provide an alternative approach to distinguish the origins of organic matter (Meyers, 1997; Hu et al., 2009; Xing et al., 2011). Although the biomarker molecules can convey detailed information of individual sources and diagenetic pathways, they only account for a very small fraction of the total organic mixture and cannot represent the whole mixture. On the contrary, the organic δ^{13}C and C/N ratio can represent the bulk composition of the entire mixture and are used more prevalently in studies examining the source and fate of organic matter in the coastal environments (Meyers, 1997; Lamb et al., 2006).

Most source partitioning studies in the estuarine and coastal sediments build on the assumptions that the isotopic ratios are conservative, and the isotopic distributions of organic matter are completely determined by the physical mixing of different endmember sources (Cifuentes et al., 1988). One can use the measured organic $\delta^{13}C$ only or $\delta^{13}C$ plus C/N of the samples, and those of the terrestrial and marine endmembers, to calculate their relative contribution fractions via a simple two endmember isotopic mixing model (He et al., 2010; Yu et al., 2010). However, these fractions can only represent the source information of the existing organic matter pool, but may not be able to represent that of the oxygen-consuming organic matter pool, which has already been oxidized by oxygen (i.e., this portion has disappeared after the microbial degradation). Whether organic matter is remineralized mainly depends on its quality rather than its quantity. Therefore, tracing the origin of oxygen-consuming organic matter cannot be resolved in a manner similar to that is widely used to differentiate the terrestrial/marine sources of the existing organic matter. A novel approach is needed to resolve the above question.

1.7 DIC and $\delta^{13}C$-DIC based method to trace the origin of the "disappeared" oxygen-consuming organic matter

In the process of aerobic respiration of organic matter (e.g., $(CH_2O)_{106}(NH_3)_{16}H_3PO_4+138O_2 \rightarrow 106CO_2+16HNO_3+H_3PO_4+122H_2O$), the organic matter (substrate) consumes oxygen and produces CO_2 (product). Then CO_2 is further dissociated into other inorganic carbon species ($CO_{2(gaseous)} \leftrightarrow CO_{2(aqueous)} \leftrightarrow H_2CO_3 \leftrightarrow HCO_3^- \leftrightarrow CO_3^{2-}$), increasing the pool of total dissolved inorganic carbon (DIC). Since aerobic respiration of organic matter typically produces DIC with minor isotopic fractionation from the substrate organic matter (Hullar et al. 1996; Breteler et al. 2002; Lehmann et al. 2002), the $\delta^{13}C$ value of the added DIC should be identical to the isotopic composition of the respired organic matter ($\delta^{13}C_{OCx}$), which is more ^{13}C-depleted as a mixture of terrestrial (< -25‰) and marine (-21~ -18‰) organic sources. Once one determines the $\delta^{13}C_{OCx}$, one can calculate the relative contributions from terrestrial and marine origins with $\delta^{13}C_{OCx}$, $\delta^{13}C_{terrestrial}$ and $\delta^{13}C_{marine}$ based on a two endmember isotopic mixing model. Overall, the big challenge of this method is to accurately quantify the portion of the added DIC and its stable carbon isotope ($\delta^{13}C$-DIC) released from aerobic respiration of organic matter.

The DIC concentration and its stable isotope composition ($\delta^{13}C$-DIC) have been extensively applied to understand the sources and cycling of carbon in reservoirs (Barth et al., 2017), lakes (Quay et al., 1986; Herczeg, 1987), streams (Doctor et al., 2008), rivers (Hélie et al., 2002; Brunet et al., 2005; Schulte et al., 2011; Sun et al., 2011), estuaries (Hellings et al., 1999; Ahad et al., 2008; Samanta et al., 2015), coastal seas (Alling et al., 2012; Hu et al., 2016; Wang et al., 2016), and the open ocean (Quay et al., 2007; Racapé et al., 2014; Quay et al., 2017). The isotopic composition of carbon released during aerobic respiration can be calculated through mass balance of DIC and its stable isotope. In an exchange-restricted water body, one can assume that the respired carbon is added to water that initially had a uniform DIC and $\delta^{13}C$-DIC (Fry et al., 1991), and get a mass balance equation as below:

$$\delta^{13}C\text{-}DIC_{meas} \times DIC_{meas} = \delta^{13}C\text{-}DIC_{ini} \times DIC_{ini} + \delta^{13}C\text{-}DIC_{resp} \times (DIC_{meas} - DIC_{ini})$$

where the subscripts *meas*, *ini* and *resp* indicate measured value, initial value and respired carbon. This equation can be rearranged:

$$\delta^{13}C\text{-}DIC_{meas} = \left(\delta^{13}C\text{-}DIC_{ini} - \delta^{13}C\text{-}DIC_{resp}\right) \times DIC_{ini} \times \frac{1}{DIC_{meas}} + \delta^{13}C\text{-}DIC_{resp}$$

A linear regression of measured δ^{13}C-DIC against the reciprocal of measured DIC (i.e., 1/DIC) will give the δ^{13}C value of the respired organic matter as the y-intercept (Fry et al., 1991). This method has been used to trace the sources of respired organic matter in hydrologically stable waters, such as incubation experiments (Wang et al., 2018b), permanently stratified fjord (van Breugel et al., 2005), and subsurface water in the Black Sea and the Cariaco Trench (Fry et al., 1991).

However, the δ^{13}C-DIC vs. 1/DIC method cannot be applied to hydrologically dynamic environments like estuaries and coastal waters where large salinity gradients exist, because in such systems the physical mixing (e.g., river water - seawater mixing) usually dominates and other biogeochemical processes (e.g., carbonate dissolution and sulfate reduction) may also contribute to the distributions of DIC concentration and its stable isotope. Thus, several steps need to be achieved before deriving the δ^{13}C of the respired organic matter. First, one needs to predict the background values resulting from physical mixing via the endmember mixing model. Second, one needs to check if the total non-conservative values (measured-predicted) are induced only by aerobic respiration or not. If not, it is necessary to further decompose the total non-conservative values into multiple components affected by each biogeochemical process. Finally, one can derive δ^{13}C value of respired organic matter from the slope of the regression between Δ(DIC×δ^{13}C-DIC) and ΔDIC, where ΔDIC is the portion of biological DIC addition solely caused by aerobic respiration (Wang et al., 2016; Su et al., 2017; Wang et al., 2018a). An example of this approach was presented by Wang et al. (2016) in the hypoxic zone of the East China Sea off the Changjiang Estuary. They used a three endmember mixing model to remove the influence of water mass mixing, then confirmed aerobic respiration as the predominant process controlling DIC and oxygen, and finally derived the $\delta^{13}C$ value of respired organic matter as -18.5‰. Thus, they concluded that marine organic matter overwhelmingly contributed to the oxygen consumption in the hypoxic zone.

Considering the dynamic estuarine circulation in both the Pearl River Estuary and the Chesapeake Bay, we applied a three endmember mixing model to the lower Pearl River Estuary and a two endmember mixing model to the Chesapeake Bay following previous work (Han et al., 2012; Cai et al., 2017). Multiple biogeochemical tracers (O_2, Ca^{2+}, H_2S) were used to quantify the fractions of DIC influenced by aerobic respiration, carbonate dissolution, and sulfate reduction in the sub-pycnocline waters. The $\delta^{13}C$ value of the respired organic matter was then derived based on mass balance of DIC and its stable isotope. Note that we also developed a novel analysis approach that can simultaneously measure DIC and $\delta^{13}C$-DIC with high accuracy and precision comparable to the traditional methods of non-dispersive infrared absorption (NDIR) for DIC analysis and isotope ratio mass spectrometry (IRMS) for $\delta^{13}C$-DIC analysis (Appendix A). By combining those analyses with an examination of the bulk composition (C/N, $\delta^{13}C$) of the suspended particulate organic matter in the surface water along the full salinity gradient, we were able to quantify the sources of oxygen-consuming organic matter. Finally, we compared the source partitioning results in the hypoxic zones of the Chesapeake Bay with the Pearl River Estuary, in order to gain new insights on the formation and maintenance of hypoxia. The case studies on source partitioning of oxygen-consuming organic matter in the lower Pearl River Estuary and the Chesapeake Bay are presented in Chapter 2 and Chapter 3, respectively.

1.8 Ocean acidification vs. coastal acidification

The CO_2 emission from fossil fuel combustion and land use changes have increased the atmospheric CO_2 concentrations from ~280 ppm in the pre-industrial era to above 400 ppm at present (www.esrl.noaa.gov/gmd/ccgg/trends/) (Canadell et al., 2007; Le Quéré et al., 2015). Meanwhile, the global ocean has captured approximately 30% of the anthropogenic CO_2 emissions from the atmosphere (Sabine et al., 2004), lowering average surface water pH by 0.1 unit and aragonite saturation state (Ω_{arag}) by 0.5 unit. This process, known as ocean acidification (Gattuso et al., 2015; Feely et al., 2017), is harmful to many marine organisms and ecosystems (Orr et al., 2005; Fabry et al., 2008; Kroeker et al., 2013).

In contrast, pH in the coastal ocean has more intense variability and more controls than the classic ocean acidification (see Fig. 1.3), which is primarily caused by the increasing oceanic uptake of anthropogenic CO_2 emission. For instance, the diel changes of pH can reach as high as 1.0 unit over the average in the metabolic-intense ecosystems (e.g., salt marshes, seagrass meadows, mangroves and coral reefs) (Duarte et al., 2013), which is significantly larger than that of the open ocean (~0.1 unit). The regulation of pH in coastal waters is much more complex as it depends on the processes affecting pH in the open ocean as well as watershed/river inputs, the upwelling of CO_2 enriched deep water, hydrological mixing, atmospheric acid deposition, and ecosystem metabolism (Feely et al., 2010; Duarte et al., 2013; Wallace et al., 2014). As a result, the observed trends in surface water pH in coastal ecosystems display a variety of patterns, including periods of stable, increasing and decreasing pH (Waldbusser et al., 2011; Duarte et al., 2013).

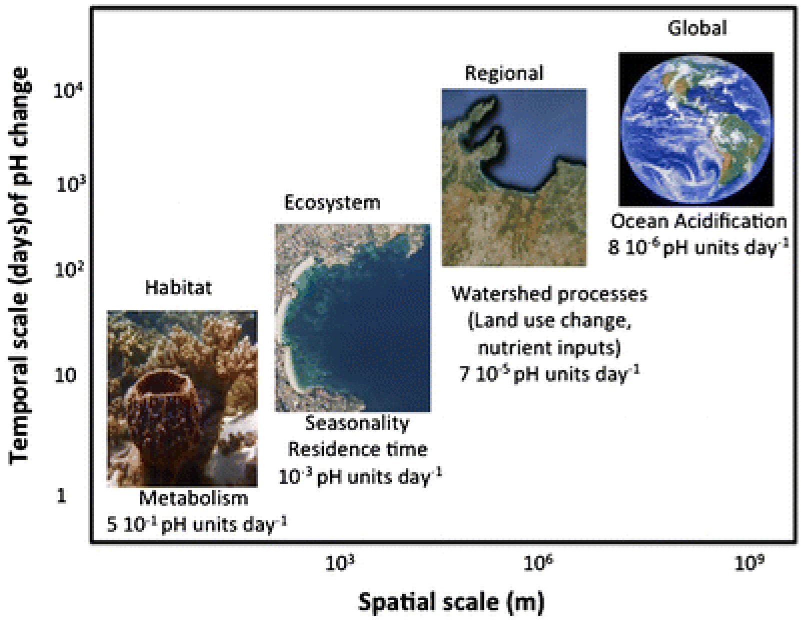

Figure 1.3: Conceptual diagram showing the multiple processes regulating pH in a wide range of spatial and temporal scales (Cited from Duarte et al. (2013)). The characteristic change rate of pH increases as the spatial scale decreases.

1.9 Enhanced coastal acidification

As mentioned in section 1.1, nutrient enrichment in coastal waters has caused the accumulation of algal biomass, and the subsequent microbial degradation of this labile organic matter consumes oxygen and contributes to the formation of hypoxia. The same aerobic respiration process ($(CH_2O)_{106}(NH_3)_{16}H_3PO_4+138O_2 \rightarrow 106CO_2+16HNO_3+H_3PO_4+122H_2O$), however, also produces CO_2 and acid, lowering the pH in the hypoxic zone (see Fig. 1.1). Thus, the eutrophication is also regarded as an important regulator controlling the pH dynamics or acidification in the coastal ocean (Sunda and Cai, 2012; Wallace et al., 2014; Feely et al., 2017). The effects of eutrophication on carbonate chemistry can exceed that of the classic ocean acidification from anthropogenic CO_2 by either increasing pH where primary production dominates (Borgesa and Gypensb, 2010), or decreasing pH where respiration dominates (Cai et al., 2011), the latter of which is usually associated with coastal hypoxia (Feely et al., 2010; Feely et al., 2017). For instance, Cai et al. (2011) revealed that the present pH in the oxygen-depleted sub-pycnocline waters of the northern Gulf of Mexico has decreased as much as 0.45 unit relative to the pre-industrial condition, in which classic ocean acidification contributes 0.11 unit and organic matter respiration contributes 0.29 unit, and the additional drop of 0.05 unit is caused by the decreasing buffering capacity of CO_2-enriched waters. Overall, acidification in the coastal waters can be enhanced by eutrophication and subsequent hypoxia/anoxia via the accumulation of CO_2 and acid, and the weakening of buffering capacity below the pycnocline (Egleston et al., 2010; Feely et al., 2010; Cai et al., 2011; Sunda and Cai, 2012; Hu and Cai, 2013; Hagens et al., 2015; Feely et al., 2017).

1.10 Eutrophication-hypoxia induced $CaCO_3$ dissolution

The addition of CO_2 from the atmosphere and respiration can increase the hydrogen ion and bicarbonate concentrations but decrease the carbonate ion and the saturation state (Ω) of $CaCO_3$ minerals (Feely et al., 2017), which threatens many marine calcifying organisms (Doney, 2006; Doney et al., 2009). The related chemical reactions are described by the equations below:

$CO_{2(aqueous)} + H_2O + CO_3^{2-} \leftrightarrow 2HCO_3^{2-}$

$\Omega = [Ca^{2+}][CO_3^{2-}]/K_{sp}^*$

where $[Ca^{2+}]$ and $[CO_3^{2-}]$ are the concentrations of dissolved calcium and carbonate ions, and K_{sp}^* is the stoichiometric solubility product at saturation for $CaCO_3$ (Feely et al., 2017). When $\Omega>1$, $CaCO_3$ precipitation or preservation is thermodynamically favored; when Ω=1, $CaCO_3$ minerals are in equilibrium with the surrounding water; and when Ω<1, $CaCO_3$ dissolution is favored (Mucci, 1983). The $CaCO_3$ dissolution induced by acidification would otherwise increase the alkalinity of water, and is thus proposed as a buffer to neutralize anthropogenic CO_2 uptake (Andersson et al., 2005; Macreadie et al., 2017). A recent study has demonstrated that $CaCO_3$ dissolution can offset a significant proportion of the metabolic CO_2 in the Chesapeake Bay, thus providing a substantial negative feedback to coastal acidification (Cai et al., 2017).

1.11 $CaCO_3$ formation

Very few studies, however, have linked $CaCO_3$ dissolution to the timing and location of its formation in coastal waters (Abril et al., 2003; Waldbusser et al., 2013). These dynamics are essential to understand, given their capacity to mediate pH and atmospheric CO_2 concentrations (Ware et al., 1992; Cai et al., 2017). While $CaCO_3$ dissolution generates alkalinity and buffers against acidification, the formation of one mole of $CaCO_3$ consumes two moles of bicarbonate and generates one mole of CO_2 ($Ca^{2+}+2HCO_3^- \leftrightarrow CaCO_3+CO_2+H_2O$), which alternatively has the potential to enhance acidification and CO_2 evasion to the atmosphere. In coastal waters, $CaCO_3$ can be formed via abiotic precipitation or biotic production, which are usually associated with coral reefs, calcareous algae (Borowitzka and Larkum, 1987), molluscs (Chauvaud et al., 2003), bacteria (Lesley A. Warren, 2001), fish (Perry et al., 2011) and aquatic plants (Borowitzka, 1984). Recently, seagrass meadows have been shown to be major sites for $CaCO_3$ accumulation and storage in high salinity waters (Mazarrasa et al., 2015). In addition to the seagrass-calcifying algae, infauna and epibiont community, the seagrass *Thalassia testudinum* itself can accumulate needle-like aragonite crystals within its cell walls and externally on the blade surface through biologically induced precipitation (Enríquez and Schubert, 2014). Inside seagrass meadows, the CO_2 released from $CaCO_3$ formation could be utilized by plant photosynthesis and thus not released to the ambient water or atmosphere. Once the $CaCO_3$ crystals escape the seagrass beds (Koch, 1999; Corlett and Jones, 2007), they have a potential to be transported to carbonate-undersaturated water where they can dissolve, increase alkalinity, and reduce the concentration of H^+.

1.12 Acidification and $CaCO_3$ dynamics in the Chesapeake Bay

The Chesapeake Bay is one of the most studied estuarine systems in the world, and has long-term biogeochemical records and an abundant literature on eutrophication, hypoxia/anoxia and organic carbon budgets (Kemp et al., 1997; Kemp et al., 2005; Murphy et al., 2011; Testa et al., 2017). However, the studies on the carbonate system and acidification were quite limited though more related publications have been coming out in recent several years. Two earlier studies examined the CO_2 system and pH in the James and York sub-estuaries and surrounding regions (Wong, 1979; Raymond et al., 2000). Waldbusser et al. (2011a, b) revealed that polyhaline surface water has suffered a long-term pH decline related to eutrophication, and lower pH in the bay waters could reduce oyster biocalcification rate and increase shell dissolution rate, especially for fresh shells. Cai et al. (2017) found a pH minimum at mid water depth where acids were generated as a consequence of oxidation of reduced chemical species (e.g., H_2S, Mn^{2+}, Fe^{2+}) in waters mixed upward from the anoxic depths. They also suggested that a large synergistic effect from river-ocean mixing, global and local atmospheric CO_2 uptake, and CO_2 and acid production from respiration and other redox reactions has led to a weak acid buffering capacity, severe acidification and increased $CaCO_3$ dissolution in the Chesapeake Bay. Brodeur et al. (2019) presented for the first time the observation-based seasonal and spatial distributions of DIC, TA and pH along the main stem of the Chesapeake Bay, and suggested that the large DIC addition in the mesohaline water was likely due to respiration and $CaCO_3$ dissolution. A recent modeling study revealed that reductions in riverine nutrient loading would decrease the acid water volume ($pH<7.5$) and reduce the duration of acidic events when bottom $pH<7.5$ in the mid-bay, but increase the duration in the upper bay (Shen et al., 2019).

As an eutrophic estuary, the Chesapeake Bay supports a productive shellfish industry (Schulte, 2017) and a diverse assemblage of submerged aquatic vegetation (SAV) (Lefcheck et al., 2018). Waldbusser et al. (2013) revealed that oyster calcification (and subsequent shell recycling) had significant impacts on the bay-wide alkalinity budget, but only accounted for a small fraction of the estimated bay-wide alkalinity loss. The SAV beds, as potential hot spots of $CaCO_3$ formation (section 1.11), may account for an important portion of the remaining alkalinity loss. Anthropogenic perturbations have altered the distribution, abundance and diversity of SAV in the shoals of the bay and its tributaries (Orth and Moore, 1983; Moore et al., 2000; Orth et al., 2010), including a bay-wide decline of SAV that began in the 1960s, accelerated in the early 1970s, and continued through 1980 (Orth and Moore, 1984). From 1984 to 2015, SAV was restored with a 316% increase in coverage due to the successful nutrient reduction (section 1.5) (Lefcheck et al., 2018). In particular, there have been widespread SAV resurgences throughout the tidal fresh and oligohaline portions of the mainstem Bay and its tributaries over the last decade (Orth et al., 2010). Brodeur et al. (2019) examined the TA to DIC ratio in the upper bay and speculated about a link between the removal of DIC, TA in the salinity <5 zone and the photosynthesis and $CaCO_3$ formation in the SAV-inhabited tidal fresh flats.

Overall, the Chesapeake Bay is an ideal system to study $CaCO_3$ dynamics because it suffers from hypoxia/anoxia-enhanced acidification and associated bottom-water $CaCO_3$ dissolution, but also supports abundant calcifying organisms. To reveal how a large estuary responds to the dual-stresses of eutrophication and acidification, we examined the spatial and temporal patterns of $CaCO_3$ formation and dissolution in the Chesapeake Bay. A cruise was conducted along the bay channel in August 2016, at a time of peak hypoxia and anoxia and SAV biomass. Supplementary cruises were conducted in the Susquehanna Flats to collect solid samples of surface sediments and SAV leaves. Electron microscopy and X-ray energy dispersive microanalysis were applied to confirm the existence of $CaCO_3$ solids precipitated on the leaf surface within the SAV beds. Non-conservative behaviour of calcium ions (Ca^{2+}), dissolved inorganic carbon (DIC) and TA in the water column was derived using a two endmember mixing model. We also quantified the contributions from different biogeochemical processes to non-conservative DIC and TA, and pH changes based on appropriate chemical proxies and stoichiometry. Finally, we estimated the supply-consumption relationship of $CaCO_3$ and proposed a bay-wide self-regulated pH buffer mechanism. The case study on acidification and $CaCO_3$ dynamics in the Chesapeake Bay is presented in Chapter 4.

REFERENCES

Abril, G., Etcheber, H., Delille, B., Frankignoulle, M. and Borges, A.V., 2003. Carbonate dissolution in the turbid and eutrophic Loire estuary. Mar. Ecol. Prog. Ser. 259, 129-138. doi:10.3354/meps259129

Ahad, J.M.E., Barth, J.A.C., Ganeshram, R.S., Spencer, R.G.M. and Uher, G., 2008. Controls on carbon cycling in two contrasting temperate zone estuaries: The Tyne and Tweed, UK. Estuar. Coast. Shelf Sci. 78, 685-693. doi:10.1016/j.ecss.2008.02.006

Alling, V., Porcelli, D., Mörth, C.M., Anderson, L.G., Sanchez-Garcia, L., Gustafsson, Ö., Andersson, P.S. and Humborg, C., 2012. Degradation of terrestrial organic carbon, primary production and out-gassing of CO_2 in the Laptev and East Siberian Seas as inferred from $\delta^{13}C$ values of DIC. Geochim. Cosmochim. Acta 95, 143-159. doi:10.1016/j.gca.2012.07.028

Andersson, A.J., Mackenzie, F.T. and Lerman, A., 2005. Coastal ocean and carbonate systems in the high CO_2 world of the Anthropocene. Am. J. Sci. 305, 875-918. doi:10.2475/ajs.305.9.875

Baldock, J.A., Masiello, C.A., Gélinas, Y. and Hedges, J.I., 2004. Cycling and composition of organic matter in terrestrial and marine ecosystems. Mar. Chem. 92, 39-64. doi:10.1016/j.marchem.2004.06.016

Barth, J.A.C., Mader, M., Nenning, F., van Geldern, R. and Friese, K., 2017. Stable isotope mass balances versus concentration differences of dissolved inorganic carbon - implications for tracing carbon turnover in reservoirs. Isotopes Environ. Health Stud. 53, 413-426. doi:10.1080/10256016.2017.1282478

Bianchi, T.S., 2011. The role of terrestrially derived organic carbon in the coastal ocean: A changing paradigm and the priming effect. Proc. Natl. Acad. Sci. U.S.A. 108, 19473-19481. doi:10.1073/pnas.1017982108

Bianchi, T.S., Wysocki, L.A., Schreiner, K.M., Filley, T.R., Corbett, D.R. and Kolker, A.S., 2011. Sources of terrestrial organic carbon in the Mississippi plume region: evidence for the importance of coastal marsh inputs. Aquat. Geochem. 17, 431-456. doi:10.1007/s10498-010-9110-3

Biggs, R.B., 1970. Sources and distribution of suspended sediment in northern Chesapeake Bay. Mar. Geol. 9, 187-201. doi:10.1016/0025-3227(70)90014-9

Biggs, R.B. and Flemer, D.A., 1972. The flux of particulate carbon in an estuary. Mar. Biol. 12, 11-17. doi:10.1007/bf00347425

Boesch, D.F., Boynton, W.R., Crowder, L.B., Diaz, R.J., Howarth, R.W., Mee, L.D., Nixon, S.W., Rabalais, N.N., Rosenberg, R., Sanders, J.G., Scavia, D. and

Turner, R.E., 2009. Nutrient Enrichment Drives Gulf of Mexico Hypoxia. Eos, Trans. Amer. Geophys. Union 90, 117-118. doi:10.1029/2009EO140001

Borgesa, A.V. and Gypensb, N., 2010. Carbonate chemistry in the coastal zone responds more strongly to eutrophication than ocean acidification. Limnol. Oceanogr. 55, 346-353. doi:10.4319/lo.2010.55.1.0346

Borowitzka, M.A., 1984. Calcification in aquatic plants. Plant, Cell Environ. 7, 457-466. doi:10.1111/j.1365-3040.1984.tb01436.x

Borowitzka, M.A. and Larkum, A.W.D., 1987. Calcification in algae: Mechanisms and the role of metabolism. Crit. Rev. Plant Sci. 6, 1-45. doi:10.1080/07352688709382246

Bratton, J.F., Colman, S.M. and Seal Ii, R.R., 2003. Eutrophication and carbon sources in Chesapeake Bay over the last 2700 yr: human impacts in context. Geochim. Cosmochim. Acta 67, 3385-3402. doi:10.1016/S0016-7037(03)00131-5

Breitburg, D., 2002. Effects of hypoxia, and the balance between hypoxia and enrichment, on coastal fishes and fisheries. Estuaries 25, 767-781. doi:10.1007/BF02804904

Breitburg, D., Levin, L.A., Oschlies, A., Grégoire, M., Chavez, F.P., Conley, D.J., Garçon, V., Gilbert, D., Gutiérrez, D., Isensee, K., Jacinto, G.S., Limburg, K.E., Montes, I., Naqvi, S.W.A., Pitcher, G.C., Rabalais, N.N., Roman, M.R., Rose, K.A., Seibel, B.A., Telszewski, M., Yasuhara, M. and Zhang, J., 2018. Declining oxygen in the global ocean and coastal waters. Science 359. doi:10.1126/science.aam7240

Brunet, F., Gaiero, D., Probst, J.L., Depetris, P.J., Gauthier Lafaye, F. and Stille, P., 2005. $\delta^{13}C$ tracing of dissolved inorganic carbon sources in Patagonian rivers (Argentina). Hydrological Processes 19, 3321-3344. doi:10.1002/hyp.5973

Brush, G.S., 2009. Historical Land Use, Nitrogen, and Coastal Eutrophication: A Paleoecological Perspective. Estuar. Coast. 32, 18-28. doi:10.1007/s12237-008-9106-z

Cai, W.-J., Dai, M., Wang, Y., Zhai, W., Huang, T., Chen, S., Zhang, F., Chen, Z. and Wang, Z., 2004. The biogeochemistry of inorganic carbon and nutrients in the Pearl River estuary and the adjacent Northern South China Sea. Cont. Shelf Res. 24, 1301-1319. doi:10.1016/j.csr.2004.04.005

Cai, W.-J., Hu, X., Huang, W.-J., Murrell, M.C., Lehrter, J.C., Lohrenz, S.E., Chou, W.-C., Zhai, W., Hollibaugh, J.T. and Wang, Y., 2011. Acidification of subsurface coastal waters enhanced by eutrophication. Nat. Geosci. 4, 766-770. doi:10.1038/NGEO1297

Cai, W.-J., Huang, W.-J., Luther, G.W., Pierrot, D., Li, M., Testa, J., Xue, M., Joesoef, A., Mann, R., Brodeur, J., Xu, Y.-Y., Chen, B., Hussain, N., Waldbusser, G.G., Cornwell, J. and Kemp, W.M., 2017. Redox reactions and weak buffering capacity lead to acidification in the Chesapeake Bay. Nat. Commun. 8, 369. doi:10.1038/s41467-017-00417-7

Canadell, J.G., Le Quéré, C., Raupach, M.R., Field, C.B., Buitenhuis, E.T., Ciais, P., Conway, T.J., Gillett, N.P., Houghton, R.A. and Marland, G., 2007.

Contributions to accelerating atmospheric CO_2 growth from economic activity, carbon intensity, and efficiency of natural sinks. Proc. Natl. Acad. Sci. U.S.A. 104, 18866. doi:10.1073/pnas.0702737104
Canuel, E.A. and Zimmerman, A.R., 1999. Composition of particulate organic matter in the southern Chesapeake Bay: sources and reactivity. Estuaries 22, 980-994. doi:10.2307/1353077
Canuel, E.A., 2001. Relations between river flow, primary production and fatty acid composition of particulate organic matter in San Francisco and Chesapeake Bays: a multivariate approach. Org. Geochem. 32, 563-583. doi:10.1016/S0146-6380(00)00195-9
Carstensen, J., Andersen, J.H., Gustafsson, B.G. and Conley, D.J., 2014. Deoxygenation of the Baltic Sea during the last century. Proc. Natl. Acad. Sci. U.S.A. 111, 5628-5633. doi:10.1073/pnas.1323156111
Chauvaud, L., Thompson, J.K., Cloern, J.E. and Thouzeau, G., 2003. Clams as CO_2 generators: The Potamocorbula amurensis example in San Francisco Bay. Limnol. Oceanogr. 48, 2086-2092. doi:10.4319/lo.2003.48.6.2086
Cifuentes, L., Sharp, J. and Fogel, M.L., 1988. Stable carbon and nitrogen isotope biogeochemistry in the Delaware estuary. Limnol. Oceanogr. 33, 1102-1115. doi:10.4319/lo.1988.33.5.1102
Corlett, H. and Jones, B., 2007. Epiphyte communities on Thalassia testudinum from Grand Cayman, British West Indies: Their composition, structure, and contribution to lagoonal sediments. Sediment. Geol. 194, 245-262. doi:10.1016/j.sedgeo.2006.06.010
Dai, M., Guo, X., Zhai, W., Yuan, L., Wang, B., Wang, L., Cai, P., Tang, T. and Cai, W.-J., 2006. Oxygen depletion in the upper reach of the Pearl River estuary during a winter drought. Mar. Chem. 102, 159-169. doi:10.1016/j.marchem.2005.09.020
Dai, M., Wang, L., Guo, X., Zhai, W., Li, Q., He, B. and Kao, S.-J., 2008. Nitrification and inorganic nitrogen distribution in a large perturbed river/estuarine system: the Pearl River Estuary, China. Biogeosciences 5, 1227-1244. doi:10.5194/bg-5-1227-2008
Dai, M., Gan, J., Han, A., Kung, H.S. and Yin, Z., 2014. Physical dynamics and biogeochemistry of the Pearl River plume. In: Bianchi, T.S., Allison, M.A. and Cai, W.-J. (Eds.), Biogeochemical dynamics at major river-coastal Interfaces linkages with global change. Cambridge University Press, New York, pp. 321-352.
Diaz, R.J. and Rosenberg, R., 2008. Spreading dead zones and consequences for marine ecosystems. Science 321, 926-929. doi:10.1126/science.1156401
Doctor, D.H., Kendall, C., Sebestyen, S.D., Shanley, J.B., Ohte, N. and Boyer, E.W., 2008. Carbon isotope fractionation of dissolved inorganic carbon (DIC) due to outgassing of carbon dioxide from a headwater stream. Hydrological Processes 22, 2410-2423. doi:10.1002/hyp.6833
Doney, S.C., 2006. The Dangers of Ocean Acidification. Sci. Am. 294, 58-65

Doney, S.C., Fabry, V.J., Feely, R.A. and Kleypas, J.A., 2009. Ocean Acidification: The Other CO_2 Problem. Annu. Rev. Mar. Sci. 1, 169-192. doi:10.1146/annurev.marine.010908.163834

Duarte, C.M., Hendriks, I.E., Moore, T.S., Olsen, Y.S., Steckbauer, A., Ramajo, L., Carstensen, J., Trotter, J.A. and McCulloch, M., 2013. Is Ocean Acidification an Open-Ocean Syndrome? Understanding Anthropogenic Impacts on Seawater pH. Estuar. Coast. 36, 221-236. doi:10.1007/s12237-013-9594-3

Egleston, E.S., Sabine, C.L. and Morel, F.M.M., 2010. Revelle revisited: Buffer factors that quantify the response of ocean chemistry to changes in DIC and alkalinity. Global Biogeochem. Cycles 24, n/a-n/a. doi:10.1029/2008GB003407

Enríquez, S. and Schubert, N., 2014. Direct contribution of the seagrass Thalassia testudinum to lime mud production. Nat. Commun. 5, 3835. doi:10.1038/ncomms4835

Fabry, V.J., Seibel, B.A., Feely, R.A. and Orr, J.C., 2008. Impacts of ocean acidification on marine fauna and ecosystem processes. ICES J. Mar. Sci. 65, 414-432. doi:10.1093/icesjms/fsn048

Feely, R.A., Alin, S.R., Newton, J., Sabine, C.L., Warner, M., Devol, A., Krembs, C. and Maloy, C., 2010. The combined effects of ocean acidification, mixing, and respiration on pH and carbonate saturation in an urbanized estuary. Estuar. Coast. Shelf Sci. 88, 442-449. doi:10.1016/j.ecss.2010.05.004

Feely, R.A., Okazaki, R.R., Cai, W.-J., Bednaršek, N., Alin, S.R., Byrne, R.H. and Fassbender, A., 2017. The combined effects of acidification and hypoxia on pH and aragonite saturation in the coastal waters of the California current ecosystem and the northern Gulf of Mexico. Cont. Shelf Res. doi:10.1016/j.csr.2017.11.002

Fennel, K. and Testa, J.M., 2018. Biogeochemical Controls on Coastal Hypoxia. Annu. Rev. Mar. Sci. 11, 4.1-4.26. doi:10.1146/annurev-marine-010318-095138

Fisher, T.R., Hagy, J.D. and Rochelle-Newall, E., 1998. Dissolved and particulate organic carbon in Chesapeake Bay. Estuaries 21, 215-229. doi:10.2307/1352470

Flemer, D.A., 1970. Primary production in the Chesapeake Bay. Chesapeake Science 11, 117-129. doi:10.2307/1350486

Fogel, M.L., Kent Sprague, E., Gize, A.P. and Frey, R.W., 1989. Diagenesis of organic matter in georgia salt marshes. Estuar. Coast. Shelf Sci. 28, 211-230. doi:10.1016/0272-7714(89)90067-X

Fry, B. and Sherr, E.B., 1989. $\delta^{13}C$ measurements as indicators of carbon flow in marine and freshwater ecosystems[1]. In: Rundel, P.W., Ehleringer, J.R. and Nagy, K.A. (Eds.), Stable isotopes in ecological research. Springer, pp. 196-229.

Fry, B., Jannasch, H.W., Molyneaux, S.J., Wirsen, C.O., Muramoto, J.A. and King, S., 1991. Stable isotope studies of the carbon, nitrogen and sulfur cycles in the

Black Sea and the Cariaco Trench. Deep Sea Research Part A. Oceanographic Research Papers 38, S1003-S1019. doi:10.1016/S0198-0149(10)80021-4
Gattuso, J.-P., Magnan, A., Billé, R., Cheung, W.W.L., Howes, E.L., Joos, F., Allemand, D., Bopp, L., Cooley, S.R., Eakin, C.M., Hoegh-Guldberg, O., Kelly, R.P., Pörtner, H.-O., Rogers, A.D., Baxter, J.M., Laffoley, D., Osborn, D., Rankovic, A., Rochette, J., Sumaila, U.R., Treyer, S. and Turley, C., 2015. Contrasting futures for ocean and society from different anthropogenic CO_2 emissions scenarios. Science 349. doi:10.1126/science.aac4722
Goñi, M.A., Teixeira, M.J. and Perkey, D.W., 2003. Sources and distribution of organic matter in a river-dominated estuary (Winyah Bay, SC, USA). Estuar. Coast. Shelf Sci. 57, 1023-1048. doi:10.1016/S0272-7714(03)00008-8
Guo, X., Cai, W.-J., Zhai, W., Dai, M., Wang, Y. and Chen, B., 2008. Seasonal variations in the inorganic carbon system in the Pearl River (Zhujiang) estuary. Cont. Shelf Res. 28, 1424-1434. doi:10.1016/j.csr.2007.07.011
Guo, X., Dai, M., Zhai, W., Cai, W.-J. and Chen, B., 2009. CO_2 flux and seasonal variability in a large subtropical estuarine system, the Pearl River Estuary, China. J. Geophys. Res. Biogeosci. 114. doi:10.1029/2008JG000905
Hagens, M., Slomp, C.P., Meysman, F.J.R., Seitaj, D., Harlay, J., Borges, A.V. and Middelburg, J.J., 2015. Biogeochemical processes and buffering capacity concurrently affect acidification in a seasonally hypoxic coastal marine basin. Biogeosciences 12, 1561-1583. doi:10.5194/bg-12-1561-2015
Hagy, J.D., Boynton, W.R., Keefe, C.W. and Wood, K.V., 2004. Hypoxia in Chesapeake Bay, 1950–2001: Long-term change in relation to nutrient loading and river flow. Estuaries 27, 634-658. doi:10.1007/BF02907650
Han, A., Dai, M., Kao, S.-J., Gan, J., Li, Q., Wang, L., Zhai, W. and Wang, L., 2012. Nutrient dynamics and biological consumption in a large continental shelf system under the influence of both a river plume and coastal upwelling. Limnol. Oceanogr. 57, 486-502. doi:10.4319/lo.2012.57.2.0486
He, B., Dai, M., Huang, W., Liu, Q., Chen, H. and Xu, L., 2010. Sources and accumulation of organic carbon in the Pearl River Estuary surface sediment as indicated by elemental, stable carbon isotopic, and carbohydrate compositions. Biogeosciences 7, 3343-3362. doi:10.5194/bg-7-3343-2010
He, B., Dai, M., Zhai, W., Guo, X. and Wang, L., 2014. Hypoxia in the upper reaches of the Pearl River Estuary and its maintenance mechanisms: A synthesis based on multiple year observations during 2000–2008. Mar. Chem. 167, 13-24. doi:10.1016/j.marchem.2014.07.003
Hedges, J.I. and Oades, J.M., 1997. Comparative organic geochemistries of soils and marine sediments. Org. Geochem. 27, 319-361. doi:10.1016/S0146-6380(97)00056-9
Hélie, J.-F., Hillaire-Marcel, C. and Rondeau, B., 2002. Seasonal changes in the sources and fluxes of dissolved inorganic carbon through the St. Lawrence River—isotopic and chemical constraint. Chem. Geol. 186, 117-138. doi:10.1016/S0009-2541(01)00417-X

Hellings, L., Dehairs, F., Tackx, M., Keppens, E. and Baeyens, W., 1999. Origin and fate of organic carbon in the freshwater part of the Scheldt Estuary as traced by stable carbon isotope composition. Biogeochemistry 47, 167-186. doi:10.1007/BF00994921

Herczeg, A., 1987. A stable carbon isotope study of dissolved inorganic carbon cycling in a softwater lake. Biogeochemistry 4, 231-263. doi:10.1007/BF02187369

Horrigan, S.G., Montoya, J.P., Nevins, J.L., McCarthy, J.J., Ducklow, H., Goericke, R. and Malone, T., 1990. Nitrogenous nutrient transformations in the spring and fall in the Chesapeake Bay. Estuar. Coast. Shelf Sci. 30, 369-391. doi:10.1016/0272-7714(90)90004-B

Hu, J., Peng, P.a. and Chivas, A.R., 2009. Molecular biomarker evidence of origins and transport of organic matter in sediments of the Pearl River estuary and adjacent South China Sea. Appl. Geochem. 24, 1666-1676

Hu, X. and Cai, W.J., 2013. Estuarine acidification and minimum buffer zone—A conceptual study. Geophys. Res. Lett. 40, 5176-5181

Hu, X., Cai, W.-J., Rabalais, N.N. and Xue, J., 2016. Coupled oxygen and dissolved inorganic carbon dynamics in coastal ocean and its use as a potential indicator for detecting water column oil degradation. Deep Sea Res. Part II Top. Stud. Oceanogr. 129, 311-318. doi:10.1016/j.dsr2.2014.01.010

Huang, L., Jian, W., Song, X., Huang, X., Liu, S., Qian, P., Yin, K. and Wu, M., 2004. Species diversity and distribution for phytoplankton of the Pearl River estuary during rainy and dry seasons. Mar. Pollut. Bull. 49, 588-596. doi:10.1016/j.marpolbul.2004.03.015

Huang, X., Huang, L. and Yue, W., 2003. The characteristics of nutrients and eutrophication in the Pearl River estuary, South China. Mar. Pollut. Bull. 47, 30-36. doi:10.1016/S0025-326X(02)00474-5

Kemp, W., Boynton, W., Adolf, J., Boesch, D., Boicourt, W., Brush, G., Cornwell, J., Fisher, T., Glibert, P. and Hagy, J., 2005. Eutrophication of Chesapeake Bay: historical trends and ecological interactions. Mar. Ecol. Prog. Ser. 303, 1-29. doi:10.3354/meps303001

Kemp, W., Testa, J., Conley, D., Gilbert, D. and Hagy, J., 2009. Temporal responses of coastal hypoxia to nutrient loading and physical controls. Biogeosciences 6, 2985-3008. doi:10.5194/bg-6-2985-2009

Kemp, W.M., Smith, E.M., Marvin-DiPasquale, M. and Boynton, W.R., 1997. Organic carbon balance and net ecosystem metabolism in Chesapeake Bay. Mar. Ecol. Prog. Ser. 150, 229-248. doi:10.3354/meps150229

Koch, E.W., 1999. Sediment resuspension in a shallow *Thalassia testudinum* banks ex König bed. Aquat. Bot. 65, 269-280. doi:10.1016/S0304-3770(99)00045-5

Kroeker, K.J., Kordas, R.L., Crim, R., Hendriks, I.E., Ramajo, L., Singh, G.S., Duarte, C.M. and Gattuso, J.P., 2013. Impacts of ocean acidification on marine organisms: quantifying sensitivities and interaction with warming. Glob. Chang. Biol. 19, 1884-1896. doi:10.1111/gcb.12179

Lamb, A.L., Wilson, G.P. and Leng, M.J., 2006. A review of coastal palaeoclimate and relative sea-level reconstructions using $\delta^{13}C$ and C/N ratios in organic material. Earth-Sci. Rev. 75, 29-57. doi:10.1016/j.earscirev.2005.10.003

Le Quéré, C., Moriarty, R., Andrew, R.M., Peters, G.P., Ciais, P., Friedlingstein, P., Jones, S.D., Sitch, S., Tans, P., Arneth, A., Boden, T.A., Bopp, L., Bozec, Y., Canadell, J.G., Chini, L.P., Chevallier, F., Cosca, C.E., Harris, I., Hoppema, M., Houghton, R.A., House, J.I., Jain, A.K., Johannessen, T., Kato, E., Keeling, R.F., Kitidis, V., Klein Goldewijk, K., Koven, C., Landa, C.S., Landschützer, P., Lenton, A., Lima, I.D., Marland, G., Mathis, J.T., Metzl, N., Nojiri, Y., Olsen, A., Ono, T., Peng, S., Peters, W., Pfeil, B., Poulter, B., Raupach, M.R., Regnier, P., Rödenbeck, C., Saito, S., Salisbury, J.E., Schuster, U., Schwinger, J., Séférian, R., Segschneider, J., Steinhoff, T., Stocker, B.D., Sutton, A.J., Takahashi, T., Tilbrook, B., Van Der Werf, G.R., Viovy, N., Wang, Y.-P., Wanninkhof, R., Wiltshire, A. and Zeng, N., 2015. Global carbon budget 2014. Earth Syst. Sci. Data 7, 47– 85. doi:10.5194/essd-7-47-2015

Lefcheck, J.S., Orth, R.J., Dennison, W.C., Wilcox, D.J., Murphy, R.R., Keisman, J., Gurbisz, C., Hannam, M., Landry, J.B., Moore, K.A., Patrick, C.J., Testa, J., Weller, D.E. and Batiuk, R.A., 2018. Long-term nutrient reductions lead to the unprecedented recovery of a temperate coastal region. Proc. Natl. Acad. Sci. U.S.A. 115, 3658-3662. doi:10.1073/pnas.1715798115

Lesley A. Warren, P.A.M.N.P.F.G.F., 2001. Microbially Mediated Calcium Carbonate Precipitation: Implications for Interpreting Calcite Precipitation and for Solid-Phase Capture of Inorganic Contaminants. Geomicrobiol. J. 18, 93-115. doi:10.1080/01490450151079833

Loh, A.N., Bauer, J.E. and Canuel, E.A., 2006. Dissolved and particulate organic matter source-age characterization in the upper and lower Chesapeake Bay: A combined isotope and biochemical approach. Limnol. Oceanogr. 51, 1421-1431. doi:10.4319/lo.2006.51.3.1421

Macreadie, P.I., Serrano, O., Maher, D.T., Duarte, C.M. and Beardall, J., 2017. Addressing calcium carbonate cycling in blue carbon accounting. Limnol. Oceanogr. Letters. doi:10.1002/lol2.10052

Mazarrasa, I., Marbà, N., Lovelock, C.E., Serrano, O., Lavery, P.S., Fourqurean, J.W., Kennedy, H., Mateo, M.A., Krause-Jensen, D., Steven, A.D.L. and Duarte, C.M., 2015. Seagrass meadows as a globally significant carbonate reservoir. Biogeosciences 12, 4993-5003. doi:10.5194/bg-12-4993-2015

Meyers, P.A., 1997. Organic geochemical proxies of paleoceanographic, paleolimnologic, and paleoclimatic processes. Org. Geochem. 27, 213-250. doi:10.1016/S0146-6380(97)00049-1

Moore, K.A., Wilcox, D.J. and Orth, R.J., 2000. Analysis of the abundance of submersed aquatic vegetation communities in the Chesapeake Bay. Estuaries 23, 115-127. doi:10.2307/1353229

Mucci, A., 1983. The solubility of calcite and aragonite in seawater at various salinities, temperatures, and one atmosphere total pressure. Am. J. Sci. 283, 780-799. doi:10.2475/ajs.283.7.780

Murphy, R.R., Kemp, W.M. and Ball, W.P., 2011. Long-Term Trends in Chesapeake Bay Seasonal Hypoxia, Stratification, and Nutrient Loading. Estuar. Coast. 34, 1293-1309. doi:10.1007/s12237-011-9413-7

Najjar, R.G., Pyke, C.R., Adams, M.B., Breitburg, D., Hershner, C., Kemp, M., Howarth, R., Mulholland, M.R., Paolisso, M., Secor, D., Sellner, K., Wardrop, D. and Wood, R., 2010. Potential climate-change impacts on the Chesapeake Bay. Estuar. Coast. Shelf Sci. 86, 1-20. doi:10.1016/j.ecss.2009.09.026

Nixon, S.W., 1995. Coastal marine eutrophication: A definition, social causes, and future concerns. Ophelia 41, 199-219. doi:10.1080/00785236.1995.10422044

Nixon, S.W., 2009. Eutrophication and the macroscope. In: Andersen, J.H. and Conley, D.J. (Eds.), Eutrophication in Coastal Ecosystems: Towards better understanding and management strategies Selected Papers from the Second International Symposium on Research and Management of Eutrophication in Coastal Ecosystems, 20–23 June 2006, Nyborg, Denmark. Springer Netherlands, Dordrecht, pp. 5-19.

Orr, J.C., Fabry, V.J., Aumont, O., Bopp, L., Doney, S.C., Feely, R.A., Gnanadesikan, A., Gruber, N., Ishida, A., Joos, F., Key, R.M., Lindsay, K., Maier-Reimer, E., Matear, R., Monfray, P., Mouchet, A., Najjar, R.G., Plattner, G.-K., Rodgers, K.B., Sabine, C.L., Sarmiento, J.L., Schlitzer, R., Slater, R.D., Totterdell, I.J., Weirig, M.-F., Yamanaka, Y. and Yool, A., 2005. Anthropogenic ocean acidification over the twenty-first century and its impact on calcifying organisms. Nature 437, 681. doi:10.1038/nature04095

Orth, R.J. and Moore, K.A., 1983. Chesapeake Bay: An Unprecedented Decline in Submerged Aquatic Vegetation. Science 222, 51-53. doi:10.1126/science.222.4619.51

Orth, R.J. and Moore, K.A., 1984. Distribution and abundance of submerged aquatic vegetation in Chesapeake Bay: an historical perspective. Estuar. Coast. 7, 531-540. doi:10.2307/1352058

Orth, R.J., Williams, M.R., Marion, S.R., Wilcox, D.J., Carruthers, T.J.B., Moore, K.A., Kemp, W.M., Dennison, W.C., Rybicki, N., Bergstrom, P. and Batiuk, R.A., 2010. Long-Term Trends in Submersed Aquatic Vegetation (SAV) in Chesapeake Bay, USA, Related to Water Quality. Estuar. Coast. 33, 1144-1163. doi:10.1007/s12237-010-9311-4

Orth, R.J., Dennison, W.C., Lefcheck, J.S., Gurbisz, C., Hannam, M., Keisman, J., Landry, J.B., Moore, K.A., Murphy, R.R. and Patrick, C.J., 2017. Submersed aquatic vegetation in Chesapeake Bay: sentinel species in a changing world. Bioscience 67, 698-712. doi:10.1093/biosci/bix058

Paerl, H.W., 2006. Assessing and managing nutrient-enhanced eutrophication in estuarine and coastal waters: Interactive effects of human and climatic perturbations. Ecol. Eng. 26, 40-54. doi:10.1016/j.ecoleng.2005.09.006

Perry, C.T., Salter, M.A., Harborne, A.R., Crowley, S.F., Jelks, H.L. and Wilson, R.W., 2011. Fish as major carbonate mud producers and missing components of the tropical carbonate factory. Proc. Natl. Acad. Sci. U.S.A. 108, 3865-3869. doi:10.1073/pnas.1015895108

Peterson, B.J., Howarth, R.W. and Garritt, R.H., 1985. Multiple stable isotopes used to trace the flow of organic matter in estuarine food webs. Science 227, 1361-1363. doi:10.1126/science.227.4692.1361

Peterson, B.J. and Fry, B., 1987. Stable isotopes in ecosystem studies. Annu. Rev. Ecol. Syst., 293-320. doi:10.1146/annurev.es.18.110187.001453

Qian, W., Gan, J., Liu, J., He, B., Lu, Z., Guo, X., Wang, D., Guo, L., Huang, T. and Dai, M., 2018. Current status of emerging hypoxia in a eutrophic estuary: The lower reach of the Pearl River Estuary, China. Estuar. Coast. Shelf Sci. 205, 58-67. doi:10.1016/j.ecss.2018.03.004

Quay, P., Sonnerup, R., Stutsman, J., Maurer, J., Körtzinger, A., Padin, X.A. and Robinson, C., 2007. Anthropogenic CO_2 accumulation rates in the North Atlantic Ocean from changes in the $^{13}C/^{12}C$ of dissolved inorganic carbon. Global Biogeochem. Cycles 21. doi:10.1029/2006GB002761

Quay, P., Sonnerup, R., Munro, D. and Sweeney, C., 2017. Anthropogenic CO_2 accumulation and uptake rates in the Pacific Ocean based on changes in the $^{13}C/^{12}C$ of dissolved inorganic carbon. Global Biogeochem. Cycles 31, 59-80. doi:10.1002/2016gb005460

Quay, P.D., Emerson, S.R., Quay, B.M. and Devol, A.H., 1986. The carbon cycle for Lake Washington—A stable isotope study1. Limnol. Oceanogr. 31, 596-611. doi:10.4319/lo.1986.31.3.0596

Rabalais, N., Cai, W.-J., Carstensen, J., Conley, D., Fry, B., Hu, X., Quiñones-Rivera, Z., Rosenberg, R., Slomp, C., Turner, E., Voss, M., Wissel, B. and Zhang, J., 2014. Eutrophication-Driven Deoxygenation in the Coastal Ocean. Oceanography 27, 172-183. doi:10.5670/oceanog.2014.21

Rabalais, N.N., Díaz, R.J., Levin, L.A., Turner, R.E., Gilbert, D. and Zhang, J., 2010. Dynamics and distribution of natural and human-caused hypoxia. Biogeosciences 7, 585-619. doi:10.5194/bg-7-585-2010

Rabouille, C., Conley, D.J., Dai, M.H., Cai, W.J., Chen, C.T.A., Lansard, B., Green, R., Yin, K., Harrison, P.J., Dagg, M. and McKee, B., 2008. Comparison of hypoxia among four river-dominated ocean margins: The Changjiang (Yangtze), Mississippi, Pearl, and Rhône rivers. Cont. Shelf Res. 28, 1527-1537. doi:10.1016/j.csr.2008.01.020

Racapé, V., Metzl, N., Pierre, C., Reverdin, G., Quay, P.D. and Olafsdottir, S.R., 2014. The seasonal cycle of $\delta^{13}C_{DIC}$ in the North Atlantic subpolar gyre. Biogeosciences 11, 1683-1692. doi:10.5194/bg-11-1683-2014

Raymond, P.A., Bauer, J.E. and Cole, J.J., 2000. Atmospheric CO_2 evasion, dissolved inorganic carbon production, and net heterotrophy in the York River estuary. Limnol. Oceanogr. 45, 1707-1717. doi:10.4319/lo.2000.45.8.1707

Roden, E.E., Tuttle, J.H., Boynton, W.R. and Kemp, W.M., 1995. Carbon cycling in mesohaline Chesapeake Bay sediments 1: POC deposition rates and mineralization pathways. J. Mar. Res. 53, 779-819. doi:10.1357/0022240953213025

Rutger, R., Stefan, A., Birthe, H., Hans, C.N. and Karl, N., 2002. Recovery of marine benthic habitats and fauna in a Swedish fjord following improved oxygen conditions. Mar. Ecol. Prog. Ser. 234, 43-53. doi:10.3354/meps234043

Sabine, C.L., Feely, R.A., Gruber, N., Key, R.M., Lee, K., Bullister, J.L., Wanninkhof, R., Wong, C.S., Wallace, D.W.R., Tilbrook, B., Millero, F.J., Peng, T.-H., Kozyr, A., Ono, T. and Rios, A.F., 2004. The Oceanic Sink for Anthropogenic CO_2. Science 305, 367-371. doi:10.1126/science.1097403

Samanta, S., Dalai, T.K., Pattanaik, J.K., Rai, S.K. and Mazumdar, A., 2015. Dissolved inorganic carbon (DIC) and its $\delta^{13}C$ in the Ganga (Hooghly) River estuary, India: Evidence of DIC generation via organic carbon degradation and carbonate dissolution. Geochim. Cosmochim. Acta 165, 226-248. doi:10.1016/j.gca.2015.05.040

Schulte, D.M., 2017. History of the Virginia Oyster Fishery, Chesapeake Bay, USA. Front. Mar. Sci. 4. doi:10.3389/fmars.2017.00127

Schulte, P., van Geldern, R., Freitag, H., Karim, A., Négrel, P., Petelet-Giraud, E., Probst, A., Probst, J.-L., Telmer, K., Veizer, J. and Barth, J.A.C., 2011. Applications of stable water and carbon isotopes in watershed research: Weathering, carbon cycling, and water balances. Earth-Sci. Rev. 109, 20-31. doi:10.1016/j.earscirev.2011.07.003

Shen, C., Testa, J.M., Li, M., Cai, W.-J., Waldbusser, G.G., Ni, W., Kemp, W.M., Cornwell, J., Chen, B., Brodeur, J. and Su, J., 2019. Controls on Carbonate System Dynamics in a Coastal Plain Estuary: A Modeling Study. J. Geophys. Res. Biogeosci. 124, 61-78. doi:10.1029/2018jg004802

Sigleo, A.C. and Macko, S.A., 2002. Carbon and Nitrogen Isotopes in Suspended Particles and Colloids, Chesapeake and San Francisco Estuaries, U.S.A. Estuar. Coast. Shelf Sci. 54, 701-711. doi:10.1006/ecss.2001.0853

Smith, E.M. and Kemp, W.M., 1995. Seasonal and regional variations in plankton community production and respiration for Chesapeake Bay. Mar. Ecol. Prog. Ser. 116, 217-231

Su, J., Dai, M., He, B., Wang, L., Gan, J., Guo, X., Zhao, H. and Yu, F., 2017. Tracing the origin of the oxygen-consuming organic matter in the hypoxic zone in a large eutrophic estuary: the lower reach of the Pearl River Estuary, China. Biogeosciences 14, 4085-4099. doi:10.5194/bg-14-4085-2017

Sun, H., Han, J., Zhang, S. and Lu, X., 2011. Transformation of dissolved inorganic carbon (DIC) into particulate organic carbon (POC) in the lower Xijiang River, SE China: an isotopic approach. Biogeosci. Disc. 8, 9471-9501

Sunda, W.G. and Cai, W.-J., 2012. Eutrophication Induced CO_2-Acidification of Subsurface Coastal Waters: Interactive Effects of Temperature, Salinity, and

Atmospheric P_{CO2}. Environ. Sci. Technol. 46, 10651-10659. doi:10.1021/es300626f
Swarzenski, P., Campbell, P., Osterman, L. and Poore, R., 2008. A 1000-year sediment record of recurring hypoxia off the Mississippi River: The potential role of terrestrially-derived organic matter inputs. Mar. Chem. 109, 130-142. doi:10.1016/j.marchem.2008.01.003
Testa, J.M., Clark, J.B., Dennison, W.C., Donovan, E.C., Fisher, A.W., Ni, W., Parker, M., Scavia, D., Spitzer, S.E. and Waldrop, A.M., 2017. Ecological forecasting and the science of hypoxia in Chesapeake Bay. Bioscience 67, 614-626. doi:10.1093/biosci/bix048
Testa, J.M., Murphy, R.R., Brady, D.C. and Kemp, W.M., 2018. Nutrient- and Climate-Induced Shifts in the Phenology of Linked Biogeochemical Cycles in a Temperate Estuary. Front. Mar. Sci. 5, 114. doi:10.3389/fmars.2018.00114
Thornton, S.F. and McManus, J., 1994. Application of Organic Carbon and Nitrogen Stable Isotope and C/N Ratios as Source Indicators of Organic Matter Provenance in Estuarine Systems: Evidence from the Tay Estuary, Scotland. Estuar. Coast. Shelf Sci. 38, 219-233. doi:10.1006/ecss.1994.1015
van Breugel, Y., Schouten, S., Paetzel, M., Nordeide, R. and Sinninghe Damsté, J.S., 2005. The impact of recycling of organic carbon on the stable carbon isotopic composition of dissolved inorganic carbon in a stratified marine system (Kyllaren fjord, Norway). Org. Geochem. 36, 1163-1173. doi:10.1016/j.orggeochem.2005.03.003
Vaquer-Sunyer, R. and Duarte, C.M., 2008. Thresholds of hypoxia for marine biodiversity. Proc. Natl. Acad. Sci. U.S.A. 105, 15452-15457. doi:10.1073/pnas.0803833105
Waldbusser, G.G., Voigt, E.P., Bergschneider, H., Green, M.A. and Newell, R.I.E., 2011. Biocalcification in the Eastern Oyster (Crassostrea virginica) in Relation to Long-term Trends in Chesapeake Bay pH. Estuar. Coast. 34, 221-231. doi:10.1007/s12237-010-9307-0
Waldbusser, G.G., Powell, E.N. and Mann, R., 2013. Ecosystem effects of shell aggregations and cycling in coastal waters: an example of Chesapeake Bay oyster reefs. Ecology 94, 895-903. doi:10.1890/12-1179.1
Wallace, R.B., Baumann, H., Grear, J.S., Aller, R.C. and Gobler, C.J., 2014. Coastal ocean acidification: The other eutrophication problem. Estuar. Coast. Shelf Sci. 148, 1-13. doi:10.1016/j.ecss.2014.05.027
Wang, H., Dai, M., Liu, J., Kao, S.-J., Zhang, C., Cai, W.-J., Wang, G., Qian, W., Zhao, M. and Sun, Z., 2016. Eutrophication-Driven Hypoxia in the East China Sea off the Changjiang Estuary. Environ. Sci. Technol. 50, 2255-2263. doi:10.1021/acs.est.5b06211
Wang, H., Hu, X., Rabalais, N.N. and Brandes, J., 2018a. Drivers of Oxygen Consumption in the Northern Gulf of Mexico Hypoxic Waters—A Stable Carbon Isotope Perspective. Geophys. Res. Lett. 45, 10,528-10,538. doi:10.1029/2018GL078571

Wang, H., Hu, X., Wetz, M.S. and Hayes, K.C., 2018b. Oxygen Consumption and Organic Matter Remineralization in Two Subtropical, Eutrophic Coastal Embayments. Environ. Sci. Technol. 52, 13004-13014. doi:10.1021/acs.est.8b02971

Ware, J.R., Smith, S.V. and Reaka-Kudla, M.L., 1992. Coral reefs: sources or sinks of atmospheric CO_2? Coral Reefs 11, 127-130. doi:10.1007/BF00255465

Wong, G.T.F., 1979. Alkalinity and pH in the southern Chesapeake Bay and the James River estuary[1]. Limnol. Oceanogr. 24, 970-977. doi:10.4319/lo.1979.24.5.0970

Wu, R.S., 2002. Hypoxia: from molecular responses to ecosystem responses. Mar. Pollut. Bull. 45, 35-45. doi:10.1016/S0025-326X(02)00061-9

Xing, L., Zhang, H., Yuan, Z., Sun, Y. and Zhao, M., 2011. Terrestrial and marine biomarker estimates of organic matter sources and distributions in surface sediments from the East China Sea shelf. Cont. Shelf Res. 31, 1106-1115. doi:10.1016/j.csr.2011.04.003

Ye, F., Huang, X., Zhang, X., Zhang, D., Zeng, Y. and Tian, L., 2012. Recent oxygen depletion in the Pearl River Estuary, South China: geochemical and microfaunal evidence. J. Oceanogr. 68, 387-400. doi:10.1007/s10872-012-0104-1

Yin, K., Lin, Z. and Ke, Z., 2004. Temporal and spatial distribution of dissolved oxygen in the Pearl River Estuary and adjacent coastal waters. Cont. Shelf Res. 24, 1935-1948. doi:10.1016/j.csr.2004.06.017

Yu, F., Zong, Y., Lloyd, J.M., Huang, G., Leng, M.J., Kendrick, C., Lamb, A.L. and Yim, W.W.-S., 2010. Bulk organic $\delta^{13}C$ and C/N as indicators for sediment sources in the Pearl River delta and estuary, southern China. Estuar. Coast. Shelf Sci. 87, 618-630. doi:10.1016/j.ecss.2010.02.018

Zhang, J., Gilbert, D., Gooday, A.J., Levin, L., Naqvi, S.W.A., Middelburg, J.J., Scranton, M., Ekau, W., Peña, A., Dewitte, B., Oguz, T., Monteiro, P.M.S., Urban, E., Rabalais, N.N., Ittekkot, V., Kemp, W.M., Ulloa, O., Elmgren, R., Escobar-Briones, E. and Van der Plas, A.K., 2010. Natural and human-induced hypoxia and consequences for coastal areas: synthesis and future development. Biogeosciences 7, 1443-1467. doi:10.5194/bg-7-1443-2010

Zhang, J., Cowie, G. and Naqvi, S.W.A., 2013. Hypoxia in the changing marine environment. Environ. Res. Lett. 8, 015025. doi:10.1088/1748-9326/8/1/015025

Zimmerman, A.R. and Canuel, E.A., 2000. A geochemical record of eutrophication and anoxia in Chesapeake Bay sediments: anthropogenic influence on organic matter composition. Mar. Chem. 69, 117-137. doi:10.1016/S0304-4203(99)00100-0

Zimmerman, A.R. and Canuel, E.A., 2002. Sediment geochemical records of eutrophication in the mesohaline Chesapeake Bay. Limnol. Oceanogr 47, 1084-1093

Chapter 2

TRACING THE ORIGIN OF THE OXYGEN-CONSUMING ORGANIC MATTER IN THE HYPOXIC ZONE IN A LARGE EUTROPHIC ESTUARY: THE LOWER REACH OF THE PEARL RIVER ESTUARY, CHINA[1]

2.1 Abstract

We assess the relative contributions of different sources of organic matter, marine vs. terrestrial, to oxygen consumption in an emerging hypoxic zone in the lower Pearl River Estuary (PRE), a large eutrophic estuary located in Southern China. Our cruise, conducted in July 2014, consisted of two legs before and after the passing of Typhoon Rammasun, which completely de-stratified the water column. The stratification recovered rapidly, within one day after the typhoon. We observed algal blooms in the upper layer of the water column and hypoxia underneath in bottom water during both legs. Repeat sampling at the initial hypoxic station showed severe oxygen depletion down to 30 μmol kg^{-1} before the typhoon and a clear drawdown of dissolved oxygen after the typhoon. Based on a three end-member mixing model and the mass balance of dissolved inorganic carbon and its isotopic composition, the $\delta^{13}C$ of organic carbon remineralized in the hypoxic zone was -23.2±1.1 ‰. We estimated that 65±16 % of the oxygen-consuming organic matter was derived from marine sources, and the rest (35±16 %) was derived from the continent. In contrast to a

---

[1] Su, J., Dai, M., He, B., Wang, L., Gan, J., Guo, X., Zhao, H. and Yu, F., 2017. Tracing the origin of the oxygen-consuming organic matter in the hypoxic zone in a large eutrophic estuary: the lower reach of the Pearl River Estuary, China. Biogeosciences 14, 4085-4099. doi:10.5194/bg-14-4085-2017

recently studied hypoxic zone in the East China Sea off the Changjiang Estuary where marine organic matter stimulated by eutrophication dominated oxygen consumption, here terrestrial organic matter significantly contributed to the formation and maintenance of hypoxia. How varying amounts of these organic matter sources drive oxygen consumption has important implications for better understanding hypoxia and its mitigation in bottom waters.

2.2 Introduction

The occurrence of hypoxia has been exacerbated worldwide (Nixon, 1995; Diaz and Rosenberg, 2008; Rabalais et al., 2010; Zhang et al., 2013). In recent decades, more than 400 coastal hypoxic systems have been reported with an exponential growth rate of 5.5±0.23 % yr^{-1}, demonstrating their persistence and complexity with respect to both science and management (Diaz and Rosenberg, 2008; Vaquer-Sunyer and Duarte, 2008). Hypoxia may not only reduce biodiversity and endanger aquatic and benthic habitats, but also alter the redox chemistry in both the water column and the underlying sediments, triggering the release of secondary pollutants (Breitburg, 2002; Rutger et al., 2002). Moreover, the management and recovery of these systems are complicated due to the hysteresis of hypoxic conditions, and the varying timescales of biological loss (within hours to weeks) and recovery from hypoxia (from months to years) (Steckbauer et al., 2011).

Coastal hypoxia usually occurs in stratified water columns where the downward mixing of oxygen from the surface is impeded (Kemp et al., 2009). Below the pycnocline, aerobic respiration is usually the predominant sink of oxygen. Organic matter, which consumes dissolved oxygen (DO) as it becomes oxidized, is thus the ultimate cause of hypoxia under favourable physical settings (Rabouille et al., 2008;

Rabalais et al., 2014; Qian et al., 2017). The organic carbon (OC) that fuels respiration-driven reduction of oxygen in these systems could originate from either eutrophication-induced primary production (marine OC; OC_{mar}), or naturally and/or anthropogenically driven delivery from terrestrial environments (terrestrial OC; OC_{terr}) (Paerl, 2006; Rabalais et al., 2010).

The question of how much OC in hypoxic zones is supplied from on-site primary production versus the quantity derived from terrestrial sources has been an issue of debate (Wang et al., 2016). A number of the phytoplankton-centric hypoxia literature suggests that OC_{mar} dominates oxygen consumption in hypoxic zones, owing to its higher microbial availability than OC_{terr} (Zimmerman and Canuel, 2000; Boesch et al., 2009; Carstensen et al., 2014). Wang et al. (2016) quantified for the first time the relative contributions of particulate OC_{mar} (POC_{mar}) and particulate OC_{terr} (POC_{terr}) in consuming DO in the bottom waters of the East China Sea (ECS) off the Changjiang Estuary (CJE), and found that POC_{mar} dominated DO consumption. However, other studies suggest that POC_{terr} may also play an important role (Swarzenski et al., 2008; Bianchi, 2011; Bianchi et al., 2011). It is thus very important to quantify the relative contributions of organic matter (OC_{mar} vs. OC_{terr}) driving the onset and maintenance of hypoxia in coastal systems, since reducing organic matter vs. nutrient inputs requires a different set of management strategies.

The Pearl River Estuary (PRE, 21.2° N–23.1° N, 113.0° E–114.5° E) is surrounded by several large cities including Hong Kong, Shenzhen and Guangzhou and has received very high loads of nutrients from the drainage basin in the last three decades. As such, eutrophication has increasingly become an issue of concern (Huang et al., 2003; Ye et al., 2012). Dissolved inorganic nitrogen (DIN) concentrations in the

PRE have increased approximately 4-fold from 1986 (19.3 μmol L^{-1}) to 2002 (76.1 μmol L^{-1}) (He and Yuan, 2007). This DIN increase has been attributed to increased inputs of domestic sewage, industrial wastewater, agricultural runoff and aquaculture in the watershed (Huang et al., 2003).

Recent observations based on monthly surveys between April 2010 and March 2011 and long term monitoring data from 1990 to 2014, have suggested that the lower PRE has emerged as a seasonal hypoxic zone (Qian et al., 2018). This is supported by our current study, as two relatively large hypoxic zones (> 300 km^2) were observed in the lower PRE with DO < 2 mg L^{-1}. However, the origin of the organic matter driving hypoxia in the lower PRE has not previously been examined. Here, we quantified the relative proportions of OC_{mar} and OC_{terr} contributing to DO drawdown in bottom waters of the lower PRE, an economically important coastal region. This study has important biological, societal and managerial implications for the region, particularly relating to water quality in the vicinity of Hong Kong in the lower PRE. For example, the government of Hong Kong is examining the efficacy of its costly Harbour Area Treatment Scheme project and if additional treatment should be implemented (http://www.gov.hk/en/residents/environment/water/harbourarea.htm).

2.3 Materials and Methods

2.3.1 Sampling and analysis

Interrupted by Typhoon Rammasun during 17-18 July 2014, our cruise was divided into two legs (Fig. 2.1). During Leg 1 between 13 and 16 July, we sampled Transects F4, F5 and Stations A08–A18. During Leg 2 between 19 and 27 July, we sampled Stations A01–A10, Transects F3 and F4, Stations A11–A17 and Transects F5, F6, F1, and F2, in sequence. In order to monitor the development of hypoxia before and after the passage of the typhoon, we revisited Station A10 three more times (13, 20 and 27 July).

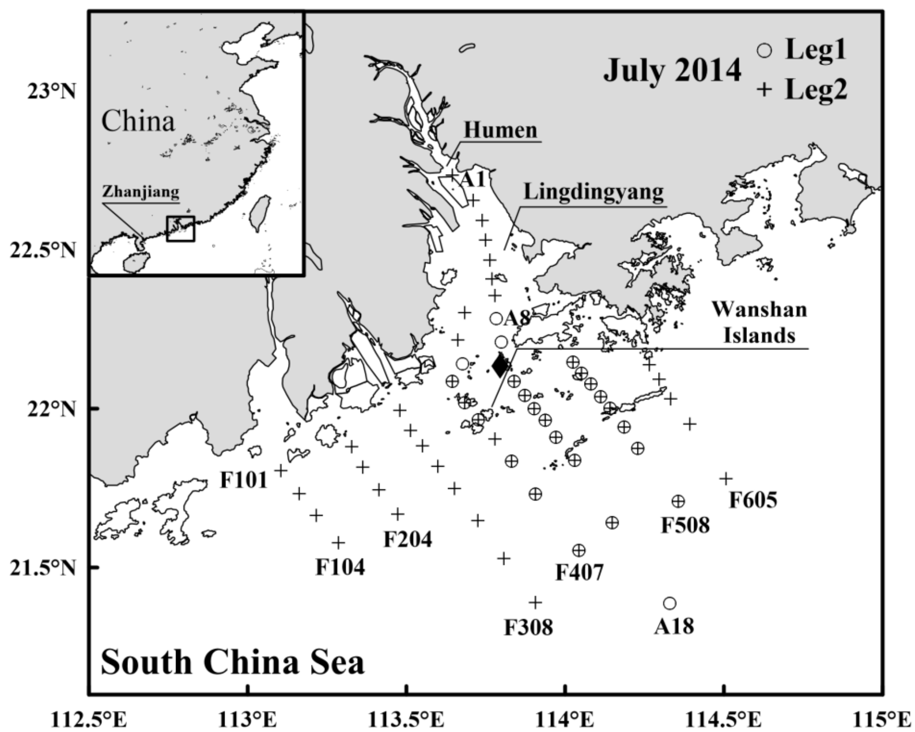

Figure 2.1: Map of the Pearl River Estuary and adjacent coastal waters. The open circles denote Leg 1 stations visited on 13–16 July 2014, and the crosses represent Leg 2 stations visited on 19–27 July 2014. Note that the filled diamond is the location of Station A10.

According to the gauge in the upper Pearl River, water discharge peaked in June and July. Typhoon Rammasun increased discharge during 15-18 July, with daily average values of 19480, 26115, 22981 and 17540 $m^3\ s^{-1}$, respectively. Nevertheless, the freshwater discharge was 18908 $m^3 s^{-1}$ in leg 1 and 15698 $m^3 s^{-1}$ in leg 2, comparable to the long-term (2000–2011) monthly average.

Temperature and salinity were determined with a SBE 25 Conductivity-Temperature-Depth/Pressure unit (Sea-Bird Co.). Water samples were collected using 4 L Go-Flo bottles (General Oceanics). DIC and DO was measured at all stations with depth profiles. Samples for $\delta^{13}C_{DIC}$ were collected primarily along Transect A as well as at depth in low oxygen layers.

The DO concentrations in discrete water samples were measured on board within 8 h using the classic Winkler titration method (Dai et al., 2006). In addition, we conducted on-deck incubation experiments using unfiltered water taken from the hypoxic zone on 27 July, 2014 following He et al. (2014). Bottom water from ~2 m above the sediment surface was collected and incubated for 24 hours in 65 mL BOD bottles in dark at ambient temperature controlled by the flowing surface water. Note that the maximum difference in temperature between the bottom and surface water was 3 °C during the incubation. Total oxygen consumption rate was determined by comparing the DO concentration at the initial and end point of the experiment.

DIC was measured with an infrared detector after acidifying 0.5–0.7 mL of water sample with a precision of 0.1 % for estuarine and sea waters (Cai et al., 2004). Dissolved calcium concentrations (Ca^{2+}) were determined using an EGTA titration with a Metrohm 809 TITRANDO potentiometer, which has a precision better than ± 5 $\mu mol\ kg^{-1}$ (Cao et al., 2011).

For $\delta^{13}C_{DIC}$ analysis, an ~20 mL DIC sample was converted into gaseous CO_2 and progressively purified through a vacuum line. The pure CO_2 sample was analyzed with an isotope ratio mass spectrometer (IRMS, Finnigan MAT 252, Bremen, Germany). The analytical precision was better than 0.1 ‰.

Water samples for TSM (total suspended matter), POC and $\delta^{13}C_{POC}$ analysis were concentrated onto preweighed and pre-combusted 0.7 μm Whatman GF/F filters after filtering 0.2–1.0 L of water under a mild vacuum (~ 25 kPa). Filters were washed with distilled water and stored at -20 °C. Prior to analysis, all filters were freeze-dried. TSM was determined using the net weight increment on the filter and the filtration volume. Filters were decarbonated with 1.0 mol L^{-1} HCl and dried at 40 °C for 48 h (Kao et al., 2012) and analyzed for POC and $\delta^{13}C_{POC}$ on an elemental analyzer coupled with an IRMS (EA-IRMS). The analytical precision for $\delta^{13}C_{POC}$ was better than 0.1 ‰. Chl-a was measured with a Turner fluorometer after extracting filters with 90 % acetone (He et al., 2010). Calibrations were performed using a Sigma Chl-a standard.

2.3.2 Three end-member mixing model

We adopted a three end-member mixing model to construct the conservative mixing scheme among different water masses (Cao et al., 2011; Han et al., 2012):

$$F_{RI}+F_{SW}+F_{SUB}=1 \tag{2.1}$$

$$\theta_{RI}\times F_{RI}+\theta_{SW}\times F_{SW}+\theta_{SUB}\times F_{SUB}=\theta \tag{2.2}$$

$$S_{RI}\times F_{RI}+S_{SW}\times F_{SW}+S_{SUB}\times F_{SUB}=S \tag{2.3}$$

where θ and S represent potential temperature and salinity; the subscripts RI, SW, and SUB denote the three different water masses (Pearl River plume water, offshore surface seawater and upwelled subsurface water); and F_{RI}, F_{SW}, and F_{SUB} represent the fractions that each end-member contributes to the in situ samples. These fractions were applied to predict conservative concentrations of DIC (DIC_{con}) and its isotopic composition ($\delta^{13}C_{DICcon}$) resulting solely from conservative mixing.

$$DIC_{\mathrm{RI}} \times F_{\mathrm{RI}} + DIC_{\mathrm{SW}} \times F_{\mathrm{SW}} + DIC_{\mathrm{SUB}} \times F_{\mathrm{SUB}} = DIC_{\mathrm{con}} \tag{2.4}$$

$$\frac{\delta^{13}C_{\mathrm{DICRI}} \times DIC_{\mathrm{RI}} \times F_{\mathrm{RI}} + \delta^{13}C_{\mathrm{DICSW}} \times DIC_{\mathrm{SW}} \times F_{\mathrm{SW}} + \delta^{13}C_{\mathrm{DICSUB}} \times DIC_{\mathrm{SUB}} \times F_{\mathrm{SUB}}}{DIC_{\mathrm{con}}} = \delta^{13}C_{\mathrm{DICcon}} \tag{2.5}$$

The difference (Δ) between measured and conservative DIC values represents the magnitude of the biological alteration of DIC (Wang et al., 2016).

2.4 Results

2.4.1 Horizontal distribution

Although the average freshwater discharge rate during our sampling period (16369 $m^3\ s^{-1}$) was slightly higher than the multi-year (2000–2011) monthly average (15671 $m^3\ s^{-1}$), typhoon Rammasun modified the system to some extent as shown from the evolution of chemical species at Station A10 before and after the typhoon (See Sect. 3.4). The interruption of Leg 1 due to the typhoon (July 17-18) led to a smaller survey area, covering only outside Lingdingyang Bay (traditionally regarded as the PRE), while Leg 2 covered Lingdingyang Bay from the Humen Outlet to the adjacent coastal sea.

As depicted in Fig. 2.2, the sea surface temperature (SST) during Leg 1 (28.9-32.2 ℃) was slightly higher than during Leg 2 (28.9-31.0 ℃). Sea surface salinity (SSS) measurements showed that plume water was restricted more landward during Leg 2 than Leg 1. However, a steeper gradient to higher SST offshore during Leg 1 was likely induced by the upwelling of bottom water, featuring by relatively high SSS (18.6), high DIC (1789 μmol kg^{-1}) and low DO saturation (DO%, 86 %). During Leg 1, the region with the most productivity was found east of the Wanshan Islands, characterized by high concentrations of Chl-a (8.0 μg kg^{-1}), low concentrations of DIC (1607 μmol kg^{-1}), and DO supersaturation, with the highest DO% greater than 160 % at Station F503. During Leg 2, there were three patches of high productivity, south of Huangmaohai, at the PRE entrance, and off Hong Kong. The central region of high productivity had the highest DO%, greater than 140% at Station A14, and was characterized by relatively high concentrations of Chl-a (7.8 μg kg^{-1}) and low concentrations of DIC (1737 μmol kg^{-1}).

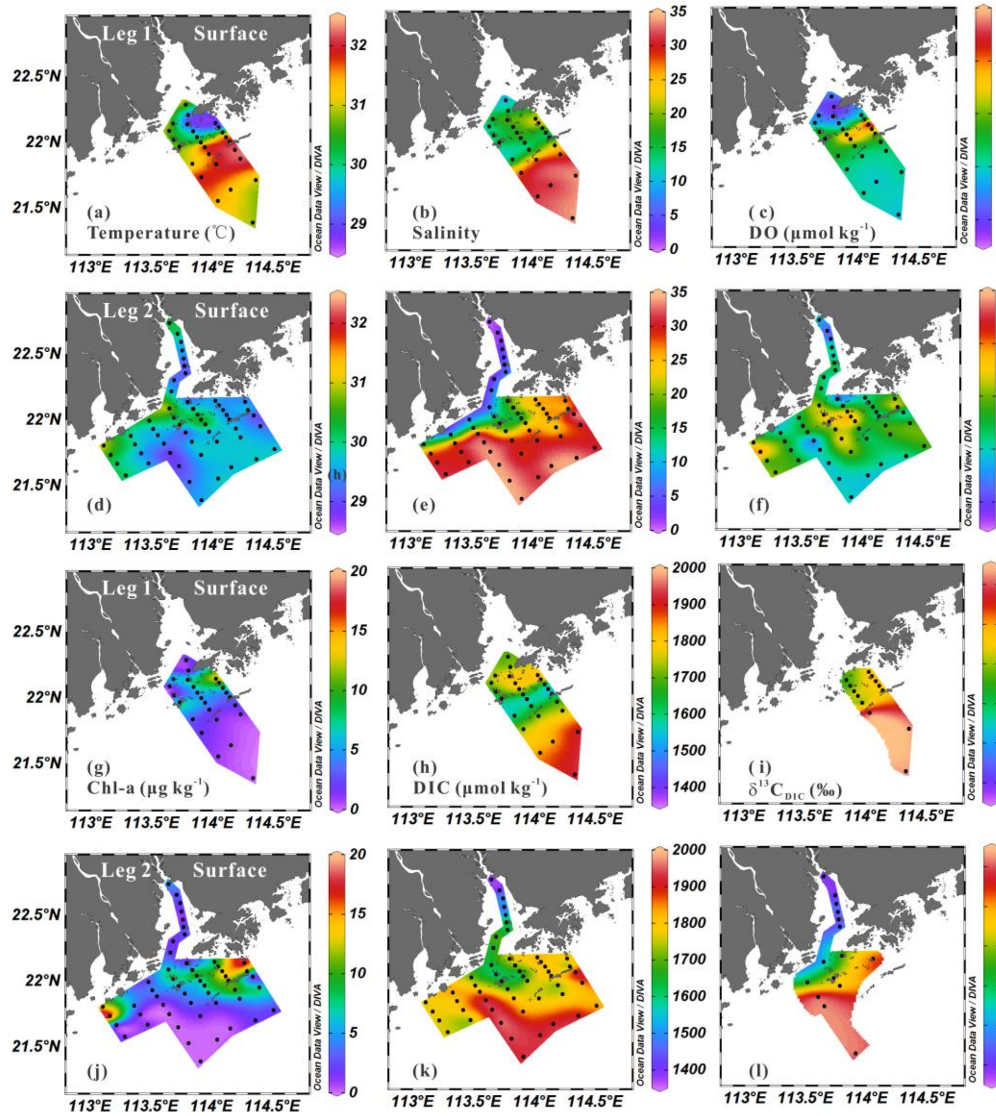

Figure 2.2: Surface water distribution of temperature, salinity, DO, Chl-a, DIC and $\delta^{13}C_{DIC}$ during Leg 1 (a–c, g–i) and Leg 2 (d–f, j–l).

As shown in Fig. 2.3, bottom water hypoxia during Leg 1 was located more centrally in the study area relative to the surface phytoplankton bloom. The center of the hypoxic zone was found at Station A10, characterized by the lowest observed DO concentrations (as low as 30 μmol kg^{-1}) and a relatively high concentration of DIC

(2075 μmol kg^{-1}). During Leg 2, hypoxic conditions were no longer found at Station A10, and instead the largest hypoxic zone was discovered to the southwest of the Wanshan Islands, where the lowest DO values were observed (as low as 7 μmol kg^{-1} at F304), and once again coincided with relatively high concentrations of DIC (2146 μmol kg^{-1}). We were unable to precisely constrain the areas of the regions impacted by bottom water hypoxia due to the limited spatial coverage, but our results suggest it covered an area of > 280 km^2 during Leg 1 and > 290 km^2 during Leg 2 according to the definition of hypoxia as DO < 2 mg L^{-1} or 63 µM, or an area of > 900 km^2 during Leg 1 and > 800 km^2 during Leg 2 assuming the threshold of the oxygen-deficit zone was < 3 mg L^{-1} or 95 µM (Rabalais et al., 2010; Zhao et al., 2017).

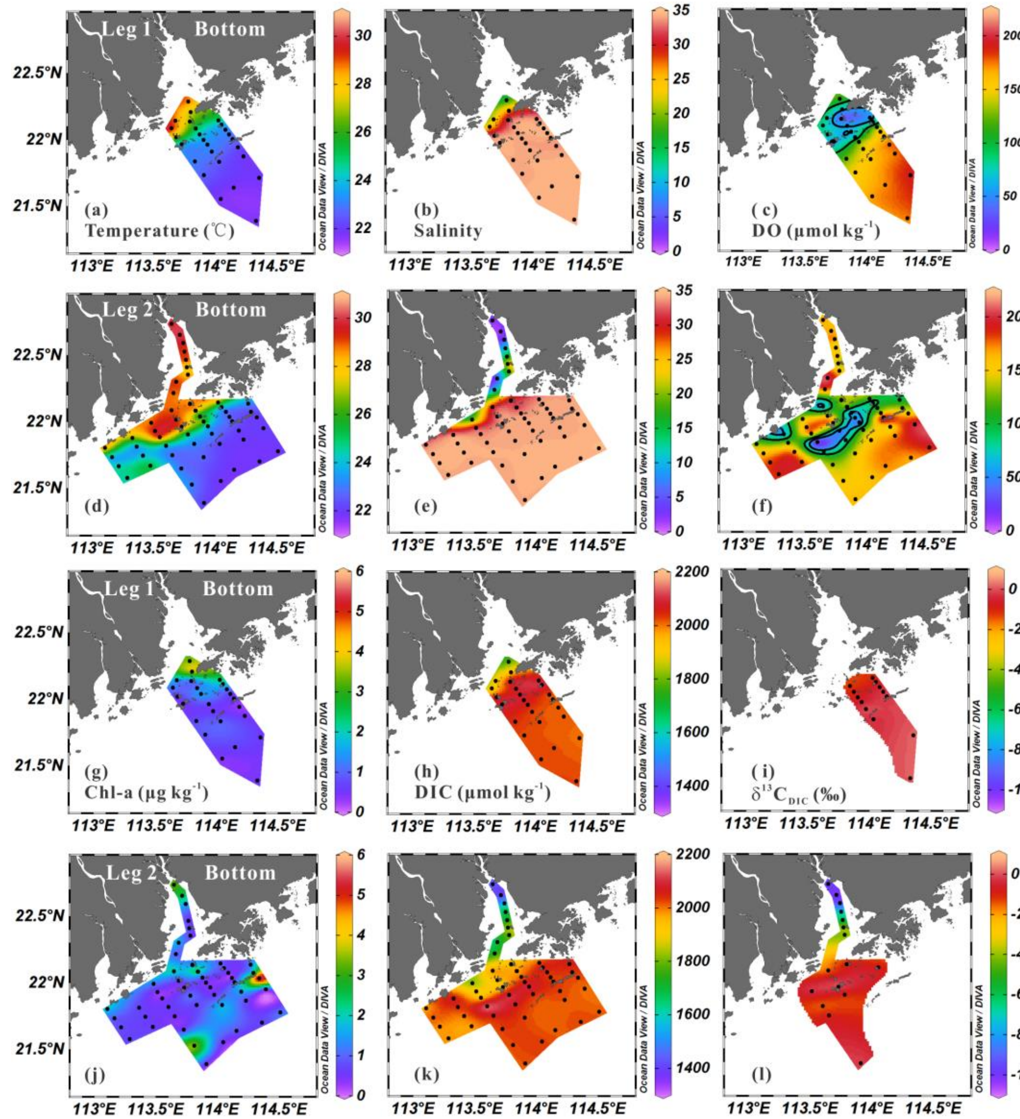

Figure 2.3: Bottom water distribution of temperature, salinity, DO, Chl-a, DIC and $\delta^{13}C_{DIC}$ during Leg 1 (a–c, g–i) and Leg 2 (d–f, j–l). Note that the black lines in (c) and (f) indicate DO contours of 63 μM and 95 μM.

2.4.2 Vertical distribution

During Leg 1, plume water reached 50 km offshore from the entrance of the PRE, forming a 5–10 m thick surface layer (Fig. 2.4b). Both the thermocline and halocline contributed to the stability of the water column structure, which favoured the formation of bottom water hypoxia. The thickness of the bottom water hypoxic layer was ~ 5 m. The region of highest productivity, however, was not observed in the same location as the hypoxic zone, but further offshore.

During Leg 2, although the passing of the typhoon would be expected to absorb large amounts of potential heat and cause extensive mixing of the water column, the enhanced freshwater discharge could rapidly re-stratify the water column and facilitate the re-formation of hypoxia. This time, the primary region of hypoxia was observed directly below the bloom, with a thickness of 3 m (Fig. 2.4i). Additionally, near the Humen Outlet we observed low DIC (1466 μmol kg^{-1}) and moderately low DO (89 μmol kg^{-1}), which reflected the input of the low DO water mass from upstream as reported previously (Dai et al., 2006; Dai et al., 2008a; He et al., 2014).

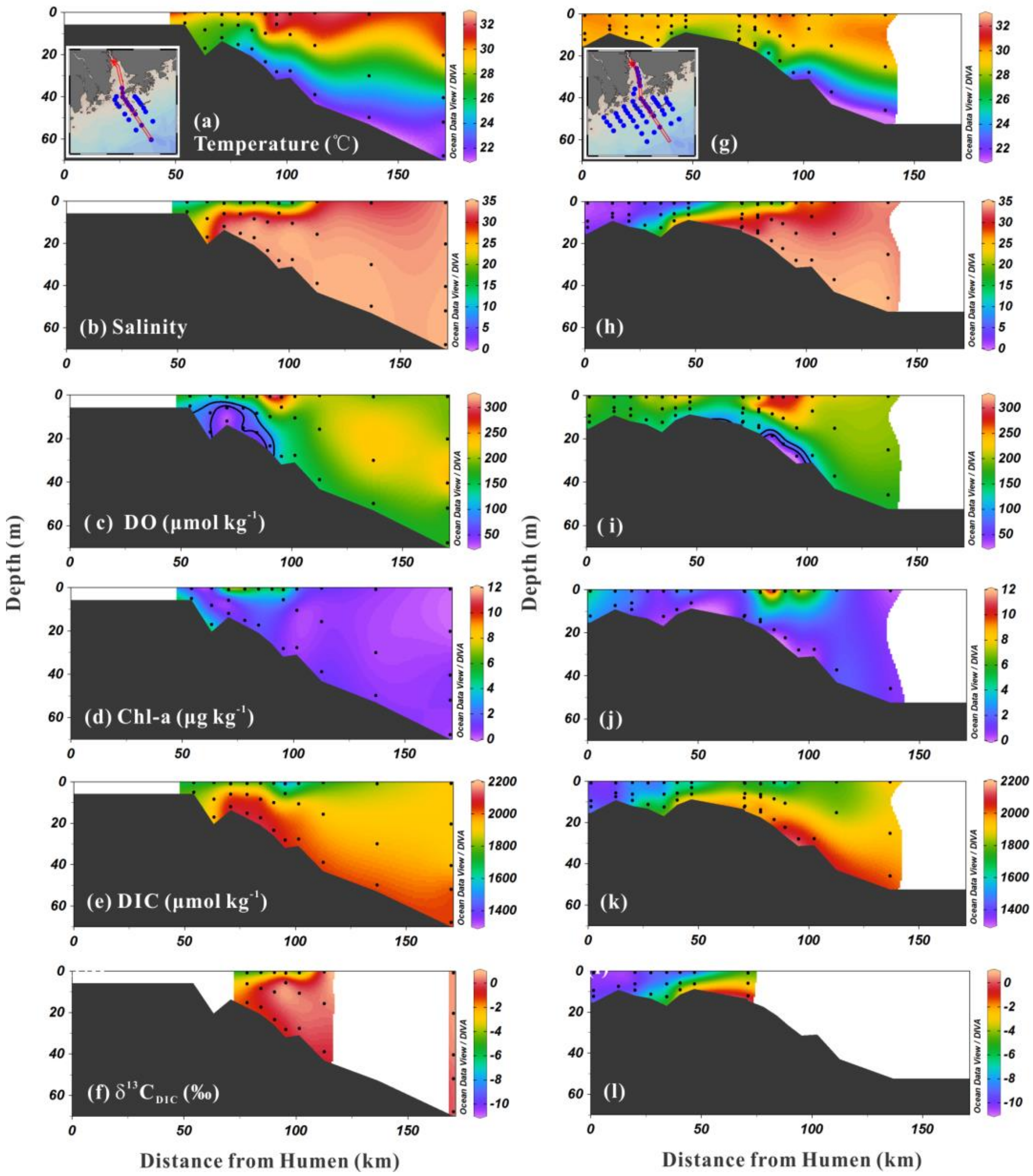

Figure 2.4: Profiles of temperature, salinity, DO, Chl-a, DIC and $\delta^{13}C_{DIC}$ along Transect A during Leg 1 (a–f) and Leg 2 (g–l). Note that the black lines in (c) and (i) indicate DO contours of 63 μM and 95 μM.

2.4.3 Isotopic composition of DIC and POC

The $\delta^{13}C$ values of DIC became progressively heavier from stations dominated by freshwater (~ -11.4 ‰) to off-shore seawater (~ -0.6 ‰), with a relatively wide range of values beyond a salinity of 13 (Fig. 2.5). Owing to a malfunction of the instrument, $\delta^{13}C_{POC}$ data from our cruise were not available. Instead, we reported a valid $\delta^{13}C_{POC}$ dataset from a 2015 summer cruise in approximately the same region. $\delta^{13}C_{POC}$ values showed a similar trend with $\delta^{13}C_{DIC}$, i.e. ^{13}C enriched seaward, from ~ -28 ‰ to ~ -20 ‰. In the bloom, where the DO% was above 125 %, the mean $\delta^{13}C$ value for POC was -19.4±0.8 ‰ (n=8), which was within the typical range of marine phytoplankton (Peterson and Fry, 1987). As shown in Fig. 2.5, there was a large $\delta^{13}C_{POC}$ decrease near a salinity of 15. Geographically, it was located at the mixing dominated zone in inner Lingdingyang Bay, where intense resuspension of ^{13}C depleted sediments may occur (Guo et al., 2009).

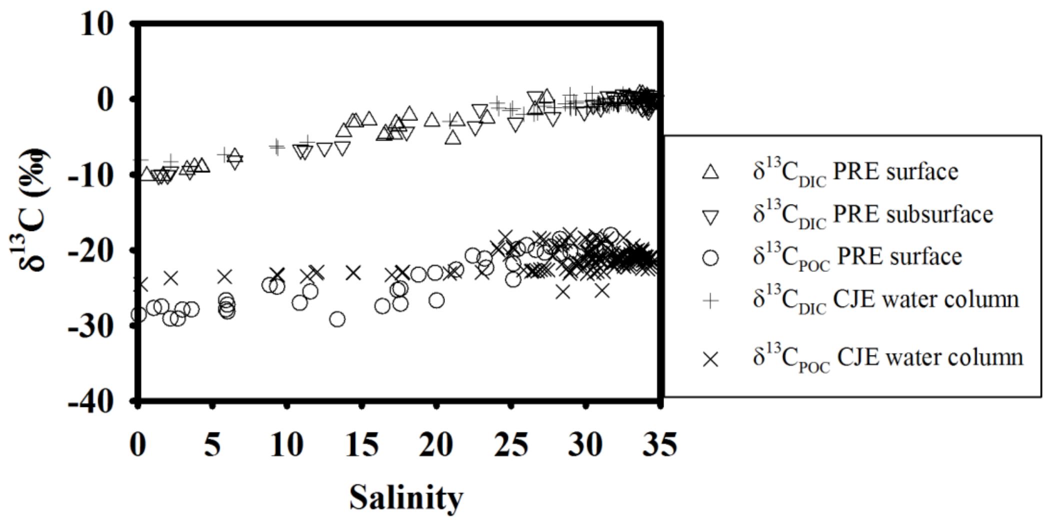

Figure 2.5: Distribution of $\delta^{13}C_{DIC}$ and $\delta^{13}C_{POC}$ with respect to salinity in the PRE. The up-facing and down-facing triangles denote surface and subsurface $\delta^{13}C_{DIC}$ data, respectively, from July 2014, while the open circles represent $\delta^{13}C_{POC}$ values in surface water from July 2015. Additionally, the plus signs and crosses show the $\delta^{13}C_{DIC}$ and $\delta^{13}C_{POC}$ data, respectively, from the Changjiang Estuary (CJE) in Wang et al. (2016).

2.4.4 Reinstatement of the hypoxic station after Typhoon Rammasun

Typhoon Rammasun made landfall at Zhanjiang, located 400 km to the southwest of the PRE, at 20:00 LT (Local Time) on 18 July, and was dissipated by 05:00 LT on 20 July. The typhoon completely de-stratified the water column during its passing. However, the associated heavy precipitation and runoff appeared to re-establish stratification rather quickly, within one day, as suggested by the salinity gradient (18–30) from 0–10 m depth during Leg 2 at 15:20 LT on 20 July (Fig. 2.6b). In order to capture the evolution of DO between the disruption and reinstatement of stratification, we resumed our cruise and revisited Station A10 (Fig. 2.6). On 13 July, the bottom water at Station A10 was the hypoxic core, with the lowest observed DO

(30 μmol kg^{-1}) and highest DIC (2075 μmol kg^{-1}) concentrations. On 20 July, the results showed that the temperature homogeneous layer in the bottom water (9–13 m) might reflect the remnants of typhoon-induced mixing (Fig. 2.6a), while the reduction in salinity at <9 m depicted the rapid re-establishment of stratification as a result of enhanced freshwater discharge (Fig. 2.6b). Bottom water DO increased to 153 μmol kg^{-1} and DIC decreased to 1901 μmol kg^{-1} as a result of the typhoon-induced water column mixing and aeration. In addition, TSM increased sharply from 20.2 before the typhoon to 36.6 mg kg^{-1}, suggesting large volumes of sediment had been resuspensed during its passing. On 27 July, one week after the typhoon, strong thermohaline stratification was re-established in the whole water column. Along with the intensifying stratification, bottom water DO decreased to 99 μmol kg^{-1} indicating continuous DO depletion and the potential for hypoxia formation. Meanwhile, bottom water DIC concentrations increased to 2000 μmol kg^{-1} and dissolved inorganic phosphate (DIP) rose from 0.28 to 0.57 μmol kg^{-1}. Moreover, bottom-water TSM returned to pre-typhoon (13 July) levels.

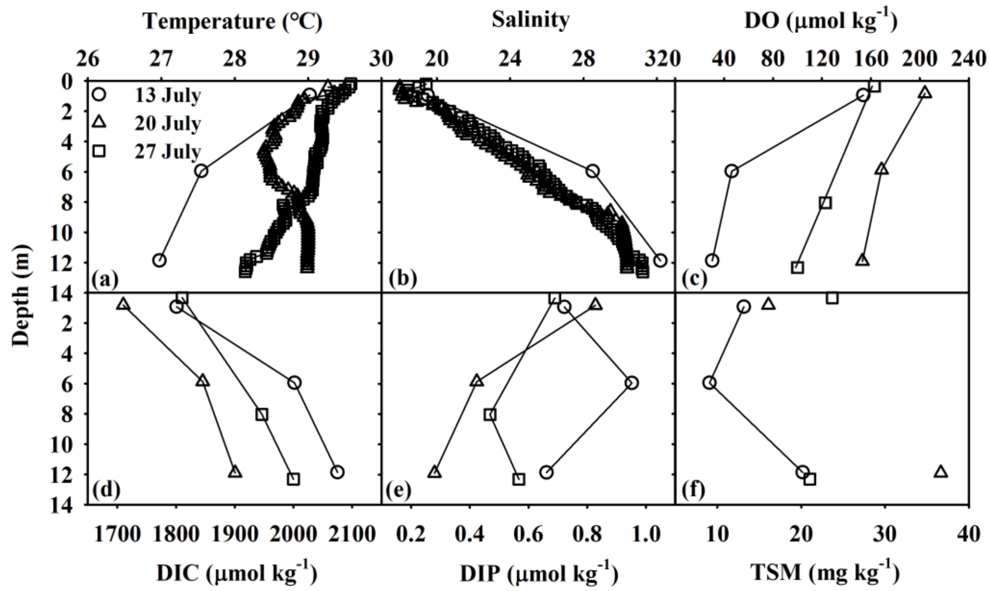

Figure 2.6: Profiles of (a) temperature, (b) salinity, (c) DO, (d) DIC, (e) DIP, (f) TSM and their evolution during repeated sampling at Station A10.

2.5 Discussion

2.5.1 Selection of end-members and model validation

The potential temperature-salinity plot displayed a three end-member mixing scheme over the PRE and adjacent coastal waters (Fig. 2.7a), consisting of Pearl River plume water, offshore surface seawater and upwelled subsurface water. During the summer, a DIC concentration of ~1917 μmol kg^{-1} was observed at S=33.7, which can be regarded as the offshore surface seawater end-member (Guo and Wong, 2015). Here, by choosing S=34.6 as the offshore subsurface water salinity end-member, we obtained a DIC value of ~2023 μmol kg^{-1}, similar to the value at ~100 m depth adopted by Guo and Wong (2015). For the plume end-member, it was difficult to directly select from the field data, because biological alteration might lead to altered values within the plume influenced area. Therefore, we first assumed that the plume water observed on the shelf consisted of a mixture of freshwater and offshore surface seawater. Then, we compiled 3 years of surface data from the summer (August 2012, July 2014 and July 2015) to extrapolate the relatively stable freshwater end-member and examine the biological effect on DIC-salinity relationships. By constraining DIC end-members (freshwater and offshore surface seawater), we observed that DIC remained overall conservative when salinity was <10.8 but showed removal when salinity was >10.8 (Han et al., 2012). Thus, we derived plume end-member values (1670±50 μmol kg^{-1}) from the DIC-salinity conservative mixing curve at S=10.8. Furthermore, S=10.8 was observed at the innermost station (A08) during Leg 1, which agreed well with the spatial and temporal scale of the actual water mass mixing in our survey. To confirm our results, we also used a freshwater end-member (S=0), but the output of the model showed little difference from that based on the plume end-member at S=10.8.

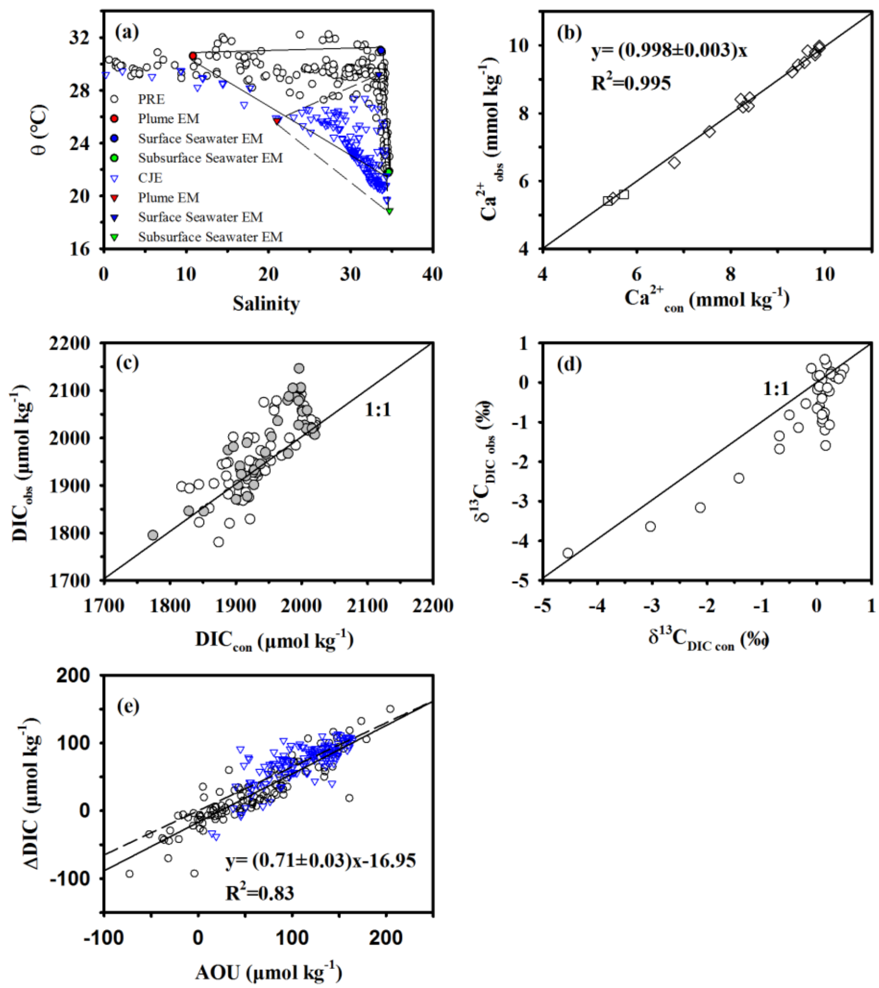

Figure 2.7: (a) Potential temperature (θ) (°C) vs. salinity in the PRE and adjacent coastal waters (open circles) based on data collected during the July 2014 cruise. The three end-members are shown as different coloured symbols. The blue triangles represent data collected during the August 2011 cruise in the Changjiang Estuary (CJE) (Wang et al., 2016); (b) Correlation between the field-observed Ca^{2+} (Ca^{2+}_{obs}) and conservative Ca^{2+} (Ca^{2+}_{con}). The straight line denotes a linear regression line of both surface (square) and subsurface (diamond) data; (c), (d) Relationship between observed and conservative DIC and $\delta^{13}C_{DIC}$ values. The straight line represents a 1:1 reference line. Note that the grey dots in (c) identify data also in (d); and (e) Correlation of ΔDIC vs. AOU for all subsurface water data. ΔDIC is the difference between the field-observed and conservative DIC concentrations. Also shown is the data from Wang et al. (2016). The straight and dashed lines indicate linear regressions of data from the PRE and CJE, respectively.

The $\delta^{13}C_{DIC}$ value was 0.6±0.2 ‰ in the offshore surface seawater at S=~33.7, where nutrient (NO_3^-+NO_2^- and DIP) concentrations were close to their detection limits and DO was nearly saturated, indicating little biological activity. As DIC remained overall conservative when salinity was < 10.8, the $\delta^{13}C_{DIC}$ value of -11.4±0.2 ‰ at S < 0.4 is representative of the freshwater source. Assuming the plume water is a mixture of freshwater and offshore surface seawater, the initial plume end-member of $\delta^{13}C_{DIC}$ at S=10.8 can be calculated via an isotopic mass balance (-7.0±0.8 ‰). A summary of the end-member values used in this study is listed in Table 2.1.

Table 2.1: Summary of end-member values and their uncertainties adopted in the three end-member mixing model.

Water Mass	θ (°C)	Salinity	DIC (μmol kg^{-1})	$\delta^{13}C_{DIC}$ (‰)	Ca^{2+} (μmol kg^{-1})
Plume	30.6±1.0	10.8	1670±50[a]	-7.0±0.8[b]	3670±16[c]
Surface	31.0±1.0	33.7±0.2	1917±3	0.6±0.2	9776±132[c]
Subsurface	21.8±1.0	34.6±0.1	2023±6	0.1±0.1	10053

[a] In order to derive a proper plume end-member value, we took advantage of 3 years of surface dataset from summer cruises (see Sect. 2.4.1). For DIC, the data is from cruises during August 2012, July 2014 and July 2015.
[b] See details in Sect. 2.4.1.
[c] The Ca^{2+} values of the plume and surface seawater end-member are derived from a conservative mixing calculation (Ca^{2+} vs. S) based on 3 years of surface data during the summer (August 2012, July 2014 and July 2015).

We calculated the fractions of the three water masses based on potential temperature and salinity equations, so as to predict conservative DIC (DIC_{con}) and its isotopic composition ($\delta^{13}C_{DICcon}$) solely from conservative mixing. We chose the concentration of Ca^{2+} as a conservative tracer to validate our model prediction, assuming $CaCO_3$ precipitation or dissolution is not significant. This assumption is supported by a strong linear relationship between surface water Ca^{2+} and salinity, and aragonite oversaturation (Ω_{arag}=2.6±0.7) in the subsurface water. Our model derived values were in good accordance with the field-observed values (Fig. 2.7b), which strongly supported our model prediction.

As shown in Fig. 2.7c, most of the observed DIC concentrations in the subsurface water were higher than the conservative values, as a result of DIC production via OC oxidation. This coincided with lighter $\delta^{13}C_{DIC}$ values than conservative, owing to the accumulation of isotopically lighter carbon entering the DIC pool from remineralized organic matter (Fig. 2.7d). Based on the differences between the observed and conservative values of DIC and $\delta^{13}C_{DIC}$, the carbon isotopic composition of the oxygen-consuming organic matter could be traced precisely (see details in Sect. 2.4.2).

In the subsurface water, the bulk of ΔDIC values varied from 0 to 132 μmol kg^{-1}, coupled with a range of apparent oxygen utilization (AOU) values from 0 to 179 μmol kg^{-1}. ΔDIC values positively correlated with AOU (Fig. 2.7e), corresponding to the fact that the additional DIC was supplied by organic matter remineralization via aerobic respiration. The slope of ΔDIC vs. AOU in the subsurface water was 0.71±0.03, which agrees well with classic Redfield stoichiometry (i.e., 106/138=0.77), providing further evidence for aerobic respiration as the source of added DIC. As a first order comparison, the water column total oxygen consumption rate of 9.8 μmol L^{-1} d^{-1} could well support the oxygen decline rate observed at Station A10 in the hypoxic zone between 20 and 27 July (Fig. 2.6), which was 7.7 μmol L^{-1} d^{-1}. This comparison along with the stoichiometry between ΔDIC and AOU strongly suggests that water column aerobic respiration may be predominate in the formation of the hypoxia in the present case.

2.5.2 Isotopic composition of the oxygen-consuming OC

The DIC isotopic mass balance is shown in Eq. (2.6) (Wang et al., 2016):

$$\delta^{13}C_{DICobs}\times DIC_{obs}=\delta^{13}C_{DICcon}\times DIC_{con}+\delta^{13}C_{DICbio}\times DIC_{bio} \quad (2.6)$$

where the subscripts obs, con and bio refer to the field-observed, conservative and biologically altered values.

Degradation of OC typically produces DIC with minor isotopic fractionation from the OC substrate (Hullar et al., 1996; Breteler et al., 2002). Thus, the isotopic composition of DIC_{bio} (i.e., $\delta^{13}C_{DICbio}$) should be identical to the $\delta^{13}C$ of the OC ($\delta^{13}C_{OCx}$), which consumed oxygen and produced DIC_{bio}. $\delta^{13}C_{OCx}$ was derived from the mass balance equations of both DIC and its stable isotope:

$$\delta^{13}C_{OCx}=\frac{\delta^{13}C_{obs}\times DIC_{obs}-\delta^{13}C_{con}\times DIC_{con}}{DIC_{obs}-DIC_{con}} \quad (2.7)$$

Equation (2.7) can be rearranged into Eq. (2.8):

$$\Delta(\delta^{13}C_{DIC}\times DIC)=\delta^{13}C_{OCx}\times\Delta DIC \quad (2.8)$$

As shown in Fig. 2.8, the slope of the linear regression represents $\delta^{13}C_{OCx}$ or $\delta^{13}C_{DICbio}$, which here is equal to -23.2±1.1 ‰. This value reflects the original $\delta^{13}C$ signature of the remineralized organic matter contributing to the observed addition of DIC.

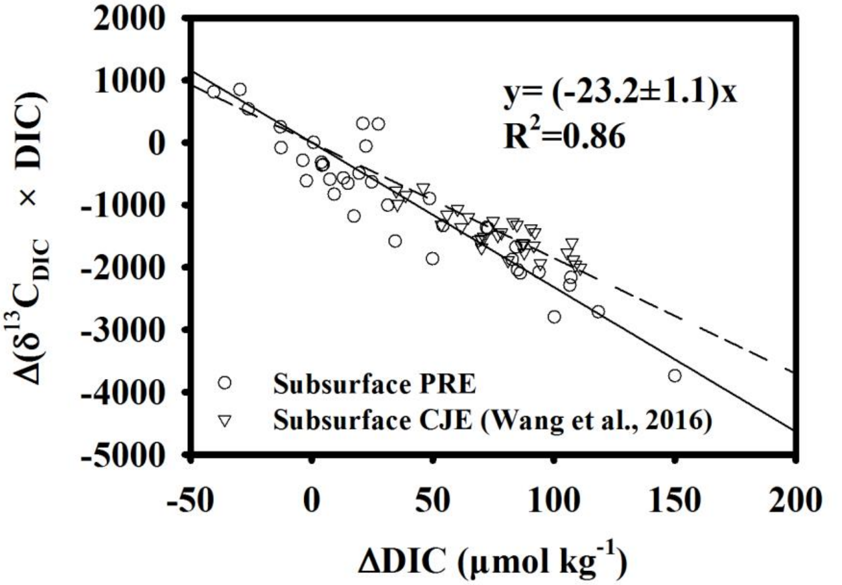

Figure 2.8: Δ ($\delta^{13}C_{DIC} \times$ DIC) vs. ΔDIC in the PRE. Samples were collected from subsurface water (> 5 m). Δ is the difference between the field-observed and conservative values. Also shown is data from the Changjiang Estuary (CJE) reported by Wang et al. (2016). The straight and dashed lines indicate linear regression lines of data from the PRE and CJE, respectively. The regression equation is shown for the PRE.

Although studies have shown selective diagenesis of isotopically heavy or light pools of organic matter (Marthur et al., 1992; Lehmann et al., 2002), these effects are small compared to the isotopic differences among different sources of organic matter (Meyers, 1997). It is thus reasonable to assume that the isotopic ratios are conservative and that physical mixing of the end-member sources determine the isotopic composition of organic matter in natural systems (Gearing et al., 1984; Cifuentes et al., 1988; Thornton and McManus, 1994). The relative contributions of marine and terrestrial sources to oxygen-consuming organic matter in our study area could be estimated based on the following equation (Shultz and Calder, 1976; Hu et al., 2006):

$$f(\%)=\frac{\delta^{13}C_{mar}-\delta^{13}C_{OCx}}{\delta^{13}C_{mar}-\delta^{13}C_{terr}}\times 100 \qquad (2.9)$$

Here, for the terrestrial end-member ($\delta^{13}C_{terr}$), we adopted the average $\delta^{13}C$ value of POC sampled near the Humen Outlet (S<4), which represents the predominant source of riverine material entering the estuary (He et al., 2010). The mean $\delta^{13}C_{POC}$ value, -28.3±0.7 ‰ (n=7), is very similar to the freshwater $\delta^{13}C_{POC}$ value of -28.7 ‰ reported by Yu et al. (2010), which reflected a terrigenous mixture of C3 plant fragments and forest soils. For the marine end-member ($\delta^{13}C_{mar}$), we calculated the mean surface water $\delta^{13}C_{POC}$ value (-19.4±0.8 ‰, n=8) from stations with S>26 where significant phytoplankton blooms were observed, as indicated by DO supersaturation (DO% > 125 %) and relatively high pH values (> 8.3) and POC contents (5.3±2.4 %). This value is similar to, although slightly heavier than the marine end-member used by Chen et al. (2008), who measured a $\delta^{13}C$ value of -20.9 ‰ in tow-net phytoplankton samples from outer Lingdingyang Bay, in the same region as this study. Additionally, He et al. (2010a) reported a $\delta^{13}C$ value of -20.8±0.4 ‰ in phytoplankton collected from the northern South China Sea. These values are consistent enough for us to compile and use an average $\delta^{13}C_{mar}$ value of -20.5±0.9 ‰. This value agrees well with the reported stable carbon isotopic signature of marine organic matter in other coastal regions. For example, mean isotopic values of phytoplankton were reported as -20.3±0.6 ‰ in Narragansett Bay (Gearing et al., 1984), -20.3±0.9 ‰ in Auke Bay and Fritz Cove (Goering et al., 1990), and -20.1±0.8 ‰ in the Gulf of Lions (Harmelin-Vivien et al., 2008).

Our model results suggest that marine organic matter contributed to 65±16 % of the observed oxygen consumption, while terrestrial organic matter accounted for the remaining 35±16 %. It is thus clear that marine organic matter from eutrophication-induced primary production dominated oxygen consumption in the hypoxic zone; however, terrestrial organic matter also contributed significantly to the formation and maintenance of hypoxia in the lower PRE and adjacent coastal waters.

2.5.3 Comparison with hypoxia in the East China Sea off the Changjiang Estuary

As one of the largest rivers in the world, the Changjiang has been suffering from eutrophication for the past few decades (Zhang et al., 1999; Wang et al., 2014). In summer, sharp density gradients with frequent algal blooms and subsequent organic matter decomposition cause seasonal hypoxia in the bottom water of the ECS off the CJE. Wang et al. (2016) revealed that the remineralization of marine organic matter (OC_{mar}) overwhelmingly (nearly 100 %) contributed to DO consumption in the ECS off the CJE. However, our present study showed that less OC_{mar} contributed to the oxygen depletion (65±16 %) in the hypoxic zone of the lower PRE.

As shown in Fig. 2.5, there is little difference between $\delta^{13}C_{DIC}$ and $\delta^{13}C_{POC}$ values of the marine end-member. However, the $\delta^{13}C_{DIC}$ and $\delta^{13}C_{POC}$ values of the freshwater end-member showed some dissimilarity, with lighter values in the PRE (-11.4±0.2 ‰, -28.3±0.7 ‰) than in the CJE (-8.8 ‰, -24.4±0.2 ‰). In Fig. 2.7e, the amplitude of ΔDIC and AOU values suggest a similar intensity of OM biodegradation, and the slope of ΔDIC vs. AOU (0.71±0.03 vs. 0.65±0.04) indicates a predominance of aerobic respiration in the two systems. As seen from Table 2.2, there is no significant difference between the $\delta^{13}C$ values of surface sediments within the hypoxic zones of the PRE and CJE. However, data in Fig. 2.7a show generally higher water temperatures in the PRE than in the CJE. For instance, the temperatures of surface and subsurface seawater end-members in the PRE were 2-3 ℃ higher than in the CJE. From a spatial point of view, the distance from the river mouth to the hypoxic zone in the CJE is 2-3 times longer than in the PRE, possibly resulting in a longer travel time of OC_{terr}. Therefore, we contend that the difference in the predicted distributions of marine and terrestrial sources of organic matter contributing to oxygen consumption in and off the PRE and CJE is likely related to differences in the bioavailability of OC_{terr} and OC_{mar}, the microbial community structures and the physical settings between these two hypoxic systems.

Table 2.2: Comparison of $\delta^{13}C$ values in surface sediments within the hypoxic zone[a] between the PRE and CJE.

$\delta^{13}C$ (‰)	Mean±SD	Stations involved	References
		Pearl River Estuary	
-23.4 ~ -22.1	-22.9±0.5	A4, A5, C1-C4, D1	Hu et al. (2006)
-23.2 ~ -22.3	-22.7±0.5	28, 29, 30	Zong et al. (2006)
-23.6 ~ -21.5	-22.5±1.1	E8-1, E7A, S7-1, S7-2	He et al. (2010a)
-[b]	-23.1±0.6	Clustering groups G6 and G7	Yu et al. (2010)
Average	-22.8±0.6		
		Changjiang Estuary	
-22.9 ~ -20.9	-21.8±0.6	-[c]	Tan et al. (1991)
-22.4 ~ -19.9	-21.2±1.0	32, 37, 38, 42, 48, 49, 54, 56, 64	Kao et al. (2003)
-22.7 ~ -20.8	-22.0±0.8	H1-12, H2-10, H2-11, S1-2, S2-4	Xing et al. (2011)
-23.5 ~ -20.4	-22.6±1.0	3, 12, 13, 20-25	Yao et al. (2014)
Average	-21.9±1.0		

[a]In the PRE, the data is from similar sites to our present study, which is in the northeast (Leg 1) and southwest (Leg 2) of the Wanshan Islands. While in the CJE, the hypoxic zone is located around 30.0° N–32.0° N, 122.7° E–123.2° E, which is frequently reported in previous studies (Li et al., 2002; Zhu et al., 2011b; Wang et al., 2016).
[b]The authors provide an average value of clustering groups instead of individual data from each site.
[c]In Fig. 7 of Tan et al. (1991), the sampling sites are shown without numbers.

Although C3 plants dominate and C4 plants are minor in both the Pearl River and Changjiang drainage basins (Hu et al., 2006; Zhu et al., 2011a), the OC_{terr} delivered from these two watersheds experiences varying degrees of degradation within the estuaries before being transported into the coastal hypoxic zones. In the CJE, approximately 50 % of OC_{terr} becomes remineralized during transport through the estuary, likely due to efficient OM unloading from mineral surfaces (Zhu et al., 2011a) and longer residence times within the estuary, facilitating microbial transformation and degradation. In contrast, the PRE appears to be a somewhat intermediate site with the export of OC_{terr} being closely associated with sedimentary regimes and not characterized by extensive degradative loss (Strong et al., 2012). Thus, the bioavailability of OC_{terr} that reached the hypoxic zone is likely higher in the PRE than in the CJE. Moreover, the increased precipitation and runoff during the typhoon may have mobilized additional fresh anthropogenic OM from surrounding megacities (e.g. Guangzhou, Shenzhen and Zhuhai) deposited in the river channel, which could lead to more labile OC_{terr} in the PRE. Additionally, the difference in bacterial community structure between the two systems may have played a role. Recent studies have demonstrated that the bacterial community in the PRE is characterized by higher relative abundances of Actinobacteria and lower relative abundances of Cytophaga-Flavobacteria-Bacteroides (CFB) than in the CJE (Liu et al., 2012; Zhang et al., 2016). Whether such differences would promote the degradation of OC_{terr} in the PRE relative to the CJE remains unknown. Finally, the temperature of the bottom water in the PRE hypoxic zone (23.7–27.0 °C) was higher than in the CJE hypoxic zone (20.5–23.0 °C), which may have accelerated the rates of bacterial growth and OM decomposition (Brown et al., 2004).

2.6 Conclusions

Based on a three end-member mixing model and the mass balance of DIC and its isotopic composition, we demonstrated that the organic matter decomposed via aerobic respiration in the stratified subsurface waters of the lower PRE and adjacent coastal waters was predominantly OC_{mar} (49-81 %, mean 65 %), with a significant portion of OC_{terr} also decomposed (19-51 %, mean 35 %). The relative distribution of organic matter sources contributing to oxygen drawdown differs in the hypoxic zone off the CJE, where it is caused almost entirely by OC_{mar}. These differences have important implications for better understanding the controls on hypoxia and its mitigation. Nevertheless, with respect to increasing coastal nutrient levels, a significant implication of the present study is that reducing and managing nutrients is critical to control eutrophication and, subsequently, to mitigate hypoxia (Conley et al., 2009; Paerl, 2009; Mercedes et al., 2015; Stefan et al., 2016). Given that OC_{terr} also contributes to the consumption of oxygen in the lower PRE hypoxic zone, it is crucial to characterize the source of this oxygen-consuming terrestrial organic matter, whether from natural soil leaching and/or anthropogenic wastewater discharge, so as to make proper policies for hypoxia remediation.

The processes involved in the partitioning of organic matter sources, their isotopic signals and their subsequent biogeochemical transformations in the PRE hypoxic zone are illustrated in the conceptual diagram in Fig. 2.9. The river delivers a significant amount of nutrients and terrestrial organic matter to the estuary, stimulating phytoplankton blooms in the surface water at the lower reaches of the estuary where turbidity is relatively low and conditions are favourable for phytoplankton growth (Gaston et al., 2006; Dai et al., 2008b; Guo et al., 2009). The subsequent sinking of this biomass along with terrestrial organic matter below the pycnocline consumes oxygen and adds respired DIC to subsurface waters, resulting in coastal hypoxia. Therefore, we conclude that within the PRE and adjacent coastal areas, the most important biological process with respect to forming and maintaining hypoxic conditions is aerobic respiration.

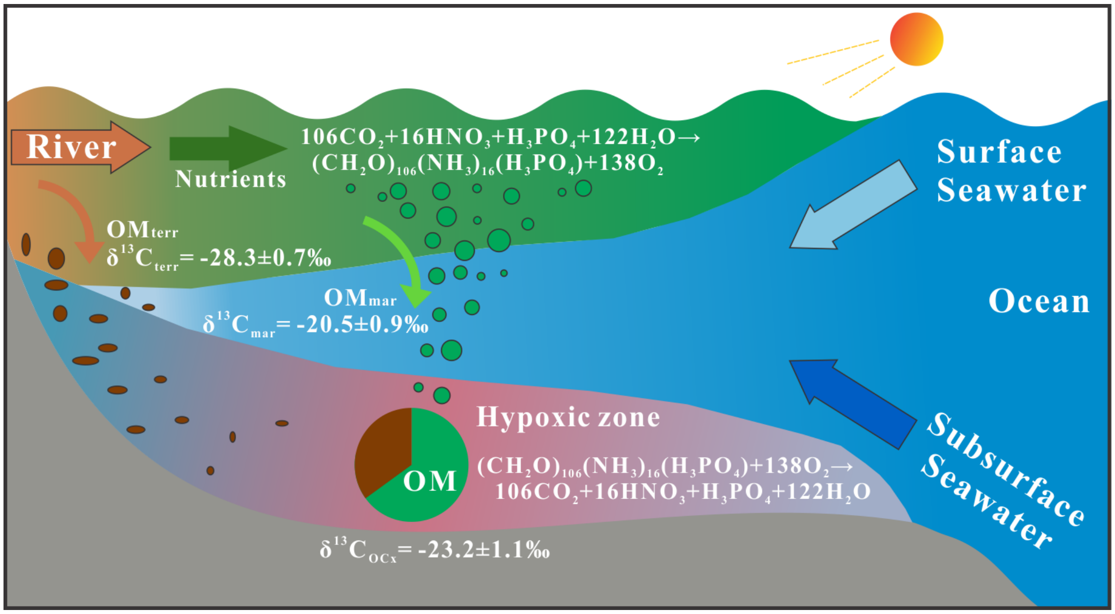

Figure 2.9: A conceptual diagram illustrating the partitioning of oxygen-consuming organic matter (OC_{mar} vs. OC_{terr}) within the hypoxic zone in the lower PRE and the adjacent coastal area. See Sect. 2.5 for explanations.

REFERENCES

Bianchi, T.S., 2011. The role of terrestrially derived organic carbon in the coastal ocean: A changing paradigm and the priming effect. Proc. Natl. Acad. Sci. U.S.A. 108, 19473-19481. doi:10.1073/pnas.1017982108

Bianchi, T.S., Wysocki, L.A., Schreiner, K.M., Filley, T.R., Corbett, D.R. and Kolker, A.S., 2011. Sources of terrestrial organic carbon in the Mississippi plume region: evidence for the importance of coastal marsh inputs. Aquat. Geochem. 17, 431-456. doi:10.1007/s10498-010-9110-3

Boesch, D.F., Boynton, W.R., Crowder, L.B., Diaz, R.J., Howarth, R.W., Mee, L.D., Nixon, S.W., Rabalais, N.N., Rosenberg, R., Sanders, J.G., Scavia, D. and Turner, R.E., 2009. Nutrient Enrichment Drives Gulf of Mexico Hypoxia. Eos, Trans. Amer. Geophys. Union 90, 117-118. doi:10.1029/2009EO140001

Breitburg, D., 2002. Effects of hypoxia, and the balance between hypoxia and enrichment, on coastal fishes and fisheries. Estuaries 25, 767-781. doi:10.1007/BF02804904

Breteler, W.C.K., Grice, K., Schouten, S., Kloosterhuis, H.T. and Damsté, J.S.S., 2002. Stable carbon isotope fractionation in the marine copepod Temora longicornis: unexpectedly low $\delta^{13}C$ value of faecal pellets. Mar. Ecol. Prog. Ser. 240, 195-204. doi:10.3354/meps240195

Brown, J.H., Gillooly, J.F., Allen, A.P., Savage, V.M. and West, G.B., 2004. Toward a metabolic theory of ecology. Ecology 85, 1771-1789. doi:10.1890/03-9000

Cai, W.-J., Dai, M., Wang, Y., Zhai, W., Huang, T., Chen, S., Zhang, F., Chen, Z. and Wang, Z., 2004. The biogeochemistry of inorganic carbon and nutrients in the Pearl River estuary and the adjacent Northern South China Sea. Cont. Shelf Res. 24, 1301-1319. doi:10.1016/j.csr.2004.04.005

Cao, Z., Dai, M., Zheng, N., Wang, D., Li, Q., Zhai, W., Meng, F. and Gan, J., 2011. Dynamics of the carbonate system in a large continental shelf system under the influence of both a river plume and coastal upwelling. J. Geophys. Res. Biogeosci. 116, G02010. doi:10.1029/2010JG001596

Carstensen, J., Andersen, J.H., Gustafsson, B.G. and Conley, D.J., 2014. Deoxygenation of the Baltic Sea during the last century. Proc. Natl. Acad. Sci. U.S.A. 111, 5628-5633. doi:10.1073/pnas.1323156111

Cifuentes, L., Sharp, J. and Fogel, M.L., 1988. Stable carbon and nitrogen isotope biogeochemistry in the Delaware estuary. Limnol. Oceanogr. 33, 1102-1115. doi:10.4319/lo.1988.33.5.1102

Conley, D.J., Paerl, H.W., Howarth, R.W., Boesch, D.F., Seitzinger, S.P., Karl, E., Karl, E., Lancelot, C., Gene, E. and Gene, E., 2009. Controlling

eutrophication: nitrogen and phosphorus. Science 123, 1014-1015. doi:10.1126/science.1167755
Dai, M., Guo, X., Zhai, W., Yuan, L., Wang, B., Wang, L., Cai, P., Tang, T. and Cai, W.-J., 2006. Oxygen depletion in the upper reach of the Pearl River estuary during a winter drought. Mar. Chem. 102, 159-169. doi:10.1016/j.marchem.2005.09.020
Dai, M., Wang, L., Guo, X., Zhai, W., Li, Q., He, B. and Kao, S.-J., 2008a. Nitrification and inorganic nitrogen distribution in a large perturbed river/estuarine system: the Pearl River Estuary, China. Biogeosciences 5, 1227-1244. doi:10.5194/bg-5-1227-2008
Dai, M., Zhai, W., Cai, W.-J., Callahan, J., Huang, B., Shang, S., Huang, T., Li, X., Lu, Z., Chen, W. and Chen, Z., 2008b. Effects of an estuarine plume-associated bloom on the carbonate system in the lower reaches of the Pearl River estuary and the coastal zone of the northern South China Sea. Cont. Shelf Res. 28, 1416-1423. doi:10.1016/j.csr.2007.04.018
Diaz, R.J. and Rosenberg, R., 2008. Spreading dead zones and consequences for marine ecosystems. Science 321, 926-929. doi:10.1126/science.1156401
Gaston, T.F., Schlacher, T.A. and Connolly, R.M., 2006. Flood discharges of a small river into open coastal waters: Plume traits and material fate. Estuar. Coast. Shelf Sci. 69, 4-9. doi:10.1016/j.ecss.2006.03.015
Gearing, J.N., Gearing, P.J., Rudnick, D.T., Requejo, A.G. and Hutchins, M.J., 1984. Isotopic variability of organic carbon in a phytoplankton-based, temperate estuary. Geochim. Cosmochim. Acta 48, 1089-1098. doi:10.1016/0016-7037(84)90199-6
Goering, J., Alexander, V. and Haubenstock, N., 1990. Seasonal variability of stable carbon and nitrogen isotope ratios of organisms in a North Pacific Bay. Estuar. Coast. Shelf Sci. 30, 239-260. doi:10.1016/0272-7714(90)90050-2
Guo, X., Dai, M., Zhai, W., Cai, W.-J. and Chen, B., 2009. CO_2 flux and seasonal variability in a large subtropical estuarine system, the Pearl River Estuary, China. J. Geophys. Res. Biogeosci. 114. doi:10.1029/2008JG000905
Guo, X. and Wong, G.T.F., 2015. Carbonate chemistry in the Northern South China Sea Shelf-sea in June 2010. Deep-Sea Res. II 117, 119-130. doi:10.1016/j.dsr2.2015.02.024
Han, A., Dai, M., Kao, S.-J., Gan, J., Li, Q., Wang, L., Zhai, W. and Wang, L., 2012. Nutrient dynamics and biological consumption in a large continental shelf system under the influence of both a river plume and coastal upwelling. Limnol. Oceanogr. 57, 486-502. doi:10.4319/lo.2012.57.2.0486
Harmelin-Vivien, M., Loizeau, V., Mellon, C., Beker, B., Arlhac, D., Bodiguel, X., Ferraton, F., Hermand, R., Philippon, X. and Salen-Picard, C., 2008. Comparison of C and N stable isotope ratios between surface particulate organic matter and microphytoplankton in the Gulf of Lions (NW Mediterranean). Cont. Shelf Res. 28, 1911-1919

He, B., Dai, M., Zhai, W., Wang, L., Wang, K., Chen, J., Lin, J., Han, A. and Xu, Y., 2010. Distribution, degradation and dynamics of dissolved organic carbon and its major compound classes in the Pearl River estuary, China. Mar. Chem. 119, 52-64. doi:10.1016/j.marchem.2009.12.006

He, B., Dai, M., Zhai, W., Guo, X. and Wang, L., 2014. Hypoxia in the upper reaches of the Pearl River Estuary and its maintenance mechanisms: A synthesis based on multiple year observations during 2000–2008. Mar. Chem. 167, 13-24. doi:10.1016/j.marchem.2014.07.003

He, G.-f. and Yuan, G.-m., 2007. Assessment of the water quality by fuzzy mathematics for last 20 years in Zhujiang Estuary. Mar. Environ. Sci. 26, 53-57

Hu, J., Peng, P.a., Jia, G., Mai, B. and Zhang, G., 2006. Distribution and sources of organic carbon, nitrogen and their isotopes in sediments of the subtropical Pearl River estuary and adjacent shelf, Southern China. Mar. Chem. 98, 274-285. doi:10.1016/j.marchem.2005.03.008

Huang, X., Huang, L. and Yue, W., 2003. The characteristics of nutrients and eutrophication in the Pearl River estuary, South China. Mar. Pollut. Bull. 47, 30-36. doi:10.1016/S0025-326X(02)00474-5

Hullar, M., Fry, B., Peterson, B. and Wright, R., 1996. Microbial utilization of estuarine dissolved organic carbon: a stable isotope tracer approach tested by mass balance. Appl. Environ. Microbiol. 62, 2489-2493

Kao, S.-J., Terence Yang, J.-Y., Liu, K.-K., Dai, M., Chou, W.-C., Lin, H.-L. and Ren, H., 2012. Isotope constraints on particulate nitrogen source and dynamics in the upper water column of the oligotrophic South China Sea. Global Biogeochem. Cycles 26, GB2033. doi:10.1029/2011GB004091

Kemp, W., Testa, J., Conley, D., Gilbert, D. and Hagy, J., 2009. Temporal responses of coastal hypoxia to nutrient loading and physical controls. Biogeosciences 6, 2985-3008. doi:10.5194/bg-6-2985-2009

Lehmann, M.F., Bernasconi, S.M., Barbieri, A. and McKenzie, J.A., 2002. Preservation of organic matter and alteration of its carbon and nitrogen isotope composition during simulated and in situ early sedimentary diagenesis. Geochim. Cosmochim. Acta 66, 3573-3584. doi:10.1016/S0016-7037(02)00968-7

Li, D., Zhang, J., Huang, D., Wu, Y. and Liang, J., 2002. Oxygen depletion off the Changjiang (Yangtze River) estuary. Sci. China Ser. D-Earth Sci. 45, 1137-1146. doi:10.1360/02yd9110

Liu, M., Xiao, T., Wu, Y., Zhou, F., Huang, H., Bao, S. and Zhang, W., 2012. Temporal distribution of bacterial community structure in the Changjiang Estuary hypoxia area and the adjacent East China Sea. Environ. Res. Lett. 7, 025001. doi:10.1088/1748-9326/7/2/025001

Marthur, J.M., Tyson, R.V., Thomson, J. and Mattey, D., 1992. Early diagenesis of marine organic matter: Alteration of the carbon isotopic composition. Mar. Geol. 105, 51-61. doi:10.1016/0025-3227(92)90181-G

Mercedes, M.C.B., Luiz Antonio, M., Tibisay, P., Rafael, R., Jean Pierre, H.B.O., Felipe Siqueira, P., Silvia Rafaela Machado, L. and Sorena, M., 2015. Nitrogen management challenges in major watersheds of South America. Environ. Res. Lett. 10, 065007. doi:10.1088/1748-9326/10/6/065007

Meyers, P.A., 1997. Organic geochemical proxies of paleoceanographic, paleolimnologic, and paleoclimatic processes. Org. Geochem. 27, 213-250. doi:10.1016/S0146-6380(97)00049-1

Nixon, S.W., 1995. Coastal marine eutrophication: A definition, social causes, and future concerns. Ophelia 41, 199-219. doi:10.1080/00785236.1995.10422044

Paerl, H.W., 2006. Assessing and managing nutrient-enhanced eutrophication in estuarine and coastal waters: Interactive effects of human and climatic perturbations. Ecol. Eng. 26, 40-54. doi:10.1016/j.ecoleng.2005.09.006

Paerl, H.W., 2009. Controlling Eutrophication along the Freshwater–Marine Continuum: Dual Nutrient (N and P) Reductions are Essential. Estuar. Coast. 32, 593-601. doi:10.1007/s12237-009-9158-8

Peterson, B.J. and Fry, B., 1987. Stable Isotopes in Ecosystem Studies. Annu. Rev. Ecol. Syst. 18, 293-320

Qian, W., Dai, M., Xu, M., Kao, S.-j., Du, C., Liu, J., Wang, H., Guo, L. and Wang, L., 2017. Non-local drivers of the summer hypoxia in the East China Sea off the Changjiang Estuary. Estuar. Coast. Shelf Sci. 198, 393-399. doi:10.1016/j.ecss.2016.08.032

Qian, W., Gan, J., Liu, J., He, B., Lu, Z., Guo, X., Wang, D., Guo, L., Huang, T. and Dai, M., 2018. Current status of emerging hypoxia in a eutrophic estuary: The lower reach of the Pearl River Estuary, China. Estuar. Coast. Shelf Sci. 205, 58-67. doi:10.1016/j.ecss.2018.03.004

Rabalais, N., Cai, W.-J., Carstensen, J., Conley, D., Fry, B., Hu, X., Quiñones-Rivera, Z., Rosenberg, R., Slomp, C., Turner, E., Voss, M., Wissel, B. and Zhang, J., 2014. Eutrophication-Driven Deoxygenation in the Coastal Ocean. Oceanography 27, 172-183. doi:10.5670/oceanog.2014.21

Rabalais, N.N., Díaz, R.J., Levin, L.A., Turner, R.E., Gilbert, D. and Zhang, J., 2010. Dynamics and distribution of natural and human-caused hypoxia. Biogeosciences 7, 585-619. doi:10.5194/bg-7-585-2010

Rabouille, C., Conley, D.J., Dai, M.H., Cai, W.J., Chen, C.T.A., Lansard, B., Green, R., Yin, K., Harrison, P.J., Dagg, M. and McKee, B., 2008. Comparison of hypoxia among four river-dominated ocean margins: The Changjiang (Yangtze), Mississippi, Pearl, and Rhône rivers. Cont. Shelf Res. 28, 1527-1537. doi:10.1016/j.csr.2008.01.020

Rutger, R., Stefan, A., Birthe, H., Hans, C.N. and Karl, N., 2002. Recovery of marine benthic habitats and fauna in a Swedish fjord following improved oxygen conditions. Mar. Ecol. Prog. Ser. 234, 43-53. doi:10.3354/meps234043

Shultz, D.J. and Calder, J.A., 1976. Organic carbon $^{13}C/^{12}C$ variations in estuarine sediments. Geochim. Cosmochim. Acta 40, 381-385. doi:10.1016/0016-7037(76)90002-8

Steckbauer, A., Duarte, C.M., Carstensen, J., Vaquer-Sunyer, R. and Conley, D.J., 2011. Ecosystem impacts of hypoxia: thresholds of hypoxia and pathways to recovery. Environ. Res. Lett. 6, 025003. doi:10.1088/1748-9326/6/2/025003

Stefan, R., Mateete, B., Clare, M.H., Nancy, K., Wilfried, W., Xiaoyuan, Y., Albert, B. and Mark, A.S., 2016. Synthesis and review: Tackling the nitrogen management challenge: from global to local scales. Environ. Res. Lett. 11, 120205. doi:10.1088/1748-9326/11/12/120205

Strong, D.J., Flecker, R., Valdes, P.J., Wilkinson, I.P., Rees, J.G., Zong, Y.Q., Lloyd, J.M., Garrett, E. and Pancost, R.D., 2012. Organic matter distribution in the modern sediments of the Pearl River Estuary. Org. Geochem. 49, 68-82. doi:10.1016/j.orggeochem.2012.04.011

Swarzenski, P., Campbell, P., Osterman, L. and Poore, R., 2008. A 1000-year sediment record of recurring hypoxia off the Mississippi River: The potential role of terrestrially-derived organic matter inputs. Mar. Chem. 109, 130-142. doi:10.1016/j.marchem.2008.01.003

Thornton, S.F. and McManus, J., 1994. Application of Organic Carbon and Nitrogen Stable Isotope and C/N Ratios as Source Indicators of Organic Matter Provenance in Estuarine Systems: Evidence from the Tay Estuary, Scotland. Estuar. Coast. Shelf Sci. 38, 219-233. doi:10.1006/ecss.1994.1015

Vaquer-Sunyer, R. and Duarte, C.M., 2008. Thresholds of hypoxia for marine biodiversity. Proc. Natl. Acad. Sci. U.S.A. 105, 15452-15457. doi:10.1073/pnas.0803833105

Wang, H., Dai, M., Liu, J., Kao, S.-J., Zhang, C., Cai, W.-J., Wang, G., Qian, W., Zhao, M. and Sun, Z., 2016. Eutrophication-Driven Hypoxia in the East China Sea off the Changjiang Estuary. Environ. Sci. Technol. 50, 2255-2263. doi:10.1021/acs.est.5b06211

Wang, Q., Koshikawa, H., Liu, C. and Otsubo, K., 2014. 30-year changes in the nitrogen inputs to the Yangtze River Basin. Environ. Res. Lett. 9, 115005. doi:10.1088/1748-9326/9/11/115005

Ye, F., Huang, X., Zhang, X., Zhang, D., Zeng, Y. and Tian, L., 2012. Recent oxygen depletion in the Pearl River Estuary, South China: geochemical and microfaunal evidence. J. Oceanogr. 68, 387-400. doi:10.1007/s10872-012-0104-1

Zhang, J., Zhang, Z.F., Liu, S.M., Wu, Y., Xiong, H. and Chen, H.T., 1999. Human impacts on the large world rivers: Would the Changjiang (Yangtze River) be an illustration? Global Biogeochem. Cycles 13, 1099-1105. doi:10.1029/1999GB900044

Zhang, J., Cowie, G. and Naqvi, S.W.A., 2013. Hypoxia in the changing marine environment. Environ. Res. Lett. 8, 015025. doi:10.1088/1748-9326/8/1/015025

Zhang, Y., Xiao, W. and Jiao, N., 2016. Linking biochemical properties of particles to particle-attached and free-living bacterial community structure along the

particle density gradient from freshwater to open ocean. J. Geophys. Res. Biogeosci. 121, 2261-2274. doi:10.1002/2016JG003390
Zhao, H.-D., Kao, S.-J., Zhai, W.-D., Zang, K.-P., Zheng, N., Xu, X.-M., Huo, C. and Wang, J.-Y., 2017. Effects of stratification, organic matter remineralization and bathymetry on summertime oxygen distribution in the Bohai Sea, China. Cont. Shelf Res. 134, 15-25. doi:10.1016/j.csr.2016.12.004
Zhu, C., Wagner, T., Pan, J.-M. and Pancost, R.D., 2011a. Multiple sources and extensive degradation of terrestrial sedimentary organic matter across an energetic, wide continental shelf. Geochem. Geophys. Geosyst. 12, Q08011. doi:10.1029/2011GC003506
Zhu, Z.-Y., Zhang, J., Wu, Y., Zhang, Y.-Y., Lin, J. and Liu, S.-M., 2011b. Hypoxia off the Changjiang (Yangtze River) Estuary: oxygen depletion and organic matter decomposition. Mar. Chem. 125, 108-116. doi:10.1016/j.marchem.2011.03.005
Zimmerman, A.R. and Canuel, E.A., 2000. A geochemical record of eutrophication and anoxia in Chesapeake Bay sediments: anthropogenic influence on organic matter composition. Mar. Chem. 69, 117-137. doi:10.1016/S0304-4203(99)00100-0

Chapter 3

SOURCE PARTITIONING OF OXYGEN-CONSUMING ORGANIC MATTER IN THE HYPOXIC ZONE OF THE CHESAPEAKE BAY[2]

3.1 Abstract

We surveyed the carbonate system along the main channel of the Chesapeake Bay in June 2016 to elucidate carbonate dynamics and the associated sources of oxygen-consuming organic matter. Using a two endmember mixing calculation, chemical proxies, and stoichiometry, we demonstrated that in early summer, dissolved inorganic carbon (DIC) dynamics were controlled by aerobic respiration in the water column (43%), sulfate reduction in the sediment (39%), atmospheric CO_2 invasion (13%), and $CaCO_3$ dissolution (5%). A mass balance of the DIC concentration and its stable isotope suggested that the apparent $\delta^{13}C$ of oxygen-consuming organic matter was -19.4±0.3‰. The bulk composition of particulate organic matter also reflected a dominance of algal material (C/N = ~6, $\delta^{13}C$ > -25‰). Therefore, we concluded that the decomposition of autochthonous organic matter (i.e. eutrophication-stimulated primary production) was the dominant process consuming oxygen, while allocthonous organic matter (terrestrially-derived) made minor contributions to oxygen consumption in the hypoxic zone in June 2016. These findings in the Chesapeake Bay contrast with another hypoxic estuarine ecosystem, the Pearl River Estuary in China,

[2] Chapter 3 is based on a manuscript in preparation by Jianzhong Su, Wei-Jun Cai, Jean Brodeur, Najid Hussain, Baoshan Chen, Jeremy M. Testa, K. Michael Scaboo, Deb P. Jaisi, Qiang Li, Minhan Dai, Jeffrey Cornwell

where allochthonous organic matter contributed significantly to oxygen consumption. The differences between these two systems in terms of hydrology, quantity and quality of organic matter, and physical characteristics are discussed to yield new insights on the formation and maintenance of hypoxia. In both systems, autochthonous organic matter dominates oxygen depletion, indicating that nutrient management and reduction are useful actions to control and mitigate the occurrence of hypoxia for the restoration of ecosystem.

3.2 Introduction

Eutrophication-induced hypoxia in coastal waters has increased in spatial extent and severity in recent decades (Diaz and Rosenberg, 2008; Breitburg et al., 2018). Respiration-driven oxygen depletion in bottom water is associated with CO_2 production and enhanced ocean acidification, threatening a variety of aquatic and benthic organisms and habitats (Wu, 2002; Orr et al., 2005; Cai et al., 2011; Kroeker et al., 2013). Hypoxia is an outcome of an imbalance between oxygen supply and demand, where water stratification physically inhibits oxygen replenishment from surface water allowing for organic matter (OM) remineralization to consume oxygen at a faster rate than reaeration of the bottom water (Rabouille et al., 2008; Testa et al., 2018). Oxygen-consuming OM may originate from outside the aquatic system (i.e. allochthonous source) or be generated internally within the system (i.e. autochthonous source) (Paerl, 2006; Rabalais et al., 2010). Allochthonous organic matter (Alloc-OC) typically originates from the watershed, including natural inputs such as vascular plant detritus, OM resulting from soil leaching and erosion, and anthropogenic inputs such as municipal and industrial wastewater, and agricultural runoff. In contrast, autochthonous organic matter (Autoc-OC) usually refers to eutrophication-stimulated primary production of phytoplankton within estuaries and the coastal oceans. Although many studies have demonstrated that highly reactive Autoc-OC dominates oxygen consumption in hypoxic waters (Turner and Rabalais, 1994; Rabalais et al., 2014), others have suggested that the seemingly refractory, but occasionally abundant Alloc-OC may be more labile than previously thought due to a priming effect, and thus may also play an important role in oxygen depletion (Swarzenski et al., 2008; Bianchi, 2011; Bianchi et al., 2011). The priming effect means the enhanced degradation of recalcitrant organic matter in the presence of possible priming substrates, such as phytoplankton exudates, heterotroph metabolites and high nutrient cycling (Bianchi, 2011), which eventually leads to the enhanced release of OM-derived carbon and nutrient as well as the enhanced consumption of oxygen. Quantifying the relative contributions of OM sources fueling oxygen consumption in the hypoxic zone allows for new insights on the formation and maintenance of hypoxia, while providing scientific support for regional management and policy-making for environmental restoration.

The Chesapeake Bay develops seasonal bottom water hypoxia and anoxia (Hagy et al., 2004; Murphy et al., 2011), due to a long water residence time of ~180 days (Du and Shen, 2016), high retention of nutrients and OM, and high rates of internal Autoc-OC production (Fennel and Testa, 2018). Previous studies have found that water column respiration dominates oxygen consumption, accounting for nearly two-thirds of the total respiration in below-pycnocline waters of the mid- Chesapeake Bay from April to August (Kemp et al., 1992; Li et al., 2016). The annual organic carbon budget for the Chesapeake Bay indicates that the input of Alloc-OC from rivers and the watershed is larger than Autoc-OC in the upper bay, while Autoc-OC represents most of the total organic carbon input in the mid- and lower bay (Biggs and Flemer, 1972; Kemp et al., 1997; Shen et al., 2019b). The volume of hypoxic/anoxic water has a positive relationship with winter-spring river flow and nutrient loading (Hagy et al., 2004; Kemp et al., 2005), indicating Autoc-OC significantly contributes to respiration in the bay's hypoxic zone. However, observation-based studies have clearly shown either net heterotrophy or high CO_2 supersaturation in landward bay regions (Smith and Kemp, 1995; Cai et al., 2017), and modeling studies have shown the organic loading from watershed and reservoir sediment scour during storm events can cause dissolved oxygen declines in the mainstem deep channel (Cerco and Noel, 2016; Linker et al., 2016), both of which would suggest that Alloc-OC is important in some bay regions at some times. The extent to which this Alloc-OC influences the mid-bay region, especially if it is transported seaward in brief events, is unclear. Furthermore, the Chesapeake Bay is a local hotspot for sea level rise and associated shoreline erosion (Stevenson et al., 1985; Stevenson et al., 1988; Najjar et al., 2010). The extent to which OM originating from these eroding marshes is labile and reaches deeper mainstem waters also remains unknown. Therefore, direct quantitative measurements of the relative contributions of Autoc-OC vs. Alloc-OC to oxygen consumption in the hypoxic zone of the Chesapeake Bay are needed to reinforce budget analyses and to improve our understanding of hypoxia drivers within the context of climate change (Najjar et al., 2010; Orth et al., 2017) and recent nutrient reductions (Lefcheck et al., 2018; Testa et al., 2018).

In this study, we investigated the OM sources driving hypoxia formation and quantified the relative contribution of key respiration reactions involved in OM degradation using a suite of isotopic measures, chemical surveys, and mixing models.

We adopted a two endmember mixing calculation to distinguish the biogeochemical processes from physical mixing in the Chesapeake Bay. Furthermore, chemical proxies and stoichiometry were used to quantify the rates of key biogeochemical processes, particularly sulfate reduction, sulfide storage in the sediments, and atmospheric CO_2 invasion. Since aerobic respiration of OM produces DIC with $\delta^{13}C$-DIC similar to the isotope value of the respired OM (Hullar et al., 1996), we utilized a mass balance of DIC and its stable carbon isotope to trace the $\delta^{13}C$ of the respired substrate or oxygen-consuming OM in the hypoxic zone of the Chesapeake Bay. By combining those analyses with an examination of the bulk composition (C/N, $\delta^{13}C$) of the particulate organic matter (POM) in the surface water of main channel as we previously did (Su et al., 2017), we were able to quantify the sources of oxygen-consuming OM. Finally, we compared the source partitioning results in the hypoxic zones of the Chesapeake Bay with the Pearl River Estuary, the largest estuary in southern China, in order to gain new insights on the formation and maintenance of hypoxia.

3.3 Materials and Methods

3.3.1 Study site

The Chesapeake Bay (36.9°N–39.6°N, 75.5°W–77.5°W) is the largest estuary in the United States. The bay has a length of over 300 km, and a mean depth of 6.5 m (Kemp et al., 2005). The deep and narrow central channel is flanked by broad shallow areas, and the southern end is confined by a sill (Boicourt et al., 1999). The large watershed area and long dendritic bay shorelines make the bay susceptible to human disturbance, such as deforestation, agriculture and urbanization. Eutrophication in the

Chesapeake Bay began after European colonization in the 17th and 18th centuries (Brush, 2009), and became more severe since the 1950s due to the growth in fertilizer use and other human activities in the watershed (Kemp et al., 2005). Nutrient loading increased steadily from the 1950s through the late-1980s (Hagy et al., 2004), after which loads stabilized and declined. Bay-wide water column nitrogen concentrations have decreased by 23%, and phosphorus concentrations have decreased by 8% from 1984 to 2015 (Lefcheck et al., 2018). Hypoxia typically begins in the late spring (late April and May) in the landward reaches of the bay's deep central basin, then expands seaward to occupy large regions of the main channel (Hagy et al., 2004; Testa and Kemp, 2014). During the last three decades, the north-ward and winter-ward migration of the spring bloom has been associated with an increased volume of early season hypoxia, but a reduced late season volume and earlier hypoxia breakup (Murphy et al., 2011; Testa et al., 2018).

3.3.2 Sampling and analytical methods

During June 6-10, 2016, we conducted a cruise aboard the R/V Rachel Carson along the bay's central axis that spanned the upper bay (CB2.1) southward to the bay mouth (AO1) (Fig. 3.1). During the cruise, we revisited the mid-bay stations 858 four times and CB4.3 twice.

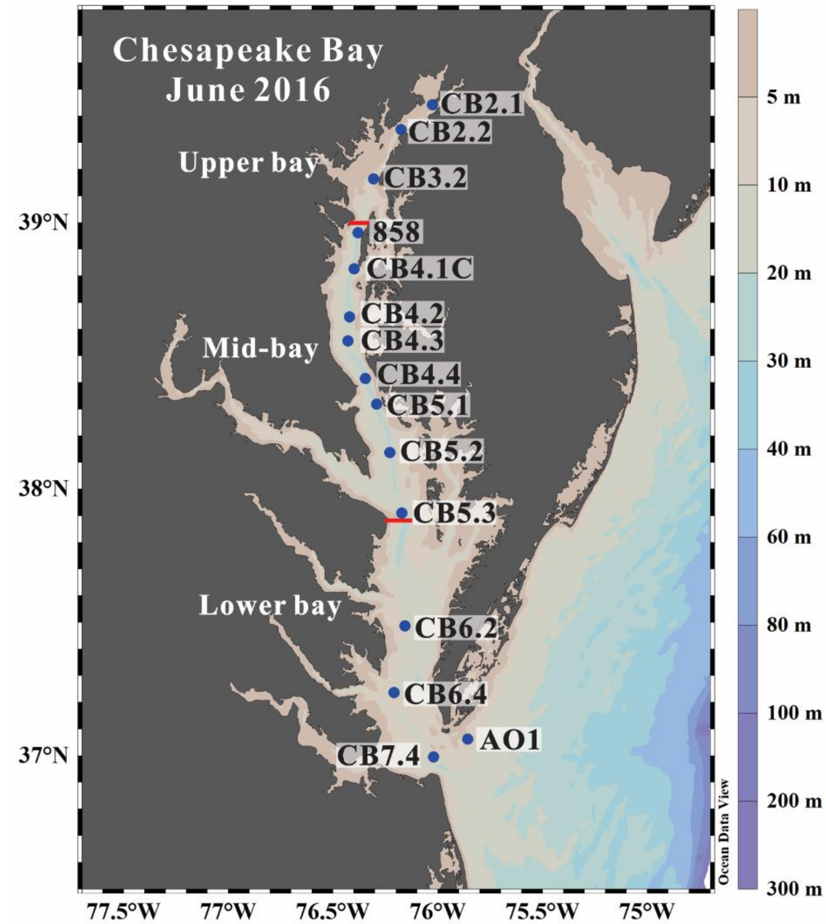

Figure 3.1: Sampling locations along the main channel of the Chesapeake Bay in early June, 2016. Following Kemp et al. (2005), we separated the main stem into three regions, i.e. upper bay (39.0-39.5°N), mid-bay (37.9-39.0 °N) and lower bay (37.0-37.9°N). The boundaries are noted with red lines.

At each station, we used a YSI 6600 attached to a submersible pump to obtain profiles of temperature, salinity, and O_2. Water was pumped from 2-7 depths to the deck for sampling, depending on the number of distinct water masses observed. We measured salinity separately in discrete TA and Ca^{2+} samples using a Cole-Parmer®

salinity meter. For each depth, a water sample was preserved in a 250 mL borosilicate glass bottle with 50 μL saturated $HgCl_2$ solution for DIC and $\delta^{13}C$-DIC analysis. For DIC, a 1 mL sample was acidified and the extracted CO_2 gas was subsequently quantified with an infrared CO_2 detector within one week after the cruise using a DIC analyzer (AS-C3, Apollo Scitech, USA) (Huang et al., 2012). The TA samples were not poisoned (Cai et al., 2017), and were analyzed within 24 h of collection using Gran titration in an open-cell setting (AS-ALK2, Apollo Scitech, USA) (Cai et al., 2010a). The overall precision for DIC and TA was ±0.1%. Both DIC and TA measurements were calibrated against Certified Reference Materials (CRMs) provided by Dr. A. G. Dickson at Scripps Institution of Oceanography (SIO), University of California, San Diego (UCSD). For $\delta^{13}C$-DIC, a 3.8 mL sample was acidified in a gas stripper, CO_2 was extracted by a carrier gas, and the gas stream passed through a moisture condenser in a pre-treatment device (AS-D1, Apollo Scitech, USA) before measurement by a cavity ring-down spectrometer detector (G2131-i, Picarro, USA). A computer program was used to derive the $\delta^{13}C$-DIC value by averaging the $\delta^{13}C$-CO_2 at the stage when the simultaneously determined CO_2 concentration was high enough (>100 ppm) for the detector to measure a stable $\delta^{13}C$-CO_2 signal with little random noise. Two to three repeat runs were carried out for each sample, and a precision of 0.1‰ was achieved. A $NaHCO_3$ solution with known $\delta^{13}C$-DIC value and CRMs were used for calibration. The details on analyzing $\delta^{13}C$-DIC are described in Su et al. (2019).

We measured pH onboard using an Orion Ross glass electrode within 1 h after the water temperature was equilibrated to 25°C in a thermal water bath. Three NIST standards, i.e. 4.01, 7.00, 10.01, were used to calibrate the electrode. We analyzed discrete dissolved oxygen (DO) samples by direct spectrophotometry of total iodine following Pai et al. (1993) with a precision of ±1 μmol kg^{-1}. Apparent oxygen utilization (AOU) was calculated by subtracting the measured DO from the saturated DO (Pilson, 2012; Zhao et al., 2017). The DO solubility was calculated based on Benson and Krause (1984). We measured Ca^{2+} samples using a modified technique of Kanamori and Ikegami (1980) with a precision better than 0.1%. Note that the Ca^{2+} samples were measured in two batches. The upper and mid-bay samples were measured in the first batch, while the lower-bay samples (mostly salinity>20) were measured in the second batch. Further analysis revealed that the deviation of Ca^{2+} (ΔCa^{2+}) relative to the conservative mixing line at salinity>20 had greater noise than the data at salinity<20, which may be due to reduced operating proficiency and electrode stability in the second batch. The pCO_2 was calculated from measured DIC and TA via a modified CO2SYS program with a H_2S component (Xu et al., 2017b). We derived the aragonite saturation state (Ω_{arag}) using measured Ca^{2+}, calculated CO_3^{2-}, and aragonite solubility based on Mucci (1983).

POM samples were collected in the surface water along the main channel in two cruises in June and August 2016. Samples were concentrated onto pre-weighed and pre-combusted 47 mm Whatman GF/F filters of 0.7 µm pore size after filtering 0.3-1.5 L water under a mild vacuum (~25 kPa). Filters were washed with distilled water and stored in a freezer. Before analysis, the filters were dried. Total suspended matter (TSM) was derived from the net weight increment on the filter and the filtration volume. Then, the filters were decarbonated with 1.0 mol L^{-1} HCl, and dried again at 40°C for 48 h (Kao et al., 2012). We analyzed the bulk composition (C, N, $\delta^{13}C$) of POM samples on a DELTA V Plus isotope ratio mass spectrometer (IRMS) coupled with an elemental analyzer (EA) (Costech, CA). The $\delta^{13}C$-POC was calibrated against two standard materials USGS40 ($\delta^{13}C$= -26.39‰) and USGS41 ($\delta^{13}C$= +37.63‰) with a precision of 0.1‰.

3.3.3 Two endmember mixing calculation

In estuarine research, a conservative mixing line of chemical concentrations against salinity between river and ocean endmembers is widely used to distinguish biogeochemical alterations from physical water mixing (Officer, 1979). Compared with the relatively consistent ocean endmember values, large variations exist in the river endmember mainly due to the temporal variations of freshwater discharge (Joesoef et al., 2017). For instance, mean monthly variations of DIC and TA in the Susquehanna River endmember of the Chesapeake Bay in 2016 were one order of magnitude larger than the uncertainty of the estuarine endmember we adopted in this study (Table 3.1) (Brodeur et al., 2019). In addition, tributaries that discharge seaward of the Susquehanna River, such as the Chesapeake-Delaware Canal, may also introduce variability into DIC and TA concentrations. Since our focus is on the hypoxic zone in the mid- Chesapeake Bay, we decided to choose an estuarine endmember from the well-mixed upper bay instead of the traditional river endmember. We considered CB2.2 to be a representative endmember, because it is a well-mixed station in a narrow section of the upper bay before the bay widens downstream, and there are no adjacent major tributaries. Further considering the large slope value of measured Ca^{2+} against salinity (Fig. 3.3b), a small salinity difference between the surface layer (salinity=3.0) and bottom layer (salinity=3.9) at Station CB2.2 would result in a significant difference on Ca^{2+}. Therefore, we adopted the measured values in the low salinity layer (surface) rather than the averaged values of the whole water column at CB2.2 as the estuarine endmember in the upper bay. For the offshore seawater endmember, we first developed linear regressions of DIC, TA, and Ca^{2+} against salinity (DIC= 79×Salinity-596, R^2=0.72, p<0.0001; TA= 54×Salinity+428, R^2=0.99, p<0.0001; Ca^{2+}= 269×Salinity+831, R^2=0.98, p<0.0001) with data from four stations (82, 83, 85 and 87) in the Mid-Atlantic Bight, which were visited during the East Coast Ocean Acidification (ECOA) cruise in July 2015 (Xu et al., 2017a). Then, we used the salinity of the ocean endmember (33.618±0.139) from Cai et al. (2017) to derive the offshore endmember values for our June 2016 cruise. According to the latitude range of the Chesapeake Bay (36°N to 40°N), we adopted the offshore δ^{13}C-DIC endmember value as 1.3±0.1‰ based on Quay et al. (2007), who compiled multi-year δ^{13}C-DIC data to delineate meridional trends of δ^{13}C-DIC in the surface Atlantic Ocean during the 1980s to 2000s. Both the offshore seawater DIC and δ^{13}C-DIC endmember values fall within the ranges in the Mid-Atlantic Bight reported by Bauer et al. (2001). All the endmember values and uncertainties are summarized in Table 3.1.

Table 3.1: Summary of endmember values and their uncertainties.

Endmembers	Salinity	DIC (μmol kg^{-1})	δ^{13}C-DIC (‰)	TA (μmol kg^{-1})	Ca^{2+} (mmol kg^{-1})
CB2.2	2.8±0.1	965±2	-6.8±0.1	929±2	1.246±0.010[a]
Offshore	33.6±0.1	2063±11	1.3±0.1[b]	2245±8	9.884±0.037

[a]Additional salinity measurements were performed on the Ca^{2+} samples (salinity=3.0±0.1).
[b]Cited from Quay et al. (2007).

Then, considering the mid- and lower bay water as a mixture between estuarine water in CB2.2 and offshore seawater, we calculated the mixing fractions of the two endmembers based on the following equations:

$$f_{estu} = \frac{S_{sw} - S_{meas}}{S_{sw} - S_{estu}} \quad (3.1)$$

$$f_{sw} = 1 - f_{estu} \quad (3.2)$$

where S is salinity; f represents the mixing fraction; the subscripts *estu* and *sw* indicate the estuarine and seawater endmember, and *meas* denotes the measured value. These fractions were then used to predict conservative concentrations (i.e. $[X]_{con}$) of certain chemical constituents (i.e. DIC, TA or Ca^{2+}) resulting solely from two endmember mixing:

$$[X]_{con} = [X]_{estu} \times f_{estu} + [X]_{sw} \times f_{sw} \quad (3.3)$$

The difference between measured and conservative values is defined as total non-conservative value of [X] (i.e. Δ[X]total) (Fig. 3.3c):

$$\Delta[X]_{total} = [X]_{meas} - [X]_{con} \quad (3.4)$$

The positive or negative $\Delta[X]_{total}$ indicates addition or removal of [X] to the water column, which is a composite result driven by multiple biogeochemical processes, such as aerobic respiration and $CaCO_3$ dissolution. Similarly, the conservative $\delta^{13}C$-DIC value in the bay resulting from physical mixing of the upper estuarine water and the seawater is:

$$\delta^{13}C_{DICcon} = \frac{\delta^{13}C_{DICestu} \times DIC_{estu} \times f_{estu} + \delta^{13}C_{DICsw} \times DIC_{sw} \times f_{sw}}{DIC_{con}} \quad (3.5)$$

3.4 Results and Discussion

3.4.1 Distribution of chemical constituents along the main channel

Spatial patterns of physical and chemical conditions in June 2016 reveal substantial variations along the salinity gradient. The surface water temperature was generally higher than the bottom water temperature (Fig. 3.2a), where in the mid-bay, the average temperature in the surface water (23.2±1.1°C) was ~5°C higher than in the bottom water (17.9±0.9°C). A two-layer estuarine circulation can clearly be seen from the salinity distribution (Fig. 3.2a), i.e. fresher water flows seaward in the surface, while saline water intrudes landward in the bottom. The salinity gradient contributed to the majority (>90%) of the density stratification (Goodrich et al., 1987; Kemp et al., 1992), with a pycnocline depth at ~10 m inferred from sectional distributions of salinity and DO in Fig. 3.2a and b. Below the pycnocline, there was a hypoxic zone in the mid-bay with the lowest DO of 21 μmol kg^{-1} observed at Station 858. A DO supersaturation zone was observed in the surface water immediately above the hypoxic zone, with the highest DO of 327 μmol kg^{-1} (equivalent to 133% of saturated DO or -81 μmol kg^{-1} of AOU) observed at Station CB3.2, indicating a close spatial coupling between sub-pycnocline aerobic respiration and surface primary production (Fig. 3.2b). Carbonate dynamics were also coupled to oxygen in the hypoxic zone and phytoplankton bloom zone. In the bottom hypoxic zone, DIC and pCO_2 were enriched (Fig. 3.2c and g), while δ^{13}C-DIC, pH, and Ω_{arag} were lower (Fig. 3.2d, g and h). In the surface phytoplankton bloom zone, however, the opposite pattern was observed: DIC and pCO_2 decreased, and δ^{13}C-DIC, pH, and Ω_{arag} increased. The distributions of TA and Ca^{2+} generally followed the pattern of salinity (Fig. 3.2e and f). The pH and Ω_{arag} remained low in the upper bay and in mid-bay bottom water, but were higher in more saline, seaward waters (Fig. 3.2g and h). H_2S was also measured at each station and depth, but concentrations were all below the detection limit (0.5 μmol L^{-1}).

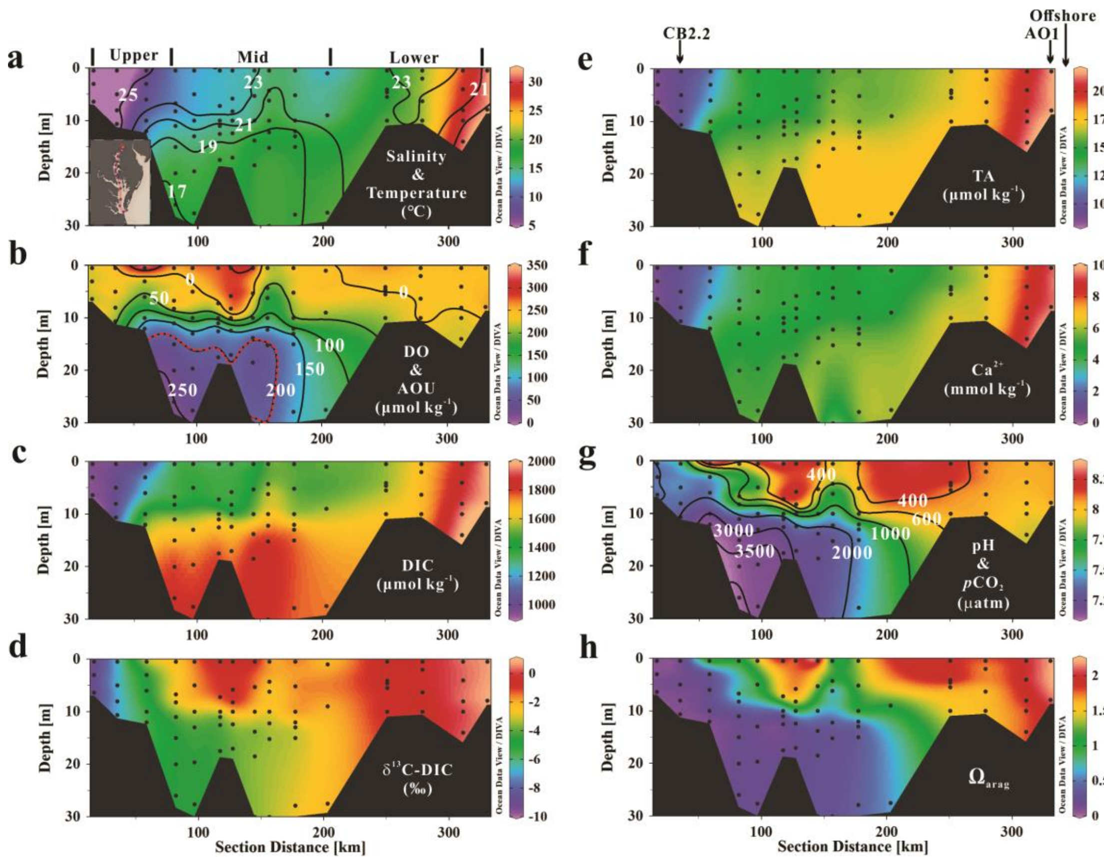

Figure 3.2: Sectional distributions of water properties in the main channel of the Chesapeake Bay in early June, 2016. (a) salinity (color) and contours of temperature, (b) DO and contours for hypoxia (63 μmol kg^{-1}), (c) DIC, (d) δ^{13}C-DIC, (e) TA, (f) Ca^{2+}, (g) pH (NBS, 25°C) and contours for pCO_2, and (h) Ω_{arag}. The inserted map shows the geological location of this section extending from Station CB2.1 to the bay mouth. Offshore stations were not included in the section profiles, because they are located much more offshore in the Mid-Atlantic Bight.

3.4.2 Apparent sources of DIC and TA in the hypoxic zone

DIC and TA behaved in a nearly conservative way in both the upper and lower bay (Fig. 3.3a), but large quantities of DIC and TA were added to the mid-bay water column, with peak addition values of 344 and 161 μmol kg^{-1}, respectively (Fig. 3.3c). AOU was low in the upper bay (< 50 μmol kg^{-1}), increased significantly up to 250 μmol kg^{-1} in the below-pycnocline water of the mid-bay, and was near equilibrium (~0 μmol kg^{-1}) with the atmosphere in the lower bay water (Fig. 3.2b). Non-conservative Ca^{2+} (ΔCa^{2+}) was close to zero at salinity <10, but increased up to 50 μmol kg^{-1} at salinity 10~20 (Fig. 3.3c), suggesting moderate $CaCO_3$ dissolution occurred in the mid-bay water. Beyond salinity 20, ΔCa^{2+} had greater noise than that at salinity <20 probably because of reduced operating proficiency and electrode stability during sample analysis. Since the general pattern of Ca^{2+} against salinity was correct (Fig. 3.3b), and the maximum non-conservative deviation value (ΔCa^{2+} = -61 μmol kg^{-1}) was small compared with the corresponding measured Ca^{2+} values (4,245 to 9,373 μmol kg^{-1}), we retained the Ca^{2+} and ΔCa^{2+} data at salinity>20 in Fig. 3.3b and c as open circles, but excluded those data in further calculations.

Assuming the oxidation state of organic carbon is zero, the aerobic respiration of organic matter characterized with a Redfield ratio (C:N:P = 106:16:1) would result in a stoichiometry of $\Delta DIC_{AR}:\Delta TA_{AR}$:AOU = 106:-17:138 (Table 3.2). Note that H_3PO_4 is a strong acid, and donates a proton in its contribution to TA (Wolf-Gladrow et al., 2007; Cai et al., 2010b). Carbonate dissolution releases Ca^{2+} and increases DIC and TA with a stoichiometry of $\Delta DIC_{CD}:\Delta TA_{CD}:\Delta Ca^{2+}$ = 1:2:1 (Table 3.2). Given that we can directly estimate AOU and ΔCa^{2+}, as well as their related chemical stoichiometry, first we can calculate the DIC and TA changes caused by aerobic respiration (ΔDIC_{AR} = 106×(AOU/138) and ΔTA_{AR} = -17×(AOU/138)) and $CaCO_3$

dissolution ($\Delta DIC_{CD} = \Delta Ca^{2+}$ and $\Delta TA_{CD} = 2\times\Delta Ca^{2+}$). Then, we subtracted the DIC and TA changes of these two processes from the total non-conservative values (ΔDIC_{total} and ΔTA_{total}). The residual DIC and TA (i.e. $\Delta DIC_{total\text{-}CD\text{-}AR}$ and $\Delta TA_{total\text{-}CD\text{-}AR}$) are significantly different from zero (Fig. 3.4), indicating that aerobic respiration and $CaCO_3$ dissolution cannot fully explain the additions of DIC and TA in the mid-bay water column. Previous studies on coastal hypoxia have shown that in addition to the dominance of aerobic respiration, other processes can significantly influence the carbonate dynamics, such as nitrification in the upper reach of the Pearl River Estuary (Dai et al., 2008; He et al., 2014) and oxidation of reduced chemical species in the water column in the Black Sea and Cariaco basin (Millero, 1991b; Rabalais et al., 2010). Considering that the mid-bay is typically where gross primary production, respiration (plankton + benthic) and sulfate reduction peak (Kemp et al., 1997), while surface pCO_2 is undersaturated with respect to the atmosphere in spring and summer (Cai et al., 2017), it is clear that sulfate reduction and atmospheric CO_2 invasion could be alternative contributors to carbonate system dynamics. These two contributors will be discussed in the next two sections.

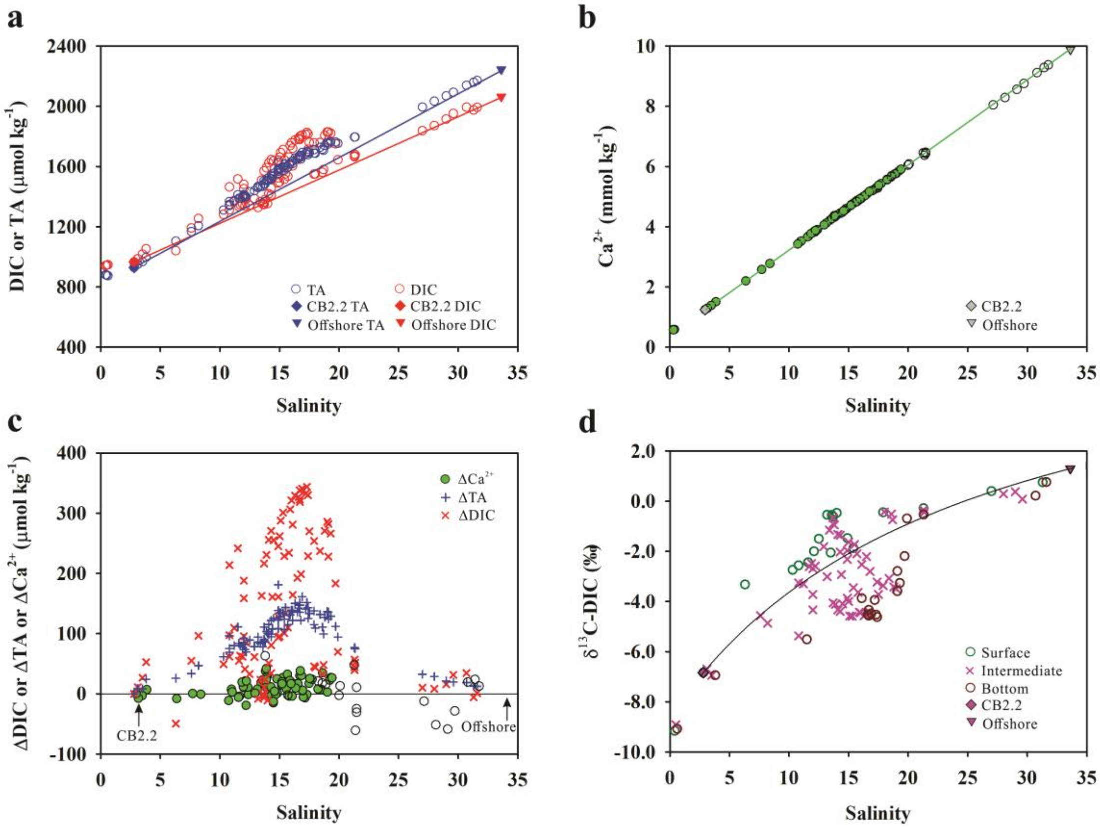

Figure 3.3: Total alkalinity, dissolved inorganic carbon and its stable isotope, calcium ion against salinity, and their deviations from the conservative mixing lines. We calculated mixing lines between CB2.2 (the estuarine endmember) and offshore seawater (the oceanic endmember) to assess the non-conservative behaviors of (a) TA, DIC, (b) Ca^{2+} and (d) $\delta^{13}C$-DIC. The deviation values of TA, DIC and Ca^{2+} are presented in (c). Note that there is a zero reference line and the endmembers are marked by arrows. The open circles in (b) and (c) represent the lower-bay Ca^{2+} and ΔCa^{2+} data, which were measured in the second batch.

Table 3.2 Biogeochemical processes that affect the stoichiometric ratios of DIC and TA.

Processes	Reaction equations	$\Delta TA/\Delta DIC$
AR	$(CH_2O)_{106}(NH_3)_{16}(H_3PO_4) + 138O_2 \rightarrow 106CO_2 + 16HNO_3 + H_3PO_4 + 122H_2O$	-(16+1)/106 = -0.16
CD	$CaCO_3 + CO_2 + H_2O \rightarrow Ca^{2+} + 2HCO_3^-$	2/1
SR[a]	$(CH_2O)_{106}(NH_3)_{16}(H_3PO_4) + 53SO_4^{2-} \rightarrow 106HCO_3^- + 53H_2S + 16NH_3 + H_3PO_4$	(106+16-1)/106 = 1.14
Sulfide oxidation	$H_2S + 2O_2 \rightarrow SO_4^{2-} + 2H^+$	-2/0
Sulfide storage[b]	$Fe(OH)_3 + 1/2H_2S + 2H^+ \rightarrow Fe^{2+} + 1/2S + 3H_2O$	2/0
	$Fe^{2+} + H_2S \rightarrow FeS + 2H^+$	-2/0
	$FeS + H_2S \rightarrow FeS_2 + H_2$	0/0

[a]Cited from Cai et al. (2017).
[b]Cited from Rassmann et al. (2019).

3.4.3 Sulfate reduction and sulfide storage in the sediment

We inferred that sulfate reduction (SR) in the mid-bay sediment had a significant influence on the carbonate system in the water column based on three lines of evidence. First, the residual DIC and TA (i.e. $\Delta DIC_{total\text{-}CD\text{-}AR}$ and $\Delta TA_{total\text{-}CD\text{-}AR}$) are generally positive and have a ratio of 0.86 with a high R^2 of 0.80 in the mid-bay (Fig. 3.4a), which approximates the ratio of DIC and TA changes induced by sulfate reduction (0.88) (Table 3.2). Second, the vertical distribution of $\Delta DIC_{total\text{-}CD\text{-}AR}$ does show higher values in deep water than in surface water, suggesting this residual DIC originates from the sediment (Fig. 3.4b). However, no H_2S was detected in June 2016, while low but detectable O_2 was observed in bottom water, indicating no significant sulfate reduction in the water column. Previous studies have demonstrated that sulfate reduction (60-80%) and aerobic respiration (20-40%) appear to be the most important pathways for organic carbon mineralization in mid-bay sediments at ≥ 10 m water depth (Burdige and Homstead, 1994; Roden et al., 1995). Alternative metabolic pathways (nitrification and methanogenesis) occur at relatively low rates in the mid-bay in summer (Kemp et al., 1990; Hill et al., 1992; Brady et al., 2013; Testa et al., 2013), while much of the metal oxide reduction is dominated by interaction with sulfide, rather than oxidation of sedimentary OM (Burdige, 1993; Lustwerk and Burdige, 1993).

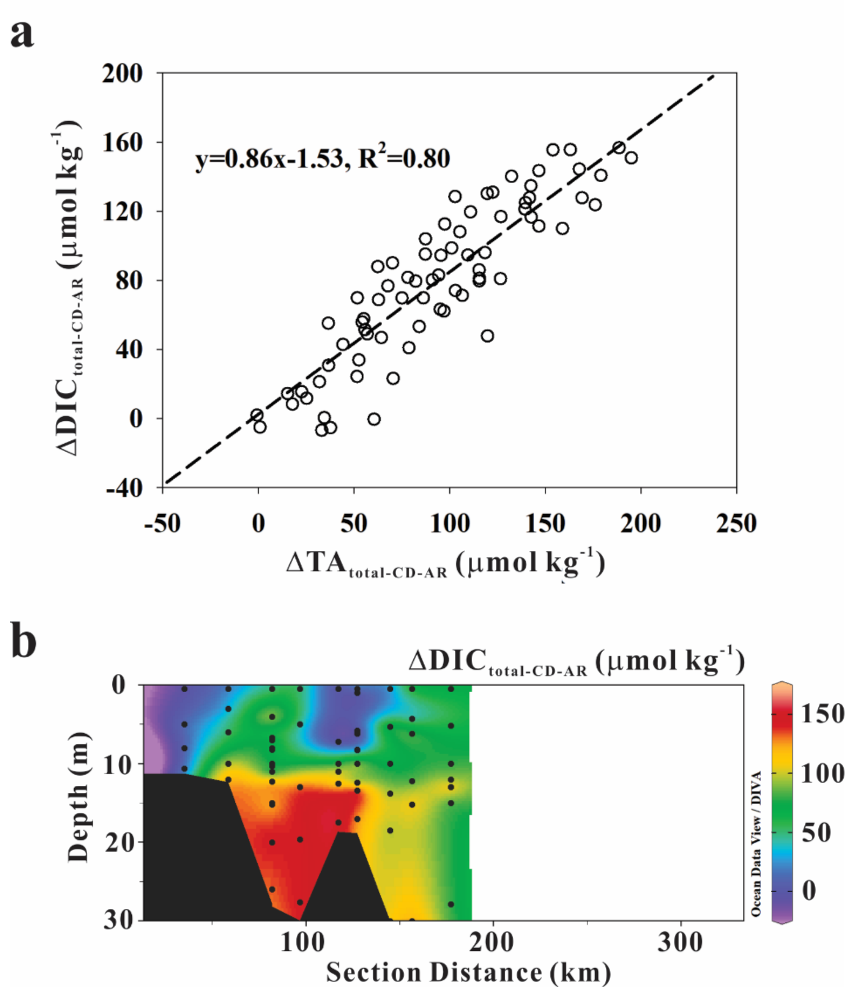

Figure 3.4: (a) The ratio of non-conservative DIC and TA excluding the portion related to carbonate dissolution (CD) and aerobic respiration (AR), and (b) the sectional distribution of the non-conservative DIC values.

In the mid-bay sediments during summer, sulfide production rates via sulfate reduction typically exceed sulfide oxidation rates (Roden and Tuttle, 1992; Roden et al., 1995), suggesting sulfide storage in the sediments (Sampou and Oviatt, 1991) or release to the overlying bottom water (Roden and Tuttle, 1993). During our cruise in June 2016, we did not observe H_2S accumulation in the water column of the hypoxic zone, indicating that H_2S released from the sediment was rapidly oxidized (Millero, 1991a). Oxidation of H_2S by O_2 would not change DIC, but it could consume a considerable fraction of the TA produced by sulfate reduction (Table 3.2). If all of the sulfate reduction-generated H_2S diffused upward and was oxidized by O_2, we would have found the sediments to be a source for DIC, and a weak sink for TA. In contrast, our data show substantial additions of both DIC and TA from the sediment to the water column (Fig. 3.4), indicating that a major proportion of H_2S was removed (or stored) in the sediment below the oxic layer. Previous observations in mid-bay sediments have revealed a dynamic seasonal cycle of iron sulfide accumulation during summer and re-oxidation in winter (Cornwell and Sampou, 1995). Since the abiotic reduction of iron oxides by H_2S coupled with either FeS or pyrite mineral does not overall alter TA (Table 3.2) (Rassmann et al., 2019), this will not influence the ratio of DIC and TA produced by bacterial sulfate reduction, which leads to the slope value nearly identical to 0.88 (Fig. 3.4a).

Based on published data for sulfate reduction rates, sediment-water fluxes, and several related assumptions, we estimated the changes to DIC and TA concentrations resulting from sediment sulfate reduction for comparison with our calculated $\Delta DIC_{total\text{-}CD\text{-}AR}$ (0 to 160 μmol kg^{-1}) and $\Delta TA_{total\text{-}CD\text{-}AR}$ (0 to 200 μmol kg^{-1}) (Fig. 3.4a). To make these calculations, we assumed 1) a mid-bay sulfate reduction rate in June between

15.6 to 70.3 mmol S m^{-2} d^{-1} (Kemp et al., 1997), 2) the ratio of sulfide storage to total sulfate reduction was 20% on an annual basis (Roden and Tuttle, 1993), 3) an average height of 20 m for the whole water column, and 4) a water residence time of 120 d for the mid-bay water (Du and Shen, 2016). Provided these assumptions, we estimated that sulfate reduction followed by sulfide storage would result in a DIC addition of 38 to 169 μmol L^{-1} and a TA addition of 43 to 193 μmol L^{-1} to the water column, comparable to what were derived from our observational-based estimates. Furthermore, previous studies have reported that the measured sediment-water fluxes of DIC were 16~84 mmol m^{-2} d^{-1} in the mid-bay in summer (Burdige and Homstead, 1994; Burdige and Zheng, 1998; Lee et al., 2015). In June, the benthic DIC flux of 30~42 mmol m^{-2} d^{-1} is equivalent to 180~252 μmol L^{-1} DIC addition to the water column under the same assumptions as above, suggesting that sulfate reduction followed by sulfide storage could largely explain the residual DIC and TA addition ($\Delta DIC_{total-CD-AR}$ and $\Delta TA_{total-CD-AR}$) that we derived using stoichiometric balances.

3.4.4 Aerobic respiration and atmospheric CO_2 invasion

In addition to aerobic respiration, oxidation of reduced chemicals (e.g. H_2S, Mn^{2+}, Fe^{2+}) mixing upward from the sediment-water interface also consumes oxygen in the water column. Therefore, it is not strictly correct to use AOU and the theoretical ratio of ΔDIC_{AR}/AOU (i.e. 106/138=0.77) to derive the DIC addition via aerobic respiration of OM. Assuming the stoichiometric ratios of $\Delta TA/\Delta DIC$ for SR (= 1.14) and AR (= -0.16) are valid (Table 3.2), we developed a mass balance of DIC and TA to independently derive their changes induced by aerobic respiration, and further examined its actual ΔDIC_{AR}/AOU ratio. We used x and y to represent the quantities of

DIC addition via SR and AR respectively, and thus the TA changes would be 1.14x for SR and -0.16y for AR.

$$\Delta DIC_{\text{total}} - \Delta DIC_{\text{CD}} = x + y \tag{3.6}$$

$$\Delta TA_{\text{total}} - \Delta TA_{\text{CD}} = 1.14x - 0.16y \tag{3.7}$$

Then, the quantity of SR-induced DIC addition was resolved as *x* and noted as $\Delta DIC_{SR(x1)}$. The actual DIC addition induced by AR was resolved as y and noted as $\Delta DIC_{total\text{-}CD\text{-}SR(x1)}$. As shown in Fig. 3.5, the $\Delta DIC_{total\text{-}CD\text{-}SR(x1)}$/AOU ratio is 0.61 (Fig. 3.5), and is close to the Redfield ratio of 0.77 (Redfield, 1934), indicating aerobic respiration of OM dominated the DO consumption in the water column.

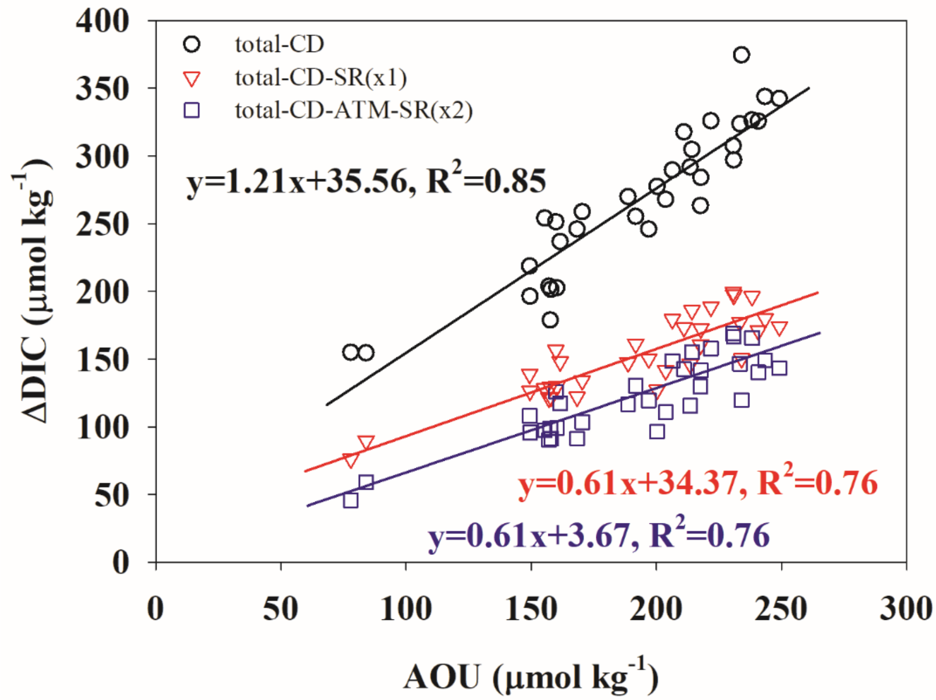

Figure 3.5: The different types of non-conservative DIC plotted against AOU in the below-pycnocline water in the mid-bay. The total-CD refers to the total ΔDIC minus the portion caused by carbonate dissolution (CD). The total-CD-SR(x1) means the part of non-conservative DIC induced by the process excluding CD and sulfate reduction (SR), which is noted as SR(x1) without considering atmospheric CO_2 invasion. Similarly, the total-CD-ATM-SR(x2) indicates the part of non-conservative DIC generated by the process excluding CD, SR and atmospheric CO_2 invasion. More details about SR(x1) and SR(x2) are in the discussion section.

The positive intercepts of $\Delta DIC_{total\text{-}CD}$ and $\Delta DIC_{total\text{-}CD\text{-}SR(x1)}$ against AOU for the below-pycnocline water in the mid-bay, however, mean that there was another DIC source unrelated to oxygen consumption (Fig. 3.5). As shown in Fig. 3.2g, the pCO_2 in the mid-bay surface water was below the atmospheric level (~400 μatm), and should have caused atmospheric CO_2 invasion, which may have contributed to water column CO_2 accumulation (Cai et al., 2017). The intercept value of ~35 μmol kg^{-1} is very close to the bottom-water DIC changes induced by atmospheric CO_2 invasion estimated by Cai et al. (2017) (~21-33 μmol kg^{-1}) and modeled by Shen et al. (2019a) (~20.4-52.3 μmol kg^{-1}). Thus, we suggest that the invasion of atmospheric CO_2 is another important control on water-column DIC, and its alteration on DIC is noted as ΔDIC_{ATM}. Assuming ΔDIC_{ATM} equals 35 μmol kg^{-1} throughout the water column, and CO_2 invasion doesn't influence TA, we can recalculate the DIC addition via AR and SR by using the modified equation (3.6) (i.e. $\Delta DIC_{total} - \Delta DIC_{CD} - \Delta DIC_{ATM} = x+y$) and the same equation (3.7) (i.e. $\Delta TA_{total} - \Delta TA_{CD} = 1.14x-0.16y$). For this time, the SR-induced DIC addition was noted as $\Delta DIC_{SR(x2)}$, while the AR-induced DIC addition was noted as $\Delta DIC_{total-CD-ATM-SR(x2)}$. Here, the regression of $\Delta DIC_{total-CD-ATM-SR(x2)}$ against AOU has a similar slope but a much smaller intercept value, which is not statistically different from zero (n=33, $p > 0.05$) (Fig. 3.5). In order to illustrate the following calculations neatly, the subscripts of $\Delta DIC_{SR(x2)}$, and $\Delta DIC_{total-CD-ATM-SR(x2)}$ were simplified as SR and AR in equations (3.8) to (3.12).

3.4.5 The apparent $\delta^{13}C$ value of oxygen-consuming OM

We have shown that in early June, the non-conservative DIC in the below-pycnocline water of the mid-bay are controlled by aerobic respiration (AR), $CaCO_3$ dissolution (CD), sedimentary sulfate reduction (SR), and the invasion of atmospheric CO_2 (ATM). This allows us to construct a mass balance equation for DIC:

$$\Delta DIC_{\mathrm{total}} = \Delta DIC_{\mathrm{CD}} + \Delta DIC_{\mathrm{ATM}} + \Delta DIC_{\mathrm{SR}} + \Delta DIC_{\mathrm{AR}} \tag{3.8}$$

By dividing the DIC changes from each process by ΔDIC_{total}, we further quantified that CD, ATM, SR and AR accounted for 5%, 13%, 39% and 43% respectively of the total non-conservative DIC in the below-pycnocline waters of the mid-bay. However, the distribution of $\delta^{13}C$-DIC was more than a result of DIC concentration change, but also influenced by the distinct $\delta^{13}C$ source values and isotopic fractionation of individual biogeochemical process (Alling et al., 2012; Samanta et al., 2015; Su et al., 2019). In contrast to the DIC addition in the mid-bay subsurface water, the correlated $\delta^{13}C$-DIC values were beneath the isotopic mixing line (Fig. 3.3d), indicating a considerable proportion of DIC addition was ^{13}C-depleted. Therefore, similar to DIC, we derived a mass balance equation for the stable carbon isotope of DIC:

$$\delta^{13}C_{DICmeas} \times DIC_{meas} - \delta^{13}C_{DICcon} \times DIC_{con} = \delta^{13}C_{DIC_{CD}} \times \Delta DIC_{CD} + \delta^{13}C_{DIC_{ATM2}} \times \Delta DIC_{ATM} + \delta^{13}C_{DIC_{SR}} \times \Delta DIC_{SR} + \delta^{13}C_{DIC_{AR}} \times \Delta DIC_{AR} \tag{3.9}$$

To derive the isotope value of oxygen-consuming OM from equations (3.9) as well as (3.1), (3.3), (3.5) and (3.8), a few assumptions or approximations are needed. The sources of $CaCO_3$ that dissolved in the water column may include marine limestone, abiotic precipitation and biogenic calcification. In Chapter 4, we show that $CaCO_3$ formation driven by submerged aquatic vegetation and shell organisms may play an important role in supplying $CaCO_3$ for further dissolution in the subsurface water of the mid- to lower bay. However, the sources and $\delta^{13}C$ values of these $CaCO_3$ solids have not yet been quantified in the Chesapeake Bay. Considering $CaCO_3$ dissolution only accounted for 5% of the DIC addition in early June 2016, the uncertainty introduced by $\delta^{13}C$-DIC_{CD} must be rather small. Thus, we tentatively assume the $\delta^{13}C$-DIC_{CD} to be 0‰, which is widely used to represent marine limestone (Craig, 1953; Presley and Kaplan, 1968).

Yet, the invasion of atmospheric CO_2 would also cause isotopic fractionation between the atmospheric CO_2 and added DIC. Given the average temperature (20.6±2.4°C) in the mid-bay water column, the fractionation factor could be calculated as -9.4‰ following Samanta et al. (2015). Assuming the $\delta^{13}C$ of atmospheric CO_2 was -8‰, we can derive the $\delta^{13}C$ of CO_2-invasion-induced DIC ($\delta^{13}C$-DIC_{ATM}) as 1.4‰. Aerobic respiration and sulfate reduction both degrade OM, but use different terminal electron acceptors, i.e. O_2 vs. SO_4^{2-}. Aerobic degradation of OM typically produces DIC with minor isotopic fractionation from the substrate OM (Hullar et al., 1996; Breteler et al., 2002; Lehmann et al., 2002). Previous studies indicate that degradation of marine POM via sulfate reduction is a non-fractionating process, and have adopted the $\delta^{13}C$ of POM undergoing degradation as the $\delta^{13}C$ value of the end-product DIC (Irwin et al., 1977; Komada et al., 2016; Fernandes et al., 2018). Therefore, the isotopic composition of DIC_{AR} (i.e. $\delta^{13}C_{AR}$) and DIC_{SR} (i.e. $\delta^{13}C_{SR}$) should be identical to the $\delta^{13}C$ of substrate OM (i.e. $\delta^{13}C_{OCx}$), which consumes oxygen or sulfate and produces DIC to the water column. Thus, the $\delta^{13}C_{OCx}$ could be derived from the following equation:

$$\delta^{13}C_{OCx} = \frac{\delta^{13}C_{DICmeas}\times DIC_{meas} - \delta^{13}C_{DICcon}\times DIC_{con} - \delta^{13}C_{DIC_{CD}}\times \Delta DIC_{CD} - \delta^{13}C_{DIC_{ATM}}\times \Delta DIC_{ATM}}{DIC_{meas} - DIC_{con} - \Delta DIC_{CD} - \Delta DIC_{ATM}} \quad (3.10)$$

where DIC_{con} and $\delta^{13}C_{DICcon}$ could be calculated from Equation (3.3) and (3.4), ΔDIC_{CD} equals to the deviation of Ca^{2+} (i.e. ΔCa^{2+}), and ΔDIC_{ATM} equals 35 μmol kg^{-1} throughout the water column. The propagated errors of the calculated $\delta^{13}C_{OCx}$ can be estimated following Wang et al. (2018). The composite uncertainty of the derived $\delta^{13}C_{OCx}$ was ±3.8‰, which was the potential maximum uncertainty when propagating all errors from the endmembers and measurements. Combining Equation (3.9) and (3.10), we get the following equation:

$$\delta^{13}C_{AR}\times \Delta DIC_{AR} + \delta^{13}C_{SR}\times \Delta DIC_{SR} = \delta^{13}C_{OCx}\times (\Delta DIC_{AR} + \Delta DIC_{SR}) \quad (3.11)$$

Note that ΔDIC_{AR} (=$\Delta DIC_{total\text{-}CD\text{-}ATM\text{-}SR(x2)}$) and ΔDIC_{SR} (=$\Delta DIC_{SR(x2)}$) are known, and $\delta^{13}C_{OCx}$ (=$\delta^{13}C_{AR}$=$\delta^{13}C_{SR}$) can be calculated for each sample by equation (3.10).

Unlike the co-dominance of AR and SR as well as a moderate contribution from CD and ATM to DIC and $\delta^{13}C_{DIC}$ dynamics in the Chesapeake Bay, AR is the most important biogeochemical process controlling DIC and $\delta^{13}C_{DIC}$ in the Pearl River Estuary (Su et al., 2017). In order to compare the magnitude of AR-induced DIC change and the apparent origin of oxygen-consuming organic matter in the two systems, we extracted the portion only induced by AR from equation (11) and expressed that as:

$$\Delta(\delta^{13}C_{DIC} \times DIC) = \delta^{13}C_{OCx} \times \Delta DIC_{AR} \qquad (3.12)$$

The term at the left side of equation (3.12) is the product of $\delta^{13}C_{OCx}$ (=$\delta^{13}C_{AR}$) and ΔDIC_{AR} for each sample. When we plot $\Delta(\delta^{13}C_{DIC} \times DIC)$ against ΔDIC_{AR} (Fig. 3.6), the slope value of -19.4±0.3‰ reflects the apparent $\delta^{13}C$ signature of oxygen-consuming OM undergoing remineralization. Note that the uncertainty of the slope (±0.3‰) is directly derived from the linear regression in Fig. 3.6, which is much smaller than the potential maximum composite uncertainty of the derived $\delta^{13}C_{OCx}$ (±3.8‰). In this case, we used marine limestone as the $CaCO_3$ source ($\delta^{13}C\text{-}DIC_{CD}$ = 0‰). However, Grimm et al. (2017) once measured the $\delta^{13}C$ of oyster shells in the James River estuary, one of the tributaries in the southwestern Chesapeake Bay, which ranged from -7.6 to 0.5‰ and had a positive relationship with salinity. Even if $\delta^{13}C\text{-}DIC_{CD}$ varies from -8 to 1‰ as measured for oyster shells (Grimm et al., 2017), the slope value changes little from -19.0 to -19.5‰, which is within the uncertainty of the slope using $\delta^{13}C\text{-}DIC_{CD}$ = 0‰. Therefore, in our case the slope value is not sensitive to the variation of $\delta^{13}C\text{-}DIC_{CD}$ because carbonate dissolution contributed only a small fraction (~5%) to the DIC addition in early June 2016. Assuming the isotopic composition of OM is conservative or regulated only by physical mixing, this apparent

$\delta^{13}C_{OCx}$ could be seen as a mixing signal from two distinct endmember sources, i.e. Autoc-OC and Alloc-OC (Thornton and McManus, 1994).

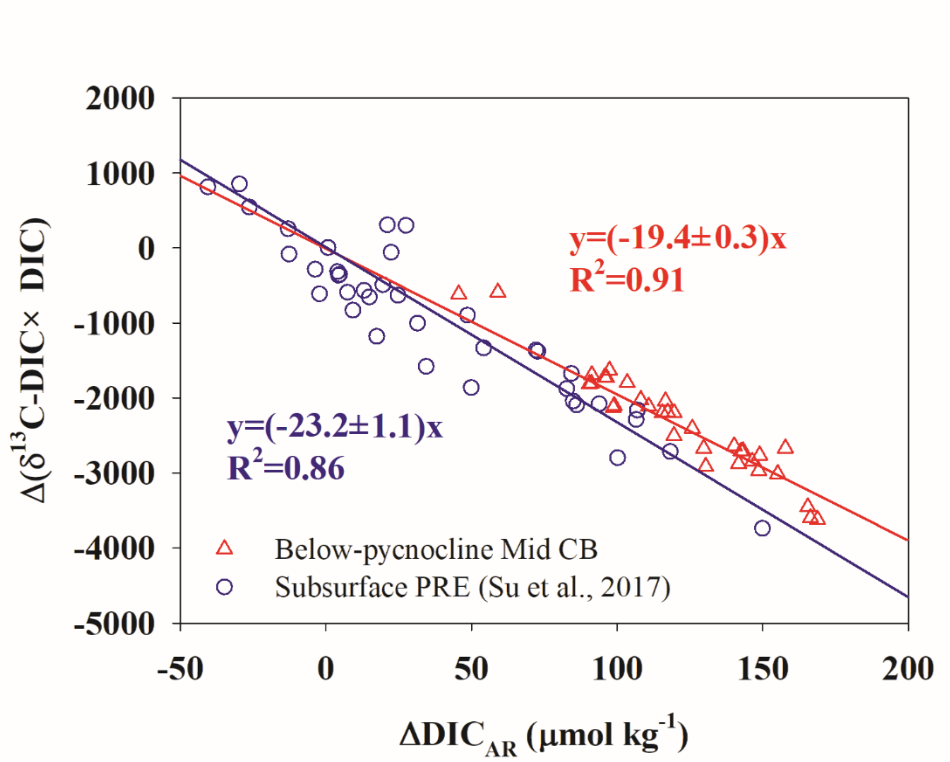

Figure 3.6: The $\Delta(\delta^{13}C\text{-DIC}\times DIC)$ vs. ΔDIC_{AR} in the below-pycnocline water of the mid- Chesapeake Bay. The slope reflects the original $\delta^{13}C$ signature of oxygen-consuming OM undergoing remineralization ($\delta^{13}C_{OCx}$). The PRE dataset is from Su et al. (2017).

3.4.6 Source partitioning of oxygen-consuming OM

We verified the relative contributions of Autoc-OC and Alloc-OC by examining the bulk composition of POM and defining the isotopic endmember values (Shultz and Calder, 1976; Thornton and McManus, 1994; Yu et al., 2010). Total suspended matter (TSM) showed a decreasing trend from the upper (~13 mg kg^{-1}) to the lower bay (~4 mg kg^{-1}) (Fig. 3.7a), while POC sharply increased in the southern portion of the upper bay, and then decreased seaward (Fig. 3.7b). The peak POC value occurred at CB3.2, which had the highest DO (327 μmol kg^{-1}) and chlorophyll-a concentration (16.0 μg L^{-1}), indicating that the POC increase was caused by strong primary production and associated phytoplankton biomass. The molar C/N ratio varied from 4.4 to 7.9, with an average value close to 6 (Fig. 3.7c), similar to the results of Boynton et al. (1985) (4.0-13.0), Horrigan et al. (1990) (6.9-12.2), Canuel and Zimmerman (1999) (4.8-9.1), Sigleo and Macko (2002) (7.0-12.0) and Loh et al. (2006) (~6.0). The δ^{13}C-POC values generally increased southward and had a range of -28.7‰ to -20.6‰ (Fig. 3.7d), similar to the results of Canuel (2001) (-27.8‰ to -19.9‰), Sigleo and Macko (2002) (-26.9‰ to -17.5 ‰) and Loh et al. (2006) (-28.0‰ to -21.4‰).

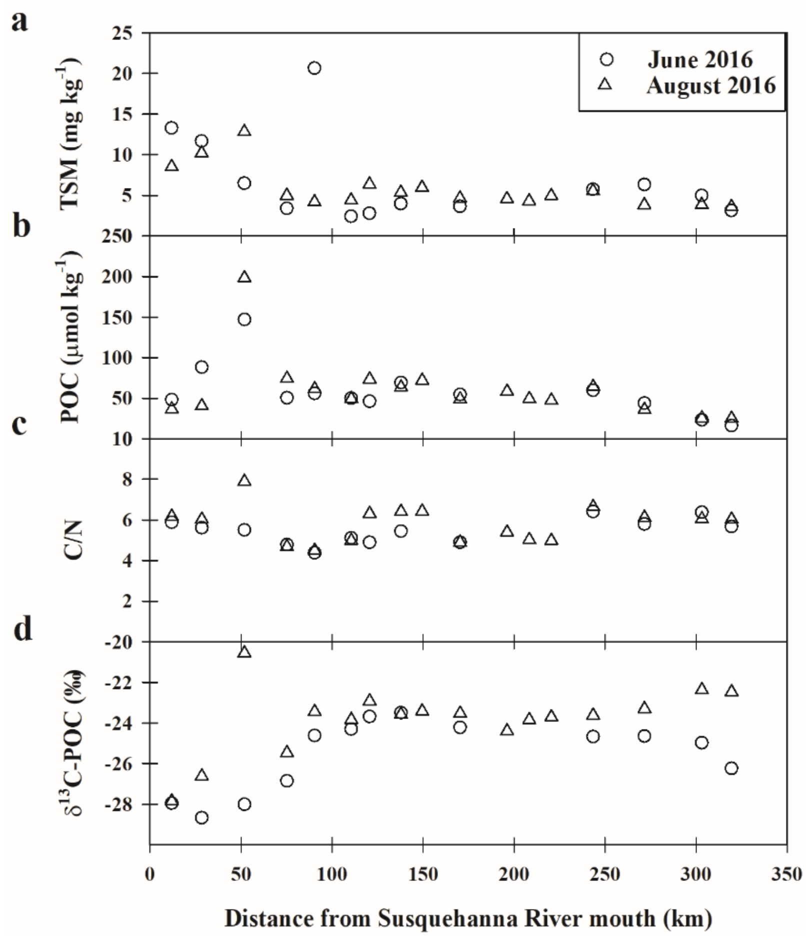

Figure 3.7: Spatial distribution of (a) TSM, (b) POC, (c) molar C/N ratio, and (d) δ^{13}C-POC along the main channel of the Chesapeake Bay in June (circle) and August (triangle), 2016. TSM and POC concentrations are expressed in per kilogram water unit.

In this study, the distributions of C/N and δ^{13}C demonstrate that Autoc-OC (estuarine/marine phytoplankton) constitutes a major portion of POM in the mid- to lower bay. This is supported by our findings of C/N ratios close to 6 and δ^{13}C > -25‰ along the majority of meso- and polyhaline waters where hypoxia exists. Our findings of low Alloc-OC (terrestrial) influence is not surprising given that the winter-spring

(January-May) river flow in 2016 was 20% lower than the long-term average (1967-2017) and freshwater input was at a seasonal minimum during our cruise period (Fig. 3.8b). These low flow conditions likely allowed any imported, terrestrial OM and freshwater phytoplankton to be trapped in the upper-bay turbidity maximum zone (Sanford et al., 2001; Cheng et al., 2013).

When we combined the lowest δ^{13}C-POC values in our study with three previous studies (Canuel, 2001; Sigleo and Macko, 2002; Loh et al., 2006), we derived a δ^{13}C-POC value of -27.9±0.7‰ as the endmember for Alloc-OC (terrestrial) or freshwater algae. Similarly, using the highest δ^{13}C-POC values in these four studies, we derived a δ^{13}C-POC endmember value for Autoc-OC (marine) of -19.9±1.7‰. Therefore, our derived δ^{13}C of oxygen-consuming OM (-19.4±0.3‰) is within the uncertainty of the Autoc-OC isotopic signal. The fact that oxygen-consuming OM signal is the approximate value of marine OM may reflect rapid settling and/or landward intrusion of marine-derived OM from the high salinity regions, consistent with well-known estuarine circulation patterns (Arzayus and Canuel, 2005). Previous studies have demonstrated that the water of the continental shelf, flowing into the bay's mouth, is the largest single source of sediment for the Chesapeake Bay (Meade, 1969; Hobbs III et al., 1992). Moreover, the $\delta^{13}C_{OCx}$ may be influenced by the high organic content (as high as 74% (dry weight) in the marsh sediment) and more ^{13}C-enriched (~-12.5‰) materials eroded from the marshes (Stevenson et al., 1985; Stribling and Cornwell, 1997). Nonetheless, we did not find any POM sample with such a ^{13}C-enriched signal in our cruises (Fig. 3.7d and 3.8a). In addition, the absence of biomarkers associated with terrestrial and marsh sources in summer precludes the possibility that admixture of terrestrial and marsh materials accounts for a major portion of organic matter that consumes oxygen (Canuel, 2001; Loh et al., 2006). However, we cannot exclude the possible contributions of terrestrial and marsh materials to oxygen-consuming organic matter pool in other periods, especially during high-flow seasons (winter and spring) and storm events (Stevenson et al., 1988; Canuel, 2001). Overall, our results demonstrate that eutrophication-stimulated primary production (Autoc-OC) dominated oxygen-consuming OM pool in the hypoxic zone of the Chesapeake Bay in June 2016.

3.4.7 Comparison with hypoxia in the lower reach of the Pearl River Estuary

It is useful to compare our isotopic analysis in the Chesapeake Bay (CB) with similar recent measurements in the Pearl River Estuary (PRE; 21.2°N–23.1°N, 113.0°E–114.5°E), a large subtropical estuarine system in southern China. The PRE also receives large amounts of nutrient and OM loadings (Zhang et al., 1999; Cai et al., 2004; Dai et al., 2006), and suffers from severe eutrophication (Huang et al., 2003). Recent observations suggest that the lower PRE has emerged as a seasonal hypoxic zone (Qian et al., 2018). Unlike the CB, with persistent summer hypoxia occurring at >10 m depth (Hagy et al., 2004), the lower PRE hypoxic zone is highly variable given a short water residence time of only a few days and strong tidal and wind mixing, especially during typhoon events (Su et al., 2017). Despite these differences, oxygen consumption in both systems is dominated by aerobic respiration of Autoc-OC (~100% in the CB vs. ~65% in the PRE), while Alloc-OC is also a significant contributor (~35%) to oxygen consumption in the PRE (Su et al., 2017). The δ^{13}C-POC values were similar in both estuaries near the freshwater zone, but differed in the seawater regions (Fig. 3.8a), likely due to additional tributary OM inputs to the lower CB (Arzayus and Canuel, 2005; Countway et al., 2007). Finally, the $\delta^{13}C$-DIC values measured during summer were generally higher or more positive in the CB than in the PRE (Fig. 3.8a), presumably because variations in carbonate weathering in the watershed and different biogeochemistry within the bay waters, such as $CaCO_3$ dissolution and atmospheric CO_2 invasion. In the mid- CB, there is atmospheric CO_2 uptake because of the strong drawdown of surface pCO_2 driven by photosynthesis and long water residence time. In contrast, within the PRE, supersaturated pCO_2 in the surface water and short water residence time lead to no CO_2 uptake into the water (Guo et al., 2009).

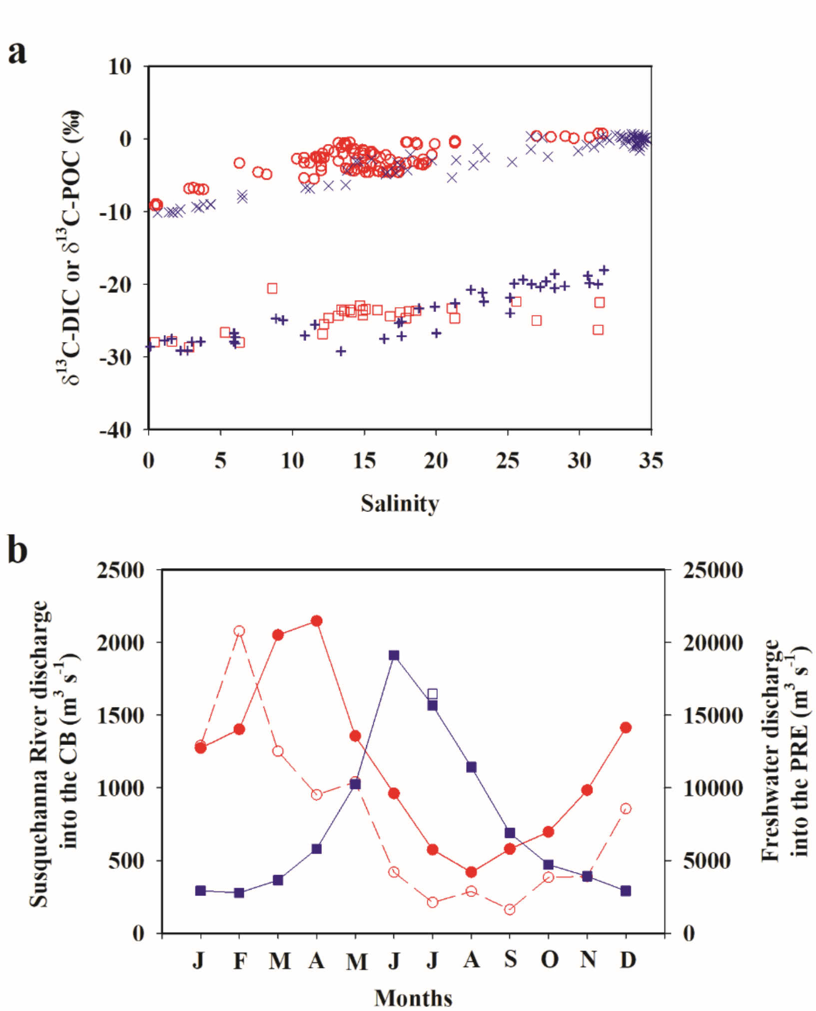

Figure 3.8: Comparisons of δ^{13}C-DIC, δ^{13}C-POC and freshwater discharge between the Chesapeake Bay and the Pearl River Estuary. In panel a, the red open circles and squares represent the δ^{13}C-DIC (June) and δ^{13}C-POC (June + August) from the CB cruises in 2016. For the PRE, the blue crosses are the δ^{13}C-DIC values from July 2014, whereas the blue pluses are the δ^{13}C-POC values from July 2015. The PRE data are from Su et al. (2017). In panel b, the red fill circles indicate the monthly average freshwater discharge rate for the Susquehanna River at Conowingo Dam (USGS site number 01578310) during 1967-2017, while the red open circles refer to 2016. The Susquehanna River supplies 50-60% of mean annual freshwater input to the Chesapeake Bay (Schubel and Pritchard 1986; Testa et al. 2018a). The blue filled and open squares show the monthly average freshwater discharges in the PRE during multiple years (2000-2011) and July 2014, respectively.

To interpret why terrestrial OM contributes significantly to the oxygen consumption in the PRE but not in the CB, we have to consider the differences in terms of hydrology, quantity and quality of both Alloc-OC and Autoc-OC, and the physical setting. As shown in Table 3.3, the CB has a smaller annual freshwater input, about one fifth of that in the PRE, but has an estuarine water volume ~10 times as large as that in the PRE. That leads to a much longer water residence time in the CB. Considering the smaller annual sediment loads in the CB, most of the Alloc-OC likely settles in the upper bay (Biggs, 1970; Boynton and Kemp, 1985; Cheng et al., 2013), except in the high discharge period of March or April (Fig. 3.8b). Thus, in summer, when freshwater discharge is low (Fig. 3.8b), little terrestrial OM reaches the mid- and lower bay, and Autoc-OC composes most of the OM pool in the CB. In contrast, the much larger annual sediment loads and much shorter water residence time in the PRE enables considerable terrestrial OM be transported to the shallow shelf region, where bottom hypoxia develops. This terrestrial OM delivery would be more substantial during the peak freshwater discharge in the PRE in summer when our measurements were made (Fig. 3.8b). There appears to be substantial amounts of bioavailable OM in both systems, but the OM is substantially influenced by Alloc-OC that is exposed to minor degradative loss during the short transport period in the PRE (Strong et al., 2012), while Autoc-OC is far more important in the CB, which is generally more productive (1-9 g C m^{-2} d^{-1}) than the PRE (1-5 g C m^{-2} d^{-1}) (Officer et al., 1984; Rabouille et al., 2008). Finally, the temperature of the hypoxic water in the PRE (23.7-27.6°C) was higher than that in the CB (17.0-18.5°C), which favors higher rates of bacterial growth and OM degradation (Brown et al., 2004), allowing for potentially higher rates of terrestrial OM degradation within the hypoxic zone of the lower PRE.

Clearly, the two large hypoxic zones in these estuarine systems have substantially different physical features and sources of OM input and lability, suggesting that future analyses are required to better understand the varied drivers of hypoxia across coastal systems worldwide.

Table 3.3: Comparison of the Chesapeake Bay and the Pearl River Estuary in terms of hydrology, quantity and quality of organic matter input and physical characteristics.

	Chesapeake Bay	Pearl River Estuary
Annual freshwater discharge ($\times10^9$ m^3 yr^{-1})	73[a]	350[b]
Timing of peak freshwater discharge	March or April	June
Estuarine water volume ($\times10^9$ m^3)	75[c]	8[d]
Water residence time (days)	180[c]	3-5[e]
Annual sediment loads ($\times10^6$ tons yr^{-1})	4.3[f]	85[b]
Primary productivity (g C m^{-2} d^{-1})	1-9[g]	1-5[e]
Bioavailability of Alloc-OC	--[h]	Relatively high[i]
Water temperature in hypoxic zone (°C)	17.0-18.5[j]	23.7-27.6[k]

[a]Kemp et al. 2005; [b]Zhang et al. 1999; [c]Du and Shen 2016; [d]Guan et al. 2009; [e]Rabouille et al. 2008; [f]Langland and Cronin 2003; [g]Officer et al. 1984; [h]This study shows there is little contribution from Alloc-OC to oxygen consumption in the hypoxic zone of the Chesapeake Bay; [i]Strong et al. 2012; [j]This study; [k]Su et al. 2017.

REFERENCES

Alling, V., Porcelli, D., Mörth, C.M., Anderson, L.G., Sanchez-Garcia, L., Gustafsson, Ö., Andersson, P.S. and Humborg, C., 2012. Degradation of terrestrial organic carbon, primary production and out-gassing of CO_2 in the Laptev and East Siberian Seas as inferred from $\delta^{13}C$ values of DIC. Geochim. Cosmochim. Acta 95, 143-159. doi:10.1016/j.gca.2012.07.028

Arzayus, K.M. and Canuel, E.A., 2005. Organic matter degradation in sediments of the York River estuary: Effects of biological vs. physical mixing. Geochim. Cosmochim. Acta 69, 455-464. doi:10.1016/j.gca.2004.06.029

Bauer, J.E., Druffel, E.R.M., Wolgast, D.M. and Griffin, S., 2001. Sources and cycling of dissolved and particulate organic radiocarbon in the Northwest Atlantic Continental Margin. Global Biogeochem. Cycles 15, 615-636. doi:10.1029/2000GB001314

Benson, B.B. and Krause, D., 1984. The concentration and isotopic fractionation of oxygen dissolved in freshwater and seawater in equilibrium with the atmosphere1. Limnol. Oceanogr. 29, 620-632. doi:10.4319/lo.1984.29.3.0620

Bianchi, T.S., 2011. The role of terrestrially derived organic carbon in the coastal ocean: A changing paradigm and the priming effect. Proc. Natl. Acad. Sci. U.S.A. 108, 19473-19481. doi:10.1073/pnas.1017982108

Bianchi, T.S., Wysocki, L.A., Schreiner, K.M., Filley, T.R., Corbett, D.R. and Kolker, A.S., 2011. Sources of terrestrial organic carbon in the Mississippi plume region: evidence for the importance of coastal marsh inputs. Aquat. Geochem. 17, 431-456. doi:10.1007/s10498-010-9110-3

Biggs, R.B., 1970. Sources and distribution of suspended sediment in northern Chesapeake Bay. Mar. Geol. 9, 187-201. doi:10.1016/0025-3227(70)90014-9

Biggs, R.B. and Flemer, D.A., 1972. The flux of particulate carbon in an estuary. Mar. Biol. 12, 11-17. doi:10.1007/bf00347425

Boicourt, W.C., Kuzmić, M. and Hopkins, T.S., 1999. The inland sea: circulation of Chesapeake Bay and the Northern Adriatic. In: Malone, T.C., Malej, A., Harding Jr, L.W., Smodlaka, N. and Turner, R.E. (Eds.), Ecosystems at the land-sea margin: drainage basin to coastal sea. American Geophysical Union, Washington, DC, pp. 81-129.

Boynton, W. and Kemp, W.M., 1985. Nutrient regeneration and oxygen consumption by sediments along an estuarine salinity gradient. Mar. Ecol. Prog. Ser. 23, 45-55. doi:10.3354/meps023045

Brady, D.C., Testa, J.M., Di Toro, D.M., Boynton, W.R. and Kemp, W.M., 2013. Sediment flux modeling: Calibration and application for coastal systems. Estuar. Coast. Shelf Sci. 117, 107-124. doi:10.1016/j.ecss.2012.11.003

Breitburg, D., Levin, L.A., Oschlies, A., Grégoire, M., Chavez, F.P., Conley, D.J., Garçon, V., Gilbert, D., Gutiérrez, D., Isensee, K., Jacinto, G.S., Limburg, K.E., Montes, I., Naqvi, S.W.A., Pitcher, G.C., Rabalais, N.N., Roman, M.R., Rose, K.A., Seibel, B.A., Telszewski, M., Yasuhara, M. and Zhang, J., 2018. Declining oxygen in the global ocean and coastal waters. Science 359. doi:10.1126/science.aam7240

Breteler, W.C.K., Grice, K., Schouten, S., Kloosterhuis, H.T. and Damsté, J.S.S., 2002. Stable carbon isotope fractionation in the marine copepod Temora longicornis: unexpectedly low $\delta^{13}C$ value of faecal pellets. Mar. Ecol. Prog. Ser. 240, 195-204. doi:10.3354/meps240195

Brodeur, J.R., Chen, B., Su, J., Xu, Y.-Y., Hussain, N., Scaboo, K.M., Zhang, Y., Testa, J.M. and Cai, W.-J., 2019. Chesapeake Bay Inorganic Carbon: Spatial Distribution and Seasonal Variability. Front. Mar. Sci. 6. doi:10.3389/fmars.2019.00099

Brown, J.H., Gillooly, J.F., Allen, A.P., Savage, V.M. and West, G.B., 2004. Toward a metabolic theory of ecology. Ecology 85, 1771-1789. doi:10.1890/03-9000

Brush, G.S., 2009. Historical Land Use, Nitrogen, and Coastal Eutrophication: A Paleoecological Perspective. Estuar. Coast. 32, 18-28. doi:10.1007/s12237-008-9106-z

Burdige, D.J., 1993. The biogeochemistry of manganese and iron reduction in marine sediments. Earth-Sci. Rev. 35, 249-284. doi:10.1016/0012-8252(93)90040-E

Burdige, D.J. and Homstead, J., 1994. Fluxes of dissolved organic carbon from Chesapeake Bay sediments. Geochim. Cosmochim. Acta 58, 3407-3424. doi:10.1016/0016-7037(94)90095-7

Burdige, D.J. and Zheng, S., 1998. The biogeochemical cycling of dissolved organic nitrogen in estuarine sediments. Limnol. Oceanogr. 43, 1796-1813. doi:10.4319/lo.1998.43.8.1796

Cai, W.-J., Dai, M., Wang, Y., Zhai, W., Huang, T., Chen, S., Zhang, F., Chen, Z. and Wang, Z., 2004. The biogeochemistry of inorganic carbon and nutrients in the Pearl River estuary and the adjacent Northern South China Sea. Cont. Shelf Res. 24, 1301-1319. doi:10.1016/j.csr.2004.04.005

Cai, W.-J., Hu, X., Huang, W.-J., Jiang, L.-Q., Wang, Y., Peng, T.-H. and Zhang, X., 2010a. Alkalinity distribution in the western North Atlantic Ocean margins. J. Geophys. Res. Ocean 115, C08014. doi:10.1029/2009JC005482

Cai, W.-J., Luther, G.W., Cornwell, J.C. and Giblin, A.E., 2010b. Carbon Cycling and the Coupling Between Proton and Electron Transfer Reactions in Aquatic Sediments in Lake Champlain. Aquat. Geochem. 16, 421-446. doi:10.1007/s10498-010-9097-9

Cai, W.-J., Hu, X., Huang, W.-J., Murrell, M.C., Lehrter, J.C., Lohrenz, S.E., Chou, W.-C., Zhai, W., Hollibaugh, J.T. and Wang, Y., 2011. Acidification of

subsurface coastal waters enhanced by eutrophication. Nat. Geosci. 4, 766-770. doi:10.1038/NGEO1297
Cai, W.-J., Huang, W.-J., Luther, G.W., Pierrot, D., Li, M., Testa, J., Xue, M., Joesoef, A., Mann, R., Brodeur, J., Xu, Y.-Y., Chen, B., Hussain, N., Waldbusser, G.G., Cornwell, J. and Kemp, W.M., 2017. Redox reactions and weak buffering capacity lead to acidification in the Chesapeake Bay. Nat. Commun. 8, 369. doi:10.1038/s41467-017-00417-7
Canuel, E.A. and Zimmerman, A.R., 1999. Composition of particulate organic matter in the southern Chesapeake Bay: sources and reactivity. Estuaries 22, 980-994. doi:10.2307/1353077
Canuel, E.A., 2001. Relations between river flow, primary production and fatty acid composition of particulate organic matter in San Francisco and Chesapeake Bays: a multivariate approach. Org. Geochem. 32, 563-583. doi:10.1016/S0146-6380(00)00195-9
Cerco, C.F. and Noel, M.R., 2016. Impact of Reservoir Sediment Scour on Water Quality in a Downstream Estuary. J. Environ. Qual. 45, 894-905. doi:10.2134/jeq2014.10.0425
Cheng, P., Li, M. and Li, Y., 2013. Generation of an estuarine sediment plume by a tropical storm. J. Geophys. Res. Ocean 118, 856-868. doi:10.1002/jgrc.20070
Cornwell, J.C. and Sampou, P.A., 1995. Environmental Controls on Iron Sulfide Mineral Formation in a Coastal Plain Estuary. In: Vairavamurthy, M.A., Schoonen, M.A.A., Eglinton, T.I., Luther III, G.W. and Manowitz, B. (Eds.), Geochemical Transformations of Sedimentary Sulfur. American Chemical Society, pp. 224-242.
Countway, R.E., Canuel, E.A. and Dickhut, R.M., 2007. Sources of particulate organic matter in surface waters of the York River, VA estuary. Org. Geochem. 38, 365-379. doi:10.1016/j.orggeochem.2006.06.004
Craig, H., 1953. The geochemistry of the stable carbon isotopes. Geochim. Cosmochim. Acta 3, 53-92. doi:10.1016/0016-7037(53)90001-5
Dai, M., Guo, X., Zhai, W., Yuan, L., Wang, B., Wang, L., Cai, P., Tang, T. and Cai, W.-J., 2006. Oxygen depletion in the upper reach of the Pearl River estuary during a winter drought. Mar. Chem. 102, 159-169. doi:10.1016/j.marchem.2005.09.020
Dai, M., Wang, L., Guo, X., Zhai, W., Li, Q., He, B. and Kao, S.-J., 2008. Nitrification and inorganic nitrogen distribution in a large perturbed river/estuarine system: the Pearl River Estuary, China. Biogeosciences 5, 1227-1244. doi:10.5194/bg-5-1227-2008
Diaz, R.J. and Rosenberg, R., 2008. Spreading dead zones and consequences for marine ecosystems. Science 321, 926-929. doi:10.1126/science.1156401
Du, J. and Shen, J., 2016. Water residence time in Chesapeake Bay for 1980–2012. J. Mar. Syst. 164, 101-111. doi:10.1016/j.jmarsys.2016.08.011

Fennel, K. and Testa, J.M., 2018. Biogeochemical Controls on Coastal Hypoxia. Annu. Rev. Mar. Sci. 11, 4.1-4.26. doi:10.1146/annurev-marine-010318-095138

Fernandes, S., Mazumdar, A., Bhattacharya, S., Peketi, A., Mapder, T., Roy, R., Carvalho, M.A., Roy, C., Mahalakshmi, P., Da Silva, R., Rao, P.L.S., Banik, S.K. and Ghosh, W., 2018. Enhanced carbon-sulfur cycling in the sediments of Arabian Sea oxygen minimum zone center. Sci. Rep. 8, 8665. doi:10.1038/s41598-018-27002-2

Goodrich, D.M., Boicourt, W.C., Hamilton, P. and Pritchard, D.W., 1987. Wind-Induced Destratification in Chesapeake Bay. J. Phys. Oceanogr. 17, 2232-2240. doi:10.1175/1520-0485(1987)017<2232:widicb>2.0.co;2

Grimm, B., Spero, H., Harding, J. and Guilderson, T., 2017. Seasonal radiocarbon reservoir ages for the 17th century James River, Virginia estuary. Quaternary Geochronology 41. doi:10.1016/j.quageo.2017.03.002

Guo, X., Dai, M., Zhai, W., Cai, W.-J. and Chen, B., 2009. CO_2 flux and seasonal variability in a large subtropical estuarine system, the Pearl River Estuary, China. J. Geophys. Res. Biogeosci. 114. doi:10.1029/2008JG000905

Hagy, J.D., Boynton, W.R., Keefe, C.W. and Wood, K.V., 2004. Hypoxia in Chesapeake Bay, 1950–2001: Long-term change in relation to nutrient loading and river flow. Estuaries 27, 634-658. doi:10.1007/BF02907650

He, B., Dai, M., Zhai, W., Guo, X. and Wang, L., 2014. Hypoxia in the upper reaches of the Pearl River Estuary and its maintenance mechanisms: A synthesis based on multiple year observations during 2000–2008. Mar. Chem. 167, 13-24. doi:10.1016/j.marchem.2014.07.003

Hill, J.M., Halka, J.P., Conkwright, R., Koczot, K. and Coleman, S., 1992. Distribution and effects of shallow gas on bulk estuarine sediment properties. Cont. Shelf Res. 12, 1219-1229. doi:10.1016/0278-4343(92)90081-T

Hobbs III, C.H., Halka, J.P., Kerhin, R.T. and Carron, M.J., 1992. Chesapeake Bay sediment budget. J. Coast. Res., 292-300

Horrigan, S.G., Montoya, J.P., Nevins, J.L., McCarthy, J.J., Ducklow, H., Goericke, R. and Malone, T., 1990. Nitrogenous nutrient transformations in the spring and fall in the Chesapeake Bay. Estuar. Coast. Shelf Sci. 30, 369-391. doi:10.1016/0272-7714(90)90004-B

Huang, W.J., Wang, Y. and Cai, W.J., 2012. Assessment of sample storage techniques for total alkalinity and dissolved inorganic carbon in seawater. Limnol. Oceanogr. Methods 10, 711-717. doi:10.4319/lom.2012.10.711

Huang, X., Huang, L. and Yue, W., 2003. The characteristics of nutrients and eutrophication in the Pearl River estuary, South China. Mar. Pollut. Bull. 47, 30-36. doi:10.1016/S0025-326X(02)00474-5

Hullar, M., Fry, B., Peterson, B. and Wright, R., 1996. Microbial utilization of estuarine dissolved organic carbon: a stable isotope tracer approach tested by mass balance. Appl. Environ. Microbiol. 62, 2489-2493

Irwin, H., Curtis, C. and Coleman, M., 1977. Isotopic evidence for source of diagenetic carbonates formed during burial of organic-rich sediments. Nature 269, 209. doi:10.1038/269209a0

Joesoef, A., Kirchman, D.L., Sommerfield, C.K. and Cai, W.-J., 2017. Seasonal variability of the inorganic carbon system in a large coastal plain estuary. Biogeosciences 14, 4949-4963. doi:10.5194/bg-14-4949-2017

Kanamori, S. and Ikegami, H., 1980. Computer-processed potentiometric titration for the determination of calcium and magnesium in sea water. J. Oceanogr. Soc. Japan 36, 177-184. doi:10.1007/bf02070330

Kemp, W., Boynton, W., Adolf, J., Boesch, D., Boicourt, W., Brush, G., Cornwell, J., Fisher, T., Glibert, P. and Hagy, J., 2005. Eutrophication of Chesapeake Bay: historical trends and ecological interactions. Mar. Ecol. Prog. Ser. 303, 1-29. doi:10.3354/meps303001

Kemp, W.M., Sampou, P., Caffrey, J., Mayer, M., Henriksen, K. and Boynton, W.R., 1990. Ammonium recycling versus denitrification in Chesapeake Bay sediments. Limnol. Oceanogr. 35, 1545-1563. doi:10.4319/lo.1990.35.7.1545

Kemp, W.M., Sampou, P.A., Garber, J., Tuttle, J. and Boynton, W.R., 1992. Seasonal depletion of oxygen from bottom waters of Chesapeake Bay: roles of benthic and planktonic respiration and physical exchange processes. Mar. Ecol. Prog. Ser. 85, 137-152

Kemp, W.M., Smith, E.M., Marvin-DiPasquale, M. and Boynton, W.R., 1997. Organic carbon balance and net ecosystem metabolism in Chesapeake Bay. Mar. Ecol. Prog. Ser. 150, 229-248. doi:10.3354/meps150229

Komada, T., Burdige, D.J., Li, H.-L., Magen, C., Chanton, J.P. and Cada, A.K., 2016. Organic matter cycling across the sulfate-methane transition zone of the Santa Barbara Basin, California Borderland. Geochim. Cosmochim. Acta 176, 259-278. doi:10.1016/j.gca.2015.12.022

Kroeker, K.J., Kordas, R.L., Crim, R., Hendriks, I.E., Ramajo, L., Singh, G.S., Duarte, C.M. and Gattuso, J.P., 2013. Impacts of ocean acidification on marine organisms: quantifying sensitivities and interaction with warming. Glob. Chang. Biol. 19, 1884-1896. doi:10.1111/gcb.12179

Lee, D.Y., Owens, M.S., Doherty, M., Eggleston, E.M., Hewson, I., Crump, B.C. and Cornwell, J.C., 2015. The Effects of Oxygen Transition on Community Respiration and Potential Chemoautotrophic Production in a Seasonally Stratified Anoxic Estuary. Estuar. Coast. 38, 104-117. doi:10.1007/s12237-014-9803-8

Lefcheck, J.S., Orth, R.J., Dennison, W.C., Wilcox, D.J., Murphy, R.R., Keisman, J., Gurbisz, C., Hannam, M., Landry, J.B., Moore, K.A., Patrick, C.J., Testa, J., Weller, D.E. and Batiuk, R.A., 2018. Long-term nutrient reductions lead to the unprecedented recovery of a temperate coastal region. Proc. Natl. Acad. Sci. U.S.A. 115, 3658-3662. doi:10.1073/pnas.1715798115

Lehmann, M.F., Bernasconi, S.M., Barbieri, A. and McKenzie, J.A., 2002. Preservation of organic matter and alteration of its carbon and nitrogen isotope

composition during simulated and in situ early sedimentary diagenesis. Geochim. Cosmochim. Acta 66, 3573-3584. doi:10.1016/S0016-7037(02)00968-7
Li, M., Lee, Y.J., Testa, J.M., Li, Y., Ni, W., Kemp, W.M. and Di Toro, D.M., 2016. What drives interannual variability of hypoxia in Chesapeake Bay: Climate forcing versus nutrient loading? Geophys. Res. Lett. 43, 2127-2134. doi:10.1002/2015GL067334
Linker, L.C., Batiuk, R.A., Cerco, C.F., Shenk, G.W., Tian, R., Wang, P. and Yactayo, G., 2016. Influence of Reservoir Infill on Coastal Deep Water Hypoxia. J. Environ. Qual. 45, 887-893. doi:10.2134/jeq2014.11.0461
Loh, A.N., Bauer, J.E. and Canuel, E.A., 2006. Dissolved and particulate organic matter source-age characterization in the upper and lower Chesapeake Bay: A combined isotope and biochemical approach. Limnol. Oceanogr. 51, 1421-1431. doi:10.4319/lo.2006.51.3.1421
Lustwerk, R.L. and Burdige, D.J., 1993. Iron and manganese reduction in Chesapeake Bay sediments. Trans. Am. Geophys. Union (EOS) 74, 326
Meade, R.H., 1969. Landward transport of bottom sediments in estuaries of the atlantic coastal plain. J. Sediment. Res. 39, 222-234. doi:10.1306/74d71c1c-2b21-11d7-8648000102c1865d
Millero, F.J., 1991a. The oxidation of H_2S in the Chesapeake Bay. Estuar. Coast. Shelf Sci. 33, 521-527. doi:10.1016/0272-7714(91)90088-S
Millero, F.J., 1991b. The oxidation of H_2S in Black Sea waters. Deep Sea Res. Part A Oceanogr. Res. Pap. 38, S1139-S1150. doi:10.1016/S0198-0149(10)80028-7
Mucci, A., 1983. The solubility of calcite and aragonite in seawater at various salinities, temperatures, and one atmosphere total pressure. Am. J. Sci. 283, 780-799. doi:10.2475/ajs.283.7.780
Murphy, R.R., Kemp, W.M. and Ball, W.P., 2011. Long-Term Trends in Chesapeake Bay Seasonal Hypoxia, Stratification, and Nutrient Loading. Estuar. Coast. 34, 1293-1309. doi:10.1007/s12237-011-9413-7
Najjar, R.G., Pyke, C.R., Adams, M.B., Breitburg, D., Hershner, C., Kemp, M., Howarth, R., Mulholland, M.R., Paolisso, M., Secor, D., Sellner, K., Wardrop, D. and Wood, R., 2010. Potential climate-change impacts on the Chesapeake Bay. Estuar. Coast. Shelf Sci. 86, 1-20. doi:10.1016/j.ecss.2009.09.026
Officer, C.B., 1979. Discussion of the behaviour of nonconservative dissolved constituents in estuaries. Estuar. Coast. Mar. Sci. 9, 91-94. doi:10.1016/0302-3524(79)90009-4
Officer, C.B., Biggs, R.B., Taft, J.L., Cronin, L.E., Tyler, M.A. and Boynton, W.R., 1984. Chesapeake Bay anoxia: origin, development, and significance. Science 223. doi:10.1126/science.223.4631.22
Orr, J.C., Fabry, V.J., Aumont, O., Bopp, L., Doney, S.C., Feely, R.A., Gnanadesikan, A., Gruber, N., Ishida, A., Joos, F., Key, R.M., Lindsay, K., Maier-Reimer, E., Matear, R., Monfray, P., Mouchet, A., Najjar, R.G., Plattner, G.-K., Rodgers, K.B., Sabine, C.L., Sarmiento, J.L., Schlitzer, R., Slater, R.D., Totterdell, I.J.,

Weirig, M.-F., Yamanaka, Y. and Yool, A., 2005. Anthropogenic ocean acidification over the twenty-first century and its impact on calcifying organisms. Nature 437, 681. doi:10.1038/nature04095

Orth, R.J., Dennison, W.C., Lefcheck, J.S., Gurbisz, C., Hannam, M., Keisman, J., Landry, J.B., Moore, K.A., Murphy, R.R. and Patrick, C.J., 2017. Submersed aquatic vegetation in Chesapeake Bay: sentinel species in a changing world. Bioscience 67, 698-712. doi:10.1093/biosci/bix058

Paerl, H.W., 2006. Assessing and managing nutrient-enhanced eutrophication in estuarine and coastal waters: Interactive effects of human and climatic perturbations. Ecol. Eng. 26, 40-54. doi:10.1016/j.ecoleng.2005.09.006

Pai, S.C., Gong, G.C. and Liu, K.K., 1993. Determination of dissolved oxygen in seawater by direct spectrophotometry of total iodine. Mar. Chem. 41, 343-351. doi:10.1016/0304-4203(93)90266

Pilson, M.E., 2012. An Introduction to the Chemistry of the Sea. Cambridge university press, New York.

Presley, B.J. and Kaplan, I.R., 1968. Changes in dissolved sulfate, calcium and carbonate from interstitial water of near-shore sediments. Geochim. Cosmochim. Acta 32, 1037-1048. doi:10.1016/0016-7037(68)90106-3

Qian, W., Gan, J., Liu, J., He, B., Lu, Z., Guo, X., Wang, D., Guo, L., Huang, T. and Dai, M., 2018. Current status of emerging hypoxia in a eutrophic estuary: The lower reach of the Pearl River Estuary, China. Estuar. Coast. Shelf Sci. 205, 58-67. doi:10.1016/j.ecss.2018.03.004

Quay, P., Sonnerup, R., Stutsman, J., Maurer, J., Körtzinger, A., Padin, X.A. and Robinson, C., 2007. Anthropogenic CO_2 accumulation rates in the North Atlantic Ocean from changes in the $^{13}C/^{12}C$ of dissolved inorganic carbon. Global Biogeochem. Cycles 21. doi:10.1029/2006GB002761

Rabalais, N., Cai, W.-J., Carstensen, J., Conley, D., Fry, B., Hu, X., Quiñones-Rivera, Z., Rosenberg, R., Slomp, C., Turner, E., Voss, M., Wissel, B. and Zhang, J., 2014. Eutrophication-Driven Deoxygenation in the Coastal Ocean. Oceanography 27, 172-183. doi:10.5670/oceanog.2014.21

Rabalais, N.N., Díaz, R.J., Levin, L.A., Turner, R.E., Gilbert, D. and Zhang, J., 2010. Dynamics and distribution of natural and human-caused hypoxia. Biogeosciences 7, 585-619. doi:10.5194/bg-7-585-2010

Rabouille, C., Conley, D.J., Dai, M.H., Cai, W.J., Chen, C.T.A., Lansard, B., Green, R., Yin, K., Harrison, P.J., Dagg, M. and McKee, B., 2008. Comparison of hypoxia among four river-dominated ocean margins: The Changjiang (Yangtze), Mississippi, Pearl, and Rhône rivers. Cont. Shelf Res. 28, 1527-1537. doi:10.1016/j.csr.2008.01.020

Rassmann, J., Eitel, E.M., Cathalot, C., Brandily, C., Lansard, B., Taillefert, M. and Rabouille, C., 2019. Benthic alkalinity and DIC fluxes in the Rhône River prodelta generated by decoupled aerobic and anaerobic processes. Biogeosciences Discuss. 2019, 1-50. doi:10.5194/bg-2019-32

Redfield, A.C., 1934. On the proportions of organic derivatives in sea water and their relation to the composition of plankton. In: Daniel, R.J. (Editor), James Johnstone Memorial Volume. Liverpool University Press, pp. 176-192.

Roden, E.E. and Tuttle, J.H., 1992. Sulfide release from estuarine sediments underlying anoxic bottom water. Limnol. Oceanogr. 37, 725-738. doi:10.4319/lo.1992.37.4.0725

Roden, E.E. and Tuttle, J.H., 1993. Inorganic sulfur cycling in mid and lower Chesapeake Bay sediments. Mar. Ecol. Prog. Ser. 93, 101-118. doi:10.3354/meps093101

Roden, E.E., Tuttle, J.H., Boynton, W.R. and Kemp, W.M., 1995. Carbon cycling in mesohaline Chesapeake Bay sediments 1: POC deposition rates and mineralization pathways. J. Mar. Res. 53, 779-819. doi:10.1357/0022240953213025

Samanta, S., Dalai, T.K., Pattanaik, J.K., Rai, S.K. and Mazumdar, A., 2015. Dissolved inorganic carbon (DIC) and its $\delta^{13}C$ in the Ganga (Hooghly) River estuary, India: Evidence of DIC generation via organic carbon degradation and carbonate dissolution. Geochim. Cosmochim. Acta 165, 226-248. doi:10.1016/j.gca.2015.05.040

Sampou, P. and Oviatt, C.A., 1991. Seasonal patterns of sedimentary carbon and anaerobic respiration along a simulated eutrophication gradient. Mar. Ecol. Prog. Ser. 72, 271-282. doi:10.3354/meps072271

Sanford, L.P., Suttles, S.E. and Halka, J.P., 2001. Reconsidering the physics of the Chesapeake Bay estuarine turbidity maximum. Estuaries 24, 655-669. doi:10.2307/1352874

Shen, C., Testa, J.M., Li, M., Cai, W.-J., Waldbusser, G.G., Ni, W., Kemp, W.M., Cornwell, J., Chen, B., Brodeur, J. and Su, J., 2019a. Controls on Carbonate System Dynamics in a Coastal Plain Estuary: A Modeling Study. J. Geophys. Res. Biogeosci. 124, 61-78. doi:10.1029/2018jg004802

Shen, C., Testa, J.M., Ni, W., Cai, W.-J., Li, M. and Kemp, W.M., 2019b. Ecosystem Metabolism and Carbon Balance in Chesapeake Bay: A 30-Year Analysis Using a Coupled Hydrodynamic-Biogeochemical Model. J. Geophys. Res. Ocean 124, 6141-6153. doi:10.1029/2019jc015296

Shultz, D.J. and Calder, J.A., 1976. Organic carbon $^{13}C/^{12}C$ variations in estuarine sediments. Geochim. Cosmochim. Acta 40, 381-385. doi:10.1016/0016-7037(76)90002-8

Sigleo, A.C. and Macko, S.A., 2002. Carbon and Nitrogen Isotopes in Suspended Particles and Colloids, Chesapeake and San Francisco Estuaries, U.S.A. Estuar. Coast. Shelf Sci. 54, 701-711. doi:10.1006/ecss.2001.0853

Smith, E.M. and Kemp, W.M., 1995. Seasonal and regional variations in plankton community production and respiration for Chesapeake Bay. Mar. Ecol. Prog. Ser. 116, 217-231

Stevenson, J.C., Kearney, M.S. and Pendleton, E.C., 1985. Sedimentation and erosion in a Chesapeake Bay brackish marsh system. Mar. Geol. 67, 213-235. doi:10.1016/0025-3227(85)90093-3

Stevenson, J.C., Ward, L.G. and Kearney, M.S., 1988. Sediment transport and trapping in marsh systems: Implications of tidal flux studies. Mar. Geol. 80, 37-59. doi:10.1016/0025-3227(88)90071-0

Stribling, J.M. and Cornwell, J.C., 1997. Identification of important primary producers in a Chesapeake Bay tidal creek system using stable isotopes of carbon and sulfur. Estuaries 20, 77-85. doi:10.2307/1352721

Strong, D.J., Flecker, R., Valdes, P.J., Wilkinson, I.P., Rees, J.G., Zong, Y.Q., Lloyd, J.M., Garrett, E. and Pancost, R.D., 2012. Organic matter distribution in the modern sediments of the Pearl River Estuary. Org. Geochem. 49, 68-82. doi:10.1016/j.orggeochem.2012.04.011

Su, J., Dai, M., He, B., Wang, L., Gan, J., Guo, X., Zhao, H. and Yu, F., 2017. Tracing the origin of the oxygen-consuming organic matter in the hypoxic zone in a large eutrophic estuary: the lower reach of the Pearl River Estuary, China. Biogeosciences 14, 4085-4099. doi:10.5194/bg-14-4085-2017

Su, J., Cai, W.-J., Hussain, N., Brodeur, J., Chen, B. and Huang, K., 2019. Simultaneous determination of dissolved inorganic carbon (DIC) concentration and stable isotope (δ^{13}C-DIC) by Cavity Ring-Down Spectroscopy: Application to study carbonate dynamics in the Chesapeake Bay. Mar. Chem., 103689. doi:10.1016/j.marchem.2019.103689

Swarzenski, P., Campbell, P., Osterman, L. and Poore, R., 2008. A 1000-year sediment record of recurring hypoxia off the Mississippi River: The potential role of terrestrially-derived organic matter inputs. Mar. Chem. 109, 130-142. doi:10.1016/j.marchem.2008.01.003

Testa, J.M., Brady, D.C., Di Toro, D.M., Boynton, W.R., Cornwell, J.C. and Kemp, W.M., 2013. Sediment flux modeling: Simulating nitrogen, phosphorus, and silica cycles. Estuar. Coast. Shelf Sci. 131, 245-263. doi:10.1016/j.ecss.2013.06.014

Testa, J.M. and Kemp, W.M., 2014. Spatial and Temporal Patterns of Winter–Spring Oxygen Depletion in Chesapeake Bay Bottom Water. Estuar. Coast. 37, 1432-1448. doi:10.1007/s12237-014-9775-8

Testa, J.M., Murphy, R.R., Brady, D.C. and Kemp, W.M., 2018. Nutrient- and Climate-Induced Shifts in the Phenology of Linked Biogeochemical Cycles in a Temperate Estuary. Front. Mar. Sci. 5, 114. doi:10.3389/fmars.2018.00114

Thornton, S.F. and McManus, J., 1994. Application of Organic Carbon and Nitrogen Stable Isotope and C/N Ratios as Source Indicators of Organic Matter Provenance in Estuarine Systems: Evidence from the Tay Estuary, Scotland. Estuar. Coast. Shelf Sci. 38, 219-233. doi:10.1006/ecss.1994.1015

Turner, R.E. and Rabalais, N.N., 1994. Coastal eutrophication near the Mississippi river delta. Nature 368, 619-621. doi:10.1038/368619a0

Wang, H., Dai, M., Liu, J., Kao, S.-J., Zhang, C., Cai, W.-J., Wang, G., Qian, W., Zhao, M. and Sun, Z., 2016. Eutrophication-Driven Hypoxia in the East China Sea off the Changjiang Estuary. Environ. Sci. Technol. 50, 2255-2263. doi:10.1021/acs.est.5b06211

Wang, H., Hu, X., Rabalais, N.N. and Brandes, J., 2018. Drivers of Oxygen Consumption in the Northern Gulf of Mexico Hypoxic Waters—A Stable Carbon Isotope Perspective. Geophys. Res. Lett. 45, 10,528-10,538. doi:10.1029/2018GL078571

Wolf-Gladrow, D.A., Zeebe, R.E., Klaas, C., Körtzinger, A. and Dickson, A.G., 2007. Total alkalinity: The explicit conservative expression and its application to biogeochemical processes. Mar. Chem. 106, 287-300. doi:10.1016/j.marchem.2007.01.006

Wu, R.S., 2002. Hypoxia: from molecular responses to ecosystem responses. Mar. Pollut. Bull. 45, 35-45. doi:10.1016/S0025-326X(02)00061-9

Xu, Y.-Y., Cai, W.-J., Gao, Y., Wanninkhof, R., Salisbury, J., Chen, B., Reimer, J.J., Gonski, S. and Hussain, N., 2017a. Short-term variability of aragonite saturation state in the central Mid-Atlantic Bight. J. Geophys. Res. Ocean, n/a-n/a. doi:10.1002/2017JC012901

Xu, Y.-Y., Pierrot, D. and Cai, W.-J., 2017b. Ocean carbonate system computation for anoxic waters using an updated CO2SYS program. Mar. Chem. doi:10.1016/j.marchem.2017.07.002

Yu, F., Zong, Y., Lloyd, J.M., Huang, G., Leng, M.J., Kendrick, C., Lamb, A.L. and Yim, W.W.-S., 2010. Bulk organic $\delta^{13}C$ and C/N as indicators for sediment sources in the Pearl River delta and estuary, southern China. Estuar. Coast. Shelf Sci. 87, 618-630. doi:10.1016/j.ecss.2010.02.018

Zhang, J., Yu, Z.G., Wang, J.T., Ren, J.L., Chen, H.T., Xiong, H., Dong, L.X. and Xu, W.Y., 1999. The Subtropical Zhujiang (Pearl River) Estuary: Nutrient, Trace Species and Their Relationship to Photosynthesis. Estuar. Coast. Shelf Sci. 49, 385-400. doi:10.1006/ecss.1999.0500

Zhao, H.-D., Kao, S.-J., Zhai, W.-D., Zang, K.-P., Zheng, N., Xu, X.-M., Huo, C. and Wang, J.-Y., 2017. Effects of stratification, organic matter remineralization and bathymetry on summertime oxygen distribution in the Bohai Sea, China. Cont. Shelf Res. 134, 15-25. doi:10.1016/j.csr.2016.12.004

Chapter 4

A BAY-WIDE SELF-REGULATED PH BUFFER MECHANISM IN RESPONSE TO EUTROPHICATION AND ACIDIFICATION IN CHESAPEAKE BAY[3]

4.1 Abstract

Additions of CO_2 and acid from the atmosphere, biological respiration, and oxidation of reduced chemical species have led to enhanced acidification in estuarine and coastal waters. However, less is known about how eutrophic and seasonally hypoxic and anoxic water bodies resist coastal acidification. Using calcium and carbonate chemistry data, geochemical model analysis, and mineralogical analysis, we reveal a bay-wide self-regulated pH buffer mechanism via spatially-decoupled $CaCO_3$ formation and dissolution to resist coastal eutrophication and acidification in the Chesapeake Bay. In summer, strong photosynthesis of submerged aquatic vegetation (SAV) in the uppermost bay and alongshore shallow areas assimilates considerable nutrients, and generates extremely high pH and $CaCO_3$ saturation state conditions, which facilitate abiotic and biotic $CaCO_3$ formation. These $CaCO_3$ solids are subsequently transported into the downstream corrosive subsurface waters, and dissolve to buffer pH decreases caused by aerobic respiration and anthropogenic CO_2,

---

[3] Chapter 4 is based on a manuscript in preparation by Jianzhong Su, Wei-Jun Cai, Jean Brodeur, Baoshan Chen, Najid Hussain, Yichen Yao, Chaoying Ni, Jeremy Testa, Ming Li, Xiaohui Xie, Wenfei Ni, K. Michael Scaboo, Yuanyuan Xu, Jeffrey Cornwell, Cassie Gurbisz, Michael S. Owens, George G. Waldbusser, Minhan Dai, W. Michael Kemp

thus providing relatively stable pH conditions. This SAV-driven pH buffer mechanism will be strengthened with future nutrient load reductions and SAV recovery. Our study suggests that coastal ecosystems can further promote their own recovery in complex, sometimes unpredictable ways as humans reduce anthropogenic stressors by policy management.

4.2 Introduction

Since the industrial revolution, the global ocean has absorbed approximately 30% of the anthropogenic carbon dioxide (CO_2) emissions from the atmosphere, lowering average surface water pH by 0.1 unit and aragonite saturation state (Ω_{arag}) by 0.5 unit. This process, known as ocean acidification (Gattuso et al., 2015; Feely et al., 2017), is harmful to some marine organisms and ecosystems (Orr et al., 2005; Fabry et al., 2008; Kroeker et al., 2013). In coastal waters, acidification is enhanced by eutrophication and the subsequent hypoxia/anoxia via the accumulation of CO_2 and acid below the pycnocline (Cai et al., 2011; Sunda and Cai, 2012; Wallace et al., 2014; Hagens et al., 2015). Carbonate dissolution can increase the total alkalinity (TA) of water, and is proposed as a buffer to neutralize anthropogenic CO_2 uptake (Andersson et al., 2005; Macreadie et al., 2017). Recent studies have demonstrated that $CaCO_3$ dissolution can offset a significant proportion of the metabolic CO_2, and increase survivorship of juvenile bivalves, thus providing a substantial negative feedback to coastal acidification (Green et al., 2009; Cai et al., 2017).

However, very few studies have linked $CaCO_3$ dissolution to the timing and location of its formation in coastal waters(Abril et al., 2003; Waldbusser et al., 2013), as a corollary to the ocean's carbonate counter pump (Abril et al., 2003; Waldbusser et al., 2013). These dynamic links are essential to understand given their capacity to mediate aquatic pH and atmospheric CO_2 concentrations (Ware et al., 1992; Cai et al., 2017). In coastal waters, $CaCO_3$ can be formed via abiotic precipitation or biotic production, which are usually associated with coral reefs, calcareous algae (Borowitzka and Larkum, 1987), molluscs (Chauvaud et al., 2003), bacteria (Lesley A. Warren, 2001), fish (Perry et al., 2011) and aquatic plants (Borowitzka, 1984). Recently, seagrass meadows have been shown to be major sites for $CaCO_3$ accumulation and storage in high salinity waters in equatorial and subtropical regions (Mazarrasa et al., 2015). In addition to the seagrass-calcifying algae, infauna and epibiont community, the seagrass *Thalassia testudinum* itself can accumulate needle-like aragonite crystals within its cell walls and externally on the blade surface through biologically induced precipitation (Enríquez and Schubert, 2014). High pH and carbonate saturation conditions will also favour biogenic shell formation. As pH is generally very high and pCO_2 is very low in these systems seasonally during daytime hours, the CO_2 released as a by-product of $CaCO_3$ precipitation should be utilized by aquatic plant biomass production and not released to the atmosphere. Once the $CaCO_3$ crystals escape out of the seagrass beds (Koch, 1999; Corlett and Jones, 2007), they can be transported to carbonate-undersaturated areas where they can dissolve, increase alkalinity, reduce the concentration of H^+, and increase carbonate saturation state.

Anthropogenic perturbations have altered the distribution, abundance and diversity of submerged aquatic vegetation (SAV) on the shoals of the Chesapeake Bay and its tributaries (Orth and Moore, 1983; Orth and Moore, 1984; Moore et al., 2000; Orth et al., 2010), including a bay-wide decline of SAV began in the 1960s, accelerated in the early 1970s, and continued through 1980. Restoring these once-abundant SAV beds has been a primary goal of efforts to reduce loads of nutrients and sediments to the estuary (Orth et al., 2002; Lefcheck et al., 2018). Lefcheck et al. (2018) demonstrated that bay-wide water column nitrogen concentrations have declined by 23%, coinciding with a 316% increase in SAV cover during 1984 to 2015. Note that nutrient loads are still sufficiently high that surface water phytoplankton bloom and subsequent subsurface water hypoxia remain a serious issue along the main channel. Although SAV populations remain well-below restoration targets in some meso- and polyhaline regions, there have been widespread resurgences throughout the tidal fresh and oligohaline portions of the mainstem Bay and its tributaries over the last decade (Orth et al., 2010). One of the largest recovered SAV beds lies in the Susquehanna Flats, which is a broad, tidal freshwater region located near the mouth of the Susquehanna River at the head of the bay. The SAV in the flats was sparse through much of the 1980s and 1990s and then recovered rapidly in size and density between 2000 and 2006, and remained persistently large and dense after 2007 (Gurbisz and Kemp, 2014).

To understand how a large estuary responds to the dual-stresses of eutrophication and acidification, we examined the spatial and temporal distribution of carbonate chemistry and derived the patterns of $CaCO_3$ formation and dissolution in the Chesapeake Bay in August 2016, at a time of peak hypoxia and anoxia and SAV biomass. Supplementary cruises were conducted in the Susquehanna Flats to collect solid samples of surface sediments and SAV leaves for mineralogical identification and to verify TA removal inside the flats. The Chesapeake Bay is an ideal system to examine these $CaCO_3$ dynamics because it suffers from hypoxia/anoxia-enhanced acidification and associated bottom-water $CaCO_3$ dissolution (Kemp et al., 2005; Murphy et al., 2011; Waldbusser et al., 2011a; Waldbusser et al., 2011b; Cai et al., 2017), but also supports a productive shellfish industry (Schulte, 2017) and a diverse assemblage of SAV (Lefcheck et al., 2018).

4.3 Results and Discussion

4.3.1 $CaCO_3$ formation in the upper Chesapeake Bay

In summer, strong gradients of salinity and temperature contributed to the formation of vertical stratification, facilitating the occurrence of hypoxia and anoxia below the pycnocline in the mid bay (Fig. 4.1a and b). The distribution of calcium ion (Ca^{2+}), dissolved inorganic carbon (DIC), and TA generally resembled the pattern of salinity, i.e., increasing seaward and from surface to the bottom, but also showed clear signatures of non-conservative removal or enrichment (Fig. 4.1d, e and f). In particular, DIC and TA in the upper bay were distinctly lower than that of the Susquehanna River. The pH and Ω_{arag} were low in the upper bay, and gradually increased seaward below the pycnocline whereas those in surface waters greatly increased seaward (Fig. 4.1g and h). The partial pressure of CO_2 (pCO_2) was high in the upper bay and in subsurface waters in hypoxic and anoxic zones (Fig. 4.1g).

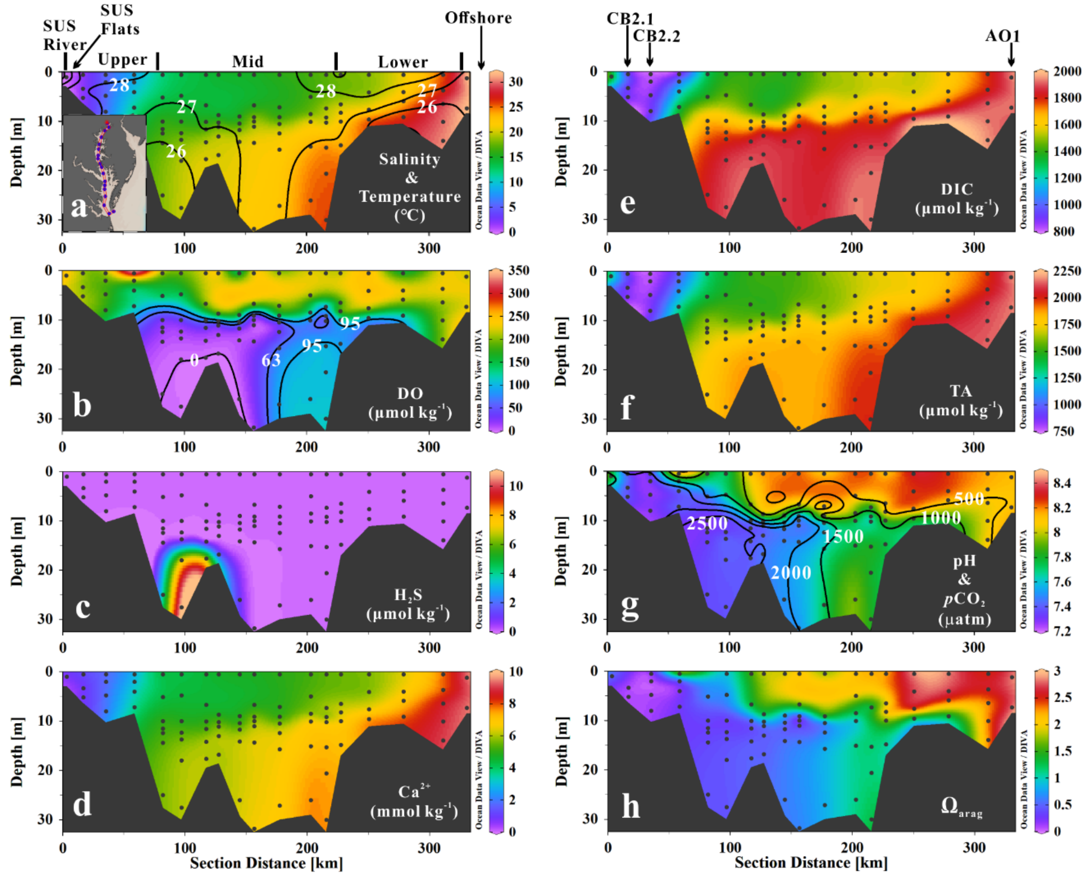

Figure 4.1: Profiles of water properties in August 2016 from Chesapeake Bay. a-h, salinity and contours of temperature (a), DO and contours for anoxia (0 μmol kg^{-1}) and hypoxia (63 μmol kg^{-1}) (Rabalais et al., 2010) (b), H_2S (c), Ca^{2+} (d), DIC (e), TA (f), pH and contours for pCO_2 (g) and Ω_{arag} (h) along the main channel. As in the previous studies (Kemp et al., 2005), the main stem was separated into three regions, i.e. upper bay (39.0-39.5°N), mid bay (37.9-39.0°N) and lower bay (37.0-37.9°N). The inserted map shows the geological location of this section. The origin of section distance starts from Susquehanna River mouth. Susquehanna (SUS) Flats locates near the river mouth at the head of Chesapeake Bay. Offshore stations were not included in the section profiles, because they locate much more offshore in the Mid-Atlantic Bight.

Using a two endmember mixing scheme between Susquehanna River water (SUS) and offshore seawater (Fig. 4.2a and b), we found a large drawdown of Ca^{2+}

and TA in the upper bay (Fig. 4.2c). The removals of Ca^{2+} and TA reached peak values of 393 and 698 μmol kg^{-1} at salinity<5 respectively, then decreased to be 53 and 28 μmol kg^{-1} at high salinity 31.7. Since the signals of removal or addition are cumulative along the salinity gradient in an estuary (Officer, 1980), we surmise that Ca^{2+} was first scavenged near the freshwater area. As we lacked samples inside the SAV beds in the freshwater region in the August 2016 cruise nor during the sensor deployment period, additional samples were collected within the Susquehanna Flats in early September, 2018. The maximum removals of Ca^{2+} and TA within this SAV bed relative to the river mouth reached up to 285 and 450 μmol kg^{-1} (Fig. 4.7d), which are close to the lower end of calculated Ca^{2+} and TA removals at Station CB2.1 (318 and 388 μmol kg^{-1}) during August 2016. Note that for $CaCO_3$ precipitation, the known stoichiometry ratio of DIC and TA changes should be 1:2. The nearly 1:1 ratio downstream of the flats at stations CB2.1 and CB2.2 however reflects contributions from other processes (Fig. 4.2c). Details on the evolution of Ca^{2+}, TA and DIC at sites CB2.1 and CB2.2 are illustrated in the Methods section and Fig. 4.9. As salinity increased (salinity>5) in the mid to lower bay, the local Ca^{2+} addition began to exceed Ca^{2+} removal, which gradually compensated the removal signal to a large extent.

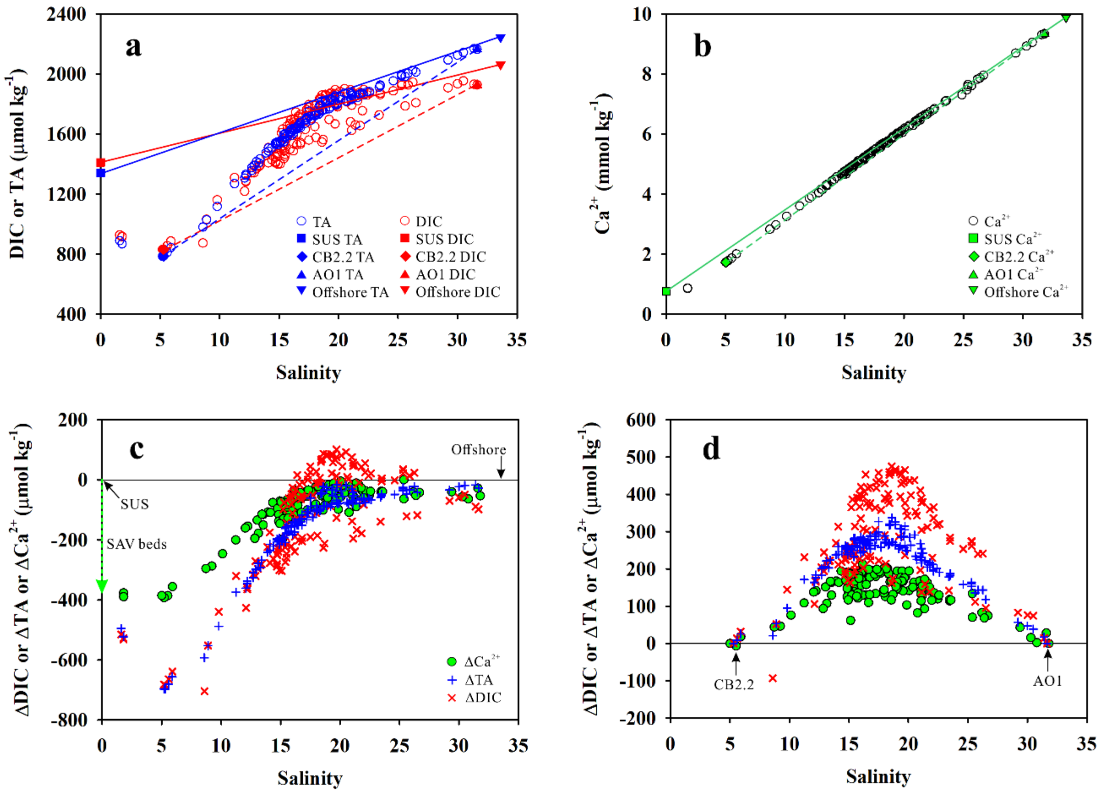

Figure 4.2: Total alkalinity, dissolved inorganic carbon and calcium ion against salinity, and their deviations relative to different conservative mixing lines. In (a) and (b), the open symbols show the cruise data, while the filled symbols represent the different endmember values. By using the mixing line (solid) between Susquehanna River water and offshore seawater, we discussed on the $CaCO_3$ formation and related biogeochemical dynamics on a bay-wide scale. The deviation values are presented in (c). Note that there is a zero reference line and the endmembers are marked by arrows. We also adopted another mixing line (dash) to focus on $CaCO_3$ dissolution and related biogeochemical variations in the region between stations CB2.2 and AO1. The alterations are shown in (d).

We postulate that the large Ca^{2+} and TA removal near the freshwater zone is attributed to $CaCO_3$ formation within the Susquehanna Flats SAV bed. Three additional lines of evidence support this postulation. First, continuous monitoring sensor data showed very high dissolved oxygen saturation (DO%) and pH inside the SAV beds during summer and fall seasons in 2016 (Fig. 4.3a), indicating that strong photosynthesis of SAV has significantly altered the carbonate chemistry in the surrounding water. For instance, in August 2016, the monthly average DO% and pH were 124±24% and 9.7±0.2 with the highest values exceeding 179% for DO% and 10.1 for pH. The water column aragonite saturation state calculated from TA and DIC was highly supersaturated (Ω_{arag}=14.3) inside the SAV beds in September 2018. Previous studies had demonstrated that photosynthesis could enhance biogenic calcification, because of the shift in the carbonate system by CO_2 removal and pH increase (Borowitzka and Larkum, 1987; Beer and Larkum, 2001; Semesi et al., 2009). Furthermore, the diffusive boundary layer immediately adjacent to the leaves within the beds could probably generate microzones with much higher pH and Ω_{arag}, where photosynthesis-induced $CaCO_3$ precipitation may quickly occur (Koch, 1994).

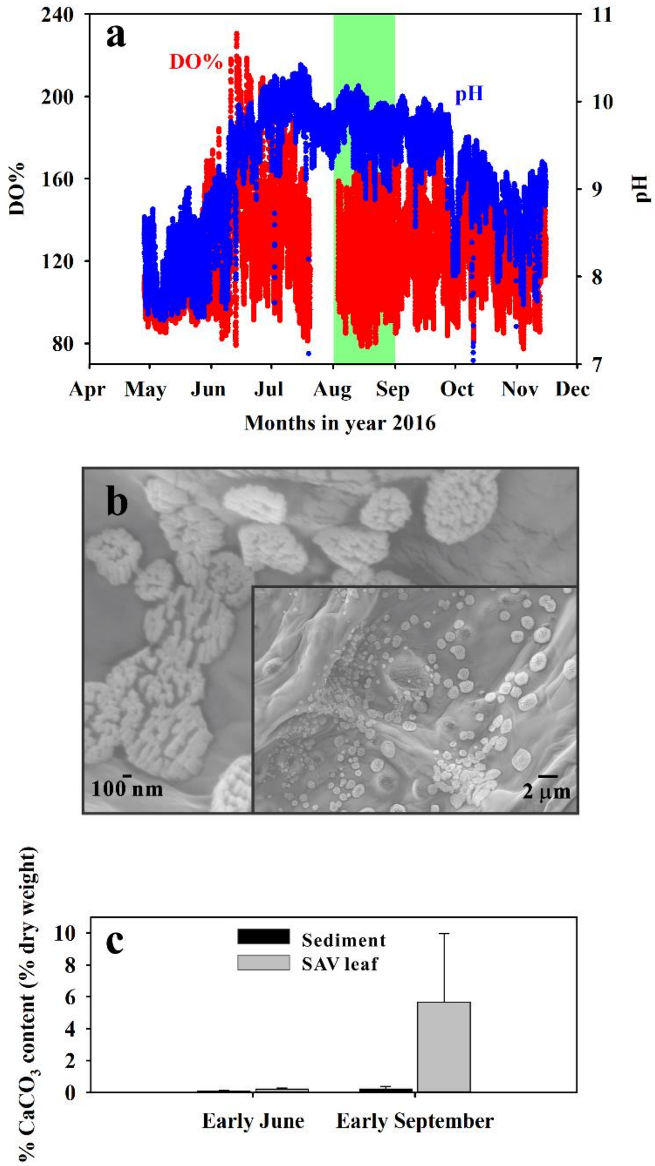

Figure 4.3: Related water chemistry and $CaCO_3$ precipitation within the SAV beds in the Susquehanna Flats. In panel (a), time-series sensor data of dissolved oxygen saturation and pH dataset extended from April to November 2016, and the green zone indicates data in August, 2016. Panel (b) shows the SEM images of $CaCO_3$ solids precipitated on the leaf surface of Vallisneria americana collected in early September, 2018. Note that the inserted panel has a larger scale of 2 μm. (c) Mean ± SD (n=3-11) of the percentage of $CaCO_3$ content (% dry weight) for surface sediments and leaves of SAV collected in early June and early September, 2018.

Second, SEM images illustrated $CaCO_3$ precipitation with varying size and morphology on the leaf surface of *Vallisneria americana* (Fig. 4.3b), which is a dominant species in the SAV beds (Gurbisz and Kemp, 2014). Most individual $CaCO_3$ solids were in the order of several hundred nanometers, but $CaCO_3$ solids could grow to several micrometers long or even larger by aggregating with other materials, such as fine-grained minerals, organic mucus and diatom fragments (Fig. 4.8). The atomic composition of the rice-like $CaCO_3$ aggregates (41.6% O; 38.1% Ca; 12.5% C) is very close to that of pure $CaCO_3$ crystals (48% O; 40% Ca; 12% C).

Third, the average percentage of $CaCO_3$ content in the SAV leaf samples (5.66 $\pm$4.31%) was 25 times more than that in the surface sediment samples (0.22$\pm$0.16%) in the late summer. Since the epiphyte shells were visually removed during pre-treatments of solid samples, the measured $CaCO_3$% is minimum and represents the SAV-driven $CaCO_3$ formation excluding the shell calcification within the SAV beds. Small shells however could usually be found in the leaf and sediment samples. For example, the live clams collected in a recent cruise during August 2019 had a mean length of 1.38$\pm$0.08 cm and a mean density of 338$\pm$61 count per m^2 in the flats (C. Gurbisz, unpublished). Thus, we conclude that the photosynthesis-induced high pH and Ω_{arag} environments could promote $CaCO_3$ precipitation and biogenic calcification within the SAV beds, leading to large decrease of Ca^{2+} and TA in the tidal freshwater flats.

4.3.2 $CaCO_3$ dissolution in the mid to lower bay

In August 2016, the subsurface waters of the mid bay were characterized with low/no oxygen, low pH and Ω_{arag}, and high pCO_2 (Fig. 4.1b, g and h). We adopted another mixing scheme between stations CB2.2 (around salinity 5 in the upper bay) and AO1 (bay mouth) (Fig. 4.2a and b) to better quantify the amount of $CaCO_3$ dissolution in mid and lower bay (Fig. 4.2d). Aerobic respiration and carbonate dissolution dominated the DIC addition in the subsurface water, accounting for 72-81% (Fig. 4.10). From the mid bay to lower bay, the intensity of all biogeochemical processes decreased. As aerobic respiration declined faster than other processes across this gradient, its percentage contribution to non-conservative DIC decreased from 33% to 14%, while the contributions of $CaCO_3$ dissolution and other processes increased from 47% and 19% to 58% and 28%, respectively. As the only process producing TA, $CaCO_3$ dissolution did significantly increase the acid buffering capacity of subsurface water. Sulfate reduction in the water column was only moderate in the summer of 2016 (Fig. 4.10), reflected by a lower concentration of H_2S (Fig. 4.1c) than that measured in previous cruises (Cai et al., 2017).

To quantify the contribution of each biogeochemical process to pH changes in subsurface waters of the mid bay, we subtracted the amount of DIC and TA altered by each process from the measured values to calculate a new pH. Then, we defined the difference between the pH calculated from measured DIC, TA and the new pH to be ΔpH contributed by this process. The ΔpH derived from $CaCO_3$ dissolution (0.607 ± 0.145) can nearly offset the portion altered by aerobic respiration (-0.565 ± 0.239), while other processes lower pH by -0.434 ± 0.158 unit relative to the conservative mixing (Fig. 4.4). If there is no $CaCO_3$ dissolution in the subsurface water of the mid bay, the pH would decrease by up to ~0.6 unit more, which is significantly larger than the pH drawdown (~0.1 unit) expected from fossil-CO_2 induced ocean acidification. Such a strong buffer effect may closely relate to the long water residence time of ~180 days (Du and Shen, 2016) and strong water stratification during summer in the

Chesapeake Bay, which prevent the rapid vertical or horizontal dilution of the TA and buffering capacity produced from $CaCO_3$ dissolution (Andersson et al., 2005).

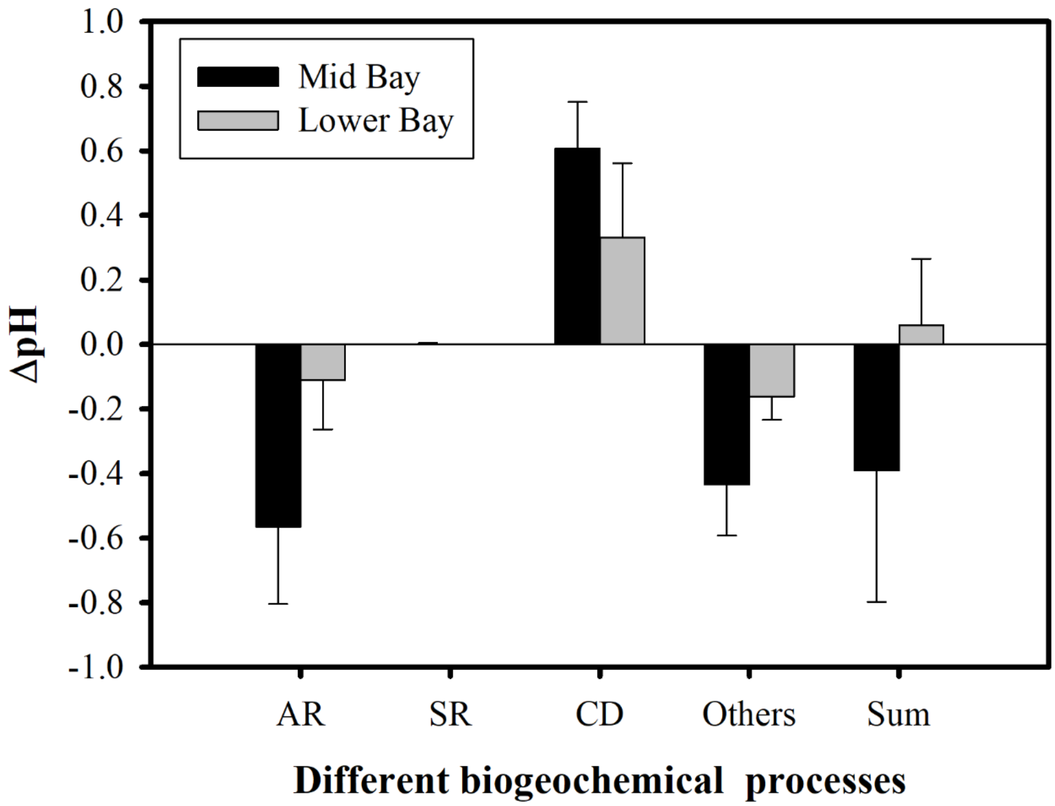

Figure 4.4: pH deviation induced by different biogeochemical processes. AR, aerobic respiration; SR, sulfate reduction; CD, carbonate dissolution; Others, other processes that influence pH dynamics. Sum means summing up the pH deviations induced by the four processes. The columnar and error bar represent the average and standard deviation of data in the subsurface water of the mid bay (black) or lower bay (grey).

4.3.3 A self-regulated pH buffer mechanism responding to eutrophication and acidification

Using an effective concentration method (Officer, 1979; Cai et al., 2000), we quantified that at least 85% of TA removal by $CaCO_3$ formation at salinity <10 was subsequently released back by $CaCO_3$ dissolution at salinity 10~22 (Fig. 4.11). The accumulated removal signal of TA in the mesohaline main channel indicates the uncompensated removal signal from the upper bay as well as local $CaCO_3$ formation in the shallow waters. The local $CaCO_3$ supply may come from the extensive SAV beds and the calcification by relatively abundant mollusks (Waldbusser et al., 2011b; Waldbusser et al., 2013; Schulte, 2017), crustaceans (Heck and Orth, 1980), and foraminifera (Karlsen et al., 2000) along the shores in the mid bay and lower bay. Beyond salinity 22, the effective concentrations of TA and Ca^{2+} become stable with a fractional loss of 13±10% and 2±9% respectively relative to river input, indicating overall the Chesapeake Bay is a weak TA sink, and has a balanced internal cycle of $CaCO_3$.

Our September 2018 survey in the Susquehanna Flats supports that aquatic biogeochemistry could be significantly different between shoals and main channel (Kemp et al., 1997) (Fig. 4.7). The $CaCO_3$ formation in the shallow areas and $CaCO_3$ dissolution in the subsurface water in the main channel are spatially-decoupled, and there should be some physical transport processes linking those two important components of carbonate cycle. As we do not have direct evidence to reveal the $CaCO_3$ transport unequivocally, we propose possible linkages as a hypothesis to be further tested. In the longitudinal direction (e.g. from Susquehanna Flats to mid bay), $CaCO_3$ precipitated on SAV leaf surfaces could likely reach the mid bay if it is fine-grained size. Without considering the trapping effect by the SAV beds, our model simulation showed that small particles (diameter<2 μm) released on the Susquehanna Flats could be transported downstream and reach the mid bay within 10 days, and had increasing impacts on the mid to lower bay from July to August (Fig. 4.14). In addition, $CaCO_3$ particles may also be laterally transported over a smaller distance from shoals to main channel via frequent resuspension and deposition during wind events (Malone et al., 1986; Valle-Levinson and Lwiza, 1995; Boicourt et al., 1999; Fugate et al., 2007). The details of the physical transport mechanisms for $CaCO_3$ solids require further research.

In addition to being a source of $CaCO_3$ solids, SAV could also buffer against eutrophication via particle trapping and nutrient assimilation and/or denitrification enhancement (Cafrey and Kemp, 1992; Gruber and Kemp, 2010; Gurbisz and Kemp, 2014). For instance, during our September 2018 sampling, nitrate concentrations in the flats were 2.2±2.7 μM compared to 95 μM in the Susquehanna River. Meanwhile, DIN at the sites below flats is also substantially lower than that at the river mouth, indicating this scavenging effect on DIN may extend beyond the SAV beds (Gurbisz et al., 2017).

These results lead us to propose a self-regulated pH buffer mechanism responding to coastal eutrophication and acidification in the Chesapeake Bay (Fig. 4.5). With increasing atmospheric CO_2, the ocean absorbs more anthropogenic CO_2 and transfers the acidification signal to the estuary via river-ocean water mixing. High anthropogenic nutrient loads from rivers induce phytoplankton blooms, promote the development of hypoxia/anoxia and introduce additional CO_2 and acid to the subsurface water, thereby further reducing pH and the carbonate saturation state (Cai et al., 2011). In the meantime, the shallow-water SAV communities can efficiently assimilate anthropogenic nutrients to satisfy the demands of intensive primary production, and increase pH and Ω in the surrounding water, especially in the microzones on the leaf surface. The high-pH environment can stimulate the formation of $CaCO_3$ solids in shallow waters (e.g. Susquehanna Flats at the head of the bay, or shoals flanking the main channel), which can subsequently be transported into the deep, oxygen-deficient zones in the main channel of the mid and lower bay via longitudinal and lateral transport. Then, $CaCO_3$ solids react with anthropogenic and metabolic CO_2 and increase TA, thus buffering the pH decrease. Moreover, nutrient reductions could have a multiplicative effect on acidification, by lowering the respiratory production of CO_2 while simultaneously promoting SAV recovery that could promote $CaCO_3$ formation, transport, and subsequent buffering. The same self-regulated mechanism may be observed in other eutrophic coastal environments with high primary production, abundant calcifying organisms and restricted water exchange with the open ocean. For instance, Abril et al. (2003) demonstrated that the authigenic $CaCO_3$ precipitated in the Loire River was closely coupled with intense primary production, meanwhile $CaCO_3$ dissolution occurred in the oxygen-deficient estuarine maximum turbidity zone.

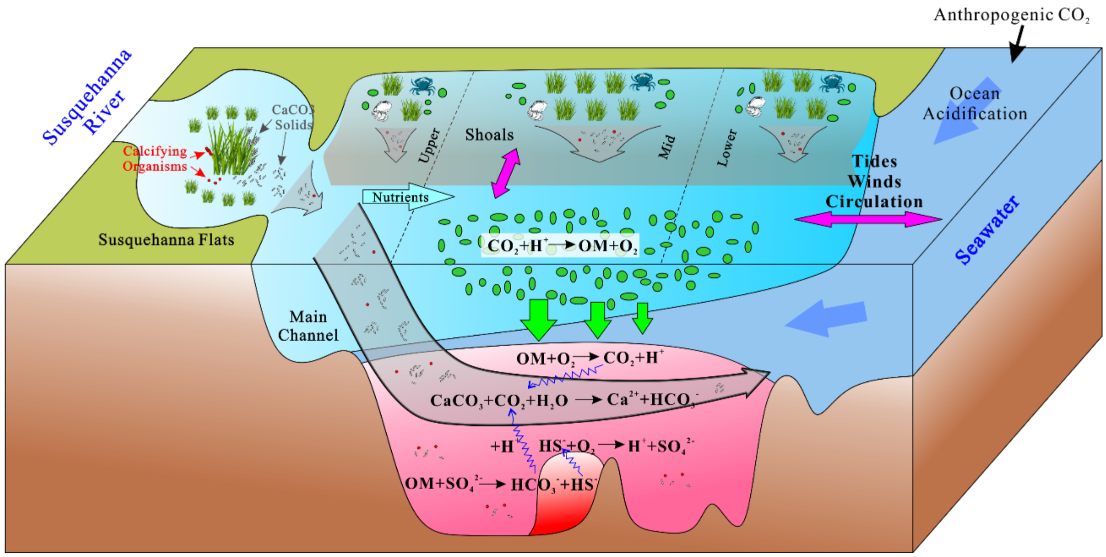

Figure 4.5: A conceptual model for self-regulated pH buffer mechanism responding to coastal eutrophication and acidification in the Chesapeake Bay. $CaCO_3$ formed within the high-pH SAV beds in the shallow waters, could be transported into the deep main channel of the mid and lower bay for further dissolution, thus increasing the pH buffer capacity and alleviating coastal acidification. See main text for details.

The unique foundation of this self-regulated mechanism is the SAV beds, where $CaCO_3$ appears to precipitate on leaf surfaces or form by other calcifying organisms and be transported to corrosive deep waters. The recovery of SAV in the Chesapeake Bay is a success of management efforts targeting nutrient load reductions (Lefcheck et al., 2018), and continued recovery should amplify SAV-induced improvements in water quality (Orth et al., 2017). Many previous reports have highlighted positive feedbacks within SAV beds that amplify their growth through improving local growing conditions (Kemp et al., 2005; Gurbisz et al., 2017). However, this study suggests SAV can mediate pH conditions far beyond the habitats where they grow, largely extending the potential ecosystem impacts of SAV. In other words, the SAV-driven pH buffer mechanism is an additional, unanticipated benefit of nutrient management efforts. These results demonstrate that coastal ecosystems can further promote their own recovery in complex, sometimes unpredictable ways as humans reduce anthropogenic stressors by policy management. This positive feedback to coastal restoration can shed light on eutrophication and acidification studies in coastal systems emerging with recovery signs.

4.4 Methods

4.4.1 Site and cruise descriptions

During August 8-12, 2016, we cruised from the upper bay (CB2.1) southwards to the bay mouth (AO1) and back to the mid bay (CB5.3) (Fig. 4.6). We revisited stations 858C four times, CB4.3 and CB5.1 three times and CB5.2 two times. On June 7 and September 4, 2018, we conducted two supplementary surveys first upstream along the western channel, and then downstream across the SAV beds in the Susquehanna Flats (Fig. 4.7).

4.4.2 Sample and analytical methods

Profiles of temperature, salinity, and O_2 were acquired by YSI 6600, which was attached to a submerged pump. According to the bottom depth and the state of mixing, we pumped water from 2-7 depths to the deck for sampling. All samples were filtered by cellulose acetate cartridge filters (pore size 0.45 μm), which is recommended by Bockmon and Dickson (2014) for reliable carbonate chemistry measurements in productive coastal environments. Salinities were double checked in discrete samples using a Cole-Parmer® salinity meter. The DIC samples were preserved in 250 mL borosilicate glass bottle with 50 μL saturated $HgCl_2$ solution (Huang et al., 2012), but TA samples were not poisoned as HgS will precipitate out and H^+ will be released in anoxic waters (Goyet et al., 1991; Hiscock and Millero, 2006; Cai et al., 2017). Some efforts were made to avoid the possible alteration of TA during storage and analysis, including 1) sample filtration to effectively remove all zooplankton, most of the phytoplankton and bacteria (Verdugo et al., 2004), 2) keeping samples at low temperature (<4 °C) to minimize the biological activity, 3) shortening sample storage time by analyzing samples overnight (<24 h) and rarely over the next day (<36 h), and 4) the duration of TA analysis (<10 min) is short compared with the oxidation of sulfide or ammonia by oxygen. Time-delay measurements on replicate filtered and un-poisoned TA samples from the Susquehanna River were performed to confirm that biological alteration was minor (within the TA measurement precision ±2 μmol kg^{-1}) even after a 13-days' delay in TA measurement. In addition, the measured TA values agree well with TA values calculated from measured DIC and pH via CO2SYS though the mean measured TA is significantly higher (~11 μmol kg^{-1}) than the mean calculated TA (paired t-test, $p<0.05$). Most of the TA differences (measured – calculated) are within ±20 μmol kg^{-1} and do not correlate with the concentrations of H_2S or NH_4^+, which could be explained by the contribution from organic alkalinity in the estuary as well as the uncertainties of glass electrode pH measurements and the dissociation constant K1 and K2 of carbonic acid used in the calculation (Cai et al., 1998; Millero, 2010; Hunt et al., 2011; Yang et al., 2015). For DIC, a 1 mL sample was acidified and the extracted CO_2 gas was subsequently quantified with an infrared CO_2 detector (AS-C3 DIC Analyzer) (Huang et al., 2012). All TA samples were analysed within 36 h of collection using Gran titration in an open-cell setting (AS-Alk2 Analyzer) (Cai et al., 2010). The overall precision for DIC and TA was ±0.1%. Both DIC and TA measurements were calibrated against Certified Reference Materials provided by Dr. A. G. Dickon at Scripps Institution of Oceanography (SIO), University of California, San Diego (UCSD).

The pH samples were measured on board by an Orion Ross glass electrode within 1 h after water temperature was stabilized at 25 °C in a thermal waterbath. The electrode was calibrated against three NIST standards, i.e. 4.01, 7.00, 10.01. Note that in the pH simulation, pH was also calculated from measured DIC and TA in NBS scale via a modified version of the CO2SYS program that include H_2S and NH_4^+ in the acid-base equilibrium calculation (Xu et al., 2017), which agrees well with the measured pH (Fig. 4.12). The $p$$CO_2$ was also calculated via the CO2SYS program. Discrete dissolved oxygen samples were analyzed by direct spectrophotometry of total iodine following Pai et al. (1993) with a precision of ±1 μmol kg^{-1}. The H_2S samples were measured by spectrophotometric method following Fonselius et al. (2007) with a precision better than 2.0%. Ca^{2+} was measured by a modified technique of Kanamori and Ikegami (1980) with a precision better than 0.1%. The Ω_{arag} was derived using measured Ca^{2+}, calculated CO_3^{2-}, and aragonite solubility based on Mucci (1983).

In the Susquehanna Flats (39.5056°N, 76.0413°W), temperature, salinity, DO, pH, turbidity and chlorophyll data were obtained by in-situ sensors. The sensors were deployed between April and October within the SAV beds, and maintained by the Maryland Department of Natural Resources (MD DNR) (http://www.eyesonthebay.net). The sensors are either YSI™ 6600 Extended Deployment Systems or YSI™ EXO2 model sondes, which are equipped with antifouling technology. SAV coverage data in year 2016 were obtained from the dataset of SAV in Chesapeake Bay and Coastal Bays (http://web.vims.edu/bio/sav/SegmentAreaTable.htm).

During the field surveys in the Susquehanna Flats in September 2018, surface water samples of DIC, TA and Ca^{2+} were taken at all sites, and solid samples of surface sediments and SAV leaves were collected in part of sites in the shallow eastern flats. The solid samples were dried at 60 ℃ for 48 hours. The microstructures and chemical composition of solids on the leaf surface were investigated using a focused ion beam and field emission scanning electron microscope (FIB-SEM, Zeiss Auriga 60) equipped with an X-ray energy-dispersive spectrometer (EDS, Oxford Instruments X-Max 80). After picking out the visible shells and epiphyte organisms, the solid samples were grounded for the determination of the percentages of $CaCO_3$ content (% dry weight) using Thermal Conductivity Detector (TCD) Gas-Chromatography (GC) generally following Stainton (1973). The coefficient of variation for the GC method used was ± 3.3%.

4.4.3 Determination of the endmembers and mixing lines

We adopted two mixing schemes in order to distinguish the apparent carbonate alterations in different geographic scales. On a bay-wide scale, we used the mixing line between the Susquehanna River endmember and the offshore seawater endmember to discuss $CaCO_3$ formation and related biogeochemical dynamics (Fig. 4.2a). For the river endmember, historical dataset of chemical concentration and discharge rate were compiled, including DIC and TA from Cai’s lab during August 2015-April 2017 (n=35 for DIC, n=35 for TA) and from USGS (Site number 01578310) during January 1996-June 2017 (n=236 for DIC, n=246 for TA), and Ca^{2+}

data from USGS (Site number 01578310) during November 1978-June 2017 (n=436) with daily discharge rate Q from USGS (Site number 01578310). Then, we obtained linear relationships of DIC or TA or Ca^{2+} with LogQ (DIC= -524*LogQ+2695, R^2=0.61, n=271, p<0.0001; TA= -530*LogQ+2642, R^2=0.62, n=281, p<0.0001; Ca^{2+}= -298*LogQ+1487, R^2=0.69, n=435, p<0.0001) (Fig. 4.13). Finally, we derived the river endmember of DIC, TA and Ca^{2+} from the specific discharge rate during the cruise period and 10 days prior (Joesoef et al., 2017). The errors were propagated from the uncertainties of slope and intercept of the linear regression and of the specific freshwater discharge based on the Taylor's expression (Taylor, 1997). Although the discharge varied 27% over time during the cruise and multiple days prior to the cruise, it had little influence on the river endmember values (< 5%) (Table 4.2), which were within the uncertainties (Table 4.1). For the offshore seawater endmember, we first made linear regressions of DIC or TA or Ca^{2+} with salinity (DIC= 79*Sal-596, R^2=0.72, p<0.0001; TA= 54*Sal+428, R^2=0.99, p<0.0001; Ca^{2+}= 269*Sal+831, R^2=0.98, p<0.0001) with data from four stations (82, 83, 85 and 87) in the Mid-Atlantic Bight, which were visited in the East Coast Ocean Acidification (ECOA) cruise in July 2015. Then, we used the salinity of the ocean endmember (33.618±0.139) in Cai et al. (2017) to derive the offshore endmember values.

To focus on $CaCO_3$ dissolution and related biogeochemical variations in the mid to lower bay, we adopted another mixing line between the southern end of upper bay and the bay mouth (Fig. 4.2a). CB2.2 is considered as a good endmember, because waters upper stream of CB2.2 were well mixed at this narrow section and no major tributaries input were there. AO1 is another good endmember, because this station is just outside the bay mouth and its water column was thoroughly mixed with maximum vertical salinity difference of 0.3. Further considering the sensitivity of Ca^{2+} against salinity, we adopted the values of low salinity layer (surface) at CB2.2 and high salinity layer (bottom) at AO1 as endmembers. All the endmember values and uncertainties are summarized in Table 4.1.

4.4.4 Calculation of total non-conservative DIC, TA and Ca^{2+}

Regarding salinity as a conservative tracer, we can calculate the mixing fractions between river water and seawater for each sample using equations (4.1) and (4.2):

$$f_R + f_{SW} = 1 \tag{4.1}$$

$$S_R \times f_R + S_{SW} \times f_{SW} = S_{meas} \tag{4.2}$$

where *S* represents salinity; *f* is the mixing fraction; the subscripts *R* and *SW* denote the river and seawater endmember, and *meas* represents the measured value. These fractions were applied to predict conservative concentrations of certain chemical constituents [X] (i.e. DIC, TA or Ca^{2+}) resulting solely from two endmember mixing:

$$[X]_{con} = [X]_R \times f_R + [X]_{SW} \times f_{SW} \tag{4.3}$$

The difference (Δ[X]) between measured and conservative values represent total non-conservative values of [X] caused by several biogeochemical processes:

$$\Delta[X]_{non\_c} = [X]_{meas} - [X]_{con} \tag{4.4}$$

where subscripts *non_c* means non-conservative and *con* stands for conservative.

4.4.5 Quantifying biogeochemical processes in the upper bay

In the upper bay, we separated the total non-conservative [X] (DIC or TA) into four components:

$$\Delta[X]_{non\_c} = \Delta[X]_{AR} + \Delta[X]_{CP} + \Delta[X]_{OG} + \Delta[X]_{Sedi} \tag{4.5}$$

where the subscripts *AR*, *CP*, *OG* and *Sedi* denote aerobic respiration, $CaCO_3$ precipitation, CO_2 outgassing and sediment-water exchange, respectively. There was no sulfate reduction in the upper bay. Sediment-water exchange includes porewater exchange with scale lengths of "milli-meters to meters" and submarine groundwater discharge (SGD) with scale lengths of "meters to kilometers", which may be comparable in magnitude in some coastal regions (Hong et al., 2017). In the Chesapeake Bay, SGD input was found near the head of the bay and in some tributaries, but the SGD rate was estimated to be much smaller than the riverine flux of freshwater to the bay (< 10%) (Hussain et al., 1999; Luek and Beck, 2014). Considering that carbonate parameters within SGD have not been reported in the Chesapeake Bay, it is difficult to further quantify the relative contributions of porewater exchange vs. SGD to the DIC and TA flux from the sediment. By considering the chemical stoichiometry involved in different biogeochemical processes (Cai et al., 2017), we can use AOU, ΔCa^{2+}, pCO_2 (calculated from measured DIC and TA) to quantify $\Delta[X]_{AR}$, $\Delta[X]_{CP}$ and $\Delta[X]_{OG}$. As shown in Fig. 4.9, we first simulated the portion of non-conservative DIC or TA caused by AR and CP, which are marked as yellow cross (DIC) and yellow plus (TA). Then, we computed the residence time at subdomains of CB2.1 (39.40-39.45°N) and CB2.2 (39.30-39.40°N) by simple volume/volumetric flow rate. Through equation $\Delta DIC_{OG} = \frac{Flux*\tau}{H}$ (*Flux* means CO_2 flux calculated from pCO_2; τ indicates residence time; *H* is the average water depth.), we could calculate the portion of non-conservative DIC caused by CO_2 outgassing, which are shown as the cyan arrows in the inserted plot (Fig. 4.9). Note that air-water CO_2 exchange doesn't influence TA. $\Delta[X]_{Sedi}$ (DIC or TA) are calculated as a residue in equation (4.5) and thus include all DIC and TA fluxes from multiple processes in sediments including porewater exchange and SGD.

Nutrient changes may also affect TA due to nutrient-H^+-compensation principle (Brewer and Goldman, 1976; Wolf-Gladrow et al., 2007). First, our approach uses the non-conservative part of Ca^{2+} concentration to estimate $CaCO_3$ formation and dissolution, thus it does not need a nutrient correction. Second, since NH_4^+ and $NO_2^-+NO_3^-$ were measured at each station and each depth during cruise in August 2016 (Cai group unpublished data), the changes of nutrients could be quantified using two endmember mixing calculations. Note that only non-conservative part contributes to TA and the concentration change due to dilution by river-ocean mixing doesn't. Results show that NH_4^+ was generally produced, while $NO_2^-+NO_3^-$ were consumed, both leading to TA increase within the bay (Cai group unpublished data). In a bay-wide mixing scenario (river-offshore), TA increase caused by NH_4^+ production and $NO_2^-+NO_3^-$ consumption ranges from 15 to 37 μmol kg^{-1} in the low salinity zone (Sal<10), which is relatively small compared with the TA removal (500~700 μmol kg^{-1}) in the upper bay. Therefore, we didn't perform nutrient corrections for TA, and mathematically, those nutrient-related TA changes could be attributed to the residual term of TA mass balance equation (4.5) (i.e. ΔTA_{sedi}), which was thought to be mainly affected by sediment processes.

4.4.6 Quantifying biogeochemical processes and the related pH changes in the mid to lower bay

For the subsurface water in the mid to lower bay, we divided the total non-conservative [X] (DIC or TA) into four components:

$$\Delta[X]_{non\_c} = \Delta[X]_{AR}+\Delta[X]_{SR}+\Delta[X]_{CD}+\Delta[X]_{Others} \quad (4.6)$$

where the subscripts *AR*, *SR*, *CD* and *Others* denote aerobic respiration, sulfate reduction, $CaCO_3$ dissolution and other processes, respectively. Following Cai et al. (2017), we can use AOU, H_2S and ΔCa^{2+} to quantify $\Delta[X]_{AR}$, $\Delta[X]_{SR}$ and $\Delta[X]_{CD}$. Then, $\Delta[X]_{Others}$ is calculated as the residue of the above equation, which is mainly influenced by sediment-water exchange as well as air-water exchange (Fig. 4.10). Note that in a regional mixing scenario (CB2.2-AO1), the average value of nutrient-related TA increase is 13±12 μmol kg^{-1}, which only accounts for ~5±5% of the total non-conservative TA addition (231±73 μmol kg^{-1}) (Cai group unpublished data). Thus, we didn't correct nutrient changes for TA, and mathematically, those nutrient-related TA changes can be attributed to ΔTA_{others}. To evaluate the extent that each biogeochemical process affects pH in the subsurface water, we subtracted the amount of DIC and TA altered by each process from the measured values to calculate a new pH. Then, we define the difference between the pH calculated from measured DIC, TA and the new pH to be ΔpH (Fig. 4.4).

4.4.7 Evolution of DIC, TA and Ca^{2+} at stations CB2.1 and CB2.2

As shown in the Fig. 4.9, the combined effect of $CaCO_3$ precipitation and aerobic respiration drew down DIC by 345 μmol kg^{-1} at CB2.1 and 333 μmol kg^{-1} at CB2.2, followed by CO_2 outgassing, which lowered DIC by 202 μmol kg^{-1} at CB2.1 and by 291 μmol kg^{-1} at CB2.2. Sediment exchange elevated DIC by 18 μmol kg^{-1} at CB2.1 and lowered DIC by 43 μmol kg^{-1} at CB2.2 to reach the total non-conservative DIC of -529 μmol kg^{-1} at CB2.1 and -667 μmol kg^{-1} at CB2.2. Thus, CO_2 outgassing was enhanced by 89 μmol kg^{-1} and sediment turned from a weak source to a weak sink from CB2.1 to CB2.2. Note that CO_2 outgassing could not influence TA. Similarly, synergy of carbonate precipitation and aerobic respiration drew down TA by 773 μmol kg^{-1} at CB2.1 and 768 μmol kg^{-1} at CB2.2, followed by sediment exchange, which elevated TA by 250 μmol kg^{-1} at CB2.1 and 85 μmol kg^{-1} at CB2.2 to reach the total non-conservative TA of -523 μmol kg^{-1} at CB2.1 and -683 μmol kg^{-1} at CB2.2. Thus, sediment exchange was weakened by 165 μmol kg^{-1} from CB2.1 to CB2.2. The evolution of DIC, TA and Ca^{2+} indicates that $CaCO_3$ precipitation plays a vital role in the carbonate dynamics in the upper bay. In addition, high spatial variability of biogeochemical processes exists in the upper bay, where water column is well-mixed and water flow is relatively high.

4.4.8 Model simulation on $CaCO_3$ particles transport

The sediment resuspension in the SAV beds is typically lower than in the unvegetated area, because SAV beds can reduce the current velocity and attenuate wave energy, and thus decrease sediment erosion and enhance particle deposition (Fonseca, 1996). However, when the water depth is larger than the maximum meadow height, wave attenuation is less efficient, and sediment is deposited as well as resuspended (Ward et al., 1984). In addition, the geomorphology of the SAV beds (e.g. Susquehanna Flats) is spatially complex and characterized by unvegetated patches and shallow channels through the SAV beds. Water flow can be diverted around and between vegetation patches, increasing current velocities and associated near-bottom shear stresses and thus promoting non-deposition and/or erosion (Russ and Palinkas, 2018). The flow intensification near the bottom can possibly cause higher total suspended solid (TSS) levels in the vegetated (featured by fine particles) than in the unvegetated area (featured by coarser particles) at low wave energy (Koch, 1999). It can be expected that sediment resuspension within SAV beds would be even higher under stronger tidal currents or episodic high wind events (Gurbisz et al., 2016), which frequently affect the Chesapeake Bay. The particle transport pathways over SAV beds is not clear so far, and may be a function of river discharge, winds, topography, vegetation, proximity to channels/SAV bed edges, and hydrodynamic gradients similar to particle transport in marshes (Marani et al., 2003; Temmerman et al., 2005; D'Alpaos et al., 2007). It is beyond the scope of our study to simulate the particle transport over SAV beds.

Without considering the trapping effect by the SAV beds, we conducted a model simulation on the transport of $CaCO_3$ particles in 2016 using sediment module incorporated into the Regional Ocean Modeling System (ROMS) (Xie et al., 2018). Particles with three different sizes (i.e. 2 μm, 8 μm, 20 μm) and settling velocities were released at all water depth (20 layers) on the Susquehanna Flats on 5/31/2016 0:00:00. Particle deposition, resuspension of deposited sediment and sea bed erosion were considered in this simulation. Our model results show that the fine-grained particles (diameter=2 μm) from the Susquehanna Flats could reach the mid bay within 10 days, and had increasing impacts on the mid to lower bay from July to August (Fig. 4.14). The medium-sized particles with a diameter of 8 μm could also reach the upper parts of the mid bay within 10 days, but had less impacts on the mid and lower bay in the following two months (Data not shown). Particles of 20 μm size were mostly trapped in the upper bay throughout the summer (Data not shown). The model results support that the fine-grained $CaCO_3$ solids like those precipitated on the SAV leaf surface could probably be transported over a long distance to the main channel of mid to lower bay. Although this numerical model simulation does help to depict a “what if” given the fine particles can escape the SAV beds, further studies are needed to reveal how particles could be transported out of the SAV beds, and more details on the longitudinal and lateral transport mechanisms along the main channel.

4.5 Supplementary Information

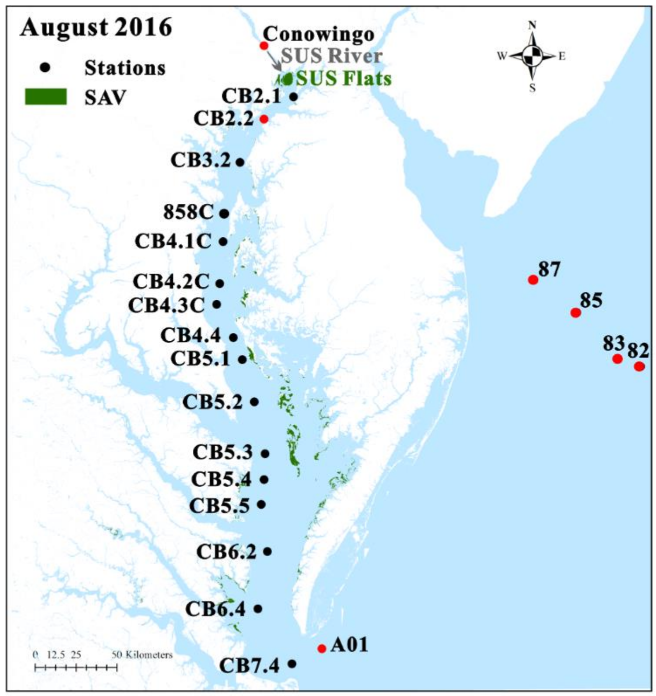

Figure 4.6: Sampling sites in August 2016 cruise in the Chesapeake Bay. Green areas show the coverage of Submersed Aquatic Vegetation (SAV) beds in the Chesapeake Bay in 2016. The upper, mid and lower bay (separated by the black lines) accounted for 16.4%, 64.0% and 19.6% of the total SAV coverage in 2016 (39,524 hectares). Arrow shows the outlet of Susquehanna River. Red circles show the related locations of the four endmembers. Note that stations 82, 83, 85 and 87 locate more offshore in the Mid-Atlantic Bight and were visited in the cruise during July 2015.

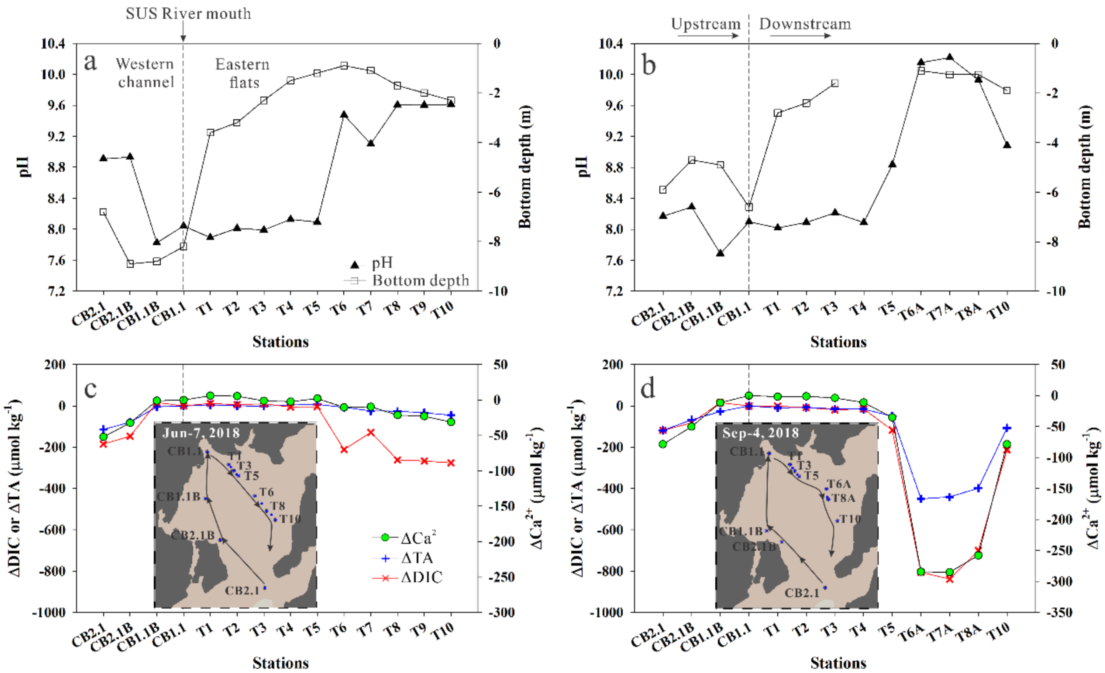

Figure 4.7: Carbonate variations and bottom depths in the Susquehanna Flats in June (a, c) and September (b, d), 2018. The dashed line separates the eastern deep channel and western shallow flats, where SAV beds existed. The arrows show the cruise directions. Sampling sites are labelled in the inserted maps. The SAV biomass was low in early June, but was high in early September 2018. The Δ values in each station are relative to CB1.1, which was our uppermost station near the Susquehanna River mouth.

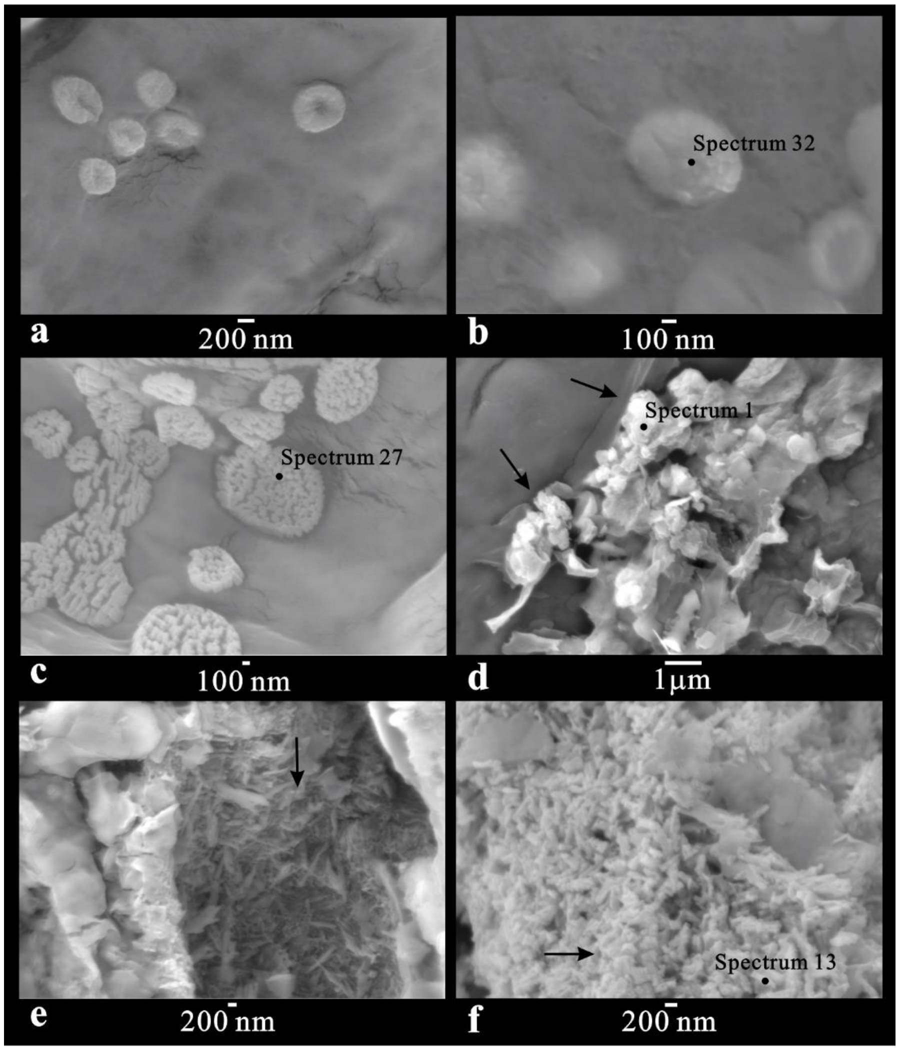

Figure 4.8: SEM images of $CaCO_3$ precipitation on the leaf surface of *Vallisneria americana*. Varying size and morphology were observed. (a) semi-spherical crystallites; (b) ellipsoidal crystallites (atomic composition in Spectrum 32: 41.8% C; 18.4% Ca; 17.2% O; 10.5% K; 6.5% Cl; 1.9% Na; 1.6% S; 1.3% Mg; 0.8% P); (c) polycrystalline maze-like aggregates (atomic composition in Spectrum 27: 40.8% C; 25.2% O; 14.4% Ca; 9.2% N; 5.3% K; 2.4% Mg; 1.6% P; 1.0% Na); (d) $CaCO_3$ aggregates with other materials (atomic composition in Spectrum 1: 42.9% O; 27.7% Ca; 25.4% C; 1.4% K; 1.2% Si; 0.9% Al; 0.2% Na; 0.2% Mg); (e) arborisation-like $CaCO_3$ aggregates (map sum spectrum: 31.1% C; 29.9% O; 22.3% Ca; 4.6% Fe; 4.4% Si; 3.8% Al; 2.0% K; 1.9% Mg); (f) rice-like $CaCO_3$ aggregates (atomic composition in Spectrum 13: 41.6% O; 38.1% Ca; 12.5% C; 3.7% K; 1.5% Cl; 1.1% Mg; 0.9% Si; 0.5% Na; 0.2% Al).

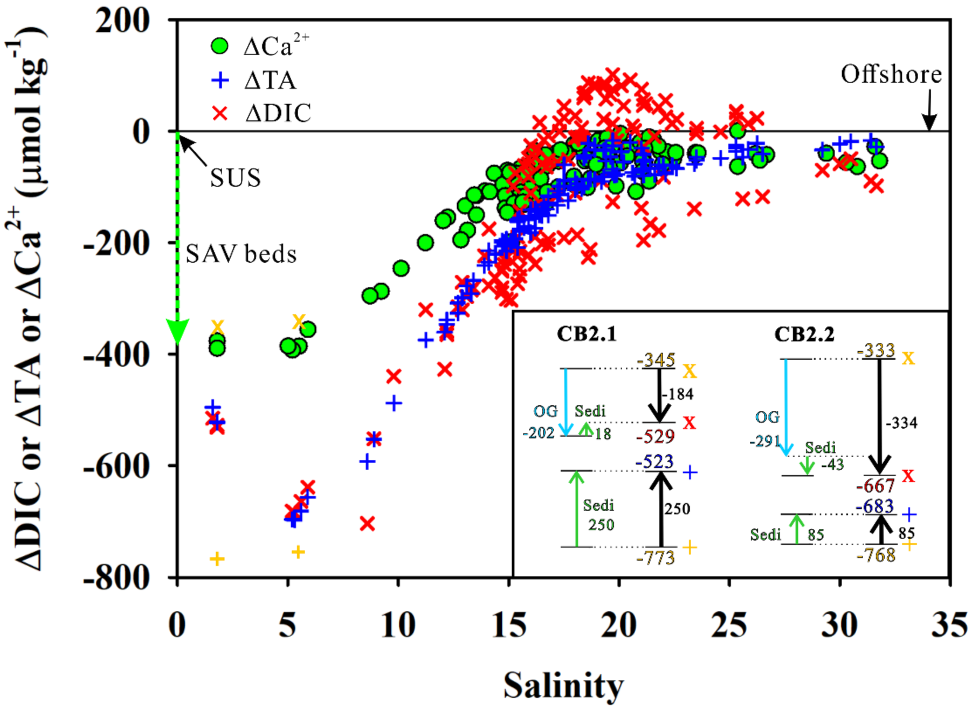

Figure 4.9: Model simulations of the evolution of Ca^{2+}, DIC and TA induced by different biogeochemical processes at stations CB2.1 and CB2.2. The large figure is the same as Figure 4.2c in the main text. The yellow cross and plus mean simulated values of DIC and TA, which are combined effect of $CaCO_3$ precipitation (CP) and aerobic respiration (AR). The inserted figure shows the DIC or TA alteration due to CO_2 outgassing (OG) and sediment-water exchange (Sedi).

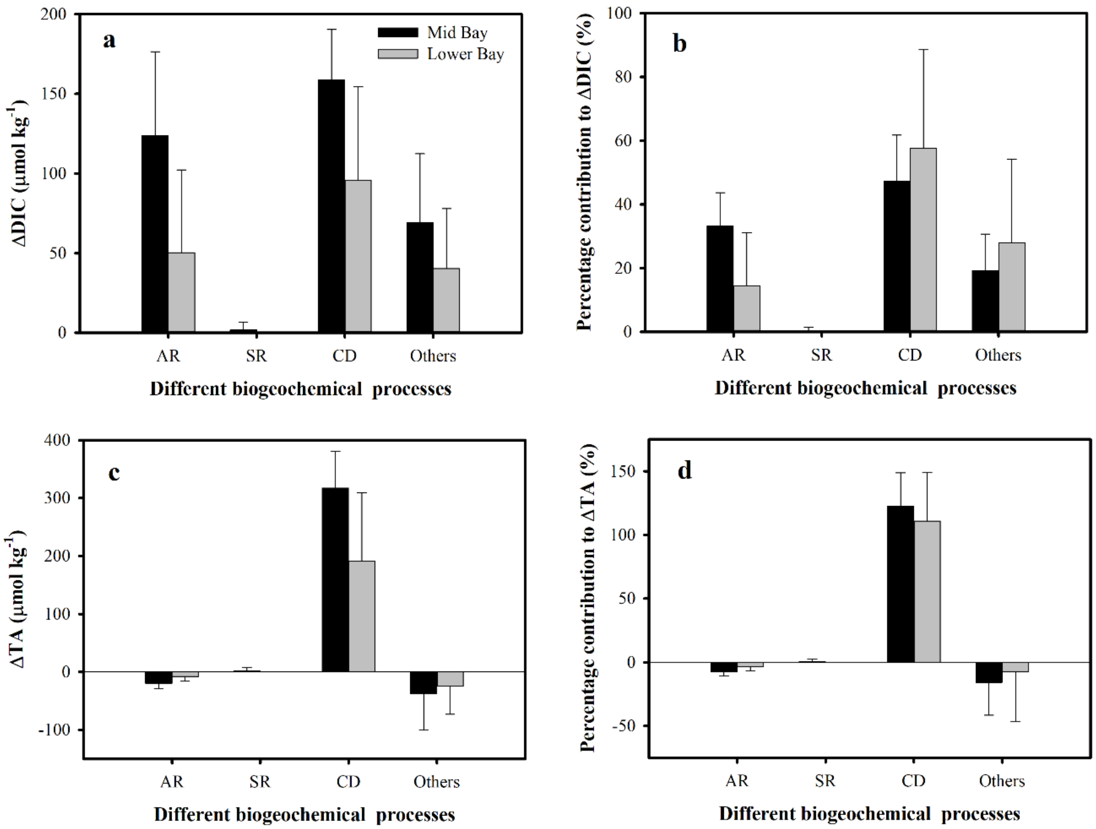

Figure 4.10: The amount and percentage contribution from different biogeochemical processes to the total non-conservative DIC (a, b) and TA (c, d).

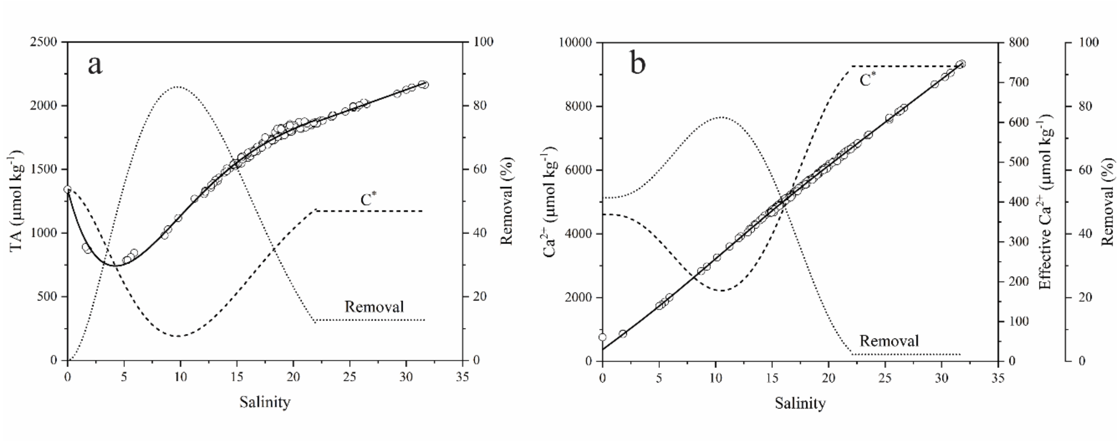

Figure 4.11: Effective concentration (C^*) and removal (percentage) of TA (a) and Ca^{2+} (b) in the Chesapeake Bay based on cruise data in August 2016. The fitting equation for TA at salinity <=22 is $C = 0.00002708 \times S^6 - 0.00336738 \times S^5 + 0.17376067 \times S^4 - 4.6574875 \times S^3 + 64.65219917 \times S^2 - 344.24526458 \times S + 1342.095396$, whereas at salinity >22 is $C = 31.791176 \times S + 1172.4787872$. The fitting equation for Ca^{2+} at salinity <=22 is $C = -0.00001835 \times S^6 + 0.00171504 \times S^5 - 0.05591518 \times S^4 + 0.67310609 \times S^3 - 0.73633157 \times S^2 + 265.9022229 \times S + 368.4115086$, whereas at salinity >22 is $C = 270.483366 \times S + 740.833973$.

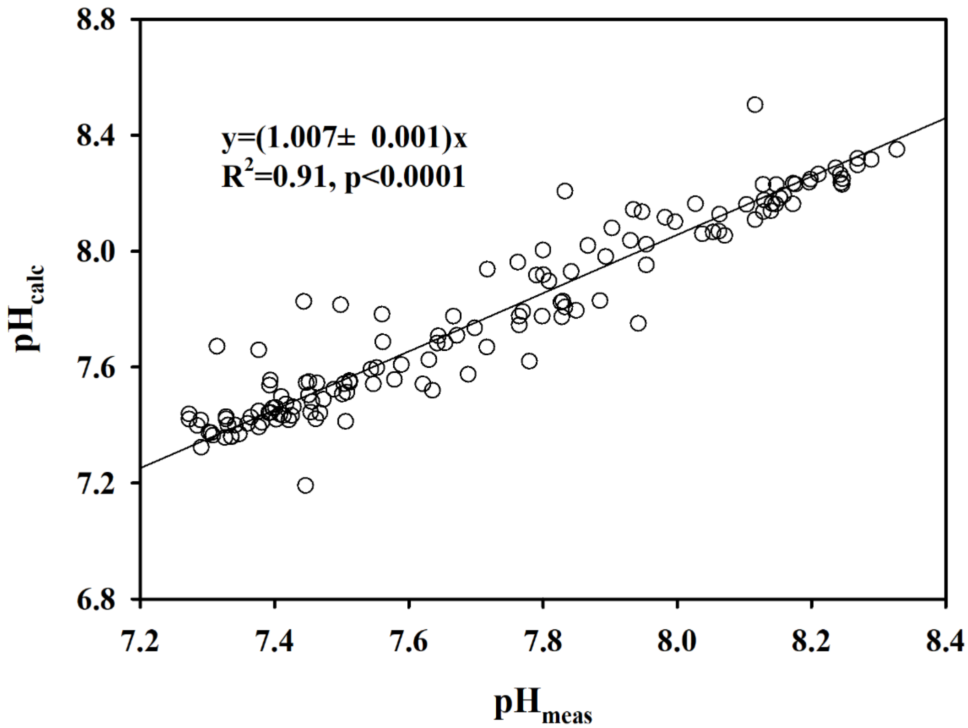

Figure 4.12: A direct comparison between calculated pH from DIC and TA and measured pH. We use DIC and TA to calculate pH in NBS scale via a modified version of the CO2SYS program.

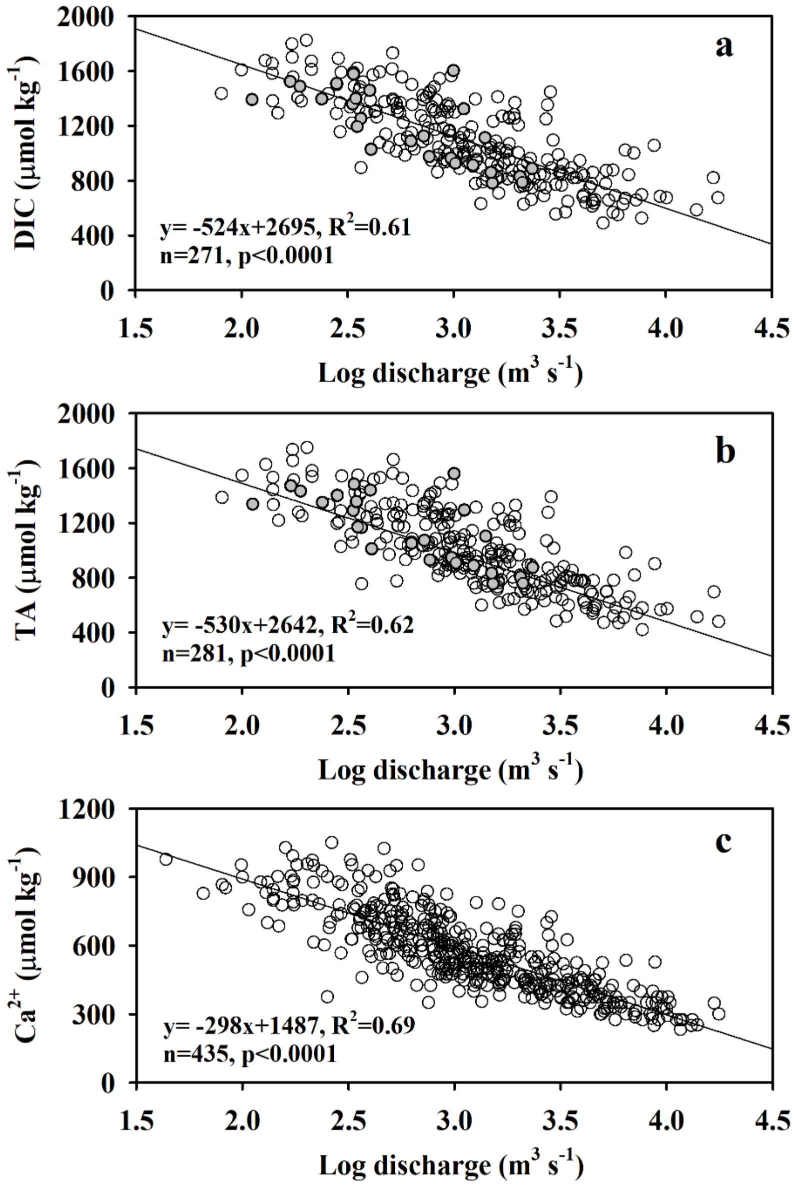

Figure 4.13: DIC, TA and Ca^{2+} versus Log discharge of Susquehanna River endmember at Conowingo. DIC (a) and TA (b) were combinations of data from Cai's lab (August 2015-April 2017, n=35 for DIC, n=35 for TA) and USGS (January 1996-June 2017, n=236 for DIC, n=246 for TA). The data from Cai's lab were filled with grey color. The Ca^{2+} (c) and daily discharge rate data were from USGS (Site number 01578310) at Conowingo during November 1978-June 2017 (n=435).

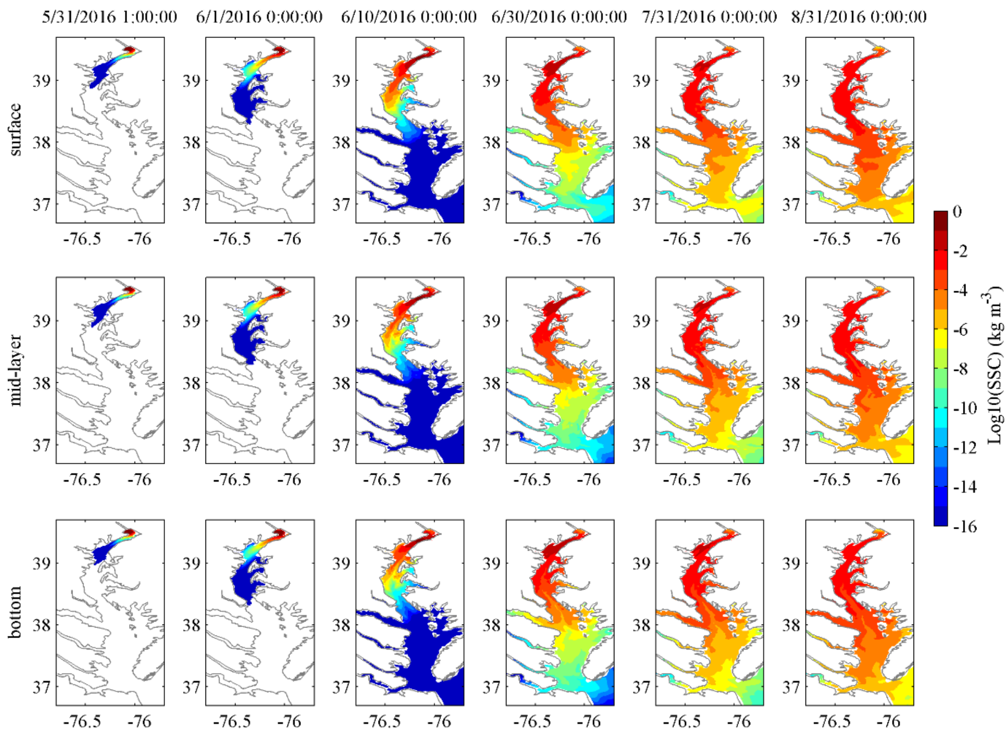

Figure 4.14: Model simulation of suspended sediment concentration (SSC) at surface, mid-depth and bottom water in the Chesapeake Bay after the initial release of sediment particle (diameter=2 μm) in all water depths on the Susquehanna Flats. The output snapshots are at 1 hour, 1 day, 10 days, 30 days, 60 days and 90 days after the initial release of particles.

Table 4.1: Summary of endmember values and their uncertainties

Endmembers	Salinity	DIC (μmol kg^{-1})	TA (μmol kg^{-1})	Ca^{2+} (mmol kg^{-1})
SUS River	0	1411±132	1342±132	0.757±0.062
CB2.2	5.3±0.1	830±2	787±2	
	5.0±0.1[a]			1.733±0.010
AO1	31.7±0.1	1927±2	2164±2	
	31.8±0.1[a]			9.335±0.010
Offshore	33.6±0.1	2063±11	2245±8	9.884±0.037

[a]Additional salinity measurements were performed on the Ca^{2+} samples.

Table 4.2: Simulation of river endmember values based on different days prior to cruise.

Days prior to cruise	Discharge (m^3 s^{-1})		DIC (μmol kg^{-1})		TA (μmol kg^{-1})		Ca^{2+} (μmol kg^{-1})	
	Average	SD	Average	SD	Average	SD	Average	SD
0	319	167	1383	156	1314	156	742	78
10	282	108	1411	132	1342	132	757	62
20	238	99	1450	137	1382	136	780	66
30	225	88	1463	133	1395	132	787	63
50	251	96	1438	132	1369	131	773	62
70	322	165	1381	154	1312	154	740	77
90	460	323	1300	190	1229	191	694	99
Average	299		1404		1335		753	
SD	80		56		56		32	
SD/Average (%)	26.9		4.0		4.2		4.2	

Note that the discharge is defined as the average of total discharge at Conowingo during cruise period and multiply days prior to cruise. All the average values in different scenarios of certain parameter were processed again to evaluate the stability of river endmembers relative to the situation of 10 days prior to cruise, which were adopted in the main text.

REFERENCES

Abril, G., Etcheber, H., Delille, B., Frankignoulle, M. and Borges, A.V., 2003. Carbonate dissolution in the turbid and eutrophic Loire estuary. Mar. Ecol. Prog. Ser. 259, 129-138. doi:10.3354/meps259129

Andersson, A.J., Mackenzie, F.T. and Lerman, A., 2005. Coastal ocean and carbonate systems in the high CO_2 world of the Anthropocene. Am. J. Sci. 305, 875-918. doi:10.2475/ajs.305.9.875

Beer, D.D. and Larkum, A.W.D., 2001. Photosynthesis and calcification in the calcifying algae Halimeda discoidea studied with microsensors. Plant, Cell Environ. 24, 1209-1217. doi:10.1046/j.1365-3040.2001.00772.x

Bockmon, E.E. and Dickson, A.G., 2014. A seawater filtration method suitable for total dissolved inorganic carbon and pH analyses. Limnol. Oceanogr. Methods 12, 191-195. doi:10.4319/lom.2014.12.191

Boicourt, W.C., Kuzmić, M. and Hopkins, T.S., 1999. The inland sea: circulation of Chesapeake Bay and the Northern Adriatic. In: Malone, T.C., Malej, A., Harding Jr, L.W., Smodlaka, N. and Turner, R.E. (Eds.), Ecosystems at the land-sea margin: drainage basin to coastal sea. American Geophysical Union, Washington, DC, pp. 81-129.

Borowitzka, M.A., 1984. Calcification in aquatic plants. Plant, Cell Environ. 7, 457-466. doi:10.1111/j.1365-3040.1984.tb01436.x

Borowitzka, M.A. and Larkum, A.W.D., 1987. Calcification in algae: Mechanisms and the role of metabolism. Crit. Rev. Plant Sci. 6, 1-45. doi:10.1080/07352688709382246

Brewer, P.G. and Goldman, J.C., 1976. Alkalinity changes generated by phytoplankton growth1. Limnol. Oceanogr. 21, 108-117. doi:10.4319/lo.1976.21.1.0108

Cafrey, J.M. and Kemp, W.M., 1992. Influence of the submersed plant, Potamogeton perfoliatus, on nitrogen cycling in estuarine sediments. Limnol. Oceanogr. 37, 1483-1495. doi:10.4319/lo.1992.37.7.1483

Cai, W.-J., Wang, Y. and Hodson, R.E., 1998. Acid-base properties of dissolved organic matter in the estuarine waters of Georgia, USA. Geochim. Cosmochim. Acta 62, 473-483. doi:10.1016/S0016-7037(97)00363-3

Cai, W.-J., Wiebe, W.J., Wang, Y. and Sheldon, J.E., 2000. Intertidal marsh as a source of dissolved inorganic carbon and a sink of nitrate in the Satilla River-estuarine complex in the southeastern U.S. Limnol. Oceanogr. 45, 1743-1752. doi:10.4319/lo.2000.45.8.1743

Cai, W.-J., Hu, X., Huang, W.-J., Jiang, L.-Q., Wang, Y., Peng, T.-H. and Zhang, X., 2010. Alkalinity distribution in the western North Atlantic Ocean margins. J. Geophys. Res. Ocean 115, C08014. doi:10.1029/2009JC005482
Cai, W.-J., Hu, X., Huang, W.-J., Murrell, M.C., Lehrter, J.C., Lohrenz, S.E., Chou, W.-C., Zhai, W., Hollibaugh, J.T. and Wang, Y., 2011. Acidification of subsurface coastal waters enhanced by eutrophication. Nat. Geosci. 4, 766-770. doi:10.1038/NGEO1297
Cai, W.-J., Huang, W.-J., Luther, G.W., Pierrot, D., Li, M., Testa, J., Xue, M., Joesoef, A., Mann, R., Brodeur, J., Xu, Y.-Y., Chen, B., Hussain, N., Waldbusser, G.G., Cornwell, J. and Kemp, W.M., 2017. Redox reactions and weak buffering capacity lead to acidification in the Chesapeake Bay. Nat. Commun. 8, 369. doi:10.1038/s41467-017-00417-7
Chauvaud, L., Thompson, J.K., Cloern, J.E. and Thouzeau, G., 2003. Clams as CO_2 generators: The Potamocorbula amurensis example in San Francisco Bay. Limnol. Oceanogr. 48, 2086-2092. doi:10.4319/lo.2003.48.6.2086
Corlett, H. and Jones, B., 2007. Epiphyte communities on Thalassia testudinum from Grand Cayman, British West Indies: Their composition, structure, and contribution to lagoonal sediments. Sediment. Geol. 194, 245-262. doi:10.1016/j.sedgeo.2006.06.010
D'Alpaos, A., Lanzoni, S., Marani, M. and Rinaldo, A., 2007. Landscape evolution in tidal embayments: Modeling the interplay of erosion, sedimentation, and vegetation dynamics. Journal of Geophysical Research: Earth Surface 112. doi:10.1029/2006jf000537
Du, J. and Shen, J., 2016. Water residence time in Chesapeake Bay for 1980–2012. J. Mar. Syst. 164, 101-111. doi:10.1016/j.jmarsys.2016.08.011
Enríquez, S. and Schubert, N., 2014. Direct contribution of the seagrass Thalassia testudinum to lime mud production. Nat. Commun. 5, 3835. doi:10.1038/ncomms4835
Fabry, V.J., Seibel, B.A., Feely, R.A. and Orr, J.C., 2008. Impacts of ocean acidification on marine fauna and ecosystem processes. ICES J. Mar. Sci. 65, 414-432. doi:10.1093/icesjms/fsn048
Feely, R.A., Okazaki, R.R., Cai, W.-J., Bednaršek, N., Alin, S.R., Byrne, R.H. and Fassbender, A., 2017. The combined effects of acidification and hypoxia on pH and aragonite saturation in the coastal waters of the California current ecosystem and the northern Gulf of Mexico. Cont. Shelf Res. doi:10.1016/j.csr.2017.11.002
Fonseca, M.S., 1996. The role of seagrasses in nearshore sedimentary processes: a review. In: Nordstrom, K. and Roman, C.T. (Eds.), Estuarine Shores: Evolution, Environments and Human Alterations. Wiley, London, pp. 261-286.
Fonselius, S., Dyrssen, D. and Yhlen, B., 2007. Determination of hydrogen sulphide, Methods of Seawater Analysis. Wiley, pp. 91-100.
Fugate, D.C., Friedrichs, C.T. and Sanford, L.P., 2007. Lateral dynamics and associated transport of sediment in the upper reaches of a partially mixed

estuary, Chesapeake Bay, USA. Cont. Shelf Res. 27, 679-698. doi:10.1016/j.csr.2006.11.012
Gattuso, J.-P., Magnan, A., Billé, R., Cheung, W.W.L., Howes, E.L., Joos, F., Allemand, D., Bopp, L., Cooley, S.R., Eakin, C.M., Hoegh-Guldberg, O., Kelly, R.P., Pörtner, H.-O., Rogers, A.D., Baxter, J.M., Laffoley, D., Osborn, D., Rankovic, A., Rochette, J., Sumaila, U.R., Treyer, S. and Turley, C., 2015. Contrasting futures for ocean and society from different anthropogenic CO_2 emissions scenarios. Science 349. doi:10.1126/science.aac4722
Goyet, C., Bradshaw, A.L. and Brewer, P.G., 1991. The carbonate system in the Black Sea. Deep Sea Research Part A. Oceanographic Research Papers 38, S1049-S1068. doi:10.1016/S0198-0149(10)80023-8
Green, M.A., Waldbusser, G.G., Reilly, S.L., Emerson, K. and O'Donnell, S., 2009. Death by dissolution: Sediment saturation state as a mortality factor for juvenile bivalves. Limnol. Oceanogr. 54, 1037-1047. doi:10.4319/lo.2009.54.4.1037
Gruber, R.K. and Kemp, W.M., 2010. Feedback effects in a coastal canopy - forming submersed plant bed. Limnol. Oceanogr. 55, 2285-2298. doi:10.4319/lo.2010.55.6.2285
Gurbisz, C. and Kemp, W.M., 2014. Unexpected resurgence of a large submersed plant bed in Chesapeake Bay: Analysis of time series data. Limnol. Oceanogr. 59, 482-494. doi:10.4319/lo.2014.59.2.0482
Gurbisz, C., Kemp, W.M., Sanford, L.P. and Orth, R.J., 2016. Mechanisms of Storm-Related Loss and Resilience in a Large Submersed Plant Bed. Estuar. Coast. 39, 951-966. doi:10.1007/s12237-016-0074-4
Gurbisz, C., Kemp, W.M., Cornwell, J.C., Sanford, L.P., Owens, M.S. and Hinkle, D.C., 2017. Interactive Effects of Physical and Biogeochemical Feedback Processes in a Large Submersed Plant Bed. Estuar. Coast. 40, 1626-1641. doi:10.1007/s12237-017-0249-7
Hagens, M., Slomp, C.P., Meysman, F.J.R., Seitaj, D., Harlay, J., Borges, A.V. and Middelburg, J.J., 2015. Biogeochemical processes and buffering capacity concurrently affect acidification in a seasonally hypoxic coastal marine basin. Biogeosciences 12, 1561-1583. doi:10.5194/bg-12-1561-2015
Heck, K.L. and Orth, R.J., 1980. Structural components of eelgrass (Zostera marina) meadows in the lower Chesapeake Bay—Decapod crustacea. Estuaries 3, 289-295. doi:10.2307/1352084
Hiscock, W.T. and Millero, F.J., 2006. Alkalinity of the anoxic waters in the Western Black Sea. Deep Sea Research Part II: Topical Studies in Oceanography 53, 1787-1801. doi:10.1016/j.dsr2.2006.05.020
Hong, Q., Cai, P., Shi, X., Li, Q. and Wang, G., 2017. Solute transport into the Jiulong River estuary via pore water exchange and submarine groundwater discharge: New insights from $^{224}Ra/^{228}Th$ disequilibrium. Geochim. Cosmochim. Acta 198, 338-359. doi:10.1016/j.gca.2016.11.002

Huang, W.J., Wang, Y. and Cai, W.J., 2012. Assessment of sample storage techniques for total alkalinity and dissolved inorganic carbon in seawater. Limnol. Oceanogr. Methods 10, 711-717. doi:10.4319/lom.2012.10.711

Hunt, C.W., Salisbury, J.E. and Vandemark, D., 2011. Contribution of non-carbonate anions to total alkalinity and overestimation of pCO_2 in New England and New Brunswick rivers. Biogeosciences 8, 3069-3076. doi:10.5194/bg-8-3069-2011

Hussain, N., Church, T.M. and Kim, G., 1999. Use of ^{222}Rn and ^{226}Ra to trace groundwater discharge into the Chesapeake Bay. Mar. Chem. 65, 127-134. doi:10.1016/S0304-4203(99)00015-8

Joesoef, A., Kirchman, D.L., Sommerfield, C.K. and Cai, W.-J., 2017. Seasonal variability of the inorganic carbon system in a large coastal plain estuary. Biogeosciences 14, 4949-4963. doi:10.5194/bg-14-4949-2017

Kanamori, S. and Ikegami, H., 1980. Computer-processed potentiometric titration for the determination of calcium and magnesium in sea water. J. Oceanogr. Soc. Japan 36, 177-184. doi:10.1007/bf02070330

Karlsen, A.W., Cronin, T.M., Ishman, S.E., Willard, D.A., Kerhin, R., Holmes, C.W. and Marot, M., 2000. Historical trends in Chesapeake Bay dissolved oxygen based on benthic foraminifera from sediment cores. Estuaries 23, 488-508. doi:10.2307/1353141

Kemp, W., Boynton, W., Adolf, J., Boesch, D., Boicourt, W., Brush, G., Cornwell, J., Fisher, T., Glibert, P. and Hagy, J., 2005. Eutrophication of Chesapeake Bay: historical trends and ecological interactions. Mar. Ecol. Prog. Ser. 303, 1-29. doi:10.3354/meps303001

Kemp, W.M., Smith, E.M., Marvin-DiPasquale, M. and Boynton, W.R., 1997. Organic carbon balance and net ecosystem metabolism in Chesapeake Bay. Mar. Ecol. Prog. Ser. 150, 229-248. doi:10.3354/meps150229

Koch, E.W., 1994. Hydrodynamics, diffusion-boundary layers and photosynthesis of the seagrasses *Thalassia testudinum* and *Cymodocea nodosa*. Mar. Biol. 118, 767-776. doi:10.1007/bf00347527

Koch, E.W., 1999. Sediment resuspension in a shallow *Thalassia testudinum* banks ex König bed. Aquat. Bot. 65, 269-280. doi:10.1016/S0304-3770(99)00045-5

Kroeker, K.J., Kordas, R.L., Crim, R., Hendriks, I.E., Ramajo, L., Singh, G.S., Duarte, C.M. and Gattuso, J.P., 2013. Impacts of ocean acidification on marine organisms: quantifying sensitivities and interaction with warming. Glob. Chang. Biol. 19, 1884-1896. doi:10.1111/gcb.12179

Lefcheck, J.S., Orth, R.J., Dennison, W.C., Wilcox, D.J., Murphy, R.R., Keisman, J., Gurbisz, C., Hannam, M., Landry, J.B., Moore, K.A., Patrick, C.J., Testa, J., Weller, D.E. and Batiuk, R.A., 2018. Long-term nutrient reductions lead to the unprecedented recovery of a temperate coastal region. Proc. Natl. Acad. Sci. U.S.A. 115, 3658-3662. doi:10.1073/pnas.1715798115

Lesley A. Warren, P.A.M.N.P.F.G.F., 2001. Microbially Mediated Calcium Carbonate Precipitation: Implications for Interpreting Calcite Precipitation and for Solid-

Phase Capture of Inorganic Contaminants. Geomicrobiol. J. 18, 93-115. doi:10.1080/01490450151079833
Luek, J.L. and Beck, A.J., 2014. Radium budget of the York River estuary (VA, USA) dominated by submarine groundwater discharge with a seasonally variable groundwater end-member. Mar. Chem. 165, 55-65. doi:10.1016/j.marchem.2014.08.001
Macreadie, P.I., Serrano, O., Maher, D.T., Duarte, C.M. and Beardall, J., 2017. Addressing calcium carbonate cycling in blue carbon accounting. Limnol. Oceanogr. Letters. doi:10.1002/lol2.10052
Malone, T.C., Kemp, W.M., Ducklow, H.W., Boynton, W.R., Tuttle, J.H. and Jonas, R.B., 1986. Lateral variation in the production and fate of phytoplankton in a partially stratified estuary. Mar. Ecol. Prog. Ser. 32, 149-160. doi:10.3354/meps032149
Marani, M., Belluco, E., D'Alpaos, A., Defina, A., Lanzoni, S. and Rinaldo, A., 2003. On the drainage density of tidal networks. Water Resour. Res. 39. doi:10.1029/2001wr001051
Mazarrasa, I., Marbà, N., Lovelock, C.E., Serrano, O., Lavery, P.S., Fourqurean, J.W., Kennedy, H., Mateo, M.A., Krause-Jensen, D., Steven, A.D.L. and Duarte, C.M., 2015. Seagrass meadows as a globally significant carbonate reservoir. Biogeosciences 12, 4993-5003. doi:10.5194/bg-12-4993-2015
Millero, F.J., 2010. Carbonate constants for estuarine waters. Marine and Freshwater Research 61, 139-142. doi:10.1071/MF09254
Moore, K.A., Wilcox, D.J. and Orth, R.J., 2000. Analysis of the abundance of submersed aquatic vegetation communities in the Chesapeake Bay. Estuaries 23, 115-127. doi:10.2307/1353229
Mucci, A., 1983. The solubility of calcite and aragonite in seawater at various salinities, temperatures, and one atmosphere total pressure. Am. J. Sci. 283, 780-799. doi:10.2475/ajs.283.7.780
Murphy, R.R., Kemp, W.M. and Ball, W.P., 2011. Long-Term Trends in Chesapeake Bay Seasonal Hypoxia, Stratification, and Nutrient Loading. Estuar. Coast. 34, 1293-1309. doi:10.1007/s12237-011-9413-7
Officer, C.B., 1979. Discussion of the behaviour of nonconservative dissolved constituents in estuaries. Estuar. Coast. Mar. Sci. 9, 91-94. doi:10.1016/0302-3524(79)90009-4
Officer, C.B., 1980. Box Models Revisited. In: Hamilton, P. and Macdonald, K.B. (Eds.), Estuarine and Wetland Processes: With Emphasis on Modeling. Springer US, Boston, MA, pp. 65-114.
Orr, J.C., Fabry, V.J., Aumont, O., Bopp, L., Doney, S.C., Feely, R.A., Gnanadesikan, A., Gruber, N., Ishida, A., Joos, F., Key, R.M., Lindsay, K., Maier-Reimer, E., Matear, R., Monfray, P., Mouchet, A., Najjar, R.G., Plattner, G.-K., Rodgers, K.B., Sabine, C.L., Sarmiento, J.L., Schlitzer, R., Slater, R.D., Totterdell, I.J., Weirig, M.-F., Yamanaka, Y. and Yool, A., 2005. Anthropogenic ocean

acidification over the twenty-first century and its impact on calcifying organisms. Nature 437, 681. doi:10.1038/nature04095
Orth, R.J. and Moore, K.A., 1983. Chesapeake Bay: An Unprecedented Decline in Submerged Aquatic Vegetation. Science 222, 51-53. doi:10.1126/science.222.4619.51
Orth, R.J. and Moore, K.A., 1984. Distribution and abundance of submerged aquatic vegetation in Chesapeake Bay: an historical perspective. Estuar. Coast. 7, 531-540. doi:10.2307/1352058
Orth, R.J., Batiuk, R.A., Bergstrom, P.W. and Moore, K.A., 2002. A perspective on two decades of policies and regulations influencing the protection and restoration of submerged aquatic vegetation in Chesapeake Bay, USA. Bull. Mar. Sci. 71, 1391-1403
Orth, R.J., Williams, M.R., Marion, S.R., Wilcox, D.J., Carruthers, T.J.B., Moore, K.A., Kemp, W.M., Dennison, W.C., Rybicki, N., Bergstrom, P. and Batiuk, R.A., 2010. Long-Term Trends in Submersed Aquatic Vegetation (SAV) in Chesapeake Bay, USA, Related to Water Quality. Estuar. Coast. 33, 1144-1163. doi:10.1007/s12237-010-9311-4
Orth, R.J., Dennison, W.C., Lefcheck, J.S., Gurbisz, C., Hannam, M., Keisman, J., Landry, J.B., Moore, K.A., Murphy, R.R. and Patrick, C.J., 2017. Submersed aquatic vegetation in Chesapeake Bay: sentinel species in a changing world. Bioscience 67, 698-712. doi:10.1093/biosci/bix058
Pai, S.C., Gong, G.C. and Liu, K.K., 1993. Determination of dissolved oxygen in seawater by direct spectrophotometry of total iodine. Mar. Chem. 41, 343-351. doi:10.1016/0304-4203(93)90266
Perry, C.T., Salter, M.A., Harborne, A.R., Crowley, S.F., Jelks, H.L. and Wilson, R.W., 2011. Fish as major carbonate mud producers and missing components of the tropical carbonate factory. Proc. Natl. Acad. Sci. U.S.A. 108, 3865-3869. doi:10.1073/pnas.1015895108
Rabalais, N.N., Díaz, R.J., Levin, L.A., Turner, R.E., Gilbert, D. and Zhang, J., 2010. Dynamics and distribution of natural and human-caused hypoxia. Biogeosciences 7, 585-619. doi:10.5194/bg-7-585-2010
Russ, E.R. and Palinkas, C.M., 2018. Seasonal-Scale and Decadal-Scale Sediment-Vegetation Interactions on the Subaqueous Susquehanna River Delta, Upper Chesapeake Bay. Estuar. Coast. 41, 2092-2104. doi:10.1007/s12237-018-0413-8
Schulte, D.M., 2017. History of the Virginia Oyster Fishery, Chesapeake Bay, USA. Front. Mar. Sci. 4. doi:10.3389/fmars.2017.00127
Semesi, I.S., Beer, S. and Björk, M., 2009. Seagrass photosynthesis controls rates of calcification and photosynthesis of calcareous macroalgae in a tropical seagrass meadow. Mar. Ecol. Prog. Ser. 382, 41-47. doi:10.3354/meps07973
Stainton, M.P., 1973. A Syringe Gas-Stripping Procedure for Gas-Chromatographic Determination of Dissolved Inorganic and Organic Carbon in Fresh Water and

Carbonates in Sediments. J. Fish. Res. Board Can 30, 1441-1445. doi:10.1139/f73-234
Sunda, W.G. and Cai, W.-J., 2012. Eutrophication Induced CO_2-Acidification of Subsurface Coastal Waters: Interactive Effects of Temperature, Salinity, and Atmospheric P_{CO2}. Environ. Sci. Technol. 46, 10651-10659. doi:10.1021/es300626f
Taylor, J.R., 1997. Introduction to error analysis, the Study of Uncertainties in Physical Measurements, 2nd Edition. University Science Books, New York.
Temmerman, S., Bouma, T.J., Govers, G. and Lauwaet, D., 2005. Flow paths of water and sediment in a tidal marsh: Relations with marsh developmental stage and tidal inundation height. Estuaries 28, 338-352. doi:10.1007/bf02693917
Valle-Levinson, A. and Lwiza, K.M.M., 1995. The effects of channels and shoals on exchange between the Chesapeake Bay and the adjacent ocean. J. Geophys. Res. Ocean 100, 18551-18563. doi:10.1029/95JC01936
Verdugo, P., Alldredge, A.L., Azam, F., Kirchman, D.L., Passow, U. and Santschi, P.H., 2004. The oceanic gel phase: a bridge in the DOM–POM continuum. Mar. Chem. 92, 67-85. doi:10.1016/j.marchem.2004.06.017
Waldbusser, G.G., Steenson, R.A. and Green, M.A., 2011a. Oyster Shell Dissolution Rates in Estuarine Waters: Effects of pH and Shell Legacy. J. Shellfish Res. 30, 659-669. doi:10.2983/035.030.0308
Waldbusser, G.G., Voigt, E.P., Bergschneider, H., Green, M.A. and Newell, R.I.E., 2011b. Biocalcification in the Eastern Oyster (Crassostrea virginica) in Relation to Long-term Trends in Chesapeake Bay pH. Estuar. Coast. 34, 221-231. doi:10.1007/s12237-010-9307-0
Waldbusser, G.G., Powell, E.N. and Mann, R., 2013. Ecosystem effects of shell aggregations and cycling in coastal waters: an example of Chesapeake Bay oyster reefs. Ecology 94, 895-903. doi:10.1890/12-1179.1
Wallace, R.B., Baumann, H., Grear, J.S., Aller, R.C. and Gobler, C.J., 2014. Coastal ocean acidification: The other eutrophication problem. Estuar. Coast. Shelf Sci. 148, 1-13. doi:10.1016/j.ecss.2014.05.027
Ward, L.G., Michael Kemp, W. and Boynton, W.R., 1984. The influence of waves and seagrass communities on suspended particulates in an estuarine embayment. Mar. Geol. 59, 85-103. doi:10.1016/0025-3227(84)90089-6
Ware, J.R., Smith, S.V. and Reaka-Kudla, M.L., 1992. Coral reefs: sources or sinks of atmospheric CO_2? Coral Reefs 11, 127-130. doi:10.1007/BF00255465
Wolf-Gladrow, D.A., Zeebe, R.E., Klaas, C., Körtzinger, A. and Dickson, A.G., 2007. Total alkalinity: The explicit conservative expression and its application to biogeochemical processes. Mar. Chem. 106, 287-300. doi:10.1016/j.marchem.2007.01.006
Xie, X., Li, M. and Ni, W., 2018. Roles of Wind-Driven Currents and Surface Waves in Sediment Resuspension and Transport During a Tropical Storm. J. Geophys. Res. Ocean 123, 8638-8654. doi:10.1029/2018JC014104

Xu, Y.-Y., Pierrot, D. and Cai, W.-J., 2017. Ocean carbonate system computation for anoxic waters using an updated CO2SYS program. Mar. Chem. doi:10.1016/j.marchem.2017.07.002

Yang, B., Byrne, R.H. and Lindemuth, M., 2015. Contributions of organic alkalinity to total alkalinity in coastal waters: A spectrophotometric approach. Mar. Chem. 176, 199-207. doi:10.1016/j.marchem.2015.09.008

Chapter 5

CONCLUSIONS

In recent decades two main consequences of eutrophication, coastal hypoxia and enhanced acidification, have become widespread environmental issues, threating a wide range of aquatic organisms and ecosystems in coastal regions heavily impacted by the anthropogenic activities. Understanding the drivers of coastal hypoxia and acidification, and the mechanisms of how coastal systems respond to anthropogenic stresses are thus very important for the regional management and policy-making in order to reverse these effects. The Pearl River Estuary (PRE) and the Chesapeake Bay (CB), two of the largest estuaries in the world, are facing similar environmental threats, i.e. eutrophication-induced hypoxia and enhanced acidification, though characterized by different duration, extent and severity. Generally, the differences derive from their distinct watershed/riverine input, hydrological mixing, physical forcing, and ecosystem metabolism. In this dissertation, I addressed the following scientific questions: What is the origin of the oxygen-consuming organic matter in these two large eutrophic estuaries, and what leads to the different source fractions? How $CaCO_3$ formation/dissolution interact with other biogeochemical processes (e.g., photosynthesis and respiration) to regulate the pH dynamics in the CB, which has recently shown signs of ecological recovery due to sustained management actions.

Our mapping survey in the lower PRE in July 2014 was disrupted by the passing of Typhoon Rammasun. Subsequent visits to the initial hypoxic stations following the storm revealed that the typhoon thoroughly mixed and oxygenated the water column, but stratification re-established rather quickly within one day after the dissipation of typhoon. One week later, significant oxygen depletion and nutrient increment were observed below the pycnocline, indicating a trend developing toward hypoxia. The spatial distributions of surface bloom and bottom hypoxia were re-distributed by the typhoon, with the coverage area of ~300 km^2 and thickness of 3-5 m in the bottom hypoxic zones. Based on a three end-member mixing model and the mass balance of DIC and its isotopic composition, we demonstrated that 1) aerobic respiration of organic matter is the most important biological process controlling dynamics of oxygen and DIC in the lower PRE, and 2) marine organic matter from eutrophication-induced primary production dominated oxygen consumption (65±16%) in the hypoxic zone; however, terrestrial organic matter also contributed significantly (35±16%) to the formation and maintenance of hypoxia in the lower PRE and adjacent coastal waters. Our study suggested that reducing and managing nutrient fluxes is critical to control eutrophication and, subsequently, to mitigate hypoxia.

We surveyed the carbonate system along the main channel of the Chesapeake Bay in June 2016 to elucidate the oxygen and carbonate dynamics and the associated sources of oxygen-consuming organic matter. Seasonal hypoxic zone existed below the pycnocline (~10 m) in the mid-bay, while a bloom zone was observed in the surface water immediately above the hypoxic zone. The DIC enrichment within the hypoxic zone was controlled by aerobic respiration in the water column (43%), sulfate reduction in the sediment (39%), atmospheric CO_2 invasion (13%), and $CaCO_3$ dissolution (5%). A mass balance of the DIC concentration and its stable isotopic composition suggested that the apparent $\delta^{13}C$ of oxygen-consuming organic matter was -19.4±0.3‰. The bulk composition of particulate organic matter also reflected a dominance of algal material (C/N = ~6, $\delta^{13}C$ > -25‰). Therefore, we concluded that the respiration of autochthonous organic matter (i.e. eutrophication-stimulated primary production) was the dominant process consuming oxygen, while allocthonous organic matter (terrestrial) made little contribution to oxygen consumption in the hypoxic zone in June 2016.

The difference of source partitioning of oxygen-consuming organic matter between the two systems is that terrestrial OM contributes significantly to the oxygen consumption in the PRE but not in the CB. This difference is a combined result of different hydrology, quantity and quality of Alloc-OC and Autoc-OC inputs, and physical setting. The CB has a smaller annual freshwater input (~ 1/5 of the PRE), and a larger estuarine water volume (~ 10 times of the PRE), resulting in a longer water residence time (months) than the PRE (days). In addition, the CB has much smaller annual sediment loads (~1/20 that of the PRE), most of which settles in the upper bay. Thus, in summer, when freshwater discharge reaches seasonal minima, little terrestrial OM reaches the mid- and lower bay, and Autoc-OC composes most of the OM pool in the CB. Note that the CB is generally more productive than the PRE (Officer et al., 1984; Rabouille et al., 2008). In contrast, the summer peak freshwater discharge in the PRE delivers more sediment loads to the shallow shelf region with minor degradative loss during the short transport period (Strong et al., 2012). Overall, there appears to be substantial amounts of bioavailable OM in both systems, but the OM is substantially influenced by Alloc-OC in the PRE, while Autoc-OC is far more important in the CB. Finally, the higher temperature of the hypoxic water in the PRE probably may favor higher rates of bacterial growth and OM degradation (Brown et al., 2004), allowing for potentially higher rates of terrestrial OM degradation within the hypoxic zone of the lower PRE. Clearly, the two large hypoxic zones in these estuarine systems have substantially different physical features and sources of OM input and lability, suggesting that future analyses are required to better understand the varied drivers of hypoxia across coastal systems worldwide.

A cruise was conducted along the bay channel in August 2016, at a time of peak hypoxia and anoxia and SAV biomass to examine the spatial and temporal patterns of $CaCO_3$ formation and dissolution. Using two endmember mixing models, we found Ca^{2+}, TA and DIC were largely removed at low salinity zone, but generally added in the mesohaline and polyhaline zones, which were inferred as results of photosynthesis-driven $CaCO_3$ formation within the SAV beds in the upper bay and acidification-driven $CaCO_3$ dissolution in the hypoxic/anoxic water in the mid- to lower bay. Three additional lines of evidence support that the large Ca^{2+} and TA removal near the freshwater zone is attributed to $CaCO_3$ formation within the Susquehanna Flats SAV bed, including 1) continuous monitoring sensor data showed very high DO saturation (DO%) and pH inside the SAV beds; 2) SEM images along with EDS data illustrated $CaCO_3$ precipitation with varying size and morphology on the leaf surface of SAV plants; and 3) the average percentage of $CaCO_3$ content in the SAV leaf samples was 25 times more than that in the surface sediment samples in the late summer. The $CaCO_3$ dissolution can nearly offset the pH decrease (~0.6 unit) caused by aerobic respiration, both of which are significantly larger than the pH drawdown (~0.1 unit) caused by fossil-CO_2 induced ocean acidification. Using an effective concentration method, we conclude that Chesapeake Bay is a weak TA sink, and has low levels of net accumulation of $CaCO_3$. Furthermore, we proposed a bay-wide self-regulated pH buffer mechanism via spatially-decoupled $CaCO_3$ formation and dissolution to resist coastal eutrophication and acidification in the Chesapeake Bay. In summer, strong photosynthesis of submerged aquatic vegetation (SAV) in the uppermost bay and alongshore shallow areas assimilates considerable nutrients, and generates super high pH and $CaCO_3$ saturation state environments, which facilitate abiotic and biotic $CaCO_3$ formation. These $CaCO_3$ solids are subsequently focused into the downstream corrosive subsurface waters, and dissolve to buffer pH decreases caused by aerobic respiration and anthropogenic CO_2, thus providing relatively stable pH conditions. Our results demonstrate that coastal ecosystems can further promote their own recovery in complex, sometimes unpredictable ways as humans decrease anthropogenic stressors by policy management. This positive feedback to coastal restoration can shed light on eutrophication and acidification studies in coastal systems emerging with recovery signs.

This dissertation includes three observation-based process studies focusing on the drivers and system response to the eutrophication-induced hypoxia/anoxia and enhanced acidification in the two large eutrophic estuaries, the Pearl River Estuary and the Chesapeake Bay. The PRE is characterized with short water residence time, large freshwater discharge and sediment loads, and increasing eutrophication intensity. In contrast, the CB represents estuaries with long water residence time, small freshwater discharge and sediment loads, and reducing nutrient loads. The endmember mixing models and mass balance method were applied to differentiate the controlling processes driving the system into hypoxic and acidified. We quantified the sources of oxygen-consuming organic matter in the hypoxic zones of two hydrologically different estuarine systems and discussed the causes for the different source partitioning results. By using calcium and carbonate chemistry data, geochemical model analysis, and mineralogical analysis, we for the first time reveal a bay-wide self-regulated pH buffer mechanism via spatially-decoupled $CaCO_3$ formation and dissolution to resist coastal eutrophication and acidification in the Chesapeake Bay. This work represents a good practice of studying the widely concerned issues, eutrophication-hypoxia-acidification, in different estuarine systems, and will benefit future researches under the context of global warming and climate change.

However, several scientific questions related with our work remain to be explored in the future. For example, 1) how to better define the riverine endmember value. The R^2 values of regressions between chemical concentration and Log discharge in main tributaries of the CB are usually < 0.6, indicating that riverine concentration cannot be fully explained by discharge, and other factors (e.g., chemical weathering of carbonate or silicate minerals, soil erosion, or land use change in the watershed) may play an important role in controlling the riverine concentration. In addition, the temporal variations in river endmember can also result in bends in mixing curves, which are commonly used to interpret non-conservative processes in estuarine systems (Loder and Reichard, 1981). Moreover, the bay water residence time and time scales of regional mixing would further complicate the choice of time span of river input. 2) Although our work has shown the dynamics of Ca^{2+} and TA mostly driven by $CaCO_3$ formation and dissolution along the salinity gradient in the main channel, specific measurements on calcification rates of SAV, mollusks, crustaceans, and foraminifera in the shallow waters and $CaCO_3$ dissolution rates in the mid-bay subsurface water remain to be undertaken. These work will deepen our understanding of the spatially-decoupled $CaCO_3$ production and consumption in the Chesapeake Bay. 3) Despite of the biogenic calcification by mollusks, crustaceans, and foraminifera and abiotic precipitation on the SAV leaf surface, whether the SAV plant itself can produce $CaCO_3$ within the cell walls and whether it is species-specific remain unknown. And 4) transport mechanisms of $CaCO_3$ solids from the shallow waters (e.g., SAV beds and oyster reefs) to the corrosive hypoxic/anoxic waters, including longitudinal and lateral transport.

REFERENCES

Brown, J.H., Gillooly, J.F., Allen, A.P., Savage, V.M. and West, G.B., 2004. Toward a metabolic theory of ecology. Ecology 85, 1771-1789. doi:10.1890/03-9000

Loder, T.C. and Reichard, R.P., 1981. The Dynamics of Conservative Mixing in Estuaries. Estuaries 4, 64-69. doi:10.2307/1351543

Officer, C.B., Biggs, R.B., Taft, J.L., Cronin, L.E., Tyler, M.A. and Boynton, W.R., 1984. Chesapeake Bay anoxia: origin, development, and significance. Science 223. doi:10.1126/science.223.4631.22

Rabouille, C., Conley, D.J., Dai, M.H., Cai, W.J., Chen, C.T.A., Lansard, B., Green, R., Yin, K., Harrison, P.J., Dagg, M. and McKee, B., 2008. Comparison of hypoxia among four river-dominated ocean margins: The Changjiang (Yangtze), Mississippi, Pearl, and Rhône rivers. Cont. Shelf Res. 28, 1527-1537. doi:10.1016/j.csr.2008.01.020

Strong, D.J., Flecker, R., Valdes, P.J., Wilkinson, I.P., Rees, J.G., Zong, Y.Q., Lloyd, J.M., Garrett, E. and Pancost, R.D., 2012. Organic matter distribution in the modern sediments of the Pearl River Estuary. Org. Geochem. 49, 68-82. doi:10.1016/j.orggeochem.2012.04.011

Appendix A

SIMULTANEOUS DETERMINATION OF DISSOLVED INORGANIC CARBON (DIC) CONCENTRATION AND STABLE ISOTOPE (δ^{13}C-DIC) BY CAVITY RING-DOWN SPECTROSCOPY: APPLICATION TO STUDY CARBONATE DYNAMICS IN THE CHESAPEAKE BAY[4]

Abstract

Dissolved inorganic carbon (DIC) and its stable isotope (δ^{13}C-DIC) are powerful tools for exploring aquatic biogeochemistry and the carbon cycle. Traditionally, they are determined separately with a DIC analyzer and an isotope ratio mass spectrometer. We present an approach that uses a whole-water CO_2 extraction device coupled to a Cavity Ring-Down Spectroscopy (CRDS) CO_2 and isotopic analyzer to measure DIC and δ^{13}C-DIC simultaneously in a 3-4 mL sample over an ~11 min interval, with an average precision of 1.5±0.6 μmol kg^{-1} for DIC and 0.09±0.05 ‰ for δ^{13}C-DIC. The system was tested on samples collected from a Chesapeake Bay cruise in May 2016, achieving a precision of 0.7±0.5 μmol kg^{-1} for DIC and 0.05±0.02 ‰ for δ^{13}C-DIC. Using the simultaneously measured DIC and δ^{13}C-DIC data, the biogeochemical controls on DIC and its isotope composition in the bay during spring are discussed. In the northern upper bay, the main controlling

---

[4] Su, J., Cai, W.-J., Hussain, N., Brodeur, J., Chen, B. and Huang, K., 2019. Simultaneous determination of dissolved inorganic carbon (DIC) concentration and stable isotope (δ^{13}C-DIC) by Cavity Ring-Down Spectroscopy: Application to study carbonate dynamics in the Chesapeake Bay. Mar. Chem., 103689. doi:10.1016/j.marchem.2019.103689

processes were CO_2 outgassing and carbonate precipitation, whereas primary production (surface) and degradation of organic carbon (subsurface) dominated in the southern upper bay and middle bay. By improving the mode of sample introduction, the system could be automated to measure multiple samples. This would give the system the potential to provide continuous shipboard measurements during field surveys, making this method more powerful for exploring the complicated carbonate system across a wide range of aquatic settings.

Introduction

Dissolved inorganic carbon (DIC) is the sum of all dissolved forms of inorganic carbon including aqueous carbon dioxide (CO_{2aq}), carbonic acid (H_2CO_3), bicarbonate (HCO_3^-) and carbonate (CO_3^{2-}), and it is the major pool of carbon in most natural waters (Zeebe and Wolf-Gladrow, 2001; Bianchi, 2011). Its stable isotope abundance is expressed as per mil deviations from the reference standard Vienna-PeeDee Belemnite (V-PDB) and denoted as $\delta^{13}C$ in ‰:

$$\delta^{13}\mathrm{C} = \left(\frac{(^{13}C/^{12}C)_{sample}}{(^{13}C/^{12}C)_{V-PDB}} - 1\right) \times 1000$$

Both DIC and $\delta^{13}C$-DIC are influenced by multiple physical and biogeochemical processes, such as mixing between river water and seawater, biological production, degradation of organic matter, formation or dissolution of calcium carbonate ($CaCO_3$), and air-sea CO_2 exchange (Samanta et al., 2015). The deviations of DIC and $\delta^{13}C$-DIC from conservative mixing can be regarded as fingerprints left by different biogeochemical processes. Therefore, together with other parameters such as salinity, nutrient concentrations and total alkalinity, DIC and $\delta^{13}C$-DIC can be used as powerful tools in studies seeking to understand the sources and cycling processes of carbon in estuarine and coastal environments (Hellings et al., 1999; Hu et al., 2016; Wang et al., 2016; Su et al., 2017; Yang et al., 2018).

In estuarine and coastal research, discrete samples are typically taken to determine DIC and $\delta^{13}C$-DIC separately. DIC can be measured through CO_2 extraction followed by different detection methodologies to quantify the released CO_2, including coulometry (Dickson et al., 2007; Amornthammarong et al., 2014), spectrophotometry (Wang et al., 2007), mass spectrometry (Cardenas-Valencia et al., 2013), isotope dilution (Huang et al., 2013; Huang et al., 2015), and non-dispersive infrared absorption (NDIR) (O'Sullivan and Millero, 1998). The NDIR method has a precision of 0.1 % or ±2 μmol kg^{-1} for seawater analysis (Friederich et al., 2002; Huang et al., 2012), and it is used in the method comparison performed in this analysis.

$\delta^{13}C$-DIC is conventionally measured by isotope ratio mass spectrometry (IRMS) with precision better than 0.1 ‰ (Humphreys et al., 2015). So far, several optical spectroscopy techniques have been developed in order to overcome the expense and laboriousness of IRMS measurement, such as tunable diode laser absorption spectroscopy (TDLAS) (Bergamaschi et al., 1994), NDIR (Jäger et al., 2005), Fourier transform infrared spectroscopy (FTIR) (Mohn et al., 2007), and cavity enhanced or cavity ring-down methods (Jost et al., 2006; Wahl et al., 2006). Several attempts have been made to determine DIC and $\delta^{13}C$-DIC simultaneously by Cavity Ring-Down Spectrometer (CRDS). For instance, Bass et al. (2012) used an acidification interface to extract CO_2 from a 350 mL sample in a chamber through ePTFE tubing, and determined the $\delta^{13}C$ of the circulated CO_2 between the CRDS and the chamber at a 15 min interval, with a precision of ±10 μmol kg^{-1} for DIC and ±0.2

‰ for δ^{13}C-DIC. However, this method requires a large sample volume, and the measurement uncertainty of DIC is larger than the accepted practice of ±2 μmol kg^{-1}. Call et al. (2017) coupled two commercial instruments, an Autonomous Infra-Red Inorganic Carbon Analyser (AIRICA) and a CRDS, to measure DIC and δ^{13}C-DIC in sequence over a 16 min cycle on a sample volume of 2 mL. They achieved a precision of 1.5-2 μmol kg^{-1} for DIC by AIRICA and 0.14±0.04 ‰ for δ^{13}C-DIC by CRDS at DIC > 1000 μmol kg^{-1}. Although their study reduced the required sample volume to several milliliters without compromising isotope precision, they had to utilize two analyzers (one NDIR and one CRDS) separately rather than a single CRDS to determine both the DIC concentration and the isotope value. No information about CRDS performance for DIC measurement was provided in their paper. Huang et al. (2013, 2015) used isotope dilution methods to examine the capability of CRDS for DIC analysis and achieved a high precision of <0.02 % in the laboratory and <0.03 % in the field survey. While highly precise, this method uses two CRDS detectors (one for δ^{13}C and one for δD and δ^{18}O as a flow tracer) and therefore is expensive and not easy to set up for many users. The motivation of this study is to achieve simultaneous determination of DIC and δ^{13}C-DIC with one CRDS detector and a small sample volume to achieve high precision comparable with the traditional methods based on NDIR and IRMS.

In our approach, a CO_2 extraction device and CRDS detector were coupled to simultaneously measure DIC and δ^{13}C in a 3-4 mL sample over an ~11 min interval, with average precision of 1.5±0.6 μmol kg^{-1} for DIC and 0.09±0.05 ‰ for δ^{13}C-DIC. Note that the average precision is calculated as the mean of uncertainties for each set of triplicate measurements. Intercomparisons with conventional NDIR and

IRMS methods were performed to assess the precision and accuracy, injection volume effect, instrument stability, and differences among three calibration methods. Furthermore, the efficacy of this approach was examined by measuring samples collected from a Chesapeake Bay cruise in May 2016, which resulted in a precision of 0.7±0.5 μmol kg^{-1} for DIC and 0.05±0.02 ‰ for δ^{13}C-DIC. Finally, we analyzed the field dataset and provided interpretations for the deviations of DIC and δ^{13}C-DIC relative to conservative mixing, which provides an example of applying this technique to distinguish the main biogeochemical processes controlling DIC and its isotope composition in estuarine and coastal ocean research.

Materials and procedures

Instrumentation principles

This system is essentially composed of a whole-water CO_2 extraction device and a CRDS isotopic analyzer (G2131-i, Picarro, www.picarro.com) (Fig. A.1). The CO_2 extraction device consists of a digital syringe pump (5.0 mL, Kloehn) for transferring accurate amounts of reagent and sample, a highly efficient gas stripping reactor, and a mass-flow-controller (Model #GFC17, Aalborg) to control the carrier gas flow precisely. This device also uses a Nafion tube to reduce the water vapor. A pump with 4-port valve was used for single-sample analysis in the present study, however recently the device has been upgraded with a 12-port valve designing for multi-sample analysis and become commercially available (AS-D1, Apollo Scitech, www.apolloscitech.com). The isotopic analyzer is based on a CRDS technique. A gas sample is introduced into a high-finesse optical cavity and the unique infrared absorption spectrums of trace gas species are determined, thus providing the concentration or isotopic ratio measurements of a particular gas species of interest, such as CO_2, H_2O and CH_4 (Crosson, 2008). More detailed principles and the performance evaluation of the CRDS instruments can be found elsewhere (Friedrichs et al., 2010; Nara et al., 2012). A single software routine is written for both units to operate CO_2 extraction procedures, read data and calculate results. For each measurement, an aliquot of sample is acidified in the gas stripper, CO_2 is extracted by the carrier gas, and the gas stream flows through a moisture condenser before measurement by CRDS. The software mentioned above can also acquire raw data from CRDS, integrate the CO_2 mixing ratio signal (Eq. (1)), and average the $\delta^{13}C$-CO_2 values (Eq. (2)). CO_2-free compressed air (UN1002, Keen Compressed Gas Co.) was used as a carrier gas to avoid the gas matrix effects on CO_2 and $\delta^{13}C$-CO_2, as demonstrated by Friedrichs et al. (2010). A vent is used to avoid pressure build-up at the inlet of the CRDS.

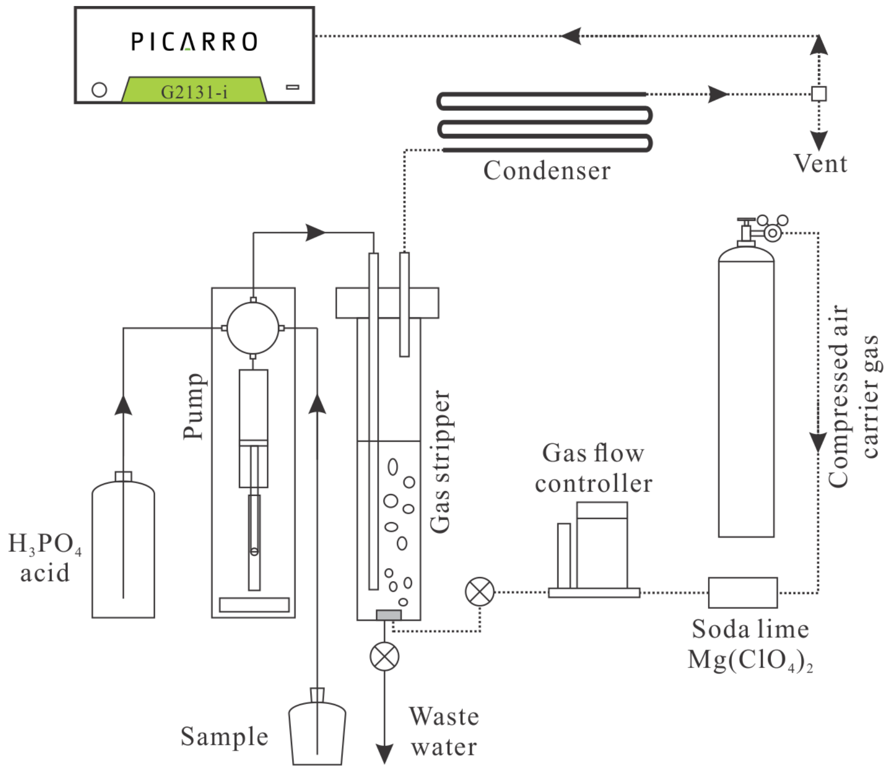

Figure A.1: A simplified schematic setup of the coupled CO_2 extraction device and Cavity Ring-Down Spectrometer (CRDS) to simultaneously measure DIC and $\delta^{13}C$-DIC. Note that the solid arrows mean liquid flow, while the dashed arrows mean gas flow. A photograph of the system can be found at the manufacturer's webpage (www.apolloscitech.com).

Procedure

The analytical procedure consists of the following steps:

Step 1: Establish baseline. At the beginning, CO_2-free carrier gas flows through the gas stripper and lowers the CO_2 value of the CRDS measurement down to 1-2 ppm.

Step 2: CO_2 stripping. The syringe pump first draws 1.5 mL phosphoric acid (5 % (vol./vol.) H_3PO_4 with 10 % (wt./vol.) NaCl), and injects 0.6 mL into the reactor for gas stripping to get rid of the contaminant CO_2. Then, the pump draws a 3.8 mL sample on top of the remaining 0.9 mL acid in the syringe, and finally injects all liquid into the reactor for gas stripping, where dispensed carrier gas continues moving upward from the bottom to the top of the reactor (Fig. A.1). DIC is thoroughly converted to CO_2, which is extracted by the carrier gas and flows through a condenser to reduce water vapor before measurement by CRDS.

Step 3: CO_2 detection. The CO_2 gas flows through the cavity and is detected by CRDS. Meanwhile, the raw data for CO_2 ($^{12}CO_2$+$^{13}CO_2$) and $\delta^{13}C$-CO_2 are read from CRDS and are recorded at ~ 1 HZ frequency for a period of ~350 s. When the change of CO_2 measurements drops below a preset threshold (i.e., standard deviation of CO_2 for 15 consecutive data points is less than 0.15 ppm), the software will terminate the analysis, because there is only a small amount of CO_2 left in the reactor and further gas stripping would change the area integration value of CO_2 very slowly. Terminating the analysis at this point results in an uncertainty of duplicate analysis less than 0.1 %.

Step 4: Discharge. After measurement termination, the acidified sample is discharged and the system is flushed by CO_2-free carrier gas to return to near-blank condition. Then, the system is ready to run the next measurement cycle. The average time for each cycle is ~ 11 min.

Determination of DIC and δ^{13}C-DIC

Following the Apollo Scitech DIC analysis method, the software has a function to integrate the area under the CO_2 curve minus the area under a baseline to measure the concentration of DIC. A typical output from CRDS is shown in Fig. A.2, in which CO_2 is stable and low (< 2 ppm) for the first 50 s, then sharply increases to a peak value, and decreases to a low value (< 10 ppm) again. The start and end points for DIC integration are set to values where standard deviation of CO_2 for 15 consecutive data points is less than 0.15 ppm. The start and end points and their corresponding CO_2 values are used to derive a baseline in order to eliminate the background effect on area integration. The net area is integrated by the equation:

$$\text{Net Area} = \sum(CO_{2i}^{meas} - CO_{2i}^{base}) \times \Delta T_i \qquad (1)$$

where CO_{2i}^{meas} represents the measured CO_2 value from CRDS at the *i*th measurement interval, CO_{2i}^{base} represents the baseline value of CO_2 on the solid line in Fig. A.2 at the same interval, and ΔT_i is the time between the two consecutive intervals i+1 and i.

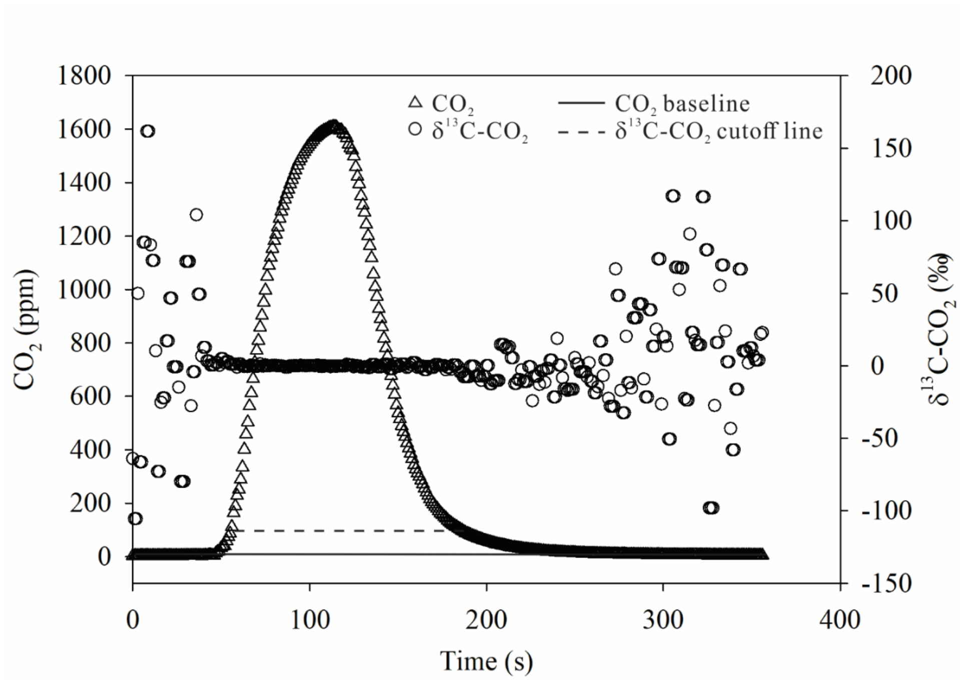

Figure A.2: Typical output from the CRDS showing data collected for one measurement for CO_2 (triangles) and $\delta^{13}C$-CO_2 (circles). Net integration area for DIC is obtained by integrating the area under the curve marked with triangles over the solid baseline. The $\delta^{13}C$-DIC is derived from the integrated area above the dashed line and beneath the triangle curve and the corresponding $\delta^{13}C$-CO_2 values.

Meanwhile, the $\delta^{13}C$-CO_2 signal is noisy and randomly distributed when CO_2 is low (e.g., when CO_2 <100 ppm, standard deviation of $\delta^{13}C$-CO_2 is ±42.1 ‰), but becomes relatively stable when CO_2 is high (e.g. when CO_2 >100 (380) ppm, standard deviation of $\delta^{13}C$-CO_2 is ±0.99 (0.70) ‰). The manufacturer states that CRDS has a precision of 0.05 % for CO_2 and 0.12 ‰ for $\delta^{13}C$-CO_2 when the CO_2 concentration ranges from 380 to 2000 ppm, but the measurement uncertainty becomes larger as CO_2 decreases to less than 380 ppm. Thus, a cutoff value of CO_2 was set in order to decrease the influence of the less accurate isotope data points at low CO_2. Above the CO_2 cutoff value, $\delta^{13}C$-CO_2 is relatively stable and suitable for averaging isotope data. The integrated net area above the cutoff line is used as a weight for isotope averaging. The $\delta^{13}C$-DIC is thus derived from the following equation:

$$\delta^{13}C\text{-}DIC = \frac{\sum (CO_{2j}^{meas} - CO_2^{cutoff}) \times \Delta T_j \times \delta^{13}C\text{-}CO_{2j}}{\sum (CO_{2j}^{meas} - CO_2^{cutoff}) \times \Delta T_j} \quad (2)$$

where CO_2^{cutoff} represents the cutoff value of CO_2, CO_{2j}^{meas} is the measured CO_2 value at *j*th measurement interval, and $\delta^{13}C\text{-}CO_{2j}$ is the measured $\delta^{13}C$-CO_2 value from CRDS at the same interval. Since the purpose of using a cutoff value is to define a period when $\delta^{13}C$-CO_2 is relatively stable, the lower end (i.e., 380 ppm) of the suitable range recommended by the manufacturer (380-2000 ppm) is ideally suitable for the cutoff value. But in our case the cutoff value was arbitrarily set to 100 ppm, because the final results of $\delta^{13}C$-DIC from one measurement were not significantly different (e.g., -0.16, -0.15, -0.16, -0.15, -0.15 and -0.16 ‰, respectively) when using different cutoff values of 100, 150, 200, 250, 300 and 380 ppm. This is largely because the detected CO_2 quickly increases beyond 380 ppm, so that the amount of data between 100 and 380 ppm is small relative to the total, which therefore has almost no influence on the final results of $\delta^{13}C$-DIC. Adopting a low cutoff value of 100 ppm may have the advantage of allowing the method to be applicable to low DIC freshwater samples though further evaluation is needed.

Evaluation of system performance

As shown in Fig. A.3, three sets of standards were employed for concentration and isotope calibrations. The DIC standard is the Dickson certified reference material (CRM; Batch 172, DIC = 2038.99 μmol kg^{-1}, Salinity = 33.450 psu) run at three different volumes (e.g., 2.0, 2.6 and 3.3 mL) to bracket the net area of unknown samples for calibration of DIC concentration. Since the curve integration approach measures the total amount of released CO_2, this approach uses three volumes of one CRM to create a three-point standard curve. This is the principle used in all Apollo Scitech DIC analyzers and its validity has been confirmed in our work by comparison using three concentrations at a single volume (e.g., 3.3 mL).

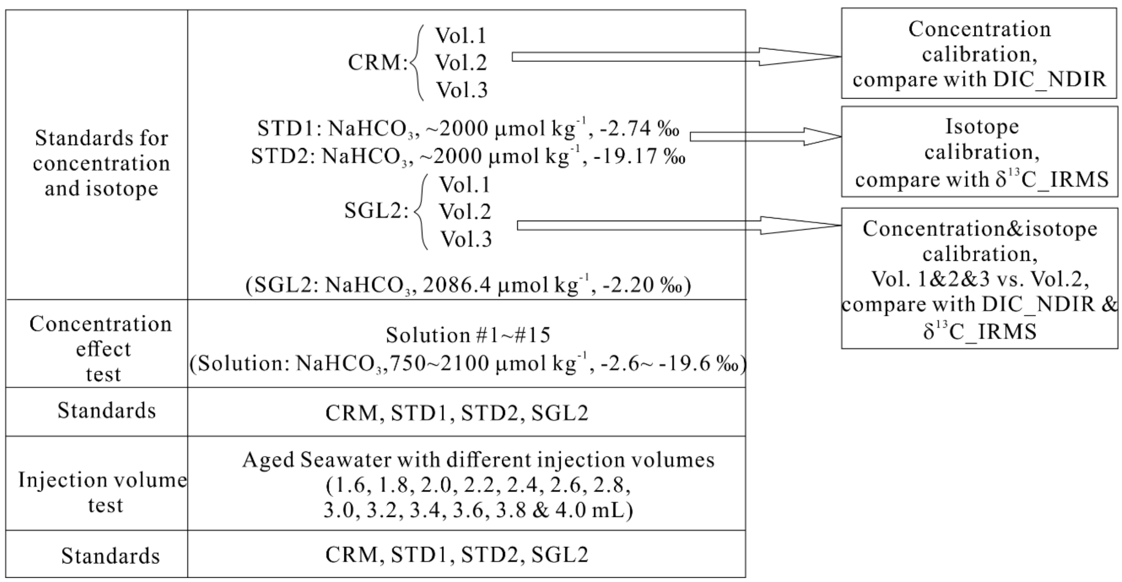

Figure A.3: Schematic showing evaluation of system performance.

The isotope standards include an isotopically heavy standard STD1 (-2.74±0.10 ‰) and a depleted standard STD2 (-19.17±0.10 ‰), which were made by dissolving $NaHCO_3$ solids (LC229431, LabChem for STD1; S-233, Fisher Scientific for STD2) in ultra-pure water (Milli-Q), and were verified by IRMS in the stable isotope facility, University of California, Davis. The third standard SGL2 was also made by dissolving $NaHCO_3$ solids in ultra-pure water (Milli-Q) but bubbling with air overnight, which was then verified by NDIR for DIC concentration (2086.4 μmol kg^{-1}) and by IRMS for $\delta^{13}C$-DIC (-2.20±0.10 ‰). SGL2 was measured using three different volumes for calibrations of both concentration and isotope. A series of prepared solutions with distinct DIC and $\delta^{13}C$-DIC values was made by diluting mixtures of two kinds of concentrated $NaHCO_3$ solutions, which have the same DIC concentration but different $\delta^{13}C$-DIC values. The prepared solutions have DIC ranging from ~750 to ~2100 μmol kg^{-1}, and $\delta^{13}C$-DIC ranging from -2.4 to -19.4 ‰. In addition, 4 L aged seawater (DIC = 2181.7 μmol kg^{-1}, $\delta^{13}C$ = -2.0 ‰) from the Gulf of Mexico (GOM) was stored in a gas-tight aluminum bag for examining the repeatability and long-term stability of the instrument.

The three sets of standards were measured before and after each batch of samples, which included prepared solutions and aged GOM seawater. Precision was evaluated based on the standard deviations of at least three replicate determinations for each sample. Accuracy was examined by comparing the DIC values between NDIR and CRDS methods, and the $\delta^{13}C$-DIC values between IRMS and CRDS methods using the prepared solutions, aged GOM seawater and CRM. To test the instrument's stability, the results calibrated by each day's working curves were compared with the first day's working curve over a period of 83 h. Also, the effect of injection volume on DIC and $\delta^{13}C$-DIC was evaluated by running GOM seawater in 13 different injection volumes. Three calibration methods were examined to correct the raw data from prepared solutions and aged GOM seawater, including i) using CRM in three different volumes to calibrate DIC, and using two isotopic standards STD1 and STD2 to calibrate $\delta^{13}C$-DIC; ii) using SLG2 in three different volumes to calibrate both DIC and $\delta^{13}C$-DIC (i.e., three-point calibration for DIC and single-point calibration for

δ^{13}C-DIC); and iii) using SLG2 in a middle volume to calibrate both DIC and δ^{13}C-DIC (i.e., single-point calibration for both DIC and δ^{13}C-DIC).

Field work in the Chesapeake Bay

The Chesapeake Bay is the largest estuary in the United States. The Bay is about 300 km long, with a relatively deep (20 to 30 m) but narrow (1 to 4 km) central channel confined by a sill in its lower bay (Kemp et al., 2005). Broad shallow areas flank the central channel throughout the bay (Boicourt et al., 1999). A three-day cruise was conducted in early May, 2016 to test the performance of the system (Fig. A.4). On 4-5 May 2016, we cruised from the upper bay (CB2.1) southwards to the middle bay (CB4.4). On 6 May, we started sampling at CB5.5 in the lower bay, and went northward to CB5.1. Waters were pumped up to the deck for sampling from 3-5 depths at each station. Salinities were measured in discrete samples using a Cole-Parmer® salinity meter (±0.1 psu). The deionized water and the Dickson CRM were used to calibrate salinity. A water sample was preserved in a 250 mL borosilicate glass bottle with 50 μL saturated $HgCl_2$ solution for DIC and δ^{13}C-DIC analysis (Huang et al., 2012). About 4-5 mL sample was first analyzed for DIC concentration using an AS-C3 DIC analyzer (Apollo Scitech), which uses an NDIR-based detector (LI-7000, Li-Cor) (Huang et al., 2012). In the NDIR-based analysis, 3-volume standardization (that is using 0.5, 0.7 and 0.9 mL of CRM Batch 150) was performed twice daily, one in the early morning and one in the late afternoon with one single CRM volume (0.7 mL) inserted in the mid-day as unknown to check the instrument stability. An analytical precision better than ±0.1 % was achieved each day.

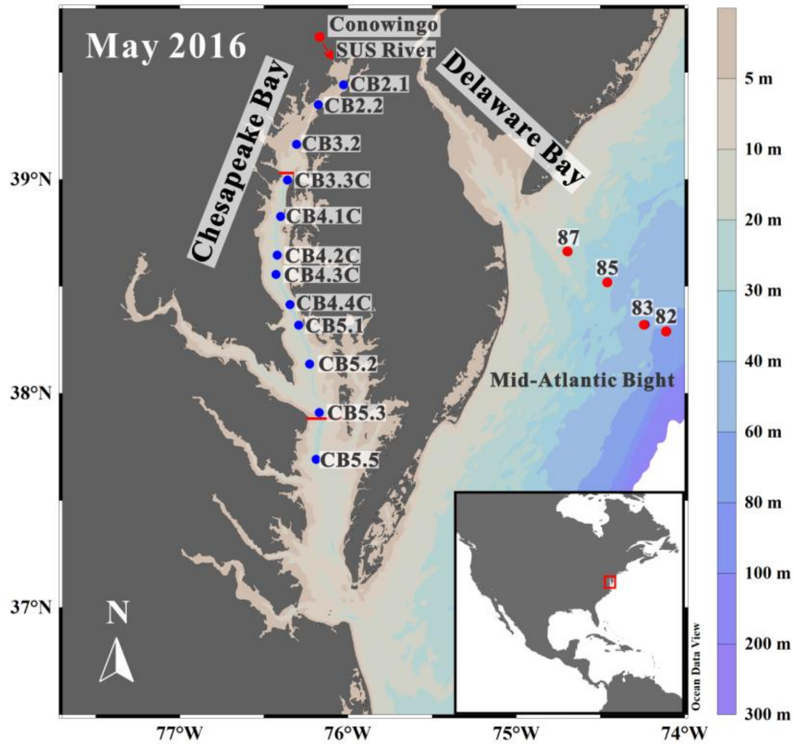

Figure A.4: Sampling stations (blue) in the Chesapeake Bay in May 2016. Red circles represent the river endmember at Conowingo in the Susquehanna River, and offshore seawater endmember at four stations in the Mid-Atlantic Bight. The arrow points to the outlet of the Susquehanna River. The red lines divide the main channel into three sub-regions, i.e., upper bay (39.0-39.5°N), middle bay (37.9-39.0°N) and lower bay (37.0-37.9°N). The inserted regional map indicates the location of the Chesapeake Bay.

The remaining sample was measured by CRDS for both DIC and δ^{13}C-DIC within 3 weeks. Since the analysis of field samples were performed before we thoroughly evaluated the different calibration methods, only a CRM (Batch 150, DIC = 2017.88 μmol kg^{-1}, Salinity = 33.343 psu) and a $NaHCO_3$ solution with known δ^{13}C-DIC (-1.95±0.02 ‰, n=3) were used as standards for calibrations of DIC concentration and isotope, respectively. The injection volumes for all standards and samples were set as 3.8 mL. Single-point calibrations were applied to both DIC and δ^{13}C-DIC of the field samples. Before isotopic analysis, the samples were stored in a cold room.

Results and discussion

Assessment of precision and accuracy

For the prepared solutions and aged GOM seawater measurement (n=87), the overall analytical uncertainty of DIC was 1.5±0.6 μmol kg^{-1} and of δ^{13}C-DIC was 0.09±0.05 ‰. The uncertainty in δ^{13}C-DIC did not increase when DIC decreased from ~2200 to ~750 μmol kg^{-1}. This is consistent with Bass et al. (2012), in which the standard deviation of δ^{13}C-DIC kept at < 0.2 ‰ at DIC above 360 μmol kg^{-1}.

The accuracy of DIC and δ^{13}C-DIC analysis was examined through direct comparison of CRDS with NDIR and IRMS measurements on the prepared solutions, aged GOM seawater and CRM (Fig. A.5). The average offset in measured DIC and δ^{13}C-DIC between methods (i.e., DIC_CRDS - DIC_NDIR, and δ^{13}C-DIC_CRDS - δ^{13}C-DIC_IRMS) was -0.7±3.1 μmol kg^{-1}, which is close to the uncertainty of the NDIR-based DIC measurement (0.1 % or ±2 μmol kg^{-1}), and 0.13±0.12 ‰, which is close to the accuracy of the IRMS measurement on δ^{13}C-DIC (0.1 ‰).

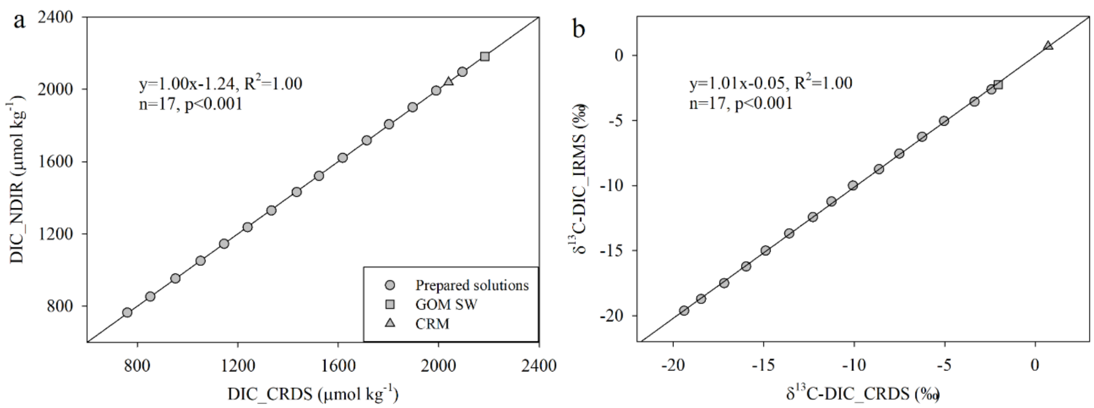

Figure A.5: Intercomparison of DIC between CRDS and NDIR (a), and δ^{13}C-DIC between CRDS and IRMS (b). Slope of ~1.00 shows excellent agreement not only between two different methodologies, but also laboratories.

The assessment of precision and accuracy is consistent with a recently published paper on a worldwide seawater δ^{13}C-DIC intercomparison exercise (Cheng et al., 2019). Identical replicate samples (CRM Batch 157 and deep ocean seawater) were sent to 16 laboratories for analysis using methods of IRMS (14 groups), CRDS (1 group), and both IRMS and Isotope Ratio Infrared Spectrometer (IRIS) (1 group). Among the 16 laboratories, Lab #9 utilized a similar apparatus (Apollo Scitech AS-D3 DIC analyzer and Picarro G2201-i CRDS detector). This work achieves a within-lab precision of ±0.12 ‰, and their average (uncorrected) deep ocean seawater results are within 0.01‰ relative to the all-lab average that was determined largely using IRMS (Cheng et al., 2019). Therefore, the system used in the present study can simultaneously determine DIC and δ^{13}C-DIC, achieving good precision and accuracy comparable to the established analysis methods for typical coastal and oceanic waters. When compared with the prevalent IRMS isotope measurements, this system has an additional advantage of getting precise DIC analysis, because the traditional IRMS method does not provide precise determination of DIC concentration as illustrated in an earlier interlaboratory comparison study (van Geldern et al., 2013).

Effect of Injection volumes on DIC and δ^{13}C-DIC

The sample injection volume can be adjusted in the software for different types of sampling sources, e.g., using a smaller injection volume for a high DIC sediment porewater sample, and using a larger injection volume for a low DIC river water sample. Therefore, a known aged GOM seawater sample (DIC_NDIR= 2181.7±2.6 μmol kg^{-1} and δ^{13}C-DIC_IRMS= -2.24±0.10 ‰) was run in a series of injection volumes to see if changes to the injection volume could affect the measurements of DIC and δ^{13}C-DIC using the CRDS system (Fig. A.3 and A.6). As shown in Fig. A.6, the average DIC_CRDS value of aged GOM seawater with different injection volumes was 2180.7±2.0 μmol kg^{-1}, which is close to the DIC_NDIR value of 2181.7±2.6 μmol kg^{-1}. This suggests that injection volume has virtually no effect on DIC in CRDS analysis. By contrast, δ^{13}C-DIC_CRDS was stable (-2.04±0.06 ‰) with larger injection volumes (2.4 to 4.0 mL), but became a little heavier (-1.84±0.08 ‰) when the injection volume was less than 2.4 mL. This may be related to the fact that when the cutoff value was fixed at 100 ppm CO_2, the smaller injection volume (< 2.4 mL) would produce a lower CO_2 peak and a smaller data pool of δ^{13}C-CO_2 above 100 ppm. Thus, the weight of the less accurate and heavier δ^{13}C-CO_2 (at 100-380 ppm CO_2 interval) may slightly increase and make the final δ^{13}C-DIC a little heavier (Eq. (2)). Although a larger injection volume may increase the analysis duration for each run, it can help to maintain a better repeatability of δ^{13}C-DIC. Note that the injection volumes for the assessment of precision and accuracy (Section 3.1) are larger than 2.4 mL. Also the overall δ^{13}C-DIC_CRDS of GOM seawater is about

0.2 ‰ heavier than the IRMS verified value (-2.24±0.10 ‰) (Fig. A.6), which may be caused by the invasion of isotopically lighter atmospheric CO_2 to the IRMS samples during the transfer of GOM seawater from the air-tight aluminum bag into 250 mL borosilicate glass bottles (Call et al., 2017).

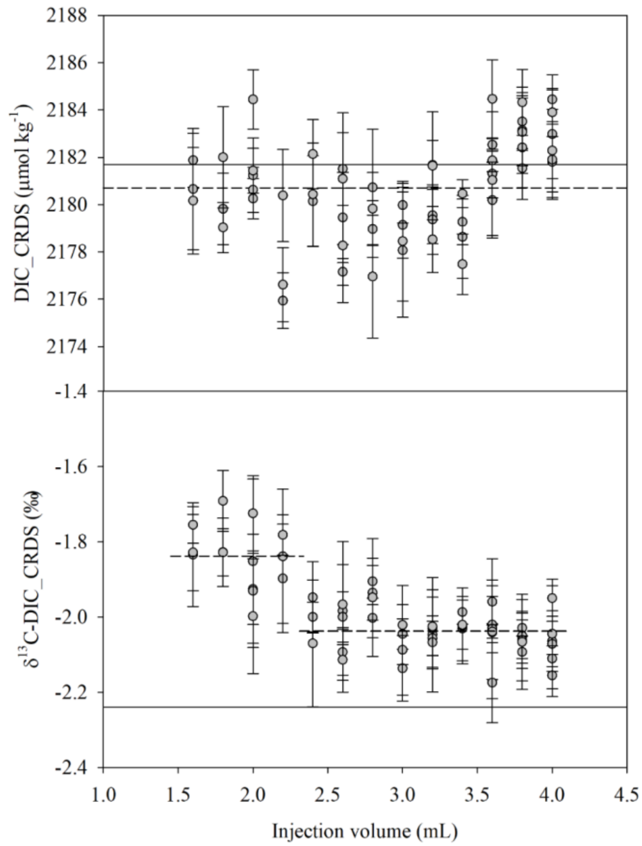

Figure A.6: The measured DIC and δ^{13}C-DIC of aged Gulf of Mexico seawater with different injection volumes. In the upper panel, the dashed line represents the average of measured DIC values from CRDS, while the solid reference line indicates the average DIC value from NDIR. In the lower panel, the dashed lines show the average δ^{13}C-DIC values from CRDS in two separate injection volume ranges. The solid reference line indicates the δ^{13}C-DIC value certified by IRMS.

Instrument stability

Standard materials were measured in three rounds during an 83-hour determination of prepared solutions and GOM seawater. The instrument stability was examined by using the DIC offset of GOM seawater between the calibration that used the first day's working curve (May 22) and the calibration that used each day's working curves (May 22-24) (Fig. A.7). The average offset value is 1.3±0.7 μmol kg^{-1}, which is within the measurement uncertainty, meaning there was almost no instrument drift for DIC. Meanwhile, the standard deviations of raw δ^{13}C-DIC for STD1 (0.08 ‰, n=9), STD2 (0.08 ‰, n=9) and aged GOM seawater with injection volume >2.4 mL (0.06 ‰, n=55) were within the measurement uncertainty, indicating there was also no significant drift for the isotope measurement. High instrument stability shows the potential for autonomous and long-term measurement of DIC and δ^{13}C-DIC with infrequent calibrations in field surveys at sea.

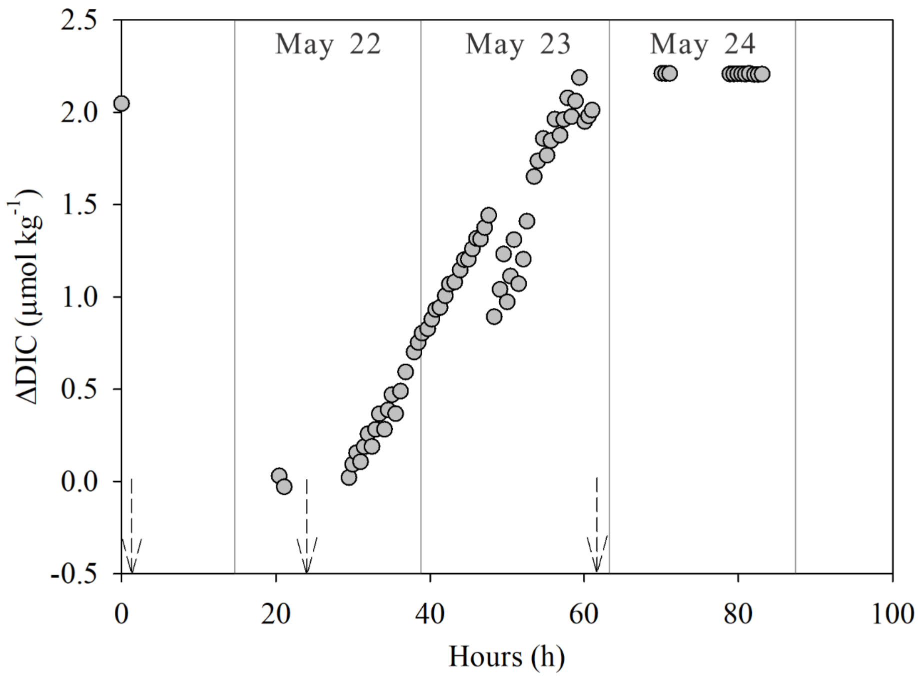

Figure A.7: Differences in DIC relative to the time of measurement. Seawater from the Gulf of Mexico was used in these analyses to check the instrument drift over time. Differences in DIC values were estimated by (i) using the calibration curve of the 1st day (May 22) and (ii) the calibration curves of each individual day (May 22-24). The three dashed arrows indicate times when standards were run. Note that the dot in May 21 is a warm up test before carrying out the standard measurement.

Comparison of different calibration methods

Three different calibration methods were compared in our lab evaluation to see if single-point calibration could substitute for regular calibrations for DIC (three-point calibration) and δ^{13}C-DIC (two-point calibration) in daily operation, so as to i) decrease the time cost spent on running reference materials and increase the sample measurement efficiency; and ii) establish a correction relationship between single-point and regular calibrations. The first method used CRM in three different sample volumes to bracket the net integration area of samples for DIC calibration and two IRMS-verified isotopic standards STD1 and STD2 to calibrate the δ^{13}C-DIC. This approach is similar to the calibrations of DIC in NDIR and of δ^{13}C-DIC in IRMS. The second method used one standard SGL2, whose DIC and δ^{13}C-DIC have been verified on NDIR and IRMS, also in three different sample volumes. Thus, SGL2 could produce a working curve of carbon content (μmol C) vs. net area bracketing all the samples for DIC calibration, and one known isotopic value to calibrate δ^{13}C-DIC. For the third method, the data of middle sample volume of SGL2 was chosen to calibrate DIC and δ^{13}C-DIC so as to minimize the calibration time.

As shown in Fig. A.8a, the first two methods had similar results for DIC offset relative to NDIR, while the third method had a more positive offset at DIC < 1200 μmol kg^{-1}, but more negative offset at DIC > 1400 μmol kg^{-1}. This is because the assumption behind single-point calibration for DIC, that is, a unit net integration area represents a constant carbon content, is not true in this case. There was an increasing trend for carbon content per unit net area at low net area < 120000, but it remained constant thereafter (Fig. A.9). The net integration area of the prepared solutions and aged GOM seawater ranged from 50505 to 10366, existing on the increasing zone. As the middle volume of SGL2 in the third method with net area of 89541±73 and 6.04×10^{-5} μmol C per unit net area was adopted for calibration, the DIC of prepared solutions and aged GOM seawater with net area < 89541 were overestimated, and > 89541 were underestimated. The over- or under-estimates are within ±4 μmol kg^{-1} compared with the first and second methods. When considering the relationship between net area and carbon content per unit net integration area of SGL2 in three different volumes (Fig. A.9), we can recalibrate the SGL2 middle volume calibration data and get similar results as the first and second methods (Fig. A.8a).

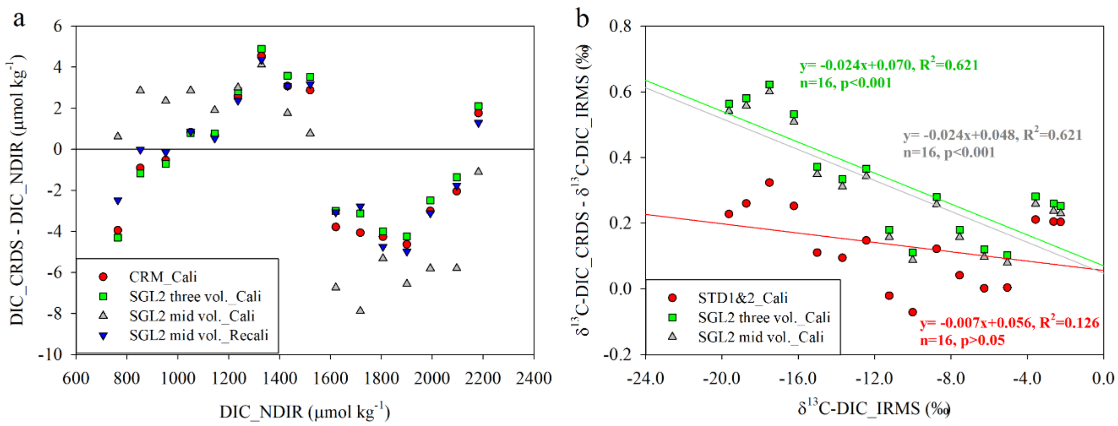

Figure A.8: Comparison of the offset values (i.e., DIC_CRDS - DIC_NDIR and δ^{13}C-DIC_CRDS - δ^{13}C-DIC_IRMS) using different calibration methods. (a) For DIC, three volumes of CRM (red), three volumes of SGL2 (green) and a middle volume of SGL2 (grey) were used to calibrate the output data. The results of the middle volume SGL2 calibration (blue) were further recalibrated so as to remove the systematic error from single-point calibration. (b) For δ^{13}C-DIC, one volume of STD1 (-2.74±0.10 ‰) and STD2 (-19.17±0.10 ‰) each (red), three volumes of SGL2 (-2.20±0.10 ‰) (green) and a middle volume of SGL2 (grey) were used to calibrate the output data.

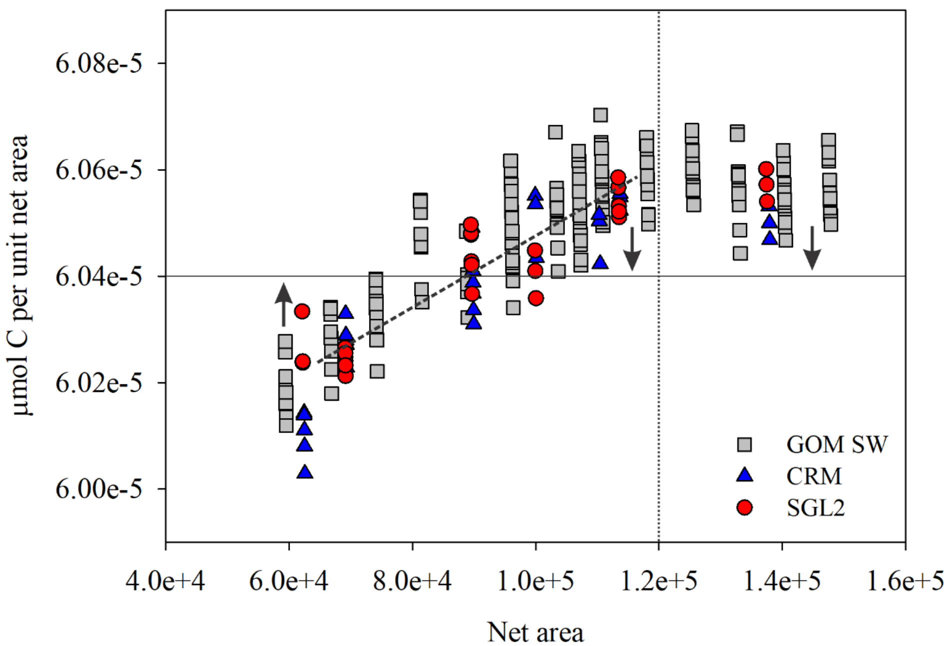

Figure A.9: The relationship between DIC content (µmol C) of unit net area and net area. The vertical dotted line is a reference line separating an increasing zone in the left and a constant zone in the right. The horizontal solid line indicates the average value (6.04×10^{-5} µmol C per unit net area) of the middle volume of SGL2 analyzed, which was adopted in the third method of DIC calibration (see text). The systematic errors affecting the third method are denoted by arrows, where an upward arrow indicates an overestimate and a downward arrow indicates an underestimate. The dashed line represents the linear regression line of three volumes (2.0, 2.6, and 3.3 mL) of SGL2 with R^2=0.89.

As for δ^{13}C-DIC, the first method uses a linear regression of measured and true δ^{13}C-DIC values of two laboratory reference standards, i.e., STD1 and STD2, to normalize the measured δ^{13}C of unknown samples to the true δ^{13}C in the isotope reference scale (Paul et al., 2007). The two-point normalization method has been proven to efficiently evaluate the consistency of δ^{13}C measurements in interlaboratory comparison work (Coplen et al., 2006), and it has been implemented in the Laboratory Information Management System distributed by the United States Geological Survey (Paul et al., 2007). The offset between the first calibration method and IRMS values is 0.13±0.12 ‰, approaching the analytical precision of isotopic measurements. The second and third calibration methods are single-point normalizations referencing a laboratory isotopic standard SGL2 (-2.20±0.10 ‰), using the measured and true values of the reference standard to calibrate the measured values of samples. Their offset relative to δ^{13}C-DIC_IRMS systematically increased from 0.08 to 0.62 ‰ as the absolute δ^{13}C-DIC difference between samples and reference standard increased from 0.04 to 17.43 ‰ (Fig. A.8b). Paul et al. (2007) mathematically demonstrated this kind of systematic error associated with single-point anchoring.

Overall, we suggest that three different CRM volumes be used to calibrate DIC concentration, and two different isotopic standards be used to calibrate δ^{13}C-DIC value, ensuring that the ranges of net area and isotope content of samples are covered by the standards.

DIC and δ^{13}C-DIC in the Chesapeake Bay

For the field samples, the DIC values measured by CRDS had an average precision of 0.7±0.5 μmol kg^{-1}, and agreed well with those measured by NDIR (DIC_NDIR=0.9921×DIC_CRDS+12.727, R^2=0.9999). The average offset between measured DIC_CRDS and DIC_NDIR was only -0.6±3.8 μmol kg^{-1}, which is close to that of the lab test. The δ^{13}C-DIC values of the field samples determined by CRDS had an average precision of 0.05±0.02 ‰, but were not verified by IRMS. However, according to the relationship between single-point calibrated δ^{13}C-DIC_CRDS and IRMS measured δ^{13}C-DIC (i.e., δ^{13}C-DIC_IRMS) in Fig. A.8b (grey), the average offset between methods was -0.12±0.05 ‰, which is also close to that of the lab test. Further corrections were not made to the single-point calibrated DIC_CRDS and δ^{13}C-DIC_CRDS because their average offset between methods were close to the precision and accuracy of measurements. As salinity increased, DIC increased from 951.2 μmol kg^{-1} at the uppermost station CB2.1 to 1894.6 μmol kg^{-1} in deep water in the middle bay (Fig. A.10). Meanwhile, δ^{13}C-DIC increased from -7.68 ‰ near the freshwater zone to -0.73 ‰ in the surface water of CB5.5. Generally, DIC was lower and δ^{13}C-DIC was heavier in the surface water of the middle bay, while DIC became enriched and δ^{13}C-DIC became more depleted as depth increased.

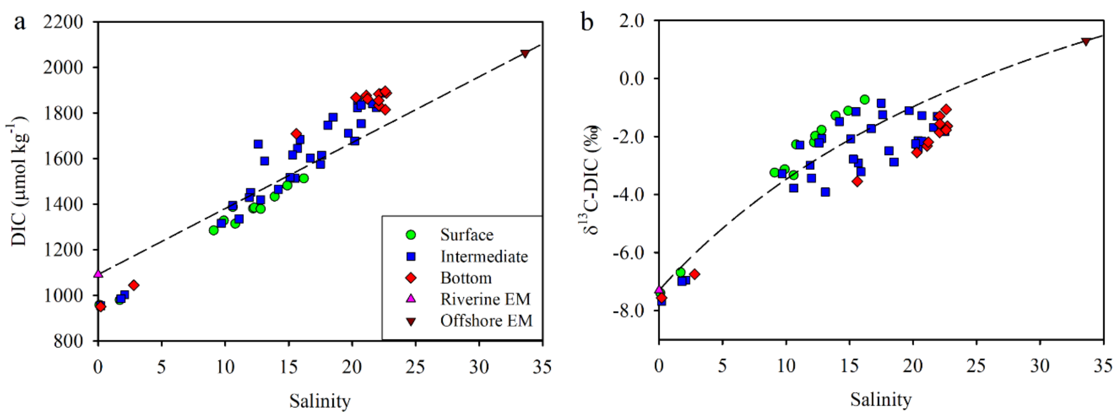

Figure A.10: Distributions of DIC and δ^{13}C-DIC against salinity in the Chesapeake Bay in May 2016. The dashed lines indicate conservative mixing between Susquehanna River water and offshore seawater in the Mid-Atlantic Bight.

Two-endmember mixing model

In estuaries and coastal environments, physical mixing between freshwater and seawater usually dominates the distribution of DIC and δ^{13}C-DIC. These parameters are also altered by different biogeochemical processes such as air-water CO_2 exchange, biological production and organic matter degradation (Alling et al., 2012; Samanta et al., 2015). In this study, we aimed to remove the effect of physical mixing and focus on the biogeochemical processes by using the DIC and δ^{13}C-DIC data. A two-endmember mixing model between the Susquehanna River endmember at Conowingo Dam and the offshore seawater endmember in the Mid-Atlantic Bight was adopted to predict the conservative values of DIC and δ^{13}C-DIC driven by physical mixing in the Chesapeake Bay.

Using salinity as a conservative tracer, the mixing fractions between river water and seawater for each sample can be quantified using equations (3) and (4):

$$f_R + f_{SW} = 1 \tag{3}$$

$$S_R \times f_R + S_{SW} \times f_{SW} = S_{meas} \tag{4}$$

S represents salinity; *f* is the mixing fraction; the subscripts *R* and *SW* denote the River and Seawater endmember, and *meas* represents the measured value. These fractions were applied to predict conservative DIC and δ^{13}C-DIC resulting solely from two-endmember mixing:

$$DIC_{mix} = DIC_R \times f_R + DIC_{SW} \times f_{SW} \tag{5}$$

$$\delta^{13}C\text{-}DIC_{mix} = \frac{\delta^{13}C\text{-}DIC_R \times DIC_R \times f_R + \delta^{13}C\text{-}DIC_{SW} \times DIC_{SW} \times f_{SW}}{DIC_{mix}} \tag{6}$$

Subscript *mix* means conservative mixing value.

For the riverine DIC endmember, we compiled the historical DIC data measured by Cai's lab during August 2015-April 2017 (n=35) with the daily discharge rate Q from USGS (Site number 01578310), and then obtained linear relationships of DIC vs. LogQ (DIC= -540*LogQ+2714, R^2=0.49, p<0.0001). Considering the relatively long residence time of ~180 days in the Chesapeake Bay (Du and Shen, 2016), the specific discharge rate during the cruise period and 30 days prior was used to derive the riverine DIC endmember value (i.e., 1091.7±73.6 μmol kg^{-1}). Although the discharge varied ~20 % during the cruise period and multiple periods (10, 20, 30, 50, 70 and 90 d) prior to the cruise, it had only a small influence on the derived riverine DIC endmember values (< 5 %), within the uncertainty listed in Table A.1. Hossler and Bauer (2012) monitored the carbon isotopes of DIC in eight rivers in the U.S. east coast, including the Susquehanna River, at approximately 3-4 month intervals during 2005-2007, and observed a general pattern of summer-depleted and winter-enriched δ^{13}C-DIC signatures. The average value of δ^{13}C-DIC in the spring and summer of 2006 was adopted as the riverine δ^{13}C-DIC endmember value (-7.3±0.2 ‰). For the offshore DIC endmember, a linear regression of DIC vs. salinity (DIC=79.1*Sal-596.5, R^2=0.72) was derived with data from four stations (Sta. 82, 83, 85 and 87) in the Mid-Atlantic Bight, which were visited in the East Coast Ocean Acidification (ECOA) cruise in July 2015. Then, the salinity of the ocean endmember (33.618±0.139 psu) in Cai et al. (2017) was used to derive the offshore DIC endmember value (2063.5±11.0 μmol kg^{-1}). Quay et al. (2007) compiled data from 28 cruises since 1986 to summarize the meridional trends of δ^{13}C-DIC in the surface Atlantic Ocean in three time domains, the 1980s, 1990s and 2000s. According to the latitude range of the Chesapeake Bay (36-40 °N), the offshore δ^{13}C-DIC endmember value was adopted as 1.3±0.1 ‰. Both the offshore seawater DIC and δ^{13}C-DIC endmember values fall into the ranges in the Mid-Atlantic Bight reported by Bauer et al. (2001).

Table A.1: Summary of endmember values and their uncertainties.

Endmembers	Salinity (psu)	DIC (μmol kg^{-1})	δ^{13}C-DIC (‰)
Riverine	0	1091.7±73.6	-7.3±0.2[a]
Offshore	33.618±0.139[b]	2063.5±11.0	1.3±0.1[c]

[a]Average value of δ^{13}C-DIC in the Susquehanna River in the spring and summer of 2006 in Hossler and Bauer (2012).
[b]The salinity of the ocean endmember in Cai et al. (2017).
[c]Cited from Quay et al. (2007) according to the latitude range of the Chesapeake Bay (36-40 °N).

Main biogeochemical controls on DIC composition in the Chesapeake Bay

Using the river and offshore endmember values determined above, conservative mixing lines for DIC and for δ^{13}C-DIC against salinity were established (Fig. A.10). A significant number of DIC and δ^{13}C-DIC data points were distributed above or beneath the conservative mixing lines, indicating that other processes played an important role in DIC and its isotope distributions in the Chesapeake Bay (Fig. A.10). Since the processes that change DIC may have distinct δ^{13}C source values and isotopic fractionation, it is advantageous to use both DIC and δ^{13}C-DIC to distinguish them. Using a method similar to Alling et al. (2012) and Samanta et al. (2015), the fractional deviations of DIC (ΔDIC) and δ^{13}C-DIC ($\Delta\delta^{13}$C-DIC) relative to the conservative mixing values were calculated according to the following equations.

$$\Delta DIC = \frac{DIC_{meas} - DIC_{mix}}{DIC_{mix}} \quad (3)$$

$$\Delta\delta^{13}C\text{-}DIC = \delta^{13}C\text{-}DIC_{meas} - \delta^{13}C\text{-}DIC_{mix} \quad (4)$$

The propagation errors of ΔDIC and $\Delta\delta^{13}$C-DIC for each sample were calculated based on Taylor's expression (Taylor, 1997; Han et al., 2012).

As shown in Fig. A.11 ($\Delta\delta^{13}$C-DIC vs. ΔDIC), the data can be explained as the combined result of five processes: CO_2 outgassing, biological production, degradation of organic carbon, carbonate precipitation and carbonate dissolution. The different vectors for the five processes were calculated according to the approach and equations given in Samanta et al. (2015). There are four likely vectors for the degradation of organic carbon, depending on the initial DIC and δ^{13}C-DIC composition in the water and the sources of organic carbon. Combining the δ^{13}C values of organic carbon from terrestrial (-28.0 ‰) and marine (-21.0 ‰) sources with the δ^{13}C-DIC endmember values in river water (-7.3 ‰) and offshore seawater (1.3 ‰), the slopes of these vectors were calculated as -20.7 (on river water or vector TR) and -29.3 (on seawater or vector TS) for degradation of terrestrial organic carbon, and -13.7 (on river water or vector MR) and -22.3 (on seawater or vector MS) for degradation of marine organic carbon. Assuming the δ^{13}C of biogenic $CaCO_3$ is 0 ‰, the slopes for carbonate dissolution were calculated as 7.3 in the low salinity zone (vector DR) and -1.3 in the high salinity zone (vector DS). As carbonate precipitation is the reverse of dissolution, the slopes of vectors for carbonate precipitation will be -7.3 and 1.3 (vectors PR & PS). Using the average temperature (13.4 °C) of the surface water in this cruise, the equilibrium fractionation factor between aqueous CO_2 and HCO_3^- were calculated as -10.2 ‰ (Rau et al., 1996). Therefore, the slope value of vector for CO_2 outgassing is -10.2. Assuming the phytoplankton preferentially utilize aqueous CO_2 as a carbon source, the photosynthesis activity would have two stages of isotopic fractionation when DIC is transferred into POC (Alling et al., 2012). In the first stage, there is a temperature-dependent equilibrium fractionation factor between δ^{13}C-DIC (approximately equal to δ^{13}C-HCO_3^-) and aqueous CO_2, which was -10.2 ‰ as mentioned before. In the second stage, the aqueous CO_2, which is equilibrated with the atmospheric CO_2 (δ^{13}C-CO_2 = -8 ‰) (Gruber et al., 1999), is incorporated into

POC with an average δ^{13}C-POC value of -23.8 ‰ (W-J. Cai unpublished data), resulting in a fractionation factor of -15.8 ‰. Thus, the total isotope fractionation between δ^{13}C-DIC and δ^{13}C-POC is calculated as -26.0 ‰ by summing up the fractionation factors in the two stages. Therefore, the slope of the vector for primary production is -26.0.

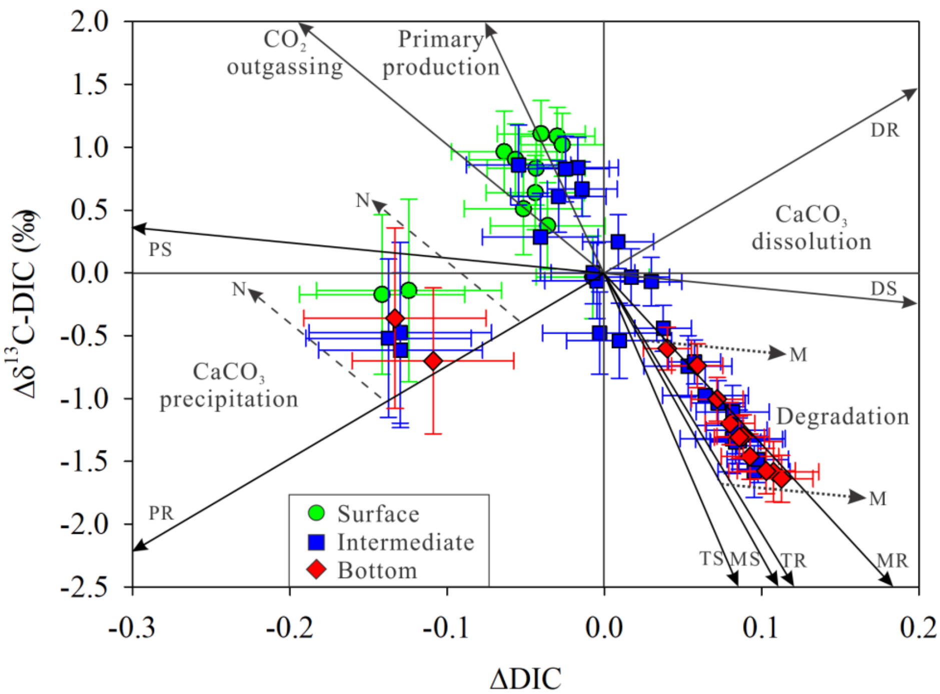

Figure A.11: The deviations of DIC concentrations (ΔDIC) and δ^{13}C-DIC ($\Delta\delta^{13}$C-DIC) relative to the conservative mixing line in the Chesapeake Bay in May 2016. Note that the origin represents the data only controlled by conservative mixing. The data points would deviate from the origin in directions shown with solid vectors if they were influenced by a specific additional process, or shown with dashed and dotted vectors if they were influenced by more than one process. See main text for details on drawing these vectors. The four vectors (TS, TR, MS, MR) represent effects of degradation of organic carbon, which depend on the sources of organic carbon (T: terrestrial source; M: marine source) and the initial DIC and δ^{13}C-DIC composition in the water (S: seawater; R: river water). Vectors DS and DR, drawn using the δ^{13}C-DIC of seawater and river water, respectively, denote the effect of $CaCO_3$ dissolution. Similarly, vectors PS and PR indicate the effect of $CaCO_3$ precipitation. Vectors in the upper left quadrant indicate the effects of primary production or CO_2 outgassing. Dashed vectors marked N, which are drawn parallel to vector CO_2 outgassing, indicate the effect of $CaCO_3$ precipitation followed by CO_2 outgassing. Dotted vectors marked M, which are drawn parallel to vector DS, illustrate the effect of degradation of organic carbon followed by $CaCO_3$ dissolution.

All data from stations CB2.1 and 2.2 in the northern part of upper bay lie on the third quadrant (Fig. A.11), which can be explained by carbonate precipitation alone or seen as the combined results of carbonate precipitation and CO_2 outgassing. When moving southward to the southern part of the upper bay and the middle bay, most of the data in the surface water fall on the second quadrant, indicating that CO_2 outgassing and/or CO_2 removal via biological production are the main processes controlling the DIC and δ^{13}C-DIC of surface water. In contrast, the majority of data in the bottom water lie on the fourth quadrant, meaning that the DIC and δ^{13}C-DIC of the bottom water in the southern part of upper bay and the middle bay are primarily controlled by degradation of organic carbon. Data from the intermediate depths are distributed between the surface and bottom data, which is understandable as water is a continuum for mixing of dissolved chemical species.

These results are consistent with previous investigations (Kemp et al., 1997; Cai et al., 2017). For instance, Kemp et al. (1997) estimated the net ecosystem metabolism of three regions in the Chesapeake Bay along the land-sea gradient, and concluded that community respiration exceeded primary production in the upper bay, which was caused by the combined effects of allochthonous organic carbon input and high turbidity conditions that enhanced respiration and inhibited photosynthesis (Smith and Kemp, 1995). Cai et al. (2017) measured supersaturated pCO_2 and undersaturated O_2 in the northern regions of the bay, confirming that the CO_2 outgassing process prevailed in the upper bay surface water. Su et al. (2018, in preparation) found that the submerged aquatic vegetation (SAV) beds in the shallow regions along the bay, such as SAVs in the Susquehanna Flats, can work as biogenic $CaCO_3$ factories to produce $CaCO_3$ solids on a local scale. Thus, carbonate precipitation and CO_2 outgassing control the distribution of DIC and δ^{13}C-DIC in the northern part of the upper bay. In contrast to net heterotrophy in the upper bay, the integrated metabolism in the middle bay is nearly balanced and net autotrophy dominates in the lower bay (Kemp et al., 1997). Given the two-layer structure in the water column in the middle bay in May (Schubel and Pritchard, 1986), the carbonate and oxygen vertical dynamics would be distinct, with pCO_2 undersaturated and oxygen supersaturated in the surface water and an increasing DIC enrichment and oxygen deficit as depth increases in the water below the pycnocline. The underway pCO_2 measurement in this cruise showed that the surface water in the middle bay is a weak sink of atmospheric CO_2 (W-J. Cai unpublished data), which is consistent with previous published work (Cai et al., 2017). In the bottom water of the middle bay, oxygen is seasonally depleted due to the deep channel topography, water stratification and supply of labile autochthonous organic matter. Oxygen-based estimates of metabolism have demonstrated that bottom-layer net O_2 consumption rates were highly correlated with surface-layer net O_2 production rates (Smith and Kemp, 1995). Although Cai et al. (2017) concluded that carbonate dissolution can contribute up to 70 % of the total amount of TA production in the middle bay in August 2013, few data points fell in the first quadrant, indicating that carbonate dissolution was not a major controlling process for DIC and δ^{13}C-DIC in the water column in early May, 2016. However, it is possible that some $CaCO_3$ dissolution may shift the bottom data points from near vector MS to closer to vector MR (Fig. A.11). Further study is needed to resolve this issue. Long-term dissolved oxygen data have revealed that hypoxia occurs in the Chesapeake Bay from early June through September in almost every year with large biweekly variability (Murphy et al., 2011). Considering the average winter-spring (January to May) Susquehanna River flow in 2016 was 20 % below the 50-year average (1967 to 2017), the onset timing of hypoxia/anoxia in the main channel would probably have occurred later than early June (Hagy et al., 2004). This is further confirmed by another cruise conducted during 6-10 June 2016, in which hydrogen sulfide was not detected in the main channel (W-J. Cai unpublished data). For our cruise in early May, it was too early to develop a severe and large hypoxic/anoxic zone in the bottom water of middle bay, which is consistent with a much weaker signal of carbonate dissolution relative to August. Therefore, DIC and $\delta^{13}C$-DIC in the middle bay were primarily controlled by biological production and degradation of organic carbon in early May, 2016.

Conclusions

Our study demonstrates that simultaneous measurement of DIC and $\delta^{13}C$-DIC by coupling a CO_2 extraction device and CRDS can generate highly accurate and precise data, comparable to the traditional methods of NDIR for DIC analysis and IRMS for $\delta^{13}C$-DIC analysis. Consequently, this approach provides efficient and economical measurements of these two parameters with a single instrument. Other advantages include the small sample volume requirement (3-4 mL), short measurement cycle (~11 min.), and easy handling. To date, the paired DIC and $\delta^{13}C$-DIC dataset remains limited (Quay et al., 2003; Becker et al., 2012; Becker et al., 2016). Much more effort is needed to expand the temporal and spatial coverage of this database. By adding an automatic sampling module or changing the 4-port to 12-port distribution valve, our instrument can automatically measure up to eight or even more samples in each batch analysis without requiring any operator attention, which could thus save time and labor during analyses. In addition, the advantages of easy handling and high stability indicate the system has the potential to conduct continuous shipboard measurements or be deployed in the field for a relatively long period. However, further testing is needed to confirm the potential of this technique. Using data of DIC and δ^{13}C-DIC from the Chesapeake Bay field survey on 4-6 May 2016, we conclude that DIC and its isotopic composition were primarily controlled by carbonate precipitation and CO_2 outgassing in the northern regions of the upper bay, but by primary production and degradation of organic carbon in the southern parts of upper bay and the middle bay. This application provides new insight for distinguishing the main controls on DIC and δ^{13}C-DIC in estuarine and coastal environments. By improving the mode of sample introduction, the system offers the potential to expand the temporal and spatial coverage of paired DIC and δ^{13}C-DIC, facilitating future research into complex carbonate system questions across a wide range of aquatic settings.

REFERENCES

Alling, V., Porcelli, D., Mörth, C.M., Anderson, L.G., Sanchez-Garcia, L., Gustafsson, Ö., Andersson, P.S. and Humborg, C., 2012. Degradation of terrestrial organic carbon, primary production and out-gassing of CO_2 in the Laptev and East Siberian Seas as inferred from $\delta^{13}C$ values of DIC. Geochim. Cosmochim. Acta 95, 143-159. doi:10.1016/j.gca.2012.07.028

Amornthammarong, N., Ortner, P.B., Hendee, J. and Woosley, R., 2014. A simplified coulometric method for multi-sample measurements of total dissolved inorganic carbon concentration in marine waters. Analyst 139, 5263-5270. doi:10.1039/C4AN01049C

Becker, M., Andersen, N., Fiedler, B., Fietzek, P., Körtzinger, A., Steinhoff, T. and Friedrichs, G., 2012. Using cavity ringdown spectroscopy for continuous monitoring of $\delta^{13}C(CO_2)$ and fCO_2 in the surface ocean. Limnol. Oceanogr. Methods 10, 752-766. doi:10.4319/lom.2012.10.752

Becker, M., Andersen, N., Erlenkeuser, H., Humphreys, M.P., Toste, T. and Körtzinger, A., 2016. An internally consistent dataset of $\delta^{13}C$-DIC in the North Atlantic Ocean - NAC13v1. Earth Syst. Sci. Data 8, 559-570. doi:10.5194/essd-8-559-2016

Bergamaschi, P., Schupp, M. and Harris, G.W., 1994. High-precision direct measurements of $^{13}CH_4/^{12}CH_4$ and $^{12}CH_3D/^{12}CH_4$ ratios in atmospheric methane sources by means of a long-path tunable diode laser absorption spectrometer. Appl. Opt. 33, 7704-7716. doi:10.1364/AO.33.007704

Bianchi, T.S., 2011. The role of terrestrially derived organic carbon in the coastal ocean: A changing paradigm and the priming effect. Proc. Natl. Acad. Sci. U.S.A. 108, 19473-19481. doi:10.1073/pnas.1017982108

Boicourt, W.C., Kuzmić, M. and Hopkins, T.S., 1999. The inland sea: circulation of Chesapeake Bay and the Northern Adriatic. In: Malone, T.C., Malej, A., Harding Jr, L.W., Smodlaka, N. and Turner, R.E. (Eds.), Ecosystems at the land-sea margin: drainage basin to coastal sea. American Geophysical Union, Washington, DC, pp. 81-129.

Cai, W.-J., Huang, W.-J., Luther, G.W., Pierrot, D., Li, M., Testa, J., Xue, M., Joesoef, A., Mann, R., Brodeur, J., Xu, Y.-Y., Chen, B., Hussain, N., Waldbusser, G.G., Cornwell, J. and Kemp, W.M., 2017. Redox reactions and weak buffering capacity lead to acidification in the Chesapeake Bay. Nat. Commun. 8, 369. doi:10.1038/s41467-017-00417-7

Call, M., Schulz, K.G., Carvalho, M.C., Santos, I.R. and Maher, D.T., 2017. Technical note: Coupling infrared gas analysis and cavity ring down spectroscopy for

autonomous, high-temporal-resolution measurements of DIC and δ^{13}C–DIC. Biogeosciences 14, 1305-1313. doi:10.5194/bg-14-1305-2017
Cardenas-Valencia, A.M., Adornato, L.R., Bell, R.J., Byrne, R.H. and Short, R.T., 2013. Evaluation of reagentless pH modification for in situ ocean analysis: determination of dissolved inorganic carbon using mass spectrometry. Rapid Commun. Mass Spectrom. 27, 635-642. doi:10.1002/rcm.6487
Cheng, L., Normandeau, C., Bowden, R., Doucett, R., Gallagher, B., Gillikin, D.P., Kumamoto, Y., McKay, J.L., Middlestead, P., Ninnemann, U., Nothaft, D., Dubinina, E.O., Quay, P., Reverdin, G., Shirai, K., Mørkved, P.T., Theiling, B.P., van Geldern, R. and Wallace, D.W.R., 2019. An international intercomparison of stable carbon isotope composition measurements of dissolved inorganic carbon in seawater. Limnol. Oceanogr. Methods 17, 200-209. doi:10.1002/lom3.10300
Coplen, T.B., Brand, W.A., Gehre, M., Gröning, M., Meijer, H.A.J., Toman, B. and Verkouteren, R.M., 2006. New Guidelines for δ^{13}C Measurements. Anal. Chem. 78, 2439-2441. doi:10.1021/ac052027c
Crosson, E.R., 2008. A cavity ring-down analyzer for measuring atmospheric levels of methane, carbon dioxide, and water vapor. Appl. Phys. B 92, 403-408. doi:10.1007/s00340-008-3135-y
Dickson, A.G., Sabine, C.L. and Christian, J.R. (Eds.), 2007. Guide to best practices for ocean CO_2 measurements. PICES Special Publication 3, 191 pp.
Du, J. and Shen, J., 2016. Water residence time in Chesapeake Bay for 1980–2012. J. Mar. Syst. 164, 101-111. doi:10.1016/j.jmarsys.2016.08.011
Friederich, G.E., Walz, P.M., Burczynski, M.G. and Chavez, F.P., 2002. Inorganic carbon in the central California upwelling system during the 1997–1999 El Niño–La Niña event. Prog. Oceanogr. 54, 185-203. doi:10.1016/S0079-6611(02)00049-6
Friedrichs, G., Bock, J., Temps, F., Fietzek, P., Körtzinger, A. and Wallace, D.W.R., 2010. Toward continuous monitoring of seawater $^{13}CO_2/^{12}CO_2$ isotope ratio and $p$$CO_2$: Performance of cavity ringdown spectroscopy and gas matrix effects. Limnol. Oceanogr. Methods 8, 539-551. doi:10.4319/lom.2010.8.539
Gruber, N., Keeling, C.D., Bacastow, R.B., Guenther, P.R., Lueker, T.J., Wahlen, M., Meijer, H.A.J., Mook, W.G. and Stocker, T.F., 1999. Spatiotemporal patterns of carbon-13 in the global surface oceans and the oceanic suess effect. Global Biogeochem. Cycles 13, 307-335. doi:10.1029/1999gb900019
Hagy, J.D., Boynton, W.R., Keefe, C.W. and Wood, K.V., 2004. Hypoxia in Chesapeake Bay, 1950–2001: Long-term change in relation to nutrient loading and river flow. Estuaries 27, 634-658. doi:10.1007/BF02907650
Han, A., Dai, M., Kao, S.-J., Gan, J., Li, Q., Wang, L., Zhai, W. and Wang, L., 2012. Nutrient dynamics and biological consumption in a large continental shelf system under the influence of both a river plume and coastal upwelling. Limnol. Oceanogr. 57, 486-502. doi:10.4319/lo.2012.57.2.0486

Hellings, L., Dehairs, F., Tackx, M., Keppens, E. and Baeyens, W., 1999. Origin and fate of organic carbon in the freshwater part of the Scheldt Estuary as traced by stable carbon isotope composition. Biogeochemistry 47, 167-186. doi:10.1007/BF00994921

Hu, X., Cai, W.-J., Rabalais, N.N. and Xue, J., 2016. Coupled oxygen and dissolved inorganic carbon dynamics in coastal ocean and its use as a potential indicator for detecting water column oil degradation. Deep Sea Res. Part II Top. Stud. Oceanogr. 129, 311-318. doi:10.1016/j.dsr2.2014.01.010

Huang, K., Cassar, N., Wanninkhof, R. and Bender, M., 2013. An isotope dilution method for high-frequency measurements of dissolved inorganic carbon concentration in the surface ocean. Limnol. Oceanogr. Methods 11, 572-583

Huang, K., Cassar, N., Jonsson, B., Cai, W.-J. and Bender, M.L., 2015. An Ultrahigh Precision, High-Frequency Dissolved Inorganic Carbon Analyzer Based on Dual Isotope Dilution and Cavity Ring-Down Spectroscopy. Environ. Sci. Technol. 49, 8602-8610. doi:10.1021/acs.est.5b01036

Huang, W.J., Wang, Y. and Cai, W.J., 2012. Assessment of sample storage techniques for total alkalinity and dissolved inorganic carbon in seawater. Limnol. Oceanogr. Methods 10, 711-717. doi:10.4319/lom.2012.10.711

Humphreys, M.P., Achterberg, E.P., Griffiths, A.M., McDonald, A. and Boyce, A.J., 2015. Measurements of the stable carbon isotope composition of dissolved inorganic carbon in the northeastern Atlantic and Nordic Seas during summer 2012. Earth Syst. Sci. Data 7, 127-135

Jäger, F., Wagner, G., Meijer, H.A.J. and Kerstel, E.R.T., 2005. Measuring $\delta^{13}C$ of atmospheric air with non-dispersive infrared spectroscopy. Isotopes Environ. Health Stud. 41, 373-378. doi:10.1080/10256010500384275

Jost, H.-J., Castrillo, A. and Wilson, H.W., 2006. Simultaneous $^{13}C/^{12}C$ and $^{18}O/^{16}O$ isotope ratio measurements on CO_2 based on off-axis integrated cavity output spectroscopy. Isotopes Environ. Health Stud. 42, 37-45. doi:10.1080/10256010500503163

Kemp, W., Boynton, W., Adolf, J., Boesch, D., Boicourt, W., Brush, G., Cornwell, J., Fisher, T., Glibert, P. and Hagy, J., 2005. Eutrophication of Chesapeake Bay: historical trends and ecological interactions. Mar. Ecol. Prog. Ser. 303, 1-29. doi:10.3354/meps303001

Kemp, W.M., Smith, E.M., Marvin-DiPasquale, M. and Boynton, W.R., 1997. Organic carbon balance and net ecosystem metabolism in Chesapeake Bay. Mar. Ecol. Prog. Ser. 150, 229-248. doi:10.3354/meps150229

Mohn, J., Werner, R.A., Buchmann, B. and Emmenegger, L., 2007. High-precision $\delta^{13}CO_2$ analysis by FTIR spectroscopy using a novel calibration strategy. J. Mol. Struct. 834-836, 95-101. doi:10.1016/j.molstruc.2006.09.024

Murphy, R.R., Kemp, W.M. and Ball, W.P., 2011. Long-Term Trends in Chesapeake Bay Seasonal Hypoxia, Stratification, and Nutrient Loading. Estuar. Coast. 34, 1293-1309. doi:10.1007/s12237-011-9413-7

Nara, H., Tanimoto, H., Tohjima, Y., Mukai, H., Nojiri, Y., Katsumata, K. and Rella, C., 2012. Effect of air composition (N_2, O_2, Ar, and H_2O) on CO_2 and CH_4 measurement by wavelength-scanned cavity ring-down spectroscopy: calibration and measurement strategy. Atmos. Meas. Tech. 5, 2689

O'Sullivan, D.W. and Millero, F.J., 1998. Continual measurement of the total inorganic carbon in surface seawater. Mar. Chem. 60, 75-83. doi:10.1016/S0304-4203(97)00079-0

Paul, D., Skrzypek, G. and Fórizs, I., 2007. Normalization of measured stable isotopic compositions to isotope reference scales – a review. Rapid Commun. Mass Spectrom. 21, 3006-3014. doi:10.1002/rcm.3185

Quay, P., Sonnerup, R., Westby, T., Stutsman, J. and McNichol, A., 2003. Changes in the $^{13}C/^{12}C$ of dissolved inorganic carbon in the ocean as a tracer of anthropogenic CO_2 uptake. Global Biogeochem. Cycles 17, 4-1-4-20. doi:10.1029/2001GB001817

Rau, G.H., Riebesell, U. and Wolf-Gladrow, D., 1996. A model of photosynthetic ^{13}C fractionation by marine phytoplankton based on diffusive molecular CO_2 uptake. Mar. Ecol. Prog. Ser. 133, 275-285

Samanta, S., Dalai, T.K., Pattanaik, J.K., Rai, S.K. and Mazumdar, A., 2015. Dissolved inorganic carbon (DIC) and its $\delta^{13}C$ in the Ganga (Hooghly) River estuary, India: Evidence of DIC generation via organic carbon degradation and carbonate dissolution. Geochim. Cosmochim. Acta 165, 226-248. doi:10.1016/j.gca.2015.05.040

Schubel, J. and Pritchard, D., 1986. Responses of upper Chesapeake Bay to variations in discharge of the Susquehanna River. Estuaries 9, 236-249. doi:10.2307/1352096

Smith, E.M. and Kemp, W.M., 1995. Seasonal and regional variations in plankton community production and respiration for Chesapeake Bay. Mar. Ecol. Prog. Ser. 116, 217-231

Su, J., Dai, M., He, B., Wang, L., Gan, J., Guo, X., Zhao, H. and Yu, F., 2017. Tracing the origin of the oxygen-consuming organic matter in the hypoxic zone in a large eutrophic estuary: the lower reach of the Pearl River Estuary, China. Biogeosciences 14, 4085-4099. doi:10.5194/bg-14-4085-2017

Taylor, J.R., 1997. Introduction to error analysis, the Study of Uncertainties in Physical Measurements, 2nd Edition. University Science Books, New York.

van Geldern, R., Verma, M.P., Carvalho, M.C., Grassa, F., Delgado-Huertas, A., Monvoisin, G. and Barth, J.A.C., 2013. Stable carbon isotope analysis of dissolved inorganic carbon (DIC) and dissolved organic carbon (DOC) in natural waters – Results from a worldwide proficiency test. Rapid Commun. Mass Spectrom. 27, 2099-2107. doi:10.1002/rcm.6665

Wahl, E.H., Fidric, B., Rella, C.W., Koulikov, S., Kharlamov, B., Tan, S., Kachanov, A.A., Richman, B.A., Crosson, E.R., Paldus, B.A., Kalaskar, S. and Bowling, D.R., 2006. Applications of cavity ring-down spectroscopy to high precision isotope ratio measurement of $^{13}C/^{12}C$ in carbon dioxide. Isotopes Environ. Health Stud. 42, 21-35. doi:10.1080/10256010500502934

Wang, H., Dai, M., Liu, J., Kao, S.-J., Zhang, C., Cai, W.-J., Wang, G., Qian, W., Zhao, M. and Sun, Z., 2016. Eutrophication-Driven Hypoxia in the East China Sea off the Changjiang Estuary. Environ. Sci. Technol. 50, 2255-2263. doi:10.1021/acs.est.5b06211

Wang, Z.A., Liu, X., Byrne, R.H., Wanninkhof, R., Bernstein, R.E., Kaltenbacher, E.A. and Patten, J., 2007. Simultaneous spectrophotometric flow-through measurements of pH, carbon dioxide fugacity, and total inorganic carbon in seawater. Anal. Chim. Acta 596, 23-36. doi:10.1016/j.aca.2007.05.048

Yang, X., Xue, L., Li, Y., Han, P., Liu, X., Zhang, L. and Cai, W.-J., 2018. Treated Wastewater Changes the Export of Dissolved Inorganic Carbon and Its Isotopic Composition and Leads to Acidification in Coastal Oceans. Environ. Sci. Technol. 52, 5590-5599. doi:10.1021/acs.est.8b00273

Zeebe, R.E. and Wolf-Gladrow, D.A., 2001. CO_2 in seawater: equilibrium, kinetics, isotopes. Elsevier, Amsterdam.

Appendix B

PERMISSION

Title: Simultaneous determination of dissolved inorganic carbon (DIC) concentration and stable isotope (δ^{13}C-DIC) by Cavity Ring-Down Spectroscopy: Application to study carbonate dynamics in the Chesapeake Bay

Authors: Jianzhong Su, Wei-Jun Cai, Najid Hussain, Jean Brodeur, Baoshan Chen, and Kuan Huang

Publication: Marine Chemistry

Publisher: Elsevier

Date: 27 July 2019

Citation: Su, J., Cai, W.-J., Hussain, N., Brodeur, J., Chen, B. and Huang, K., 2019. Simultaneous determination of dissolved inorganic carbon (DIC) concentration and stable isotope (δ^{13}C-DIC) by Cavity Ring-Down Spectroscopy: Application to study carbonate dynamics in the Chesapeake Bay. Mar. Chem., 103689. doi:10.1016/j.marchem.2019.103689

Please note that, as the author of this Elsevier article, I retain the right to include it in a thesis or dissertation, provided it is not published commercially. For more information on this, please visit: https://www.elsevier.com/about/our-business/policies/copyright#Author-rights